Exploring ultracold trapped cesium Feshbach molecules

Dissertation
zur Erlangung des akademischen Grades
Doktor der Naturwissenschaften

eingereicht an der
Fakultät für Mathematik, Informatik und Physik
der Universität Innsbruck

von

Michael Mark

Betreuer der Dissertation:
Univ.-Prof. Dr. Rudolf Grimm,
Institut für Experimentalphysik

Innsbruck, Jänner 2008

Abstract

Cesium is an outstanding candidate in the field of ultracold quantum gases as it provides a very rich molecular energy structure. Various Feshbach resonances are available to efficiently produce ultracold molecules. Moreover, these resonances serve as "entrance doors" into the complex molecular structure near threshold. In the context of this thesis, we have thoroughly explored the molecular quantum states at low magnetic fields using various techniques.

In our experiment, we use several magnetically tunable Feshbach resonances to create Cs_2 molecules from ultracold ^{133}Cs atoms. Up to 20000 molecules confined in a crossed CO_2-laser dipole trap can be prepared at temperatures of about 250 nK. We have developed elaborate methods to transfer molecules to various internal states, to clean the population in the optical trap from remaining atoms and from molecules in unwanted states, and to detect the molecular population via controlled dissociation. In particular, we have investigated states with high orbital angular momentum which so far have been unexplored. For these states direct Feshbach association is not possible because of negligible coupling to the atomic threshold.

We have explored ro-vibrational molecular quantum states using two different techniques. Magnetic moment spectroscopy is a versatile technique which has allowed to map out the molecular spectrum up to binding energies of $E_b = h \times 10\,\mathrm{MHz}$ in a magnetic field range from 5 to 55 G. Using microwave spectroscopy, we have performed highly precise measurements of the binding energy of a particularly important s-wave state in an energy range $E_b < h \times 20\,\mathrm{MHz}$. The microwave results show the transition into a weakly bound state with quantum-halo character. Precise knowledge about this s-wave state is important for applications related to the research of universal few-body quantum physics such as Efimov's effect.

As an example for coherent manipulations of the molecular states, we have realized a time-domain molecular 'Stückelberg interferometer'. A coherent superposition of two internal molecular states is achieved by means of an appropriately chosen magnetic field ramp over an avoided crossing. In a Ramsey-type interferometer scheme we observe macroscopic matter-wave interference between the two dimer states. As a first application, we have determined the precise position and the coupling strength of the avoided crossing in good agreement with theory.

Contents

Abstract **iii**

1. Introduction **1**

2. Feshbach molecules **5**
2.1. An overview . . . 5
2.2. Interactions of ultracold atoms . . . 8
2.2.1. Long-range interactions . . . 8
2.2.2. Scattering at low temperatures . . . 9
2.2.3. Feshbach resonances . . . 12
2.2.4. Feshbach association . . . 16
2.3. Energy structure of Cesium dimers . . . 18
2.3.1. Overview of s-wave molecular states . . . 19
2.3.2. Molecular states at low magnetic field . . . 21

3. Overview of experimental methods **25**
3.1. Atomic sample preparation . . . 25
3.2. Central experimental chamber . . . 27
3.3. Magnetic field control . . . 29
3.4. Microwave setup and magnetic field calibration . . . 32
3.4.1. Microwave setup . . . 32
3.4.2. Magnetic field calibration . . . 33
3.5. Optical pre-cooling . . . 35
3.6. Optical dipole traps . . . 35
3.6.1. Large volume reservoir trap(s) . . . 35
3.6.2. 1064nm laser trap: Bose-Einstein condensation . . . 38
3.6.3. CO_2-laser trap without levitation . . . 39
3.7. Diagnostics . . . 40

4. Preparation of Cs_2 Molecules in various internal states **43**
4.1. Molecule production through Feshbach resonances . . . 43

4.2. Transfer between different molecular states 46
4.3. Molecule detection 48

5. Spectroscopy of the molecular energy structure 51
5.1. Magnetic moment spectroscopy 52
5.1.1. Bare energy levels 52
5.1.2. Avoided crossings 57
5.2. Microwave spectroscopy 61

6. Molecular 'Stückelberg interferometer' 67
6.1. Introduction 67
6.2. Interferometer playground 68
6.3. Internal-state interferometry 70
6.4. New tool for precision measurements 73

7. Outlook 77
7.1. Metastable Feshbach molecules 77
7.2. Few-body scattering phenomena 78
7.2.1. Dimer-Dimer interactions 79
7.2.2. Atom-dimer collision resonances 80

A. Magnetic field: setup and parameters 83

B. Analysis for magnetic field calibration 89

C. Model functions to analyze interferometer images 91

D. Publications 93
D.1. Metastable Feshbach molecules in high rotational states 95
D.2. Spectroscopy of ultracold, trapped cesium Feshbach molecules 99
D.3. 'Stückelberg interferometry' with ultracold molecules 113
D.4. Evidence for Efimov quantum states in an ultracold gas of caesium atoms 117
D.5. Observation of Feshbach-like resonances in collisions between ultracold molecules 121
D.6. Efficient creation of molecules from a cesium Bose-Einstein condensate . . 125
D.7. Optimized production of a cesium Bose-Einstein condensate 132
D.8. Preparation of a Pure Molecular Quantum Gas 140

Bibliography 145

1. Introduction

The development of laser cooling techniques for neutral atoms in the 1980's initiated the research field of ultracold atomic gases. Rapid success such as atomic clocks with greatly increased precision [Biz05, Hol05] came along with an enormous research interest in ultracold matter. One of the major goals right from the beginning was the experimental realization of a Bose-Einstein condensate (BEC), which allows the study of macroscopic quantum states of weakly interacting particles. In 1995, about 70 years after the theoretical prediction of condensation by Bose and Einstein [Bos24, Ein25], the alkali atoms ^{87}Rb, ^{23}Na and ^{7}Li were condensed for the first time in the lab [And95, Dav95, Bra95]. For this milestone in atomic physics the Nobel prize was awarded in 2001 [Cor02, Ket02]. Since then Bose-Einstein condensation has been in the focus of intensive research [Ing99]. The fundamental properties of BECs have been demonstrated in various experiments. Striking examples are the observation of matter-wave interference [And97] and quantized vortices [Mat99, Mad00, AS01], the formation of matter-wave solitons [Den00, Str02, Kha02] or the quantum phase transition from a superfluid to a Mott insulator [Gre02].

In view of these impressive achievements with atomic gases there has always been a substantial interest in obtaining a similar level of control for molecular quantum gases. One of the main research targets is Bose-Einstein condensation of molecular ensembles. A molecular BEC represents a system with many internal degrees of freedom and allows to study novel physical and chemical processes. A molecular BEC has been achieved for the special case of dimers composed from fermions [Joc03a, Gre03, Zwi03] and has led to an ongoing series of studies on the crossover regime between strongly and weakly bound pairs [Ing06]. Another interest in molecular systems is because of their rich internal structure, which greatly extends the application range for possible precision measurements. For example, ultracold molecular samples could highly increase the sensitivity in measurements of fundamental physical properties such as the existence of an electron dipole moment [Hud02] and a possible time variation of the fine-structure constant [Hud06, Chi06].

The reliability of preparing ultracold atomic ensembles in the lab as well as the aforementioned perspectives have motivated expanded studies on the production of ultracold molecules from atomic samples in the last few years. In general the preparation of

ultracold molecules is a great challenge. However, the use of so-called Feshbach resonances has proven to be the most fruitful approach to associate atoms into weakly bound dimers. Feshbach resonances arise as a result of resonant couplings between a two-atom scattering state and bound molecular states [Fes58, Köh06] and can be induced by applying an external magnetic field. Pure samples of Feshbach molecules were created from atomic Bose-Einstein condensates first in 2003 [Her03, Xu03, Dür04a]. Together with various achievements within this time, such as the demonstration of coherent atom-molecule coupling [Don02], the formation of ultracold molecules from atomic Fermi gases [Joc03b, Reg03, Str03, Cub03] and the observation of molecular Bose-Einstein condensation [Joc03a, Gre03, Zwi03], molecular quantum gases have come to the forefront of research. Since then Feshbach molecules were exploited for various applications [Köh06]. Prominent examples are given by investigations on strongly interacting superfluids in atomic Fermi gases [Ing06], experiments on few-body collision physics [Chi05b], the realization of molecular matter-wave optics [AS05], and by the demonstration of exotic pairs in optical lattices [Win06]. Recent experimental progress has shown that full control over all degrees of freedom can be expected for such molecules [Tha06, Vol06, Win07]. The fast progress in preparing cold molecular samples promises further developments, including fascinating perspectives for precision measurements.

Cesium, the heaviest stable alkali atom, features very unusual quantum-mechanical scattering properties and is particularly rich for experiments with molecular quantum gases. Cs offers a unique variety of different Feshbach resonances and molecular states [Chi04b]. Pronounced relativistic effects lead to strong higher-order coupling between atom pairs and molecules and between different molecular states. For the attainment of Bose-Einstein condensation in cesium [Web03b], the understanding of the complex molecular structure was a crucial factor. The interaction properties of cesium atoms were characterized by a series of atom scattering experiments where many Feshbach resonances were observed [Vul99, Chi00, Chi04b]. These experiments allowed for theoretical conclusions on the molecular energy structure [Leo00, Chi04b], obtained at the National Institute of Standards and Technology (NIST). Throughout this thesis, we will refer to the cesium molecular structure as presented in Ref. [Chi04b] as the "NIST model". It represents the theoretical basis for the experiments discussed in the following chapters.

In the context of this thesis, we report on a thorough investigation of the energy structure of weakly bound Cs_2 Feshbach molecules. These experiments are performed on ultracold molecular samples confined in a CO_2-laser trap [Tak98, Chi05b, Sta06, Zah06] and extend previous work [Chi04b] in three important ways. First, we show how all of the weakly bound molecular states can be populated based on elaborate time-dependent magnetic field control. Spectroscopy performed on various molecular states confirms

the main predictions of the NIST model and provides input for further refinements of the model. Second, we demonstrate how one can indirectly populate states with high rotational angular momentum, so-called l-wave states, by taking advantage of avoided level crossings. For these l-wave states, direct Feshbach association is not feasible because of negligible coupling with the atomic scattering continuum. Third, spectroscopy on avoided crossings between bound states yields precise information about the coupling strengths between molecular states.

In addition, we present the realization of a time-domain 'Stückelberg interferometer' based on the energy structure of the Feshbach molecules. Two subsequent passages through a weak avoided crossing between two molecular states in combination with a variable hold time lead to high-contrast population oscillations. This allows for a precise determination of the energy difference between the two molecular states. We demonstrate a high degree of control over the interferometer dynamics. The interferometric scheme provides new possibilities for precision measurements with ultracold molecules.

This thesis is organized as follows. Chapter 2 gives an overview on weakly bound Feshbach molecules. After a brief historical introduction into the field, the basics related to atomic interactions and the occurrence of Feshbach resonances are discussed. The energy structure of weakly bound Cs_2 molecules is also described in detail therein. In Chap. 3 we then present the experimental methods used for atomic sample preparation and subsequent molecule experiments. The following three chapters 4, 5 and 6 refer to our experimental findings. Chapter 4 addresses the preparation of Cs_2 molecules in various internal states. We detail our techniques for transfers between different molecular states and show how to detect the dimers. In Chap. 5 we report on spectroscopic measurements using magnetic moment and microwave techniques. We present our results on the molecular energy structure and on coupling strengths of various avoided crossings. Chapter 6 shows the realization of the time-domain internal state interferometer. Finally, Chap. 7 gives an outlook on the thesis. We present measurements on meta-stable Feshbach molecules that exist in the atomic continuum and report on recent investigations related to atom-dimer and dimer-dimer collisions.

2. Feshbach molecules

This chapter gives an introduction on weakly bound molecules associated via Feshbach resonances. Section 2.1 gives an overview on the research field of translationally cold molecular samples. Section 2.2 introduces then the various interactions between two colliding atoms together with basics of atom scattering, Feshbach resonances, and the description of weakly bound diatomic states. Finally in Sec. 2.3 the particular energy structure of Cs_2 molecules near threshold is presented.

2.1. An overview

The most efficient approach for the production of high-phase space density molecular samples is the association of ultracold atoms by using Feshbach resonances [Köh06]. Feshbach resonances are scattering resonances in binary collisions of ultracold atoms where the two-atom scattering state couples to weakly bound molecular states. Originally Feshbach resonances have been introduced in nucleon scattering physics by Feshbach [Fes58]. In the context of atom physics such scattering resonances were predicted by Stwalley [Stw76], and later by Tiesinga, Verhaar and Stoof in connection with laser-cooled atomic gases [Tie93]. During the last few years, the Feshbach resonance technique has been exploited with great success to produce large, ultracold ensembles of diatomic molecules. Prominent examples for spectacular achievements are the observation of molecular Bose-Einstein condensation [Joc03a, Gre03, Zwi03] and the creation of strongly interacting superfluids in atomic Fermi gases [Ing06].

Strategies for ultracold molecule production

In general, the creation of translationally cold molecular ensembles is quite difficult. In the research field of atomic quantum gases, laser cooling was the key technique that led to great achievements such as Bose-Einstein condensation. However, molecules have typically a complex internal energy-level structure, which makes the implementation of a simple closed cooling cycle very difficult. Thus molecules have not been accessible to direct laser cooling techniques so far. There are two basic strategies to produce ultracold

molecules, the *direct cooling* of molecules and the *association of molecules* from pre-cooled atoms.

The first strategy relies on the direct cooling of molecules coming from molecular beams or molecular vapors by means other than laser cooling. The most established technique here is sympathetic cooling of molecules with helium buffer gas [Wei98] or Coulomb crystals [Bly05]. Further examples are the slowing of polar molecules in supersonic jets with pulsed electric fields in Stark decelerators [Bet00], the formation of cold dimers on helium nano-droplets [Mud04], and the application of a velocity filter for electrostatic trapping of polar molecules [Rie05]. So far these methods have achieved temperatures in the mK range and the phase-space densities of the molecular samples are orders of magnitudes below quantum degeneracy. However, the advantage of these methods is the large variety of molecular species that can be addressed and even complex molecules can be cooled and trapped.

Another strategy is the association of molecules from atomic samples that are pre-cooled to ultralow temperatures by laser or evaporative cooling techniques. In view of the possibilities offered by ultracold atoms, this soon became a very promising route for producing ultracold molecules, which may also be quantum degenerate. The formation of bound molecules from a gas of trapped Cs atoms was demonstrated first by using photo-association techniques [Fio98]. In photo-association, two colliding atoms absorb a photon while they are transferred to an electronically excited molecular state. These molecules can then form weakly bound ground state molecules by spontaneous de-excitation [Wei99]. Although photo-association can lead to μK temperatures [Fio98, MS01, Van02], the resulting molecular phase-space densities are still far from quantum degeneracy.

Not long after the achievements via photo-association, evidence for molecules created by a Feshbach resonance was reported [Don02]. In these experiments atomic condensates of ^{85}Rb were exposed to time-dependent magnetic fields in the vicinity of a Feshbach resonance. The formation of molecules was indicated by the observation of coherent oscillations between the atomic and molecular states [Don02]. The oscillation frequency of the atom number was a measure of the binding energy of the molecules. However, up to that point the molecular ensembles could not be observed directly.

Feshbach molecules

In a series of experiments conducted in 2003, the production efficiency of molecules was increased dramatically by using magnetic field sweeps across Feshbach resonances. The group of Jin and co-workers in Boulder was able to create ultracold molecules from

a degenerate Fermi gas of ^{40}K atoms. The molecule formation was probed by radio-frequency spectroscopy [Reg03]. Shortly thereafter, our group in Innsbruck realized a pure, high phase-space density molecular sample of Cs_2 from an atomic BEC [Her03]. In this experiment molecule formation was observed by spatially separating atoms and molecules via the Stern-Gerlach technique [Her03]. Similar achievements were obtained using atomic condensates of ^{23}Na and ^{87}Rb [Xu03, Dür04a].

Around the same time this Feshbach association technique was applied to spin mixtures of ultracold fermionic atoms [Joc03b, Cub03, Str03]. With respect to inelastic collisions the molecules formed from fermionic constituents showed a remarkable stability near Feshbach resonances, which is associated with a Pauli-blocking effect [Pet04]. The lifetimes of such dimers, ranging up to seconds in $^6Li_2$ gases, allowed for the observation of molecular Bose-Einstein condensation [Joc03a, Gre03, Zwi03]. Thus the way was opened for an ongoing series of studies on the crossover between molecular condensation and superfluid Cooper pairing, also called BEC-to-BCS crossover regime [Bar04, Bar05, Chi04a, Reg04, Zwi05].

In the case of Feshbach dimers created from cold bosonic atom gases it was possible to prepare molecular ensembles near quantum degeneracy [Her03]. It was found that both, atom-molecule and molecule-molecule inelastic collisions lead to strong quenching of the 'bosonic molecules'. As a result rapid loss from the trap is observed, thus limiting the lifetime of the molecules. In atom-molecule mixtures lifetimes up to a few ten milliseconds are observed [Muk04, Kno08a]. For pure molecular samples increased lifetimes were reported only at very low densities [Chi05b] or in a lattice environment [Tha06], where the lattice prevents collisional quenching of the molecules. Hence, for dimers from bosonic atoms it is still a challenging quest for evaporative cooling towards molecular samples at high phase-space densities or even the observation of molecular Bose-Einstein condensation [Rom04].

Most of the Feshbach molecule experiments have addressed association [Mar05, Hod05, Tho05b] and dissociation processes [Muk04, Dür04b, Tho05a, Kno08b], precision spectroscopy [Cla03, Mar07a], and single molecule physics [AS05, Mar07b]. Of great research interest are also collisional properties of the weakly bound molecules for both dimer-dimer and for atom-dimer interactions [Muk04, Chi05b, Sya06, Smi07, Fer08, Kno08a]. Thus, new ways have opened up to study few-body physics with ultracold atoms [Chi05b] and to further explore universal Efimov physics [Kra06b, Kno08a]. Recently, controlled molecule formation in optical lattices [Stö06, Tha06, Osp06] has allowed the creation of novel correlated states in a crystal-like environment [Win06, Vol06]. Finally, recent approaches for transferring dimers to deeply bound molecular states [Win07] promise the realization of a molecular BEC from bosonic atoms [Kok01, Jak02].

2.2. Interactions of ultracold atoms

The properties of ultracold quantum gases are to a large extent the result of particle interactions. For example, atomic interactions lead to elastic and inelastic collisions and to higher-order scattering processes such as three-body recombination [Web03c]. In case of Bose-Einstein condensates, particle interactions are responsible for e. g. the BEC dynamics or for superfluid effects [Pit03]. Finally, scattering processes can be strongly suppressed for fermionic atoms [Ing06], while near Feshbach resonances they can be resonantly enhanced [Chi00]. Therefore, the understanding of atomic interactions is crucial.

The following section gives an overview of the basic scientific background to understand the physics of weakly bound Feshbach molecules. Section 2.2.1 describes the different interaction mechanisms between neutral ground state atoms. We then briefly introduce in Sec. 2.2.2 substantial definitions in the context of binary collisions between atoms. In Sec. 2.2.3 the scenario of a Feshbach resonance is discussed. Finally in Sec. 2.2.4 the association of molecules through Feshbach resonances is described. An extensive discussion on the physics of weakly bound Feshbach molecules can be found in the review article by Köhler [Köh06].

2.2.1. Long-range interactions

The interaction potential of two scattering atoms is determined by various interaction mechanisms between the two particles and depends on the inter-particle distance r. In the case of two neutral atoms in their ground state, the dominant interactions are the *van der Waals interaction*, the *exchange interaction*, and the *dipolar interaction*. At very large inter-atomic distances, the asymptotic energy of the two-particle system is given by the energy of the individual atoms, i. e. the kinetic energy, hyperfine interaction, and Zeeman energy.

Van der Waals and exchange interaction

The van der Waals interaction represents several induced electric multipole interactions, all of which are attractive. The largest contributing part of these electric interactions comes from the induced electric dipoles of the atoms. At large inter-atomic distances the van der Waals interaction scales as $-C_6\, r^{-6}$, with C_6 being the van der Waals coefficient. The exchange interaction arises when the two colliding atoms are close enough so that the wave functions of their electrons can overlap. As this overlap decreases exponentially with increasing r, the exchange interaction scales similarly [Wei85]. This makes the van

der Waals interaction dominant at large distances.

The coupling of the electronic spins of the individual atoms via the exchange interaction results in the well known singlet and triplet interaction potential. The singlet potential is lower as the electronic spatial wave function is symmetric.

In the process of atomic collisions, a spin-dependent interaction is required to induce transitions between the singlet and triplet states. While the van der Waals interaction only depends on the inter-atomic distance, the exchange interaction can couple singlet and triplet contributions. Consequently, this can lead in general to inelastic spin-exchange collisions. However, by spin polarizing the atoms into a stretched state this coupling is suppressed. Atoms being in their absolute ground state are also immune against exothermic inelastic processes.

Dipolar interactions

Although dipolar interactions are much weaker than the previously discussed interactions they have to be considered. Together with the atomic hyperfine structure, these weaker interactions are crucial for understanding the characteristic scattering properties of cesium and its molecular energy structure [Leo00, Chi04b].

The dipolar interactions stem from the spin-spin interactions between two atoms. To these interactions belongs a direct magnetic dipole-dipole interaction and a second-order spin-orbit interaction. The latter one is also called indirect spin-spin coupling[1] and exceptionally large for Cs atoms. Regarding the spatial dependence of the two dipolar interactions, the direct dipole-dipole coupling scales as r^{-3}. The indirect coupling drops exponentially with inter-nuclear distance, since this interaction is again proportional to the overlap of the electronic wave functions [Wei85].

The dipolar interactions couple the spins to the inter-nuclear axis [Tie93, Chi01]. As a consequence, these interactions allow an exchange of angular momentum between the internal and relative orbital angular momentum degrees of freedom. As discussed later, this corresponds to a coupling of different partial waves. Dipolar interaction is even responsible for allowing two polarized atoms to relax into other internal states and lead to inelastic processes. This is also termed inelastic spin-dipolar relaxation.

2.2.2. Scattering at low temperatures

The atomic interaction potential as discussed in the previous section determines the framework for binary scattering processes at low temperatures. In the stationary scattering-

[1] The second-order spin-orbit interaction is mediated through electronically excited states and mimics the effect of the direct spin-spin interaction [Tie93], leading to the name indirect spin-spin coupling.

picture, the collision results in a scattering wave function that contains both, the incident and the outgoing waves [Dal99, Wei99]. A convenient description of the wave function is given by a partial wave expansion, where the rotational quantum number ℓ plays a central role. For two identical bosons (fermions) the wave function is symmetric (antisymmetric) and consequently only waves with even (odd) ℓ exist. For bosonic atoms such as Cs, partial waves associated with $\ell = 0$, 2, or 4 are commonly denoted *s*-, *d*- or *g*- waves [Rus29]. A specific atomic interaction potential, defined by the internal state of each atom, represents a so-called scattering channel. Due to atomic hyperfine interactions, various scattering channels with different internal energies, i. e. the asymptotic potential energy at large distances, are provided. If the channel energy is less than the total energy of the system, the incident scattering channel is said to be 'open'. Channels with an internal energy larger than the total energy of the incident wave are no longer possible outgoing channels, and are referred to as 'closed'. For Cs atoms, the ground state hyperfine splitting is $\sim h \times 9.2$ GHz (h is Planck's constant) and thus much larger than the typical thermal collision energy of the atoms.

s-wave scattering length

At sufficiently low temperatures the relative kinetic energy of the scattering atoms E_c is small and the collision is solely reduced to scattering of incident *s*-waves, which greatly simplifies the scattering problem. Atoms with orbital angular momentum $\ell \neq 0$ are screened from the interaction range by the repulsive centrifugal potential. The collision energy $E_c = \hbar^2 k^2 / 2m^*$ is determined by the reduced mass m^* and the relative momentum $\hbar k$ with $\hbar$ being Planck's constant divided by 2π. In the limit of zero collision energy, where the relative momentum of the colliding atoms approaches zero, all information about the collision is contained in a phase shift $\delta_0(k)$ between the incident and the outgoing wave function. Equivalently, this phase shift can be represented by the so-called *s*-wave scattering length a according to $a = -\lim_{k\to 0} \tan(\delta_0(k))/k$ [Dal99]. The sign of the scattering length describes an effective repulsive ($a > 0$) or attractive ($a < 0$) interaction between the atoms. Therefore, in the context of ultracold gases, the scattering length is very useful since the intrinsically complex effects of a collision between two atoms are characterized by this single quantity[2]. The scattering length also fully determines the elastic scattering cross section in the zero-energy limit and scales as a^2 [Dal99]. At higher collision energies, the elastic cross section is well described by $\sigma_{\mathrm{el}}(k) = 8\pi a^2/(1 + k^2 a^2)$ for bosons. While the condition $ka \ll 1$ recovers the zero-energy limit $\sigma_{\mathrm{el}} = 8\pi a^2$, the

[2] Note that for the singlet and triplet interaction potentials the scattering problem leads to a singlet and a triplet scattering length a_S and a_T, respectively.

condition $ka \gg 1$ yields the so-called unitarity limit $\sigma_{\mathrm{el}} = 8\pi/k^2$ leading to a maximum possible elastic cross-section for s-wave collisions. Throughout this thesis the scattering length is given in units of Bohr's radius, $\mathrm{a}_0 \simeq 0.53 \times 10^{-10}$ m.

The scattering length depends very sensitively on the presence of the last, most weakly bound molecular state. If the potential depth is sufficient to support a new bound molecular state that is located just below the zero-energy threshold, the scattering length is large and positive. By contrast, if a molecular state is located slightly above the threshold it becomes virtual and the scattering length is large and negative. If the last bound state coincides with the zero-energy threshold, the scattering length diverges and is called zero-energy resonance.

Universal regime and halo molecules

In the limit of large positive scattering lengths a, the properties of the last bound molecular state are fully determined by the scattering length. In particular, the binding energy E_{b} of such a molecular state can be described by the well-known formula [Lan77, Köh06]

$$E_{\mathrm{b}} = \frac{\hbar^2}{ma^2} \tag{2.1}$$

where m is the atom mass. The respective wave function of the bound state assumes the general form [Köh06]

$$\Phi(r) = \frac{1}{\sqrt{2\pi a}} \frac{e^{-r/a}}{r}. \tag{2.2}$$

The condition for such a simple description is that the scattering length must be much larger than the characteristic range of the interaction potential. For the van der Waals potential this range is given by the van der Waals length

$$L_{\mathrm{vdW}} = \frac{1}{2} \left(\frac{mC_6}{\hbar^2} \right)^{1/4}. \tag{2.3}$$

Consequently, the condition can be expressed as $a \gg L_{\mathrm{vdW}}$. This regime of large scattering length is also called "universal regime" because properties such as the binding energy or the bound state wave function only depend on the scattering length but not on details of the interaction potential[3] [Köh06].

[3] For Cs atoms, the van der Waals length $L_{\mathrm{vdW}} = 101\ \mathrm{a}_0$. This value corresponds to a binding energy of $E_b \sim h \times 2.7$ MHz.

In accordance with Eq. (2.2), the scattering length gives a direct measure for the mean distance between the two atoms, i. e. mean molecular bond length, to be

$$\langle r \rangle = a/2. \tag{2.4}$$

This length very much exceeds the intuitive force range associated with the potential well that can be represented by the so-called outer classical turning point of the molecular bound state. Using the condition $C_6\, r^{-6} = E_\mathrm{b}$, the turning point of the bound state can be expressed by [Köh06]

$$r_\mathrm{cl} = \left[a(2L_\mathrm{vdW})^2\right]^{1/3}, \tag{2.5}$$

where C_6 is substituted according to Eq. (2.3). Because the wave function of such a loosely bound state has most of its weight outside the classical turning point ($\langle r \rangle \gg r_\mathrm{cl}$), this kind of molecules is often called *halo molecules*. The large spatial extent of the bound state obscures details of the binary interaction.

It is important to note that up to now we have considered the scattering problem of two particles with no internal structure. In this scenario of a single interaction potential (single channel), we have considered only one molecular state slightly below threshold. As an example, the system of two ^{4}He ground state atoms provides such a weakly bound state that fulfills the requirements of a halo molecule [Sch94].

In experiments with ultracold atoms usually more than one scattering channel is available[4] and various molecular states are present. As we will see in the following sections, many of these bound states can be addressed experimentally and the regime $\langle r \rangle \gg r_\mathrm{cl} > L_\mathrm{vdW}$ can easily be entered in the experiments. However, for most of the bound states the simple halo-state description can not be applied without restrictions. The above theory is most suitable for molecular states which are associated with the initial scattering channel (s-wave molecular states) and which are slightly below threshold.

2.2.3. Feshbach resonances

In ultracold collisions the hyperfine interaction of the atoms provide various interaction potentials, i. e. scattering channels. As shown in Fig. 2.1(a), the occurrence of a Feshbach resonance can be described by considering an entrance channel and a closed channel supporting a single molecular bound state, also called *bare Feshbach resonance state*. A Feshbach resonance arises when the scattering state of two free atoms associated with the entrance channel can couple to the molecular bound state [Fes58, Köh06]. If the

[4] For example, channels belonging to different hyperfine states of the atoms.

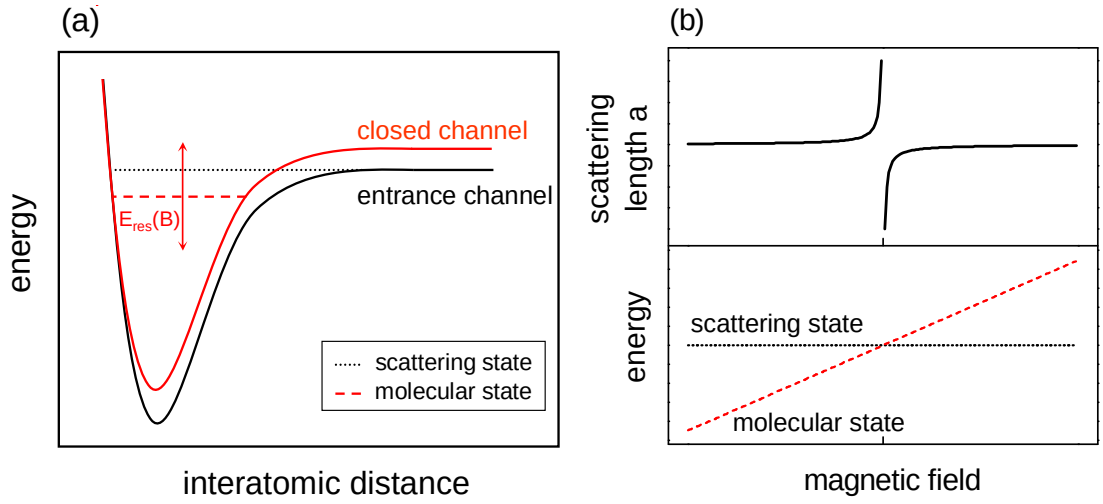

Figure 2.1.:
Feshbach resonances occur when the scattering state of two free atoms couples to a bound molecular state. (a) Assuming the scattering state associated with the entrance-channel potential and the bound state supported by a closed-channel potential have different magnetic moments, an external magnetic field can be used to tune the two states into energetic degeneracy. The vertical arrow indicates the magnetic field dependence of the bound state energy $E_{\mathrm{res}}(B)$. (b) In the vicinity of the state crossing the scattering length a diverges.

scattering and bound state have different magnetic moments, the two states can be brought into energetic degeneracy by applying an external magnetic field. The degeneracy allows for a resonant Feshbach coupling between both states. The Feshbach coupling is mediated through electronic interactions such as the exchange interaction and weaker dipolar interactions (cf. Sec. 2.2.1). The exchange interaction preserves the relative orbital angular momentum of the scattering and the bound state and leads to broad Feshbach resonances. The weaker interactions allow an exchange of the internal and relative orbital angular momentum of the coupling states and lead to narrow resonances.

In the vicinity of a Feshbach resonance all scattering observables such as elastic and inelastic cross sections are greatly modified [Dal99, Chi01]. In particular, the s-wave scattering length a is strongly enhanced in comparison to its off-resonance background value a_{bg} near the resonance. As illustrated in Fig. 2.1(b), the scattering length shows a dispersive divergence as a function of the magnetic field strength B. It can be expressed by [Köh06]

$$a(B) = a_{\mathrm{bg}} \left(1 - \frac{\Delta B}{B - B_0} \right), \tag{2.6}$$

where B_0 denotes the resonance position. The width of the resonance ΔB characterizes the distance in magnetic fields between B_0 and the zero of the scattering length and is determined by [Köh06]

$$\Delta B = \frac{m\,(2\pi\hbar)^3}{4\pi\hbar^2\, a_{\mathrm{bg}}\, \Delta\mu}\, |M|^2. \tag{2.7}$$

ΔB depends mainly on the difference in magnetic moments $\Delta\mu$ and the coupling strength $|M|^2$ [Köh06] between the scattering state and the bare Feshbach resonance state[5]. While $\Delta\mu$ is typically on the order of 2 Bohr magneton, μ_B, for alkali atoms, the coupling strength $|M|^2$ can vary over a large range. Therefore Feshbach resonances can have widths ranging from μG up to hundreds of Gauss.

Feshbach molecule state

The Feshbach coupling between the two-atom scattering state and the bare molecule state leads to a dressed state, the so-called *Feshbach molecule state*, see Fig. 2.2. The coupling between the two states shifts the position of the Feshbach resonance from B_{res}, where the bare Feshbach state would intersect with threshold, to B_0. In the region of magnetic fields outside B_0 the admixture of the closed channel to the Feshbach molecule state dominates and the bare resonance state E_{res} determines the slope of the linear magnetic field dependence of the molecule binding energy. By contrast, in the vicinity of B_0 the scattering length becomes very large and the admixture to the dressed state is negligible and vanishes at the resonance position.

Within a limited range of magnetic field strength about B_0, the Feshbach molecule state can therefore be described in terms of just its entrance-channel component (single-channel approach). This range, which corresponds to the universal regime (cf. Sec. 2.2.2), is usually far inside the resonance width. As a consequence, the binding energy of the Feshbach molecule state can be expressed by

$$E_{\mathrm{b}} = \frac{\hbar^2}{m a_{\mathrm{bg}}^2 \Delta B^2}\, (B - B_0)^2, \tag{2.8}$$

which recovers Eq. (2.1) in the limit $B \to B_0$. The corresponding molecular state represents a proper molecular halo state with universal properties as described previously. In general, a limited range of magnetic field strengths in which the universal regime applies and a single-channel description is possible can be associated to any Feshbach resonance.

[5] M is the coupling matrix element between the entrance-channel zero-momentum wave function and the bare Feshbach resonance state as defined in Ref. [Köh06].

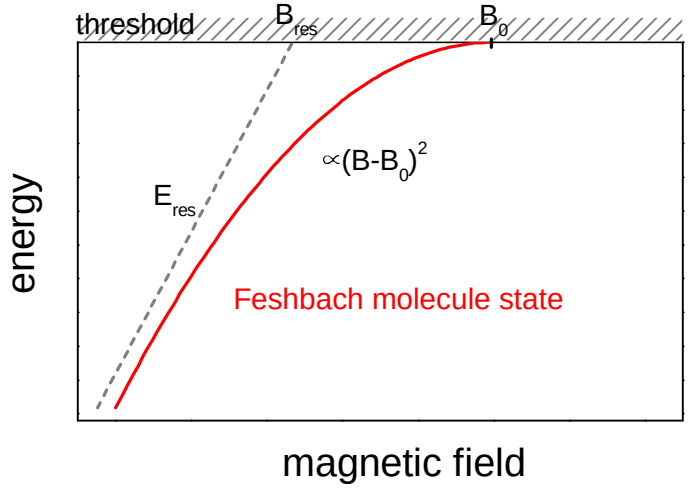

Figure 2.2.:
Feshbach coupling between a two-atom scattering state (line at threshold) and a bare Feshbach resonance state E_{res} (dashed line) as a function of magnetic field. B_{res} is the position of the zero-energy resonance where the two states intersect. Because of the coupling between the states the Feshbach resonance position is shifted to B_0. In the vicinity of B_0 the binding energy of the bound sate can be described by a formula $\propto (B - B_0)^2$, for details see text. The range of validity of this binding energy dependence is mainly determined by the coupling strength and typically well within the width of the resonance.

The range of validity of such a description gives rise to classify Feshbach resonances according to whether they are *entrance-channel dominated* or *closed-channel dominated* Feshbach resonances.

Classification of resonances

The principal question of the applicability of single channel approaches outside the universal regime of magnetic field strengths can be answered by considering the amount of closed channel admixtures near the resonance. The criterion for an entrance-channel dominated Feshbach resonance can be expressed by [Köh06]

$$\frac{\bar{a}}{a_{\mathrm{bg}}} \frac{\hbar^2/m\bar{a}^2}{\Delta\mu\,\Delta B} \ll 1 \tag{2.9}$$

where $\bar{a}$ is the so-called Gribakin-Flambaum mean scattering length introduced by a semi-classical treatment of the entrance-channel wave functions at large separations [Gri93]. The mean scattering length $\bar{a}$ depends only on the van der Waals length and is given

by $\bar{a} \approx 0.96 \times L_{\mathrm{vdW}}$. $\bar{a}$ represents the average range of the interaction potential. The coefficient can be used as a first order correction to the assumption of the simple square well plus hard core interaction potential for alkali atoms. One can show that in the limit of $a \gg \bar{a}$ the energy of the highest excited vibrational state associated with an entrance-channel dominated Feshbach resonance is well approximated by [Köh06]

$$E_{\mathrm{b}} \approx \frac{\hbar^2}{m(a-\bar{a})^2}. \tag{2.10}$$

In the opposite limit, a *closed-channel dominated* Feshbach resonance requires the description within at least a two-channel model [Köh06]. The properties of the Feshbach molecules associated with this type of resonance are not universal as they depend on the precise nature of the closed channel. In practice, closed-channel dominated Feshbach resonances are narrow and their universal range of magnetic field strength is difficult to control experimentally. In contrast, entrance-channel dominated resonances are broad and easily controllable. Thus such resonances are prime candidates for the search for effects in the universal regime such as Efimov physics [Kra06b].

Feshbach resonance notation

In this thesis Feshbach resonances are labelled according to the relative orbital angular momentum quantum number ℓ of the associated molecular state. By following the convention of spectroscopic notation, Feshbach resonances that arise from molecular states with quantum number $\ell = 0, 1, 2, 3, 4, 5, 6, 7, 8, \ldots$ are labelled as $s, p, d, f, g, h, i, k, l, \ldots$ -wave Feshbach resonances [Rus29].

2.2.4. Feshbach association

As described above, at a magnetic Feshbach resonance the resonantly enhanced atom-molecule coupling can be used to produce molecules [Köh06]. In particular, by sweeping the magnetic field across a resonance the atoms can be transferred into the corresponding Feshbach molecule state. As illustrated in Fig. 2.3, for an adiabatic sweep of the magnetic field the system remains in the energetically lowest state. Therefore an atom pair in the scattering state changes into the bound Feshbach molecule state. Such an association scenario of two atoms via a linear magnetic field sweep can be described within the two-level Landau-Zener model [Lan32, Zen32]. According to this model, the probability for an asymptotic transition between the two states is given by $1 - e^{-\varepsilon}$, with $\varepsilon = 2\pi|M|^2/(\hbar\,|\Delta\mu|\,|\dot{B}|)$ [Köh06]. Here, $\dot{B}$ is the ramp speed of the magnetic field sweep. The validity of this approach has been demonstrated for an ensemble of atom pairs bound

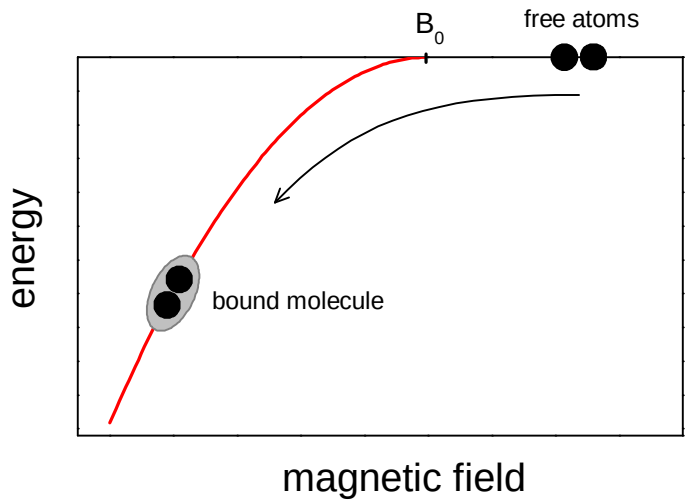

Figure 2.3.:
Feshbach molecule association scheme. Two free atoms can form a bound Feshbach molecule by sweeping the magnetic field adiabatically across the Feshbach resonance at B_0.

to the individual sites of an optical lattice [Tha06]. For atomic clouds in which the atom pairs are not shielded from each other by an optical lattice, the Landau-Zener model remains valid but loss processes have to be taken into account. Therefore the relevant number is the *conversion efficiency*, defined as the number of atoms transferred to the molecular state divided by the initial atom number. It was found that the conversion efficiency directly depends on the phase-space density of the atoms and in principal 100 % transfer efficiency could be achieved using Bose-Einstein condensates as a starting point [Hod05].

However, in molecule experiments involving condensates the conversion efficiencies are typically 10 % and mainly limited by inelastic atom-molecule and molecule-molecule collision processes that lead to rapid loss of the dimers [Muk04, Sya06, Smi07, Fer08, Kno08a]. Moreover, spontaneous dissociation of molecules caused by optical pumping from the trapping laser light [Mar05] or simply the presence of lower lying open channels [Tho05a] can strongly contribute to the molecule losses from the trap.

A detailed discussion on the association of molecules using magnetically tunable Feshbach resonances is given in Ref. [Köh06].

2.3. Energy structure of Cesium dimers

Weakly bound Cs dimers exhibit a highly complex energy structure. Current knowledge of the molecular spectrum near threshold is based on theoretical calculations of the molecular energy structure in combination with a series of cesium atom scattering experiments performed at Stanford University [Vul99, Chi00, Chi04b]. In these scattering experiments the magnetic field positions of many Feshbach resonances up to g-wave character were measured for various scattering channels. This provided the necessary experimental input for theoretical calculations of the molecular energy structure [Leo00, Chi04b], performed at the National Institute of Standards and Technology (NIST). In the following, we will refer to the cesium molecular structure as presented in Ref. [Chi04b] as the "NIST model". It constitutes the theoretical basis for the experiments discussed in this work.

Cs molecular states near threshold are for the most part sufficiently well characterized by the quantum numbers $|f,\ m_f;\ \ell,\ m_\ell\rangle$ [Köh06]. Here, f represents the sum of the total atomic spins $F_{1,2}$ of the individual atoms according to $\mathbf{f} = \mathbf{F}_1 + \mathbf{F}_2$. The quantum number ℓ is the nuclear mechanical angular momentum quantum number. The respective projection quantum numbers are given by m_f and m_ℓ. We follow the convention of labelling states with $\ell = 0, 2, 4, 6, 8, \ldots$ as $s, d, g, i, l, \ldots$ -wave states [Rus29] and the associated Feshbach resonances as $s, d, g, i, l, \ldots$ -wave resonances as mentioned before. As a consequence of the bosonic nature of Cs atoms, only even values of ℓ occur. The quantum numbers F_1 and F_2 determine the closed channel to which the molecular state belongs. In special cases these quantum numbers also have to be specified.

To account for the molecular structure below threshold, not only the exchange and van der Waals interaction, the atomic hyperfine structure, and the Zeeman energy, but also the weaker relativistic spin-spin dipole and second-order spin-orbit interactions have to be considered [Mie96, Chi04b]. The exchange and van der Waals interactions conserve ℓ and f, whereas the two relativistic interactions weakly mix states with different ℓ and f. The complete interaction Hamiltonian conserves the total angular momentum $f + \ell$ at zero magnetic field. More importantly, it always conserves the projection of the total angular momentum $m_f + m_\ell$. In our experiments, we start with an ultracold, spin-polarized atomic sample of Cs atoms in their absolute hyperfine ground state $|F=3, m_F=3\rangle$. At ultralow scattering energies only incoming s-waves ($\ell = 0$) need to be considered. The atomic scattering state is hence $|f=6, m_f=6; \ell=0, m_\ell=0\rangle$. Consequently all molecular states relevant to the present work obey $m_f + m_\ell = 6$.

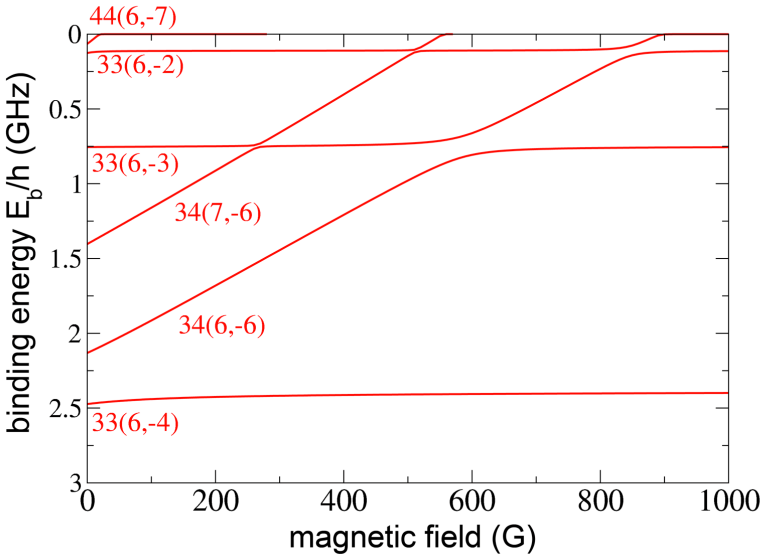

Figure 2.4.:
Overview of Cs s-wave molecular states below the threshold of two free atoms in the absolute ground state $|F=3, m_F=3\rangle$ as a function of the magnetic field. The labels of the states indicate the corresponding closed channel quantum numbers $F_1F_2(f,-\nu)$, where ν is the vibrational quantum number as counted from threshold at zero magnetic field. The figure barely resolves the state $44(6,-7)$ which turns over at about 20 G into the weakly bound state $33(6,-1)$ (see Fig. 2.7). This state is not resolved. Together with the states $34(7,-6)$ and $34(6,-6)$ this weakly bound state $33(6,-1)$ leads to broad Feshbach resonances at 550 G and 800 G as indicated in Fig. 2.5. Figure adapted from E. Tiesinga [Tie07].

2.3.1. Overview of s-wave molecular states

Figure 2.4 gives an overview of s-wave molecular states in the magnetic field range from 0 to 1000 G. The threshold energy is given by two Cs atoms in the absolute hyperfine ground state sublevel $|F=3, m_F=3\rangle$. The states are labelled using the notation $F_1F_2(f,-\nu)$. The quantum number ν is the vibrational quantum number as counted from threshold of the corresponding F_1F_2 scattering channel. States belonging to the channel with $F_1F_2=33$ and with $f=6$ appear horizontal in the plot with quantum number $\nu=-2$,-3, and -4. The last bound state $33(6,-1)$ is only slightly below threshold (binding energy $\sim h\times 10\,\mathrm{kHz}$) and not resolved in the figure. However, this state is responsible for the large background scattering length of about $2000\,a_0$ of Cs atoms. The $33(6,-1)$ state can be regarded as a universal dimer state. States belonging to other channels with either $F_1F_2=34$ or $F_1F_2=44$ are inclined in the plot. They

lead to strong avoided level crossings and to the occurrence of Feshbach resonances when intersecting threshold. The positions of the Feshbach resonances are shifted to lower magnetic fields as one would infer from Fig. 2.4. The shift is because of strong coupling between the molecular state $33(6,-1)$ with any one of the inclined states.

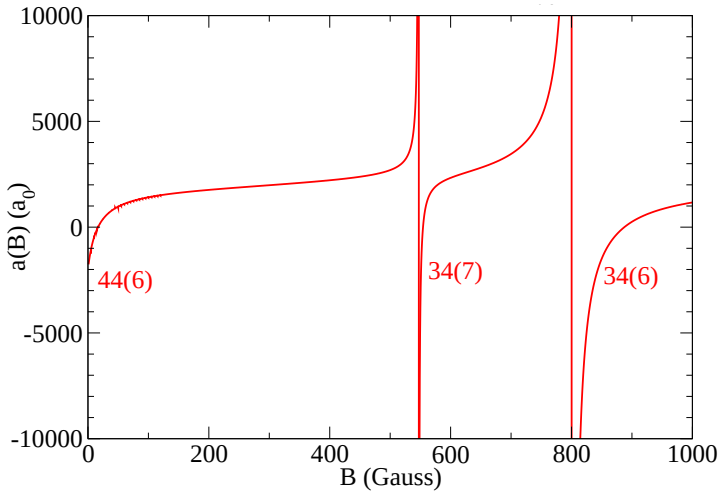

Figure 2.5.:
The Cs s-wave scattering length a for atoms in the $|F=3,m_F=3\rangle$ state as a function of magnetic field B. The broad Feshbach resonances are caused by the states $44(6,-7)$, $34(7,-6)$ and $34(6,-6)$ as indicated in Fig. 2.4. For the resonance in the region from 0 - 150 G only the right-hand "shoulder" can be seen. Figure by courtesy of E. Tiesinga.

The avoided crossing between the $33(6,-1)$ and $44(6,-7)$ leads to a Feshbach resonance position corresponding to about -12 G and determines the behavior of the s-wave scattering length for magnetic fields below 150 G. In a similar way couplings of the state $33(6,-1)$ with $34(7,-6)$ and $34(6,-6)$ result in broad Feshbach resonances arising at magnetic field values of 550 G and 800 G, respectively. Figure 2.5 shows the resulting s-wave scattering length of Cs atoms in the state $|F=3,m_F=3\rangle$ for magnetic fields up to 1000 G. Three s-wave Feshbach resonances can be identified corresponding to the molecular states $44(6,-7)$, $34(7,-6)$ and $34(6,-6)$. For the lowest resonance only a part of the right-hand "shoulder" can be seen. All of these resonances are mediated by the exchange interaction that allows for a large coupling to the scattering state. As a result, the resonance widths are on the order of several tens of Gauss. For magnetic fields of up to 1000 G only these three Feshbach resonances are clearly open-channel dominated.

In the following we focus on the scattering properties of Cs atoms at low magnetic field.

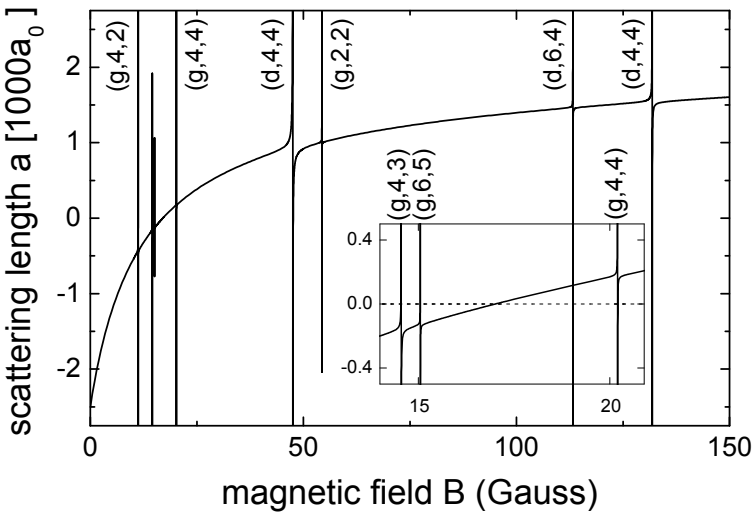

Figure 2.6.:
Scattering length at low magnetic fields for atoms in the $|F=3, m_F=3\rangle$ state. The smooth variation of the scattering length from $-2500\,a_0$ at zero Gauss to $1600\,a_0$ at 150 G with a zero crossing at 17 G is caused by a universal dimer state. Several narrow g- and d-wave Feshbach resonances are visible, characterized by the quantum numbers according to (f, ℓ, m_f). The inset shows the region where the scattering length crosses zero. The 20.1 G resonance is actually located at 19.8 G [Mar05]. Figure by courtesy of E. Tiesinga and P. Julienne, NIST.

Note that in the current experimental setup magnetic field strengths of up to 250 G can be produced.

2.3.2. Molecular states at low magnetic field

Figure 2.6 shows the scattering length in more detail in the magnetic field range up to 150 G. In this case also molecular states with non-zero relative orbital angular momentum ($\ell \neq 0$) have been included in the NIST calculations. As a result several narrow Feshbach resonances appear. The smooth variation of the scattering length arises from the right hand branch of the broad s-wave Feshbach resonance located at -12 G. The scattering length varies from about $-2500\,a_0$ at zero magnetic field and $+1600\,a_0$ at about 150 G with a zero-crossing at ~ 17 G. On top of this smooth variation narrow d-wave and g-wave Feshbach resonances can be seen.

The narrow resonances are caused by the relatively weak dipolar interactions. For Cs atoms these weaker relativistic interactions allow even g-wave states to couple sufficiently

to the atomic threshold and to produce experimentally observable Feshbach resonances. The widths of d-wave resonances is typically a few hundred mG as the magnetic dipole-dipole coupling is the main contribution. For g-wave resonances the leading term is the second-order spin-orbit interaction. Therefore these resonances are much narrower and usually only a few mG broad. Note that higher-order molecular states with e. g. $\ell = 6, 8$ do not sufficiently couple to the atomic threshold and no Feshbach resonances occur.

Molecular energy structure near threshold

Figure 2.7 gives an overview of the molecular states relevant to the present work, covering the magnetic field region up to 55 G and binding energies up to $h \times 10\,\mathrm{MHz}$. The figure is a zoom-in of Fig. 2.4, where besides s-wave states also d-, g-, and l-wave states are included. The solid lines in Fig. 2.7 represent states resulting from the NIST model [Chi04b], including s-, d- and g-wave states. One can identify the s-wave state $44(6, -7)$ as shown in Fig. 2.4 which turns over into the state $33(6, -1)$ around 20 G as a result of strong coupling. For two interacting Cs atoms relativistic spin-spin dipole and second-order spin-orbit interactions are particularly important [Leo00]. Therefore, in Cs not only s- and d-wave states but also g-wave states couple sufficiently to the atomic threshold to produce experimentally observable Feshbach resonances. In the figure, each intersection of the atomic threshold with a molecular state corresponds to a Feshbach resonance. As discussed previously, the magnetic field positions of these Feshbach resonances were determined experimentally in an optically confined atomic Cs gas and then used as input parameters for the NIST model [Vul99, Chi00, Chi04b]. The dashed lines illustrate molecular l-wave states, which will be discussed later.

To label the molecular states, we use the three quantum numbers $f\ell(m_f)$. For states with $m_f = f$ and $m_\ell = \ell$, we only use f and ℓ for brevity. Table 2.1 gives the full set of angular momentum quantum numbers for all molecular states relevant to the present work.

Coupling between molecular states

Coupling between two molecular states with the same f and ℓ in general leads to very broad avoided crossings between the states as mentioned above. The strong curvature of the $6s$ state in Fig. 2.7 is a result of such a crossing. Narrow avoided crossings arise when molecular states of different f and ℓ intersect. These narrow crossings are mediated by the weaker spin-spin dipole and second-order spin-orbit interactions. In the NIST model weaker couplings were only taken into account for special cases where it was necessary to assign the experimentally observed Feshbach resonances. Consequently, the molecular

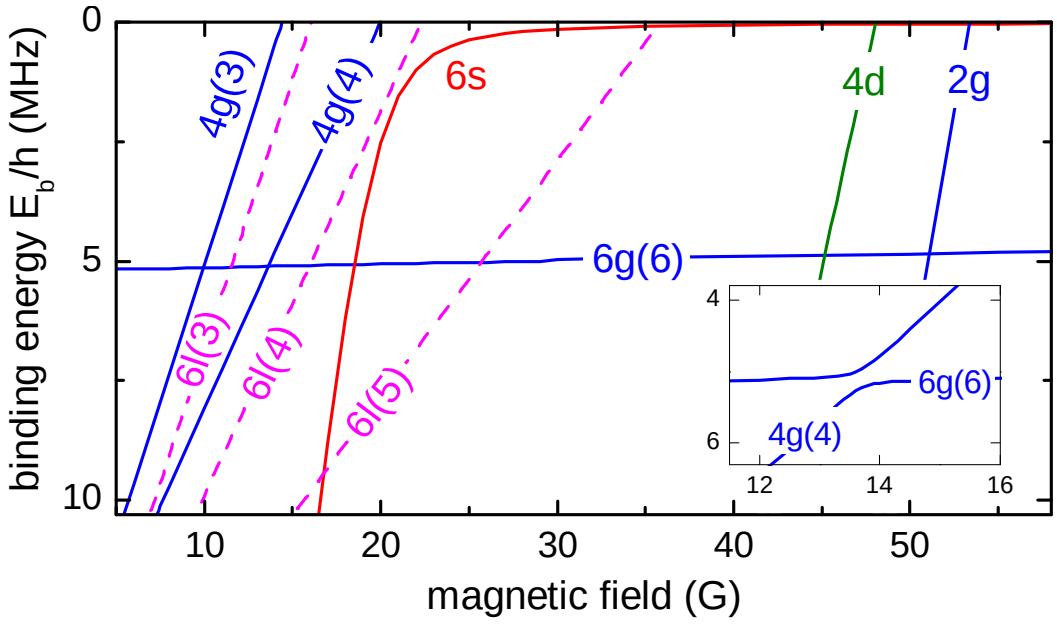

Figure 2.7.:
Molecular energy structure below the threshold of two free Cs atoms in the absolute ground state $|F=3, m_F=3\rangle$. Molecular state labeling is according to the quantum numbers $f\ell(m_f)$, $m_\ell = 6 - m_f$. The quantum number m_f is omitted for states with $m_f = f$ and $m_\ell = \ell$. The solid lines represent the s, d and g-wave states included in the NIST model [Chi04b]. The intersections of the d- and g-wave states with the threshold cause narrow Feshbach resonances that can be used for molecule production. The curvature of the $6s$ state arises from a large avoided crossing between two states of the same $f\ell$ quantum numbers. The NIST model does not take into account weak avoided crossings between bound molecular states mediated by the relativistic spin-spin dipole and second order spin-orbit interactions. If these interactions are taken into account, the crossings between bound molecular states become avoided as illustrated in the inset for the example of the $4g(4)/6g(6)$ crossing. The dashed lines represent l-wave states ($\ell = 8$) obtained from extended calculations based on the NIST model.

label of state	$6s$	$4d$	$2g$	$4g(3)$	$4g(4)$	$6g(6)$	$6l(3)$	$6l(4)$	$6l(5)$
f, m_f	6,6	4,4	2,2	4,3	4,4	6,6	6,3	6,4	6,5
ℓ, m_ℓ	0,0	2,2	4,4	4,3	4,2	4,0	8,3	8,2	8,1

Table 2.1.:
List of angular momentum quantum numbers for the relevant molecular states. Each state is represented by four quantum numbers: the total internal angular momentum f and the rotational angular momentum ℓ with m_f and m_ℓ as the respective projections along the quantization axis.

states in Fig. 2.7 are shown as intersecting lines. Nevertheless, the existence of avoided crossings between molecular states of different $f\ell$ is crucial for the present work as it allows the transfer of molecules from one state to another. As an example, the inset in Fig. 2.7 schematically illustrates the avoided crossing between the $4g(4)$ state and the $6g(6)$ state at $\sim 13.5\,\mathrm{G}$.

l-wave molecules

The dashed lines in Fig. 2.7 represent l-wave states. As states with higher angular momentum ($\ell > 4$) do not sufficiently couple to the s-wave scattering continuum, the l-wave states cannot be observed by Feshbach spectroscopy in an ultracold atomic gas. Consequently, no experimental input for higher angular momentum states was available for the NIST model. It is not a surprise, however, that for Cs l-wave states exist in the low magnetic field region. This follows from a general property of the asymptotic van der Waals potential [Gao00]. In the case of an s-state being close to threshold, angular momentum states with $\ell = 4, 8, \ldots$ should also occur near threshold. The observation of both g- and l-wave states in a system with near-resonant s-wave background scattering properties nicely illustrates this general property. When the NIST model is extended to states with higher angular momentum it indeed predicts l-wave states in the low-field region [Tie07]. The calculations are expected to accurately predict the magnetic moments, i. e. the slopes, of these states but they leave some uncertainty concerning the exact binding energies [Tie07]. The l-wave states shown in Fig. 2.7 result from the extended NIST model, but they are energetically adjusted to the experimental observations (Chap. 5) by equally down-shifting all three states by about $h \times 2\,\mathrm{MHz}$.

3. Overview of experimental methods

In this chapter we give a brief overview of the experimental methods used to prepare atomic samples, which are the starting point for experiments involving Feshbach molecules. Most of the applied experimental techniques have not or only marginally been modified since 2002, when the experiment was operational for the first time. We therefore discuss the basic experimental concepts and concentrate on up-to-date developments and setups. An extensive description of the apparatus and vacuum-system, the laser setups for optical pre-cooling, magnetic field control and other experimental techniques is given in the PhD theses of my former colleagues, Tino Weber, Jens Herbig and Tobias Kraemer [Web03a, Her05, Kra06a].

In Sec. 3.1 the preparation of ultracold Cs atoms is summarized. Section 3.2 and 3.3 briefly describe the central vacuum chamber and the setup for magnetic field control. In Sec. 3.4 we discuss the setup to produce microwave radiation at 9.2 GHz, which we also use for magnetic field calibration. In Sec. 3.5 we then briefly explain the procedure for optical pre-cooling of the atoms which are then loaded into optical dipole traps. The various setups of dipole traps are described in Sec. 3.6. Finally in Sec. 3.7 the optical technique to obtain information from the atoms is briefly given.

3.1. Atomic sample preparation

For our experiments we use a steel chamber providing ultra-high vacuum conditions to isolate the atoms from the lab environment. A typical experimental sequence to prepare an atomic sample looks as follows: A thermal beam of Cs atoms coming from an oven [Web03a] is initially slowed by using the Zeeman-slowing technique [Met99]. The atoms are then captured in a magneto-optical trap (MOT) [Met99] in the central section of the chamber. For pre-cooling the atoms, the MOT is briefly compressed and a short molasses phase is applied [Met99]. To further cool the sample we use degenerate Raman-sideband cooling [Ker00]. Simultaneously this technique polarizes the Cs atoms into their lowest hyperfine ground state $|F = 3, m_F = 3\rangle$. The atoms are then transferred into far-off resonance optical dipole traps [Gri00]. The employment of several stages of dipole traps allows for the final preparation of the atoms.

For the molecule experiments presented in this work we use as a starting point atomic samples near degeneracy (Chap. 5) or a Bose-Einstein condensate (BEC) of Cs atoms (Chap. 6). In both cases, our key strategy for the atomic sample preparation is to employ a sequence of optical dipole traps [Web03a, Kra04]. As shown in Fig. 3.5, we use two different setups of dipole traps, resulting in two preparation sequences. While setup 1 in Fig. 3.5 is optimized for producing BECs, setup 2 is optimized for molecule trapping and molecular state manipulation, and not for BEC production. For both setups the experimental strategy is similar.

In particular, we first use a shallow, large-volume crossed laser trap as a "reservoir" to collect as many atoms as possible before forced evaporative cooling is implemented in a tighter optical trap. The relatively weak optical potential of the reservoir trap requires magnetic "levitation" where a magnetic field gradient compensates for the gravitational force [Web03a, Kra04]. The reservoir trap is efficiently loaded with atoms that are pre-cooled by degenerate Raman-sideband cooling [Ker00]. We then load the atoms into a small-volume "dimple" trap, which allows for forced evaporative cooling [Met99, Web03a]. The remaining atoms are removed by turning off the reservoir trap and evaporative cooling is proceeded by lowering the potential depth of the dimple trap. We therefore achieve atomic samples near degeneracy or BECs, which are then a good starting point to produce and study Feshbach molecules.

The ability to levitate the atoms and molecules against gravity by using a magnetic field gradient is one of the important features in our experiments on Cs BEC and the production of Feshbach molecules [Web03b, Chi05b]. Magnetic levitation turns out to be very useful in two ways: First of all, in the limit of very weak optical trapping only one spin state is held in the trap which assures perfect spin polarization of the sample. Further, efficient evaporation can be performed without the effect of gravitational sag in the trap. The dc magnetic-field offset remains a free parameter for flexible tuning of the scattering length. However, we will see later in Chap. 4 that for the preparation of molecular samples in various states the use of magnetic field gradients is problematic. This is because molecules can have widely different magnetic moments and thus require different levitation gradients. By using a tightly focused laser beam in the final preparation phase, we can hold the molecules against gravity without the levitation gradient field.

For an optimized production of atomic condensates we use a dipole trap sequence as illustrated in Fig. 3.5 by setup 1. We realize the large-volume reservoir trap by crossing two CO_2-laser beams. The reservoir is then crossed with the tightly focused dimple trap, generated by a broad-band fiber-laser at a wavelength of 1064 nm. After loading the dimple trap, the surrounding reservoir is removed and forced evaporative cooling

can proceed towards condensation. To optimize the evaporation the scattering length is magnetically tuned during the evaporation process [Web03a, Kra04].

The atomic BEC turned out to be an excellent starting point to produce Feshbach molecules [Her03]. Unfortunately we observed strong light-induced trap losses for the molecules when using the near-infrared laser light at 1064 nm. The losses are presumably a result of excitation of molecular bound-bound transitions. However, the experiments and measurements presented in Chap. 6 are based on this BEC preparation scheme. The experiments have been performed in free space and the trapping light of the final stage was switched off.

To overcome the problem of light-induced molecule losses we use an alternative method of atomic sample preparation which is illustrated by setup 2 in Fig. 3.5. The main difference here is the finally obtained dipole trap, realized by crossing two CO_2-laser beams. The far-infrared CO_2-laser trap avoids the use of near-infrared radiation. The CO_2-light is sufficiently off resonance. Thus the light allows for long molecule trapping times [Chi05b, Sta06, Zah06] and facilitates efficient in-trap production of molecules. Using setup 2, we produce an atomic sample near degeneracy, from which we obtain sufficient efficiencies for molecule formation. The central part of this work presented in Chap. 4 and 5 has been carried out by using this preparation scheme.

3.2. Central experimental chamber

The experiments with ultracold Cs atoms and molecules are performed in a twelve-sided polygonal stainless-steel vacuum chamber as shown in Fig. 3.1. The pressure in the chamber is well below 10^{-12} mbar. On two of the twelve sides of the polgygon the central chamber is connected to other sections of the vacuum apparatus, which features an oven as source for the Cs atoms, a Zeeman-slowing range and pumping sections to maintain the ultra-high vacuum conditions. In total four pairwise opposite viewports of the central chamber are sealed with special ZnSe-viewports (22 mm clear view diameter), which are transparent for the wavelength of 10.6 μm of CO_2-laser light[1]. The remaining six pairwise opposite viewports are made of quartz-glass (35 mm clear view diameter) for the near-infrared laser cooling and trapping light and for imaging.

For maximum optical access along the vertical axis the central experimental chamber features large re-entrant viewports on top and bottom as illustrated by the side view of Fig. 3.1. The viewports have a clear view diameter of 95 mm and are made of quartz-glass

[1] Providing optical access for CO_2-laser light is the reason for using a steel vacuum chamber. At the beginning of the experiment, no high-power near-infrared lasers have been available for an alternative glass-cell vacuum setup to prevent magnetically induced eddy currents.

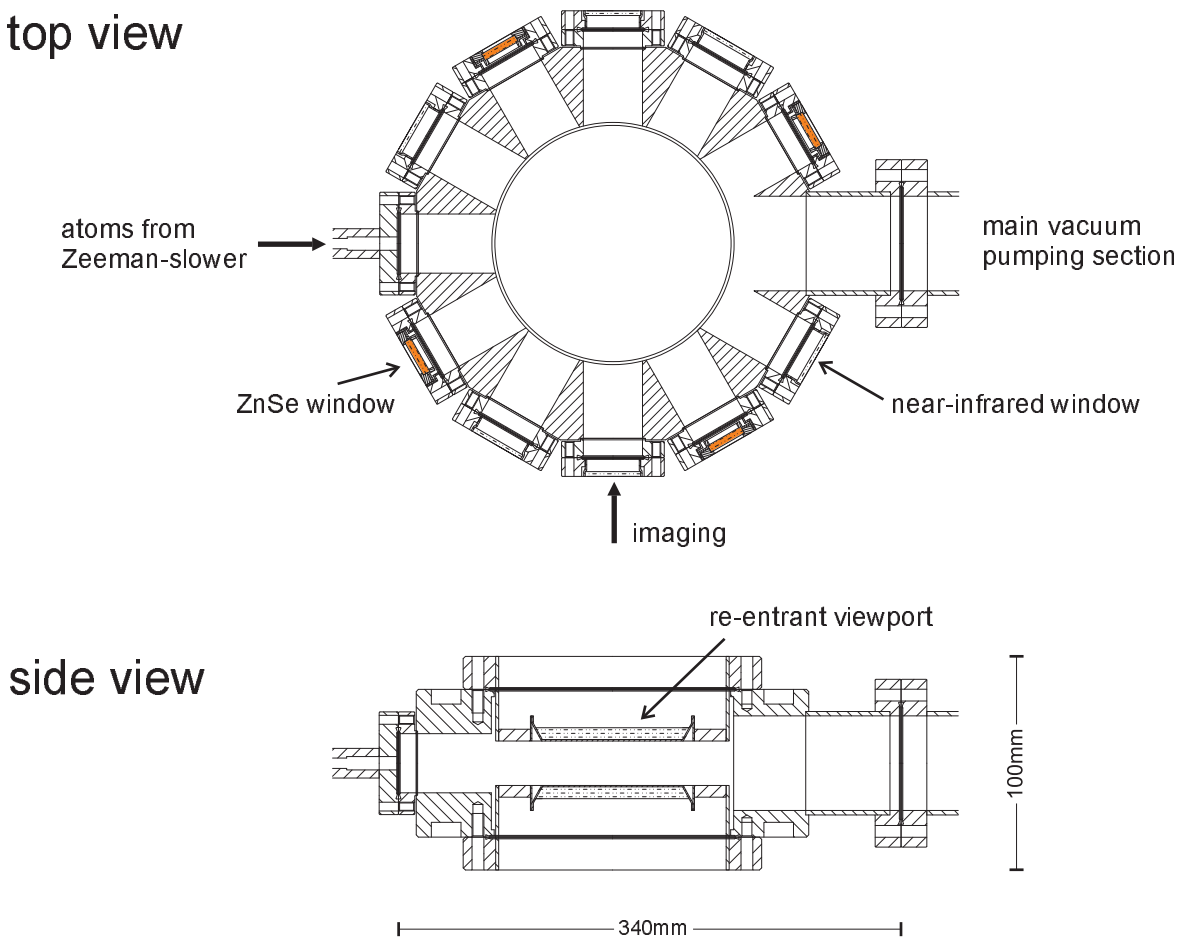

Figure 3.1.:
The central experimental chamber: The vacuum chamber has the shape of a twelve-sided polygon with two re-entrant viewports on top and bottom. Four viewports of the twelve sides of the experimental chamber are sealed with special ZnSe-windows, which are necessary for CO_2-laser light transmission. In total six pairwise opposite viewports are for the near-infrared laser-cooling and trapping light and for imaging. The two remaining opposite openings are reserved for the atomic beam, the Zeeman slowing laser beam, and the vacuum pumps.

with anti-reflection coating for $852 - 1064\,\mathrm{nm}$. The distance of the inner surfaces of the two re-entrant viewports is 34 mm.

3.3. Magnetic field control

In the experiment, the magnetic field has to fulfill several requirements: A homogenous magnetic field is necessary to tune the atomic interaction and to produce molecules. Also, small offset fields have to be applied to cancel residual stray fields such as the earth's magnetic field. Finally, to operate the magneto-optical trap and to levitate atoms or molecules against gravity, a magnetic quadrupole field is needed.

The required magnetic field is produced by several sets of coils, mounted on the steel chamber or placed on top of the re-entrant viewports closer to the trap center. The presence of the metal limits the magnetic field switching times as a result of eddy currents. Nevertheless we achieve a maximum of experimental flexibility by combining the larger fields of the bigger coils with the more rapidly switchable fields of the smaller coils inside the viewports. Figure 3.2 shows a cut through the main chamber including the arrangement of the various coil setups. The description here is focused on the most important components and technical features, for further information see App. A and Ref. [Her05].

Bias field

The vertical offset field for molecule production and manipulation is created by a pair of water cooled coils with a mean radius of 66 mm approximately in Helmholtz configuration. The coils are integrated in setup (B) as shown in Fig. 3.2 and placed inside the re-entrant viewports along the rim of the windows. They allow magnetic fields up to 60 G for dc-operation with a typical $1/e$-switching time of 1.5 ms. The current from a programmable power supply is servo-loop controlled, for details see Ref. [Kra06a]. A second pair of large coils is attached to the outside of the flanges that hold the re-entrant viewports, see setup (A) in Fig. 3.2. These coils with a mean radius of 112.5 mm can provide an additional dc-field of up to 190 G. The dissipated electrical power of coil setup (A) and (B) is heat-dumped by water cooling.

For the molecule transfer schemes described later in Sec. 4.2, one further set of coils and a single "booster" coil are used. Both coil setups are mounted on plastic holders inside the re-entrant viewports as illustrated in Fig. 3.2 by (C) and (D). Setup (C) is a pair of coils in approximate Helmholtz configuration with a radius of 44 mm and placed near the vaccum window as close to the trap center as possible. The coils with a servo-

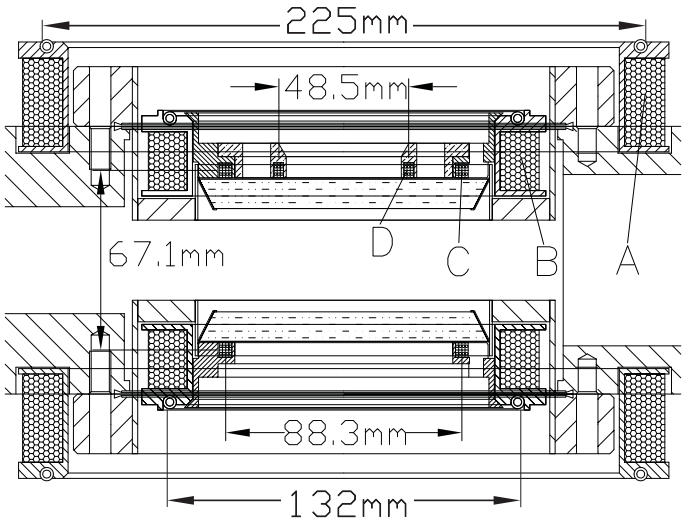

Figure 3.2.:
Cut through the main chamber with the configuration of various coil setups. (A) The outer coils produce two separately controllable homogenous magnetic fields, one setup is for large magnetic field strengths up to 190 G and one features the vertical offset compensation field. (B) The inner coils provide two configurations, the creation of a homogeneous magnetic field up to 60 G and the generation of the magnetic gradient field. While the gradient field is used to levitate the atoms or molecules against gravity, the homogenous field here is the standard field used for molecule production. The aluminium housings of the setups (A) and (B) are water cooled to heat-dump the dissipated electrical power of the coils. (C) This coil-pair provides a much faster homogenous field of up to 10 G due to its mounting on plastic holders and its distance to the metallic chamber. (D) A single coil is used to produce steps of the magnetic field of up to 7 G at switching times of below 1 μs.

loop controlled current produce a magnetic field of up to 10 G, while the $1/e$ switching time is $\sim 300\,\mu$s. As a result, ramp speeds in the range of 30 G/ms can be achieved. The fastest magnetic field changes are realized by a small, single booster coil placed inside the top re-entrant viewport, setup (D) of Fig. 3.2. The booster coil has only 4 windings with a radius of about 24 mm and is mounted at a distance of 34 mm to the trap center. Using a capacitor bench and servo-loop control for the current we achieve magnetic field pulses with amplitudes of up to 7 G, for details see App. A. The maximum pulse duration of 1 ms is sufficiently long to adjust the offset field of the other coils within this time. With a typical switching time of 400 ns we achieve ramp speeds of up to 17000 G/ms. To change the ramp speed we vary the pulse amplitude as the rise-time cannot be adjusted. The coupling of ramp speed and pulse amplitude is somewhat problematic. It limits the possible ramp speeds at certain avoided level crossings, because too large pulse amplitudes can produce uncontrolled ramps over other avoided crossings nearby. Note that the booster coil also produces a magnetic field gradient. As we will see later in Chap. 6, this small gradient bears limitations for the molecular interferometer experiments. However, for most of the experiments presented in this thesis this gradient is irrelevant.

The relative stability of the servo-loop controllers is about 10^{-5} and thus well below the ambient magnetic line noise (~ 10 mG).

Gradient field

The magnetic gradient field is produced by a pair of water cooled coils in approximate anti-Helmholtz configuration. These coils, with a mean radius of 66 mm, are also integrated in setup (B) as shown in Fig. 3.2. They allow a dc-gradient field of up to 80 G/cm. Large field gradients can be switched within ~ 3 ms, limited only by eddy currents. For small gradients such as 13 G/cm, as used in the magnetic moment spectroscopy measurements of Chap. 5, we measure somewhat lower magnetic switching times of ~ 1 ms. Note that the superposition of the gradient field with a homogeneous field results in a force on atoms (or molecules) which is outward directed from the trap center [Her05].

The position of the optical traps finally used in the experiments (Sec. 3.6) is below the zero position of the gradient field. As a consequence of this spatial displacement, the magnetic gradient field introduces a negative shift of the applied magnetic offset field. We find a value of -0.033 G/A, for the levitation condition of the atoms this corresponds already to a shift of about -1.2 G.

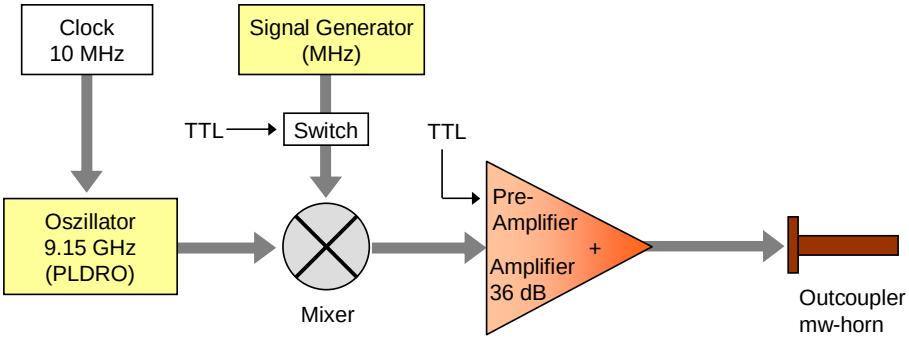

Figure 3.3.:
Schematic of the microwave setup. A phase locked dielectric resonator oscillator (PLDRO), referenced to a commercial 10 MHz Rb-clock, provides the carrier frequency at 9.15 GHz. To generate the required frequency around 9.2 GHz, we mix the carrier with the signal of a function generator. After an amplifier stage, we use a microwave-horn to couple out the signal and irradiate the atoms or molecules. Two digital switches ensure the precise control of the microwave pulse duration during the experiment.

3.4. Microwave setup and magnetic field calibration

In experiments with ultracold atoms or molecules, microwave radiation provides a powerful technique for various applications. A prominent example is the calibration of magnetic field as described in Sec. 3.4.2. But also a more sophisticated use of this technique is possible such as removing atoms from the trap for molecule preparation [Tha06]. Further, spectroscopy of the molecular energy structure is possible by driving transitions between a bound molecular and a free atomic state [Reg03, Bar05] or between two bound states. The latter case was used for the measurements presented in Chap. 5.

3.4.1. Microwave setup

For Cs atoms, the two hyperfine levels $F = 3$ and $F = 4$ of the $6^2S_{1/2}$ ground state are separated by roughly 9.2 GHz. Figure 3.3 shows a schematic of our setup to generate microwave radiation in this frequency range. We use a phase locked dielectric resonator oscillator (PLDRO) from Amplus Communication (AM-4000-0910) to provide a carrier frequency at 9.15 GHz. The oscillator is phase locked to a 10 MHz reference signal provided by a commercial Rb-clock (Stanford Research Systems) from a neighboring lab. To attain the 9.2 GHz range we sum the carrier frequency with the MHz-signal of a programmable function generator (HP 8657A) by using a frequency mixer (Mini-Circuits,

ZMX-10G). Thus we generate tunable sidebands which are used as a probe signal. After the signal generator we use a digitally controlled switch (Mini-Circuits, ZMSW-1211) to drive the duration of the microwave in the experimental sequence. The output signal of the mixer is then pre-amplified (Mini-Circuits, ZJL-7G) to optimize the performance of the final amplifier (Quinstar, QPJ-08103036-JO). Although the carrier frequency is sufficiently off-resonant and does not perturb the atoms or molecules, we switch the amplifiers using a second digital logic control to ensure full control of the microwave. Finally a microwave-horn is used as an out-coupler and to irradiate the microwave into free space. The horn is mounted on top of the central chamber, slightly tilted with respect to the vertical axis. The distance of the horn to the trapping position is about 4 cm.

The output power of the microwave radiation is controlled by adjusting the amplitude of the signal generator. Figure 3.4(a) illustrates the available power for the microwave horn as a function of the amplitude from the signal generator. The data are taken at a signal generator frequency of 100 MHz, which is a typical value used in the experiment. Usually we operate the horn with powers of around 10 dBm (10 mW), at most 25 dBm (316 mW) are available. Often in the experiment the frequency of the signal generator is scanned such as for magnetic field calibrations. Figure 3.4(b) shows the dependence of the available microwave power on the frequency of the signal generator. Here a fixed signal generator amplitude of -26 dBm was used. We observe a continuous decrease of the microwave power with increasing frequency. For large frequencies around 1000 MHz the power is by a factor of ~ 10 lower. However, as we work in a magnetic field range of below 150 G the required frequency from the signal generator is < 200 MHz. In this range the microwave power stays nearly constant, see inset of Fig. 3.4(b).

3.4.2. Magnetic field calibration

To measure the magnetic field strength we use directly the atoms. They represent excellent magnetic field sensors because of their Zeeman shift of their internal energy levels. For calibration we prepare an optically trapped atomic sample in the hyperfine ground state $|F=3, m_F=3\rangle$ at a magnetic field B. We then apply a microwave pulse for typically 5 ms with a signal generator amplitude smaller than -25 dBm. The microwave drives the hyperfine transition $|F=3, m_F=3\rangle \rightarrow |F=4, m_F=4\rangle$ and a mixture of the two atomic states in equal shares is produced. Note that for such magnetic dipole transitions only $\Delta m_F = 0$ and $\Delta m_F = \pm 1$ is allowed. In our case the $\Delta m_F = +1$ transition is preferred due to the tilting of the microwave horn with respect to the vertical magnetic field axis. After the pulse the atoms are kept in the trap for ~ 100 ms. The microwave excitation results in resonant loss from the atomic sample because of increased inelastic

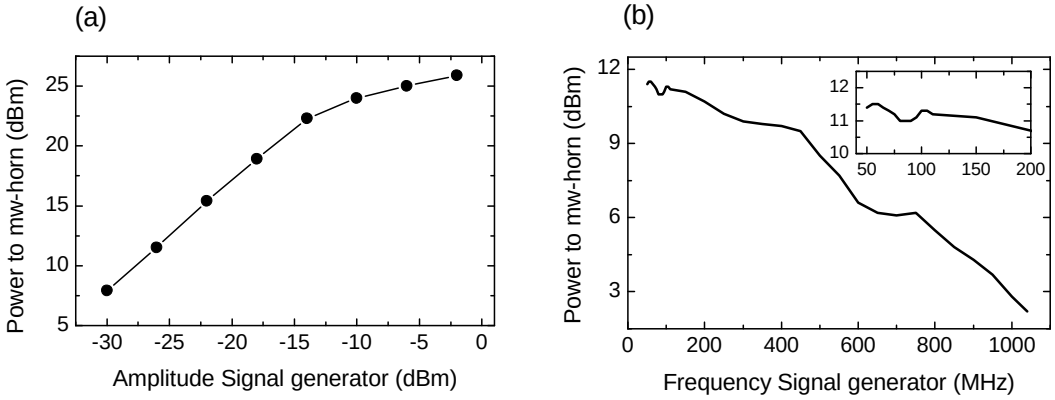

Figure 3.4.:
Dependence of the power feed to the microwave horn with respect to the amplitude and frequency of the signal generator for typical parameters. (a) We scan the amplitude of the signal generator at a fixed frequency of 100 MHz. Within the typically used amplitudes between -30 to -15 dBm the microwave power increases linearly. The maximum microwave power is $\sim$ 25 dBm (316 mW). (b) The frequency of the signal generator is scanned at a fixed amplitude of -26 dBm. We observe a strong decrease of the microwave power with increasing frequency. In a magnetic field range of < 150 G corresponding to a frequency range for the signal generator of < 200 MHz we observe a nearly constant power, see inset.

collisions between the mixed atomic states[2]. By detecting the remaining atom number of the initially prepared sample in dependence on the microwave frequency, we obtain a loss resonance. From this measurement the atomic hyperfine transition frequency $\nu_{\mathrm{at}}(B)$ is extracted. Using the Breit-Rabi formula we determine the magnetic field value B, for details see App. B.

For calibration measurements we usually use atomic samples where no magnetic field gradient is applied for levitation. There, the measured line-width (FWHM) of a typical calibration resonance is on the order of 30 kHz. The width is a consequence of the relatively long storage time of the atomic mixture after the microwave pulse, which introduces a slight broadening of the resonance. For an optimized calibration procedure we measure line-widths of $\sim$ 10 kHz, corresponding to a magnetic field width of 10 mG. This value is essentially limited by line noise and represents the absolute stability of our magnetic field in the experiment. When using magnetically levitated atoms, the typical line-width of a resonance is about 200 kHz. The width is dominated by the magnetic

[2]The loss process is due to hyperfine spin relaxation. The released energy in a collision (0.44 K) is orders of magnitudes larger than typical trap depth ($\sim \mu$K) and atoms can escape from the trap [Söd98].

field spread across the atomic sample resulting from the gradient field.

3.5. Optical pre-cooling

The initial collection and cooling of Cs atoms is achieved by conventional techniques of laser cooling and trapping [Met99]. The required technologies such as the various diode-laser setups and control are described in detail in Refs. [Mar03, Web03a]. Here, we briefly summarize the typical procedure to prepare atomic samples before transferring them into optical dipole traps.

The Cs atoms are loaded into a magneto-optical trap (MOT) from a Zeeman slowed atomic beam until up to 3×10^8 atoms have accumulated after about 6 s. The MOT loading is followed by a short optical molasses phase to compress and further cool the atomic sample. Using the technique of Raman sideband cooling in an optical lattice [Tre01], the atoms are then cooled and simultaneously polarized into the desired state $|F=3, m_F=3\rangle$. After typically 6 ms of cooling time the ensemble is adiabatically released from the lattice. When releasing the ensemble into free space, we obtain up to 3×10^7 atoms at a temperature of ~ 700 nK.

3.6. Optical dipole traps

Optical dipole traps created by far-detuned laser light represent versatile tools to confine and manipulate ultracold atomic and molecular gases. A detailed review on this trapping method is given in Ref. [Gri00].

Dipole traps are based on the electric polarizability of particles in the light field. In our experiment we use laser light near 1064 nm and 1070 nm wavelength delivered from Ytterbium fiber lasers, but also high-power CO_2-lasers operating at a wavelength of 10.6 μm are employed. As a consequence of the near- and far-infrared laser light, the generated trap potentials are attractive potentials for Cs atoms and molecules [Gri00]. Note that for typical experimental parameters for these large detunings of the laser frequency the photon scattering rate is effectively suppressed or completely negligible such as for CO_2-laser light.

3.6.1. Large volume reservoir trap(s)

After the pre-cooling phase, the polarized atomic sample is adiabatically released from the optical lattice for Raman-sideband cooling into a large volume dipole trap. We generate this "reservoir" trap by horizontally crossing two laser beams, each with a beam

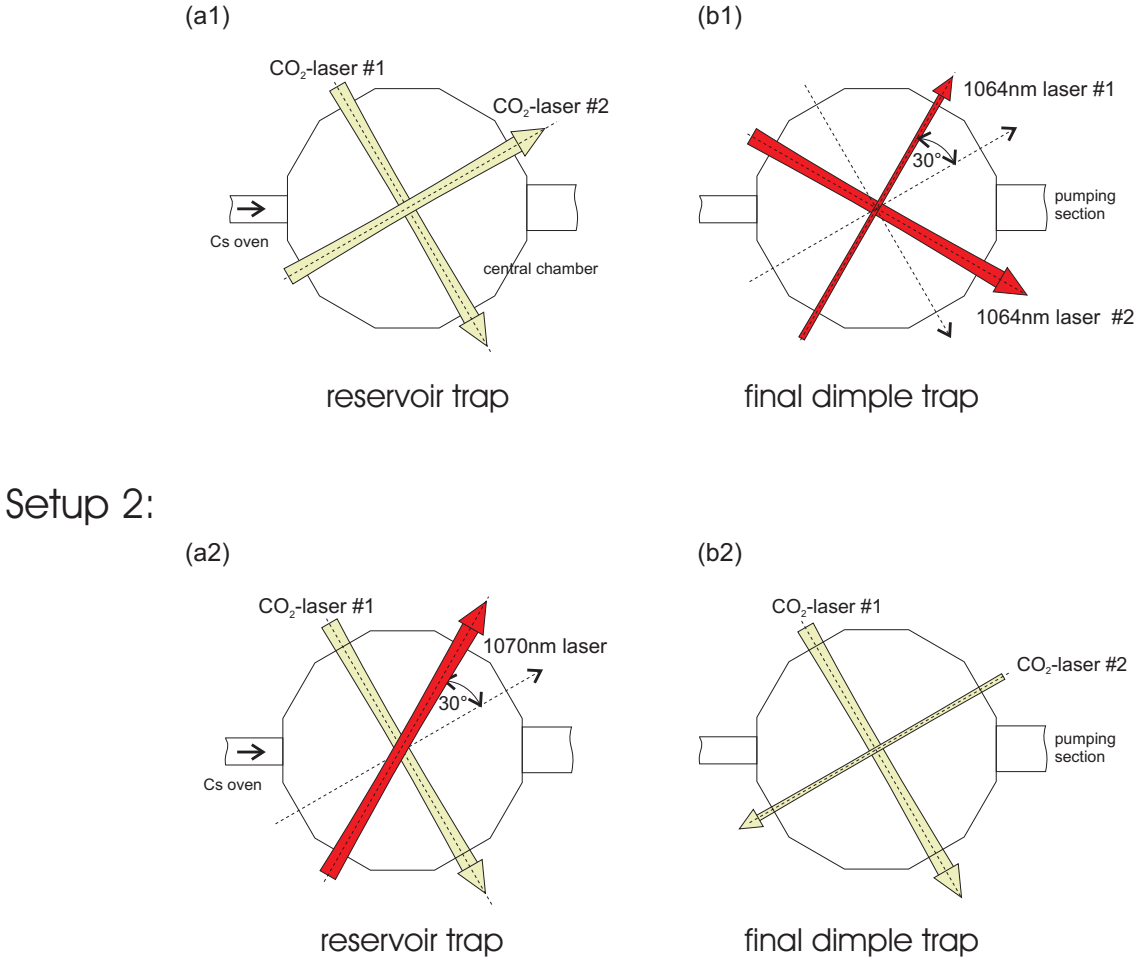

Figure 3.5.:
Two setups of dipole traps as seen from above: Setup 1 is optimized to produce atomic Bose-Einstein condensates. (a1) The large volume "reservoir" trap is generated by crossing CO_2-laser beam #1 and #2 at right angle. (b1) From the reservoir trap we load a crossed 1064 nm laser trap which is rotated by 30° with respect to the CO_2 beam paths. This trap allows for efficient forced evaporative cooling and the production of BECs. Unfortunately, this trap is not appropriate to trap molecules, as we observe strong light induced molecule losses. Setup 2 is optimized for molecule trapping and molecular state manipulation and not for BEC production. (a2) Here, the reservoir trap is realized by crossing CO_2-laser beam #1 and the 1070 nm fiber-laser beam at an angle of 60°. (b2) From the reservoir a tightly focused CO_2-laser beam #2 is loaded. By switching off the 1070 nm beam a crossed CO_2-laser trap is obtained which allows for trapping without a magnetic levitation field.

waist of around 650 μm. As illustrated in Fig. 3.5 (a1), we realize the reservoir in setup 1 by crossing two far-infrared CO_2-laser beams at right angles. Alternatively, in setup 2 we use for the reservoir one CO_2-laser beam and one near-infrared 1070 nm laser beam which cross at an angle of 60°, see Fig. 3.5 (a2). However, the resulting optical potential of the reservoir laser beams is very shallow and has to be complemented by applying a magnetic field gradient to hold the atoms against gravity.

The CO_2-laser light has a wavelength of 10.6 μm and comes from two separate, linearly polarized single-frequency lasers, each delivering about 100 W optical output power. The power and frequency of the lasers is not stabilized actively. To avoid mode-hops we stabilize the cooling water for the lasers within $\pm 0.02\,^{\circ}$C [Web03a]. For the light of the 1070 nm beam we use a broad-band, single mode Ytterbium fiber laser (IPG-Laser, Mod. YLR-50) with a maximum optical output power of about 50 W. Also this laser runs freely and the power is not servo-loop controlled. All laser beams are switched by using external acousto-optical modulators.

The use of different laser light for the reservoir in setup 1 and setup 2 is for technical reasons. In the experiment two CO_2-lasers are available. Historically, they have been used as reservoir lasers. As discussed in Sec. 3.1, for trapping molecules a CO_2-laser dimple trap is required. Changing the focus of one CO_2-laser beam during the experiment cycle from a large to a small beam waist would be great technical effort. It is much easier to use another laser beam such as the 1070 nm laser to complete the reservoir trap. Thus the remaining CO_2-laser can be used for the required dimple beam.

The applied magnetic field gradient to levitate the atoms against gravity is produced by combining a magnetic quadrupole field with a homogeneous bias field (Sec. 3.3). A magnetic field gradient of about 31.3 G/cm is necessary to levitate Cs atoms in the $|F=3, m_F=3\rangle$ state. The combination with the bias field leads to a field curvature in the horizontal plane, causing an anti-trapping force which depends on the strength of the bias field [Web03a]. This magnetic anti-trapping effect reduces the effective trap depth in the horizontal direction. For magnetic fields above 20 G the trap depth of the reservoir is about 7 μK and the anti-trapping effect is less than 5 % and negligible. Consequently, the effect on the horizontal trap frequencies is also minor. The typical geometrically averaged trap frequency for the reservoir is around $2\pi \times 13$ Hz. The magnetic levitation also affects the horizontal motion of free atoms when the optical trap is switched off. The atom expansion follows then hyperbolic functions [Web03a] while the vertical motion is not affected[3].

[3] For this work, the anti-trapping effect is not important as magnetic levitation is not applied for the experiments discussed in Chap. 4 or 6. In the spectroscopy experiments as presented in Chap. 5, the molecule cloud expands while a small gradient field is applied. For the typical expansion times in

After releasing the atoms from the Raman-lattice into the reservoir trap, 2 s of plain evaporation are necessary to thermalize the sample in the trap. The thermalization is performed at a magnetic field of 75 G, corresponding to a scattering length of about 1200 a_0. We measure typically 5×10^6 atoms at a temperature of $\sim 1\mu$K. The phase-space density is a few 10^{-3} and the atomic peak density about 5×10^{11} cm^{-3}.

3.6.2. 1064nm laser trap: Bose-Einstein condensation

To obtain a Bose-Einstein condensate, we use setup 1 as illustrated in Fig. 3.5. In particular, we load atoms from the reservoir trap in a small-volume dimple trap allowing for efficient forced evaporative cooling [Met99, Web03a]. As shown in Fig. 3.5 (b1), we generate the dimple trap by crossing in the horizontal plane one tightly focused laser beam with waist 34 μm (1064nm laser #1) and another less focused beam with waist 260 μm (1064nm laser #2) at right angles, rotated by 30° with respect to the CO_2-laser reservoir beams. The two beams have a wavelength of 1064 nm and are derived from a single-mode, broad-band Yb fiber-laser (IPG-Laser, Mod. YLR-2). The power of the laser beams is ramped up linearly within 1.5 s to a maximum power of 130 mW for laser #1 and 350 mW for #2. During the ramping up phase of the two laser beams, we reduce the magnetic field offset to about 23 G, corresponding to a scattering length of 300 a_0. This procedure ensures efficient collisional loading of the dimple from the reservoir while with increasing number and phase-space density losses from three-body recombination are reduced [Web03c, Kra04]. After the dimple loading, the remaining atoms from the reservoir are released by switching off CO_2-laser beam #2. At this stage, the trap contains about 1.5×10^6 atoms at a temperature of $\sim 1\,\mu$K, the density and phase space density is approximately 4×10^{13} cm^{-3} and 0.15, respectively.

We start forced evaporative cooling by ramping down the power in all three remaining laser beams. For the dimple beam we approximately follow an exponential ramp over a time of 5.5 s to a final power of 0.5 mW. Simultaneously we linearly lower the power of the 1064nm laser beam #2 to 280 mW, the CO_2-laser #1 is ramped to zero within this time. At the end of the evaporation the 1064nm laser beam #2 exclusively assures the longitudinal confinement of the atoms. We find that a magnetic field value of 21 G with scattering length $a = 210\,a_0$ is optimal during the forced evaporation phase. The phase transition to Bose-Einstein condensation occurs after 2 s of forced evaporative cooling with about 5×10^5 atoms at a temperature of about 200 nK. After the evaporation is completed, we obtain an almost pure BEC which contains typically 2×10^5 atoms. We

these measurements the influence of this effect on the cloud is on the order of a few percent and not relevant.

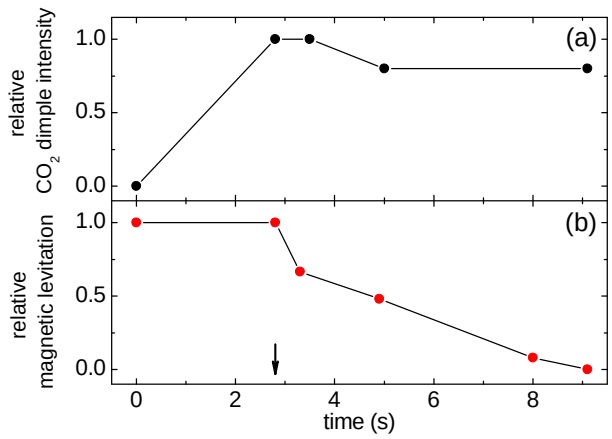

Figure 3.6.:
Loading of the CO_2 dimple beam (a) and evaporation procedure (b) to prepare an atomic sample in the crossed CO_2-laser trap without magnetic levitation. The time $t = 0$ corresponds the end of 2 s plain evaporation in the reservoir trap. Within 2.8 s we ramp up the CO_2 dimple power to 2.5 W to load atoms from the reservoir. The remaining atoms are released from the reservoir trap by switching off the 1070 nm beam, indicated by the arrow. Simultaneously forced evaporative cooling is started by lowering the magnetic field gradient to zero within 6.3 s. During the evaporation also the CO_2 dimple power is slightly reduced.

measure for the trap frequencies $2\pi \times 21\,\mathrm{Hz}$ in the radial direction and $2\pi \times 4.5\,\mathrm{Hz}$ in axial direction of the dimple beam. For the Thomas-Fermi radii [Pit03] we infer about 9 and 43 μm along the radial and axial directions, respectively. The peak density of the condensate is about $2.5 \times 10^{13}\,\mathrm{cm}^{-3}$.

3.6.3. CO_2-laser trap without levitation

We use setup 2 of Fig. 3.5 to produce an atomic sample near degeneracy in a pure CO_2-laser trap where magnetic levitation is not required. The trap is realized by using a tightly focused CO_2-laser beam as indicated by CO_2-laser #2 in Fig. 3.5 (b2). The waist of this "CO_2 dimple" is about 80 μm. This value is diffraction-limited by the aperture of the window of the vacuum chamber. Note that a smaller beam waist of the dimple trap would be advantageous for forced evaporative cooling at high efficiency [Met99]. Nevertheless, with this beam waist a laser power of only a few watt is needed to generate a potential which is deep enough to confine atoms (or molecules) without magnetic leviation. The axial confinement is provided by CO_2-laser #1, also used for the reservoir trap.

The CO_2 dimple is loaded with atoms as we cross it with the reservoir trap. For the

loading we linearly ramp up the power of the beam within 2.8 s to ~ 2.5 W, see Fig. 3.6(a). The loading power corresponds to a trap depth of about 17 μK. Simultaneously the magnetic field is ramped down to 35 G, corresponding to a scattering length of 700 a_0. This procedure provides efficient collisional loading of the CO_2 dimple [Kra04]. The remaining atoms in the reservoir trap are released by switching off the 1070 nm laser beam. In the finally obtained crossed CO_2 trap we measure at this point typically 1×10^6 atoms at a temperature of 1 μK.

As illustrated in Fig. 3.6(b), we then apply forced evaporative cooling by lowering the magnetic field gradient within 6.3 s to zero. Atoms thus mainly escape from the trap along the vertical direction. Simultaneously we adjust the scattering length by decreasing the magnetic field to a final value of ~ 22 G to minimize three-body losses [Web03c]. We also slightly decrease the power of the CO_2 dimple to 2 W resulting in an effective trap depth without levitation of $\sim 2\,\mu$K.

We finally obtain $\sim 4 \times 10^5$ Cs atoms at a temperature of about 200 nK in the crossed CO_2-laser trap. The trap frequencies of the final configuration without magnetic field gradient are measured to be 84(1) Hz and 10(1) Hz in the horizontal plane, and 80(1) Hz in the vertical direction. The resulting peak density of the atoms is $\sim 1 \times 10^{13}\,\mathrm{cm}^{-3}$, and the phase-space density is about 0.4.

3.7. Diagnostics

Any information about the atomic ensemble is obtained optically. In particular we measure the spatial density distribution of the sample using absorption imaging [Ket99], where the atomic cloud is illuminated by a laser beam and the shadow is then imaged on a CCD camera. This well-established technique is simple and robust, but destructive and after each image a new sample has to be prepared.

For taking an absorption picture at zero magnetic field, at first the atoms are pumped from the ground state to the $F = 4$ state. To do so we illuminate the atoms for about 500 μs using the re-pumper light from the MOT, resonant to the $F = 3 \rightarrow F' = 3$ transition. We then turn on the imaging light for typically 200 μs, which is resonant on the closed $F = 4 \rightarrow F' = 5$ optical transition. By taking a second picture without atoms, residual imaging noise is canceled in the subsequent analysis procedure.

In the experiments, it is often convenient to take absorption images at some 'final' magnetic field such as for molecule detection. Currently we are able to take images in a magnetic field range of up to 55 G. The re-pumping light of the MOT is not adjusted in frequency as it is sufficiently close to the $F = 3 \rightarrow F' = 3$ transition within this magnetic field range. Using a re-pumping time of about 1 ms we sufficiently transfer

the atoms into the $|F=4, m_F=4\rangle$ state. For the imaging light we have adapted the setup to take the Zeeman-shift of the states into account. The imaging light is tuned to the $|F=4, m_F=4\rangle \rightarrow |F'=5, m_{F'}=5\rangle$ optical transition. As the absorption cross section differs at non-zero magnetic fields from the usual one [Kra06a], the measured atom number is about 77% to low.

The imaging beam propagates in the horizontal plane in transverse direction to the atomic beam line, see top view of Fig. 3.1. Using a lens-system we obtain the vertical and horizontal extension of the atom cloud on the CCD-camera (Theta Systems). The spatial resolution is on the order of $8\,\mu$m. The computer read-out of the images and subsequent analysis provides experimental information such as particle number and cloud size. By monitoring the expansion of atomic clouds in a series of images with increasing delay times after release from the trap, the temperature of a thermal gas can also be determined. Similarly, by measuring the position or size of the cloud as a function of the holding time after an excitation of the sample in the trap, we can determine trap frequencies and characterize the trapping potentials [Web03a, Her05].

A detailed description of the imaging techniques and the analysis procedure is given in Ref. [Web03a], for absorption imaging at small magnetic fields see Ref. [Kra06a].

4. Preparation of Cs_2 Molecules in various internal states

In this chapter, we present our methods to prepare Cs_2 Feshbach molecules in various internal states. The starting point for the molecule preparation is an optically trapped ensemble of ultracold Cs atoms. In particular the atoms are prepared in the crossed CO_2-laser dipole trap without magnetic levitation as described in Sec. 3.6.3. In Sec. 4.1 the creation of optically trapped Cs_2 molecules based on different Feshbach resonances is presented. These resonances serve as "entrance doors" into the rich molecular structure near threshold. We then discuss in Sec. 4.2 our techniques to transfer molecules to various internal states by application of elaborate time-variations of the magnetic field. We make use of the possibility of adiabatic or diabatic passages through avoided crossings. In Sec. 4.3 finally the detection of the molecular samples through controlled dissociation is discussed.

4.1. Molecule production through Feshbach resonances

We magnetically associate ultracold cesium atoms to dimers on Feshbach resonances [Her03, Xu03, Dür04a, Köh06]. We use *three different* resonances, the two g-wave resonances at $B = 19.8\,\mathrm{G}$ and $53.4\,\mathrm{G}$ and the d-wave resonance at $47.9\,\mathrm{G}$, see Fig. 4.1. The width of the g-wave resonances is only a few mG, the d-wave resonance is about $200\,\mathrm{mG}$ wide. While the molecule formation at the $19.8\,\mathrm{G}$ g-wave resonance results in g-wave molecules, the association at the $47.9\,\mathrm{G}$ d-wave resonance leads in practice to s-wave molecules. This is a consequence of an avoided level crossing close to threshold between the states $4d$ and $6s$, see Fig. 4.1. Similarly, the association at the $53.4\,\mathrm{G}$ g-wave resonance results in d-wave molecules.

For the association of molecules at the Feshbach resonances two different schemes are used. Depending on the character of the Feshbach resonance, we apply a ramping or a switching scheme to produce dimers [Mar05]. The switching scheme works particularly well at the narrow g-wave Feshbach resonances. We set the magnetic field typically $0.5\,\mathrm{G}$ above the resonance. The field is then suddenly changed to the resonance position and

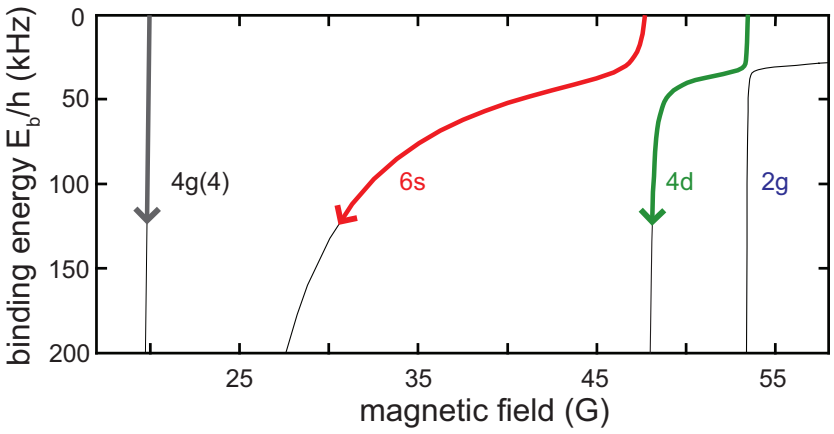

Figure 4.1.:
The molecular energy structure for very small binding energies in the region of the 19.8 G, 47.9 G and 53.4 G Feshbach resonances. Above 45 G two avoided crossings are present in the energy structure. We use all three Feshbach resonances to associate molecules by ramping or switching the magnetic field. The arrows indicate the pathway after molecule association as the magnetic field is ramped down to allow for the optical removal of the atoms from the molecules.

kept there for ~ 5 ms. In contrast, at the much broader 47.9 G d-wave Feshbach resonance we find superior efficiency by applying a linear magnetic field ramp (ramping scheme). We start typically 350 mG above the resonance and linearly ramp the magnetic field within 5 ms to about 350 mG below the resonance. The efficiencies for molecule production range from a few percent up to 20%. Starting from 4×10^5 atoms we typically obtain 15000 molecules, see Table 4.1.

To prepare a maximum number of molecules in the trap, it is necessary to separate atoms and molecules as fast as possible, since atom-dimer collisions dramatically reduce the lifetime of the molecular sample [Muk04]. Figure 4.2 shows two loss measurements of $6s$ molecules in the trap. When atoms are present, 50% of the molecules are lost within 5 ms. In contrast, for a pure molecular sample we observe the same loss fraction after a time of about 150 ms. For that reason we remove the atoms from the dipole trap using a 'blast' technique similar to Ref. [Xu03]. First, the atoms are pumped out of the $|3,3\rangle$ state by light close to the $F = 3 \rightarrow F' = 3$ transition. The blast pulse is tuned to the closed optical transition $|F = 4, m_F = 4\rangle \rightarrow |F' = 5, m_{F'} = 5\rangle$, which we also use for imaging (see Sec. 3.7). The optical cleaning process causes some unwanted loss and heating of the molecules. Particularly if the molecules are very weakly bound

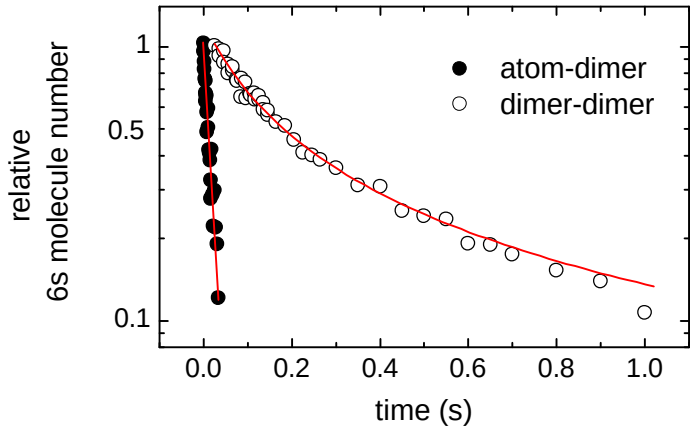

Figure 4.2.:
Example of collisional decay curves of $6s$ molecules in a pure molecular sample (open circles) or in a mixture of atoms and dimers (filled circles). The samples are prepared in the crossed CO_2 dimple trap at a magnetic field of about 40 G. The timescale for 50% loss of molecules is for the atom-dimer mixture typically 30 times smaller than for the pure molecular sample.

($\lesssim h \times 1\,\mathrm{MHz}$) or the blast duration is too long ($\gtrsim 1\,\mathrm{ms}$) these effects are not negligible. Therefore immediately after the association we rapidly ramp the magnetic field further down. When the binding energy of the molecular state is on the order of $h \times 5\,\mathrm{MHz}$ the molecules are much less affected by the blast light. When using the 19.8 G resonance the magnetic field has to be ramped down only a few Gauss to reach such a binding energy. In case of the 47.9 G resonance (53.4 G resonance) the lowering of the magnetic field transfers the molecules into the $6s$-state ($4d$-state) through the present avoided crossings, see Fig. 4.1. Therefore, to reach a sufficiently large binding energy a larger change in the magnetic field is required, resulting in a longer time to reach the field. However, with a typical blast duration of $400\,\mu$s we achieve a sufficient removal of the atoms from the trap while keeping the blast-induced molecule losses small ($\sim 10-15\%$).

The precise timing for molecule production, the magnetic field for the purification, and the obtained number of molecules strongly depend on the particular Feshbach resonance. Table 4.1 summarizes the relevant experimental parameters of our molecule production. We measure a typical temperature of 250 nK for the molecular samples. This is slightly higher than the temperature of the atoms, presumably because of the effects of the blast cleaning technique. The corresponding peak density of the molecules is about $7 \times 10^{11}\,\mathrm{cm}^{-3}$.

Feshbach resonance position (G)	19.8	47.9	53.4
entrance state	$4g(4)$	$4d$	$2g$
ramp speed (G/s)	-	140	-
state at B_r	$4g(4)$	$6s$	$4d$
B_r (G)	14.5	19.7	45
time to reach B_r (ms)	0.4	3	1
number of molecules	19000	9000	15000

Table 4.1.:
Parameters for molecule production using three different Feshbach resonances. B_r is the field value at which the atoms are removed with the blast technique.

4.2. Transfer between different molecular states

Other molecular states than the ones that we can directly access through the Feshbach creation schemes can be populated by controlled state transfer. The experimental key is the precise control of Landau-Zener tunneling at avoided crossings through elaborate magnetic field ramps. By means of the ramp speed we can choose whether a crossing is followed adiabatically (slow ramp) or jumped diabatically (fast ramp). An important application of controlled ramps through avoided crossings is the coherent splitting of the molecular wave function for intermediate ramp speeds, as discussed later in Chap. 6.

Within the Landau-Zener model [Lan32, Zen32] an avoided level crossing is characterized by two parameters, the coupling strength and the differential slope of the states. For the coupling strength we introduce the parameter V as one-half the energy splitting between the two states at the crossing point. To characterize the slope we use $\Delta\mu$ as the magnetic moment difference between the two states. With these two parameters one commonly defines a critical ramp speed

$$r_c = \frac{2\pi V^2}{\hbar \Delta\mu}. \tag{4.1}$$

For fast ramps with ramp speed $\dot{B} \gg r_c$, the passage through the crossing is diabatic and the molecules stay in the same bare state. For slow ramps ($\dot{B} \ll r_c$), an adiabatic transfer into the other molecular state takes place. For Cs Feshbach dimers the typical coupling strengths for crossings between states of different $f\ell$ (see Sec. 2.3) are such that the critical ramps speeds are found in a range convenient for experiments. Full control ranging from completely diabatic Landau-Zener tunneling to full adiabatic transfer can be achieved for most crossings (see Sec. 5.1.2).

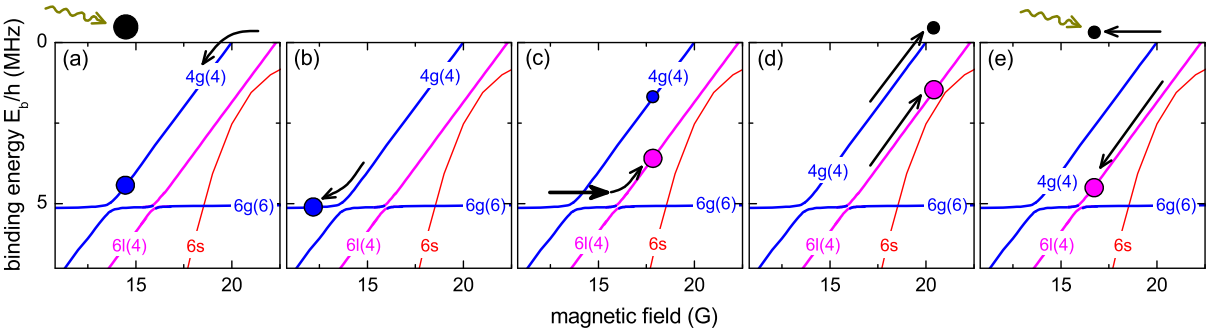

Figure 4.3.:
Illustration of the experimental toolbox for the preparation of molecules in various internal states. As an example the production of molecules in the $6l(4)$ state is shown. (a) First, we produce $4g(4)$ molecules at the g-wave Feshbach resonance at 19.8 G and remove the remaining atoms by a short blast pulse, indicated by the rippled arrow. (b) The $4g(4)$ state is transferred into state $6g(6)$ by slowly lowering the magnetic field. (c) To overcome the avoided level crossing between state $4g(4)$ and $6g(6)$ a very fast magnetic field ramp is applied. The target state $6l(4)$ is then accessed by using a second adiabatic ramp. (d) To remove the residual $4g(4)$ from the $6l(4)$ molecules we ramp the magnetic field slightly above 20 G, dissociating the $4g(4)$ molecules into atoms while not affecting the l-wave molecules. (e) The magnetic field is lowered again to increase the binding energy of the target state molecules. A second blast pulse removes the remaining atoms and a pure sample of $6l(4)$ molecules is obtained.

To illustrate the experimental procedure for transferring molecules into different states, we now consider the preparation of a molecular sample in a selected "target" state. As an example we discuss the population of the target state $6l(4)$ in detail. The state transfer strongly relies on the technical performance of the set-up for magnetic field control, a detailed description of which is given in Sec. 3.3.

As shown in Fig. 4.3(a), we first create $4g(4)$ molecules at the 19.8 G Feshbach resonance. We then lower the magnetic field to about 14.5 G and remove the remaining atoms with the blast pulse. In a second step, see Fig. 4.3(b), we lower the magnetic field to ~ 12 G within a few ms. Consequently, we pass the avoided crossing between the two states $4g(4)$ and $6g(6)$ at about 13.5 G. For this crossing the critical ramp speed, given by Eq. 4.1, is $r_c \sim 1100$ G/ms as the coupling strength is $V \simeq h \times 150$ kHz [Chi05b]. With the applied ramp speed of ~ 2 G/ms the transfer into state $6g(6)$ is therefore fully adiabatic. Fig. 4.3(c) illustrates the transfer of the $6g(6)$ molecules to the target state $6l(4)$. First we apply a fast magnetic field ramp to overcome the $4g(4)/6g(6)$ crossing, indicated by the straight arrow. The high ramp speed required is accomplished by a specially designed "booster" coil, described in Sec. 3.3. With a maximum possible ramp speed of 7500 G/ms we achieve a transfer efficiency of typically 70%. After the jump we enter the target state $6l(4)$ by adiabatically following the next avoided crossing between state $6g(6)$ and $6l(4)$ at ~ 15.5 G. For this crossing we find a fully adiabatic transfer when ramping the magnetic field from 15 G to ~ 17 G within a few ms. In the fourth step, illustrated in Fig. 4.3(d), we prepare the cleaning of the sample from the residual $4g(4)$ molecules. The magnetic field is ramped up to ~ 20 G and kept constant for a few ms. While the remaining $4g(4)$ molecules break up into atoms, the $6l(4)$ molecules are not affected as their dissociation threshold is at a higher magnetic field. Finally, we ramp down the magnetic field to $B \simeq 16$ G where the target molecules are well below threshold, see Fig. 4.3(e). Again we remove the residual atoms using a blast pulse. As a result, we obtain a pure molecular sample in the state $6l(4)$.

In analogous ways, we apply these techniques to populate any of the states shown in Fig. 2.7 of Sec. 2.3. The time to prepare the molecular sample together with the duration of all subsequent measurements is about 20 to 25 ms. Molecule-molecule collisions [Chi05b, Zah06] are not relevant on this timescale for the given molecular densities.

4.3. Molecule detection

The standard detection scheme for Feshbach molecules relies on the controlled dissociation by reverse magnetic field ramps [Her03, Dür04b]. When ramping the magnetic field above the dissociation theshold, the molecules become quasi-bound and decay into

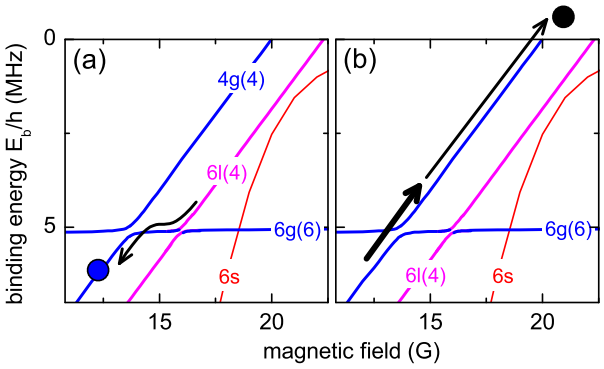

Figure 4.4.:
(color online) Example of a detection scheme for l-wave molecules. (a) First the $6l(4)$ molecules are adiabatically transferred into the state $4g(4)$ via the state $6g(6)$ by ramping down the magnetic field. (b) The avoided crossing at 13.6 G is passed by using a fast magnetic field ramp. When ramping up to a field of $\sim$ 21 G, the molecules are brought above threshold and dissociate. The resulting atom cloud is detected using the standard absorption imaging technique.

the atomic scattering continuum. The resulting atom cloud can then be detected using standard absorption imaging.

Magnetic dissociation by inverse magnetic field ramps is straightforward for states with large coupling to the scattering continuum, and hence any of the Feshbach resonances up to g-wave can be used. We ramp the magnetic field typically 2 G above threshold and wait a few ms at the dissociation field before the image is taken. l-wave molecules do not sufficiently couple to the atomic continuum and significant dissociation is prevented. One way to detect l-wave dimers is to transfer these molecules into one of the s-, d- or g-wave states which allow for dissociation and hence for detection.

To illustrate the detection by controlled dissociation, we resume our previous example of Sec. 4.2, where we have described the preparation of a molecular sample in the $6l(4)$ state. Fig. 4.4 shows the detection scheme that we use for this state. First the molecular sample is adiabatically transferred to the state $4g(4)$ via the state $6g(6)$ by lowering the magnetic field to about 12.5 G, see Fig. 4.4(a). We then perform a diabatic state transfer over the avoided crossing at $\sim$14 G as indicated in Fig. 4.4(b). Finally, we ramp the magnetic field up to $\sim$21 G, which is well above the dissociation threshold of the $4g(4)$ state.

An alternative method for the detection of l-wave molecules relies on the particular energy structure of Cs atoms above the dissociation threshold. We find that the decay of

metastable l-wave dimers can be mediated by coupling to a quasi-bound g-wave molecular state above threshold. Such a coupling with $\Delta\ell = 4$ is sufficiently strong. For example the detection of l-wave molecules in the $6l(3)$ state relies on this dissociation process. As discussed later in Chap. 6, the $6l(3)$ state is used to realize a molecular interferometer. A more detailed analysis of this dissociation mechanism will be presented elsewhere [Kno08b].

For imaging of the resulting atomic cloud, the atoms are first pumped to the $|4,4\rangle$ state using light close to the $F=3 \rightarrow F'=3$ transition. The imaging light is resonantly tuned to the closed $|F=4, m_F=4\rangle \rightarrow |F'=5, m_{F'}=5\rangle$ optical transition, taking the Zeeman shift at the imaging magnetic field into account.

5. Spectroscopy of the molecular energy structure

The rich energy structure of Cs_2 Feshbach molecules requires flexible methods to determine the molecular energy spectrum. Previous studies on Feshbach molecules have mostly addressed the last, most weakly bound state responsible for the respective Feshbach resonance. Molecular binding energies have been measured by applying various methods either to atomic [Don02, Cla03, Tho05b, Osp06] or to molecular samples [Reg03, Bar05, Chi05b, Mar07b].

In this Chapter, we present our results on spectroscopy of weakly bound molecules. For all measurements the molecules are prepared in the crossed CO_2-laser trap using the techniques as described in Chap. 4. To measure the binding energies of the molecular states we apply two different techniques. Both techniques are suitable for probing weakly as well as deeply bound molecular states.

The first method (Sec. 5.1) is based on a measurement of the molecular magnetic moment [Chi05b]. Magnetic moment spectroscopy is a very general method, independent of selection rules and wave function overlap requirements. It can be applied to any molecular state and thus it is an important tool to identify molecular states. In particular this method allows us to follow and investigate the avoided level crossings between different molecular states. Transfers between different molecular states are observed as sudden changes of the magnetic moment. In this way, we are able to completely map out the molecular spectrum below the atomic scattering continuum, including three l-wave states, two of which had so far not been discovered.

The second method (Sec. 5.2) uses microwave radiation to measure binding energies of trapped molecules with very high precision. We use a microwave pulse to drive a hyperfine transition from a molecular bound state to a higher molecular bound state that is associated with another channel of the electronic ground-state manifold. Rapid spontaneous dissociation loss [Tho05a] provides the spectroscopic signal. In contrast to the magnetic-moment technique the microwave technique can not induce a change of the molecular orbital angular momentum quantum number ($\Delta\ell = 0$) which restricts the applicability of this method. In our experiment we apply the microwave spectroscopy on

a molecular s-wave state.

5.1. Magnetic moment spectroscopy

5.1.1. Bare energy levels

We measure the molecular magnetic moment using the Stern-Gerlach effect. Optically trapped molecules are initially prepared in a single quantum state at a certain magnetic field B by following the procedure described in Chap. 4. The molecular sample is then released from the trap. It starts to expand while simultaneously a vertical magnetic field gradient $B' = \partial B/\partial z$ of typically 13 G/cm is turned on. During the time of flight, both the gravitational force and the magnetic force displace the center-of-mass position of the molecular cloud along the vertical direction. The magnetic force acting on the molecules is given by

$$F_z = \mu_{\mathrm{mol}} B', \tag{5.1}$$

where μ_{mol} is the molecular magnetic moment. The vertical relative displacement Δz_{mol} of the molecular cloud with respect to the position after expansion at zero magnetic gradient is proportional to μ_{mol},

$$\Delta z_{\mathrm{mol}} = \frac{1}{2}\frac{\mu_{\mathrm{mol}} B'}{m_{\mathrm{mol}}} t_{\mathrm{SG}}^2, \tag{5.2}$$

where $m_{\mathrm{mol}} = 2m_{\mathrm{at}}$ is the molecular mass and equal to the mass of two atoms. t_{SG} is the time spent by the molecules in the magnetic field gradient during the Stern-Gerlach procedure.

To minimize uncertainties resulting from B', t_{SG}, and the spatial calibration of the imaging system, it is convenient to measure μ_{mol} relative to the well-known magnetic moment μ_{at} of the atoms. Consequently, μ_{mol} can be written as

$$\mu_{\mathrm{mol}} = \frac{\Delta z_{\mathrm{mol}}}{\Delta z_{\mathrm{at}}} 2\mu_{\mathrm{at}}, \tag{5.3}$$

where Δz_{at} is the measured displacement of atoms for the same $B^{'}$ and t_{SG}.

In previous experiments, we have determined μ_{mol} by measuring the magnetic field gradient needed to levitate the molecules against gravity [Her03, Chi05b]. For each magnetic field value B, the value of B' was adjusted to maintain the levitation condition. This method is not practical when B is changed over a wide range. In the present experiments, we measure the displacement of the molecular gas for a fixed B' and for $B' = 0$.

Once the magnetic moment μ_{mol} is known as a function of B, the molecular binding energy E_b is calculated by integrating

$$\frac{\partial E_b}{\partial B} = 2\mu_{\mathrm{at}} - \mu_{\mathrm{mol}}. \tag{5.4}$$

The integration constant is fixed by the atomic scattering threshold where $E_b = 0$. Eq. 5.4 establishes a one-to-one correspondence between μ_{mol} and E_b at each magnetic field.

An example of a magnetic moment measurement is shown in Fig. 5.1. We produce $6s$ molecules from the 47.9 G resonance as discussed in Sec. 4.1. We then follow the path indicated by the arrow in Fig. 5.1(b) and measure the molecular magnetic moment at different values of B. We observe a strong magnetic field dependence of the magnetic moment of the $6s$ molecules. Above 30 G, where the $6s$ level runs almost parallel to the atomic threshold (see Fig. 5.1(b)), μ_{mol} is nearly constant with a value close to $2\mu_{\mathrm{at}}$ ($=1.5\,\mu_B$, with Bohr's magneton μ_B, for which $\mu_B/h \approx 1.400\,\mathrm{MHz/G}$). When lowering B below 30 G, we start to observe a decrease of μ_{mol}, which drops to one tenth of the initial value within a magnetic field range of about 10 G. This behavior is explained by the strong coupling between two different $6s$ states. When further lowering the magnetic field, μ_{mol} suddenly changes from $0.19\,\mu_B$ to $1.5\,\mu_B$ as the molecules are transferred to the $6g(6)$ state via the $6s/6g(6)$ avoided crossing. The $6g(6)$ state has a nearly constant magnetic moment, slightly less than $1.5\,\mu_B$. Upon further lowering of B the next avoided crossing (to the state $4g(4)$, see Fig. 2.7) would be expected at ~ 13.5 G [Chi05b, Mar07b]. However, μ_{mol} undergoes a rapid change to a value of about $1\,\mu_B$ at ~ 16 G. This indicates the presence of a new avoided crossing and hence the presence of a new state. The existence of this state cannot be explained within the original NIST model [Leo00, Chi04b], which includes molecular states only up to g-waves. The extension of the model to higher order molecular states (Sec. 2.3) identifies this state as a $6l(4)$ state [Tie07].

Our method generally works well when the magnetic moment is constant. The typical error resulting from the determination of the cloud position is less than $0.03\,\mu_{\mathrm{B}}$. Systematic errors are the result of some magnetic-field curvature. For non-constant magnetic moment, e. g. near avoided crossings, systematic errors are introduced as a result of the cloud expansion and fall in the magnetic gradient field. The limitations are briefly discussed below.

Similar measurements have been performed for most of the molecular states in the magnetic field range from 5 to 55 G. The results of our magnetic moment spectroscopy are summarized in Table 5.1 and the molecular energy spectrum derived using Eq. (5.4) is shown in Fig. 5.2 (open circles) along with the results of the extended NIST model (solid lines). We detect all the s-, d-, g- and l-wave states in the range of interest. Note

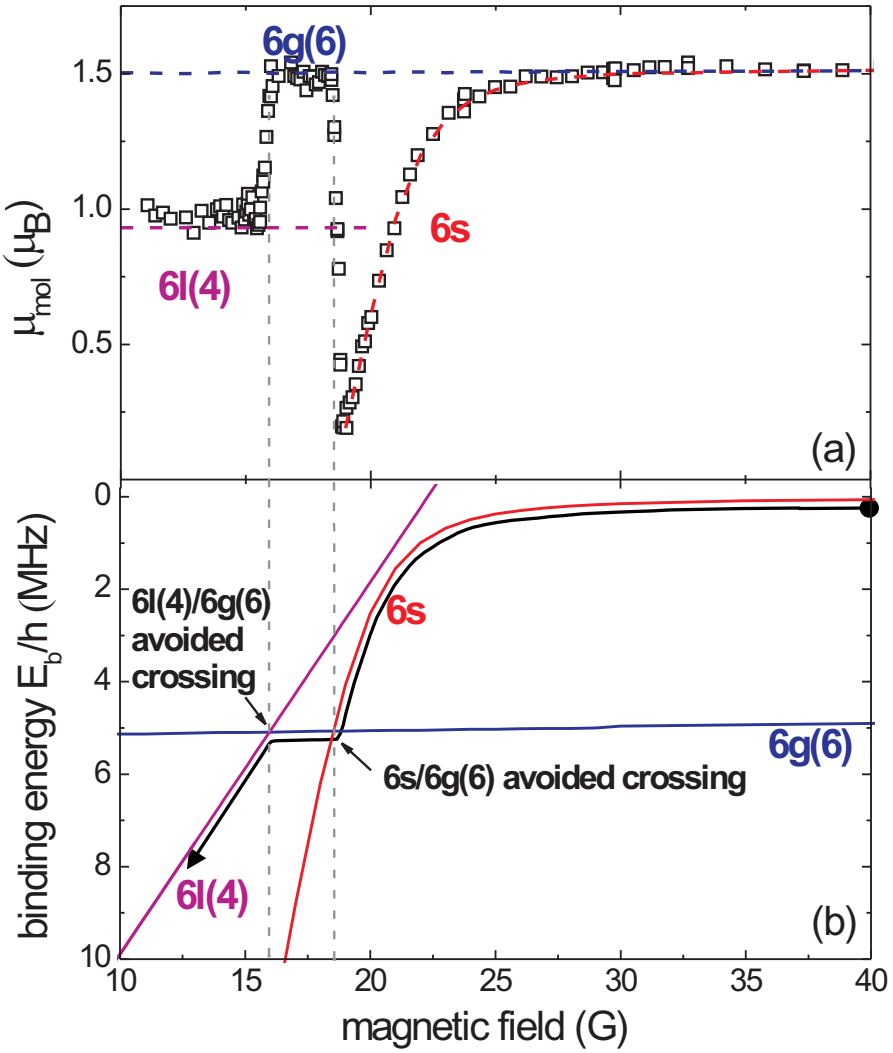

Figure 5.1.:
Magnetic moment of Cs dimers across the $6s$ - $6g(6)$ - $6l(4)$ molecular path. (a) The measured magnetic moments (open squares) are compared to the NIST calculations (dashed lines). The fast changes of the magnetic moment at 18.5 G and 16 G result from the $6l(4)/6g(6)$ and $6s/6g(6)$ avoided crossings, respectively. (b) Molecular binding energies of the $6s$, $6g(6)$ and $6l(4)$ levels calculated from the NIST model, see also Fig. 2.7. The molecular path followed in the measurement is indicated by the black arrow.

Molecular state	B (G)	μ_{mol}/μ_B	
		measured	NIST model
$6l(3)$	4 - 9	0.75(4)	0.702
	12 - 16	0.75(2)	0.702
$4g(4)$	5.5 - 12	0.95(4)	0.912
	15.5 - 20	0.949(6)	0.932
$6l(4)$	11 - 15	0.98(3)	0.931
	16 - 24	0.96(1)	0.931
$6s$	19	0.192	0.191
	45	1.519	1.515
$6l(5)$	15.5 - 23.5	1.15(3)	1.155
	26 - 37	1.15(2)	1.155
$4d$	41 - 43.2	0.39(1)	0.310
	45.5 - 47.1	0.36(2)	0.310
$2g$	51.7 - 52.2	0.05(3)	0.001
$6g(6)$	19 - 24	1.49(1)	1.503
	26 - 40	1.5(1)	1.503

Table 5.1.:
Measured magnetic moment μ_{mol} of Cs_2 molecules in different internal states with the corresponding magnetic field range. Assuming a constant magnetic moment μ_{mol} in each range considered, the error of μ_{mol} accounts for the statistical error and a slight change of μ_{mol}. For each state the theoretical magnetic moment from the NIST model is also listed.

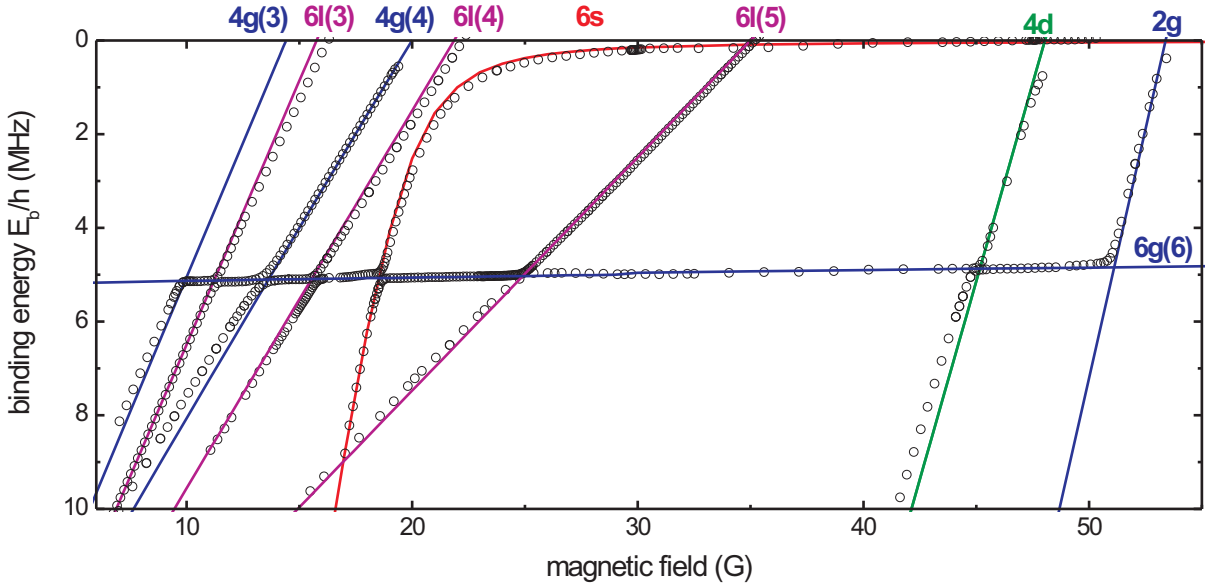

Figure 5.2.:
Energy spectrum of weakly bound Cs molecules as a function of the magnetic field. The binding energies for the different molecular states are derived from magnetic moment spectroscopy (open circles). The solid lines are the molecular binding energies resulting from the extended NIST model (for details see Sec. 2.3).

that there are no i-wave states in this range. All d-, g- and l-wave states exhibit a rather constant magnetic moment. Consequently, we find a nearly linear dependence of the binding energy on B, as shown in Fig. 5.2.

In Table 5.1 and Fig. 5.2 we compare our results with the NIST model. In general, we find good agreement with the theoretical predictions for the binding energies and magnetic moments of the s-, d- and g-wave states. The small discrepancies observed for the lower branch of the $4g(4)$ state and for the $4d$ state are probably the result of the more complicated production schemes introducing larger systematic errors in the measurements.

An important result of the magnetic moment spectroscopy is the detection and characterization of three l-wave states, the states $6l(3)$, $6l(4)$ and $6l(5)$. Signatures of the $6l(3)$ state have been observed earlier [Chi05b] and triggered the interferometric measurements shown in Chap. 6. The other two l-wave states had so far not been discovered. In contrast to the s-, d- and g-wave states, the l-wave states do not reveal themselves via Feshbach resonances in atomic scattering as the coupling to the atomic scattering state

is too weak. Therefore these states had previously not been included in the NIST model. The extended NIST model shows the existence of these three l-wave states and predicts their magnetic moments. Despite the accuracy of these predictions, the model is not able to precisely determine the binding energies. Our measurements now completely characterize the three l-wave states and in particular give a value for the binding energy at zero magnetic field where all three states are degenerate. We find the binding energy of the $6l$ manifold of states at zero magnetic field to be 17.61(9) MHz. In Fig. 2.7 and Fig. 5.2 we have down-shifted the NIST prediction of the $6l$ states by ~ 2.25 MHz to match the experimentally obtained binding energies. The measurements also locate the magnetic field positions where the three $6l$ states intersect the atomic scattering continuum. We find the crossing positions for the $6l(3)$, $6l(4)$, and $6l(5)$ states at 16.1(2) G, 22.0(2) G, and 35.0(2) G, respectively.

5.1.2. Avoided crossings

Magnetic moment spectroscopy also allows a direct observation of the avoided crossings between different molecular states. As is well known, the coupling V between two generic molecular states, state 1 and state 2, modifies the bare energies E_1 and E_2 by opening an energy gap $2V$ at the crossing position. In the limit of a coupling strength V that is small compared to the energy separation to all other states, the avoided crossings can be studied within a simple two-state model. This model takes the two interacting bound states into account while both the couplings with the scattering continuum and with other molecular states are neglected. The coupled energy levels are given by

$$E_{\pm} = \frac{(E_1 + E_2) \pm \sqrt{(E_1 - E_2)^2 + 4V^2}}{2}. \tag{5.5}$$

The energies E_+ and E_- refer to the upper and lower adiabatic levels of the avoided crossing. The derivatives $-\partial E_{\pm}/\partial B$ correspond to the magnetic moments μ_+ and μ_- of the coupled states with

$$\mu_{\pm} = \frac{1}{2}(\mu_1 + \mu_2) \mp \frac{1}{2}\frac{(\mu_2 - \mu_1)^2(B - B_0)}{\sqrt{(\mu_2 - \mu_1)^2(B - B_0)^2 + 4V^2}}. \tag{5.6}$$

Here, B_0 is the magnetic field at the avoided-crossing position, and μ_1 and μ_2 are the magnetic moments of the two bare molecular states.

In the following we focus on the avoided crossings between the $6g(6)$ state and the other $f\ell(m_f)$ states. Figure 5.3 shows the magnetic moments μ_+ (circles) and μ_- (triangles) across the $6g(6)/4g(4)$ avoided crossing. To derive the coupling strength between these two states, we fit our data using Eq. (5.6) by leaving μ_1, μ_2, B_0, and V as free parameters.

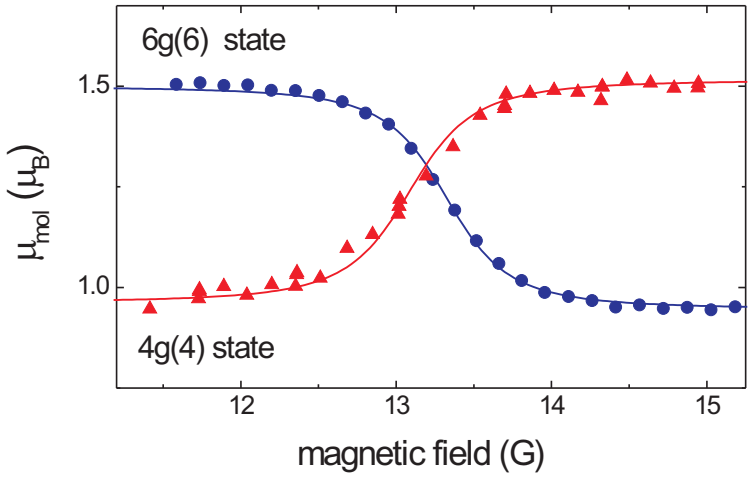

Figure 5.3.:
Magnetic moments of Cs dimers across the $6g(6)/4g(4)$ avoided crossing. Both the change in magnetic moment from the $6g(6)$ to the $4g(4)$ state (circles) and the one from the $4g(4)$ to the $6g(6)$ state (triangles) are shown. The measured magnetic moments are fitted using Eq. (5.6) (solid lines).

$f\ell(m_f)$	B_0 (G)	V/h (kHz)	
$6l(3)$	11.22(2)		16(3) [a], 14(1) [b]
$4g(4)$	13.29(4)	164(30)	150(10) [c]
$6l(4)$	15.50(3)	64(13) [d]	
$6l(5)$	25.3(1)	63(22) [d]	
$4d$	45.15(4)	120(21)	

Table 5.2.:
Avoided crossing positions B_0 and coupling strengths V/h between the $6g(6)$ state and the intersecting $f\ell(m_f)$ molecular states obtained by fitting the measured magnetic moments with Eq. (5.6). The errors are the one-sigma statistical uncertainties. V/h measured with different techniques are also reported (see notes).

[a] Landau-Zener method.
[b] Interferometric method (Chap. 6).
[c] Magnetic levitation method [Chi05b].
[d] These values should be considered as upper limits.

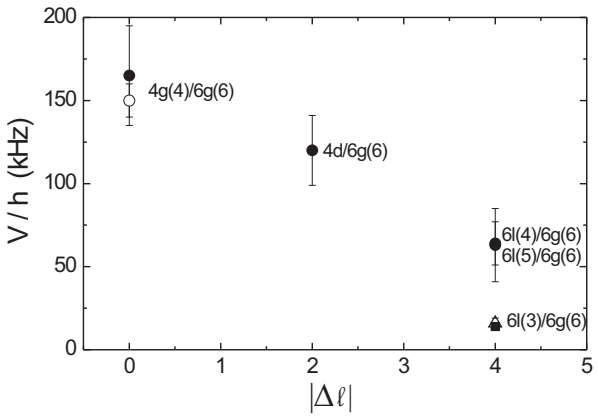

Figure 5.4.:
Coupling strengths V/h between the $6g(6)$ state and the intersecting $f\ell(m_f)$ molecular states as a function of the difference between their orbital angular momentum quantum numbers, $|\Delta\ell|$. The data refer to the values obtained via the magnetic moment spectroscopy (filled circles), a magnetic levitation method (empty circle) [Chi05b], an interferometer method (square) as discussed in Chap. 6, and the Landau-Zener method (triangle).

The same procedure is adopted to analyze the other crossings. The coupling strengths and the avoided crossing positions are listed in Table 5.2. For comparison, we include in Table 5.2 measurements of V obtained with other techniques, such as the Landau-Zener method discussed below, an interferometric method as presented in Chap. 6, and a magnetic levitation method [Chi05b].

In Fig. 5.4 we plot the measured coupling strengths V between the $6g(6)$ state and the other intersecting states as a function of the difference in orbital angular momentum $|\Delta\ell|$. While the $6g(6)/4g(4)$ and the $6g(6)/4d$ crossings are the result of the first order spin-spin dipole interaction, the crossings with the l-wave states are second order. As a general trend, crossings with larger $|\Delta\ell|$ tend to have a weaker coupling.

Systematic errors in our avoided crossing measurements stem from the finite size of the molecular cloud and the change of μ_{mol} during the free fall and expansion in the presence of the magnetic-field gradient. This effect causes a smoothening of the rapid magnetic moment changes (see Fig. 5.1) and hence an apparent broadening of the avoided crossings leading to an overestimation of the coupling strengths, in particular for the narrower crossings. We find a limit on the minimum coupling strength that can be extracted with reasonable precision. We estimate from simulations that coupling strengths below $h \times 50\,\mathrm{kHz}$ can no longer be sensitively measured with our present method.

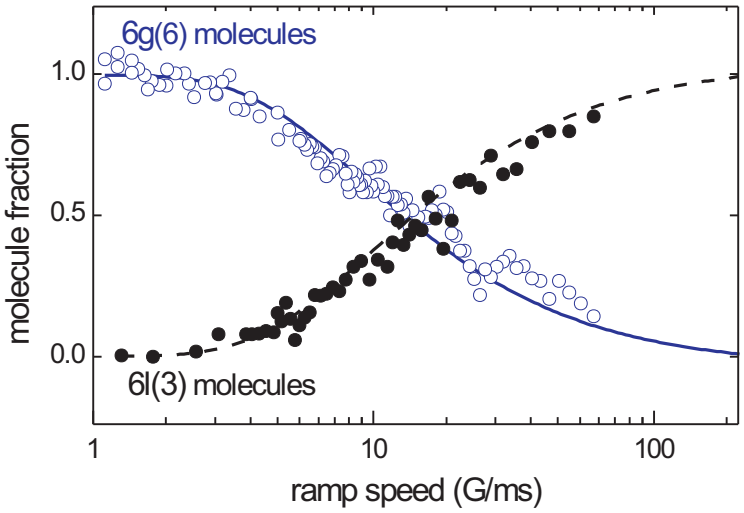

Figure 5.5.:
Conversion efficiency on the $6g(6)/6l(3)$ avoided crossing as a function of the ramp speed. A pure sample of $6l(3)$ molecules is partially transferred into the $6g(6)$ state at different ramp speeds. We measure either the fraction of transferred $6g(6)$ molecules (open circles) or the fraction of non-converted $6l(3)$ molecules (filled circles). The solid line refers to the Landau-Zener formula for the transfer probability p given by Eq. (5.7), while the dashed line is $1 - p$.

An alternative method to determine the coupling strengths of avoided crossings is based on the Landau-Zener tunneling model [Lan32, Zen32, Jul04], already discussed in Sec. 4.2. Equation (4.1) shows a quadratic dependence of the critical ramp speed r_c on the coupling strength V. The probability to transfer molecules from one bare state to the next in a single passage through the avoided crossing is given by the well-known Landau-Zener formula [Lan32, Zen32]

$$p = 1 - \exp\left(-r_c/\dot{B}\right), \tag{5.7}$$

where $\dot{B}$ is the ramp speed of the magnetic field.

As an example, we apply this method to the $6g(6)/6l(3)$ avoided crossing. We measure the conversion efficiency of molecules from the $6l(3)$ state below the crossing to the $6g(6)$ state by sweeping the magnetic field across the $6g(6)/6l(3)$ crossing at various ramp speeds $\dot{B}$. The results are shown in Fig. 5.5. For $\dot{B} \ll r_c$, the molecules are adiabatically transferred to the $6g(6)$ state (open circles) whereas, for $\dot{B} \gg r_c$, they end up in the $6l(3)$ state above the crossing. The conversion efficiency is measured by detecting the

$6g(6)$ molecules (open circles) and also by detecting the $6l(3)$ molecules (filled circles). By fitting our data with Eq. (5.7), we estimate the coupling strength of the $6l(3)/6g(6)$ crossing to be $V = h \times 16(3)\,\mathrm{kHz}$. This value is consistent with the result of $14(1)\,\mathrm{kHz}$ obtained in Sec. 6.4 using the more precise interferometric technique.

5.2. Microwave spectroscopy

Molecules in the $6s$ state (see Fig. 2.7) are of particular interest as *quantum halo* states [Jen04]. As described in Sec. 2.2.2, halo states are extremely weakly bound dimers characterized by a large interatomic separation that greatly exceeds the van der Waals length L_{vdW} and by a binding energy much smaller than the van der Waals energy (for Cs, $\hbar^2/mL_{\mathrm{vdW}}^2 \approx h \times 2.708\,\mathrm{MHz}$) [Köh06]. These states are universal in the sense that they are fully characterized by a large atomic s-wave scattering length a. In particular, the wave function does not depend on the microscopic details of the scattering potential. The precise knowledge of the $6s$ state is crucial for understanding universal two-body physics and for studying universal three-body Efimov-type states [Kra06b].

Basic concept

We detect molecular transitions induced by microwave radiation to probe the binding energy of the $6s$ molecules. The relevant atomic states are the lowest hyperfine state $|F=3, m_F=3\rangle$ and the doubly-polarized state $|F=4, m_F=4\rangle$. Figure 5.6(a) shows the energy level structure of the two scattering channels $|F=3, m_F=3\rangle + |F=3, m_F=3\rangle$ and $|F=3, m_F=3\rangle + |F=4, m_F=4\rangle$. The bound states involved in the molecular transition are the $6s$ state and a $7s$ state that lies slightly below the atomic scattering channel $|F=3, m_F=3\rangle + |F=4, m_F=4\rangle$.

The weakly bound $7s$ state is directly related to the large triplet scattering length a_T that dominates the $|F=3, m_F=3\rangle + |F=4, m_F=4\rangle$ scattering channel. The Cs triplet scattering length, predicted by the NIST model, is $(2400 \pm 100)a_0$, and consequently the $7s$ state has a small binding energy of $E_b' = \hbar^2/ma_T^2 \approx h \times 5\,\mathrm{kHz}$.

Measurement procedure

We map out the binding energy of the $6s$ molecules by measuring the transition frequency ν_{mol} from the $6s$ to the $7s$ state as a function of B. The binding energy is then given by

$$E_b(B) = h \times [\nu_{\mathrm{mol}}(B) - \nu_{\mathrm{at}}(B)] + E_b', \tag{5.8}$$

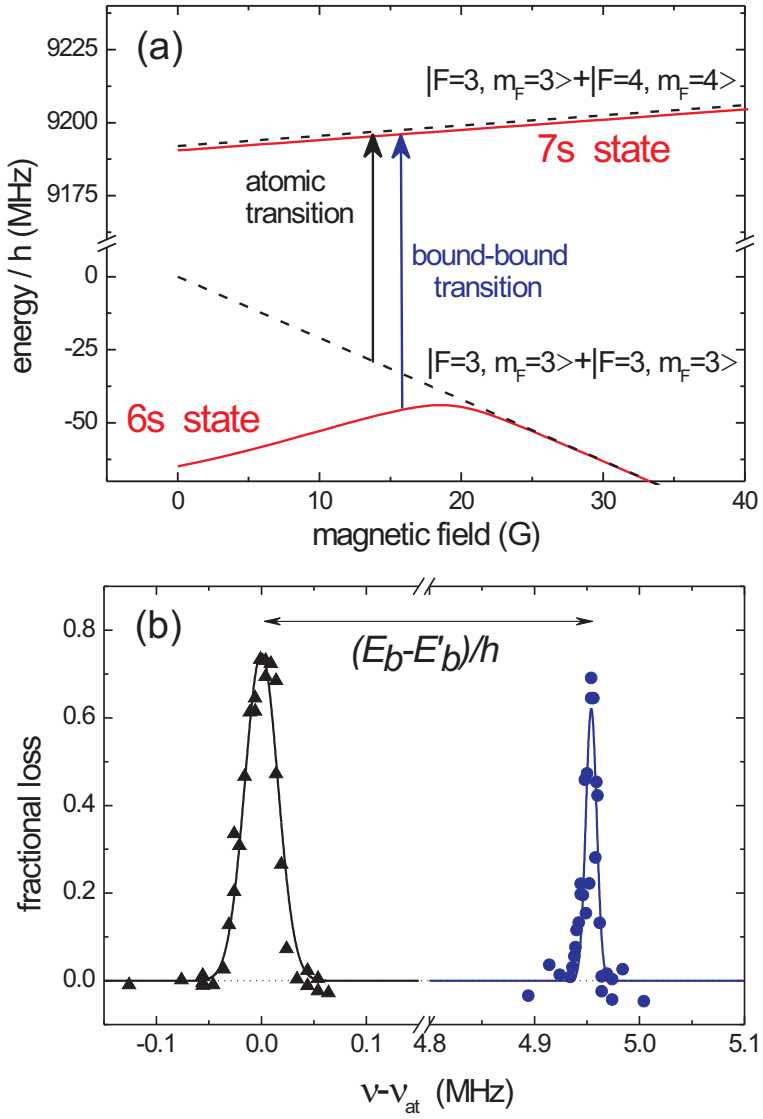

Figure 5.6.:
Microwave spectroscopy of Cs dimers. (a) A bound-bound transition is driven from the $6s$ state to a $7s$ state slightly below the $|F=3, m_F=3\rangle + |F=4, m_F=4\rangle$ scattering channel, as illustrated by the longer arrow. The $7s$ state is offset from the scattering channel for clarity. The frequency corresponding to the $|F=3, m_F=3\rangle \rightarrow |F=4, m_F=4\rangle$ atomic transition at zero-field is $\nu_{\mathrm{at}} \approx 9.193\,\mathrm{GHz}$. (b) Microwave spectrum of atoms (triangles) and $6s$ molecules (dots) at $B \sim 18.7\,\mathrm{G}$ as a function of the frequency offset $\nu - \nu_{\mathrm{at}}$. The molecular transition corresponds to a sharp loss resonance. We determine the center position to be 4.9545(3) MHz and the resonance width to 12(3) kHz from a gaussian fit (solid line).

where $\nu_{\mathrm{at}}(B)$ is the $|F=3, m_F=3\rangle \rightarrow |F=4, m_F=4\rangle$ atomic transition, which follows the Breit-Rabi formula and is used here as frequency reference. In our experiment, we again start with optically trapped $6s$ molecules at some magnetic field B. A microwave pulse of typically 5 ms duration drives the bound-bound transition, and partially transfers molecules from the $6s$ state to the $7s$ state. We then hold the sample in the trap for 10 ms and we detect the total number of remaining molecules using the techniques described in Sec. 4.3. We perform similar measurements at different magnetic fields to recover E_b within the magnetic field range of investigation.

As a frequency reference, we measure $\nu_{\mathrm{at}}(B)$ in analogy to a magnetic field calibration measurement as described in Sec. 3.4.2. In brief, we prepare a trapped sample of typically 4×10^5 Cs atoms at $T \sim 200$ nK, initially in the hyperfine ground state $|F=3, m_F=3\rangle$. For each B, we apply a microwave pulse resonant to the $|F=3, m_F=3\rangle \rightarrow |F=4, m_F=4\rangle$ hyperfine transition. The atoms are then detected after a holding time in the trap of typically 100 ms. The microwave excitation results in resonant loss from the atomic sample.

The particle losses observed in both the atomic and the molecular sample are the result of hyperfine spin relaxation [Tho05a, Köh05]. In the atomic case, the relaxation is driven by the binary collision of two free atoms, while in the molecular case it can be considered as being driven by a collision within the molecule [Köh05], leading to spontaneous dissociation. In any case, one of the atoms is subject to a spin flip, releasing the hyperfine energy that greatly exceeds the trap depth and leading to trap loss. According to the NIST model, the $7s$ state is coupled to several possible decay channels, causing a decay width of the state of $\sim 2\pi \times 70$ Hz [Tie07]. We in fact observe a decay of $7s$ molecules on a timescale of a few ms. In the case of Cs atoms in the $|F=3, m_F=3\rangle + |F=4, m_F=4\rangle$ scattering channel, we measure a lifetime of ~ 50 ms consistent with the predicted two-body loss coefficient of $5 \times 10^{-12}\,\mathrm{cm}^3/\mathrm{s}$ [Tie07].

Results

A typical microwave spectrum for both atoms and molecules is shown in Fig. 5.6(b). The resonant frequencies and the line widths are determined by fitting the data with gaussian profiles. The molecular transition shows a narrow and symmetric loss resonance. From the fit, we find a line width of 12(3) kHz. This value is close to our experimental resolution of ~ 10 kHz, essentially resulting from magnetic field fluctuations. As demonstrated in Refs. [Bar05, Chi05a], the symmetry of the line shape indicates that a bound-bound transition occurs, even in the presence of magnetic field broadening. We cannot distinguish bound-bound from possible bound-free transitions due to the small

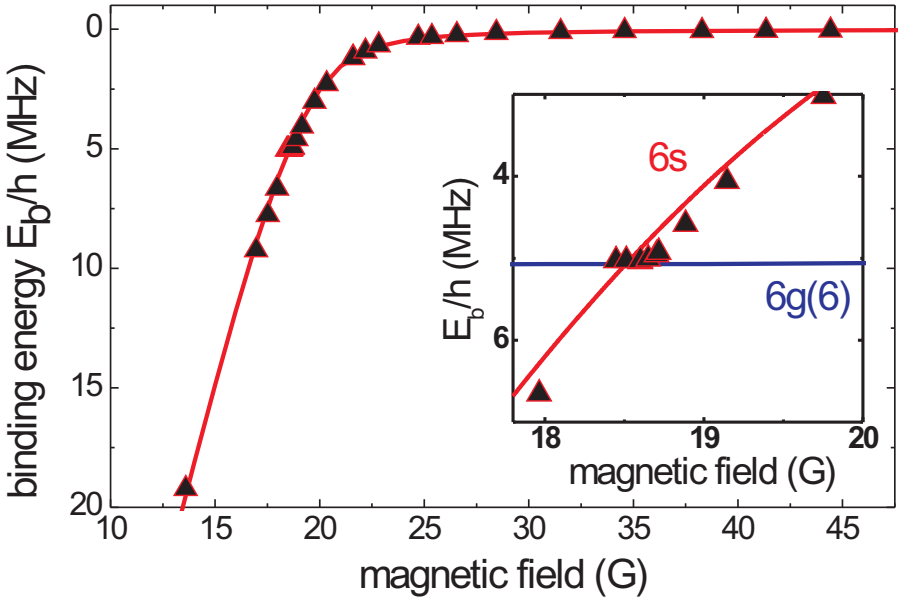

Figure 5.7.:
Binding energy of the $6s$ molecules as a function of the magnetic field (triangles). The binding energies correspond to the measured frequency shift from the expected $|F=3, m_F=3\rangle \rightarrow |F=4, m_F=4\rangle$ atomic transition (see Eq. (5.8)). The statistical errors are about 1 kHz, i.e. much smaller than the data symbol size. The solid line is the result of the NIST model. The inset is an expanded view of the binding energy close to the $6s/6g(6)$ avoided crossing.

energy difference between the $|F=3, m_F=3\rangle + |F=4, m_F=4\rangle$ scattering channel and the $7s$ state. However, we believe that the bound-bound transition dominates since the transition probability for a bound-free transition is expected to be much weaker due to the smaller Franck-Condon overlap between the initial and final state [Chi05a].

Figure 5.7 shows the binding energies of $6s$ molecules in a magnetic field range from 12 to 45 G together with the predictions from the NIST model. The inset shows an expanded view of the binding energy in the proximity of the $6s/6g(6)$ avoided crossing around 18.5 G. We observe an increase of the microwave power needed to drive the bound-bound transition when the avoided crossing is approached. The $6s$ and $6g(6)$ state couple and the molecules are in a dressed state. A microwave pulse can drive molecular transitions that change the total angular momentum f and its projection m_f, while the orbital momentum ℓ has to be conserved. The bound-bound transition between the $6g(6)$ and the $7s$ state with $\Delta\ell = 4$ is hence forbidden.

The microwave measurements on the $6s$ state provide precise binding energies of up to about $h \times 20\,\mathrm{MHz}$. Higher binding energies can in principle be accessed by further lowering the magnetic field. The comparison between our results and the NIST model generally shows very good agreement. We have observed small deviations between theory and experiment when the $6s$ state starts to bend towards larger binding energies (see inset of Fig. 5.7). This deviation suggests that the $6s$ state is perturbed by the coupling to other molecular states. Our data provide high precision input for further refinements of the NIST model.

6. Molecular 'Stückelberg interferometer'

In this chapter we present the realization of an internal-state interferometer with Cs_2 molecules. A brief introduction on our interferometer is given in Sec. 6.1. In Sec. 6.2 we then discuss the preparation and detection of the involved molecular states for the experiments. The interferometric scheme with full control over its dynamics is presented in Sec. 6.3. The interferometer allows precise measurements of binding energy differences of molecular states. As a first application of the interferometer we map the position of the avoided crossing as presented in Sec. 6.4.

6.1. Introduction

In contrast to the previous chapters the starting point for these molecular interferometer experiments is an atomic Bose-Einstein condensate. We prepare the atomic condensate in the crossed 1064nm dipole trap, i. e. setup 1 according to Sec. 3.6.2. Unfortunately the 1064nm laser light induces strong molecular losses from the trap (cf. Sec. 3.1). Therefore all molecule experiments of this chapter are performed in free space.

We realize a 'beam splitter' for molecular states by ramping the magnetic field through a weak avoided crossing. This is a result of partial Landau-Zener tunneling through the crossing. Using the avoided crossing twice, first for splitting, and then for recombination of molecular states, leads to the well-known 'Stückelberg oscillations' [Stü32]. We thus call our scheme a 'Stückelberg interferometer'.

Our realization of this interferometer allows full control over the interferometer dynamics. In particular, the hold time between splitting and recombination can be freely chosen. In analogy to the well-known Ramsey interferometer [Ram56] the acquired interferometer phase is mapped onto the relative populations of the two output states that can be well discriminated upon molecular dissociation. To demonstrate the performance of the Stückelberg interferometer we use it for precision molecular spectroscopy to determine the position and coupling strength of the avoided crossing.

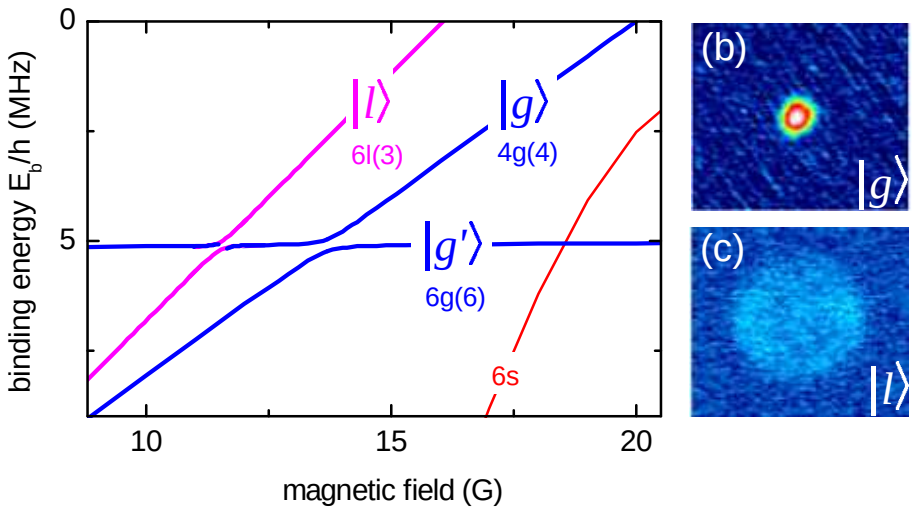

Figure 6.1.:
(a) Part of the molecular energy structure of Fig. 2.7 below the dissociation threshold. The relevant states for the present experiment are the two g-wave states $4g(4)$ and $6g(6)$ and the l-wave state $6l(3)$. For simplicity these states are labeled within this chapter by $|g\rangle$, $|g'\rangle$, and $|l\rangle$. Molecules in state $|g\rangle$ or $|l\rangle$ are detected upon dissociation as shown in (b) and (c). The crossing used for the interferometer is the one between $|g'\rangle$ and $|l\rangle$ near 11.4 G. Initially, the molecules are produced in state $|g\rangle$ on the Feshbach resonance at 19.8 G.

6.2. Interferometer playground

The energy structure of weakly bound Cs_2 dimers in the relevant magnetic field range is shown in Fig. 6.1 and represents a zoom-in of Fig. 2.7. As described in Sec. 2.3, zero binding energy corresponds to the threshold of dissociation into two free Cs atoms in the $|F = 3, m_F = 3\rangle$ state. The molecular states relevant for this work are the two g-wave states $4g(4)$ and $6g(6)$ and the l-wave state $6l(3)$. For the notation of the molecular states see Sec. 2.3. In the following we rename the involved states for simplification and label them $|g\rangle$, $|g'\rangle$, and $|l\rangle$, respectively. The avoided crossing between the states $|g'\rangle$ and $|l\rangle$ at about 11 G plays the central role in the present interferometer experiment.

Although in principal other avoided crossings (particularly crossings involving l-wave states) are available in the molecular energy spectrum (cf. Sec. 2.3), it is crucial to be able to discriminate the interfering states when dissociating and imaging the molecules. This ability strongly depends on how the energy structure looks in detail. As discussed later, the molecular states used here can nicely be discriminated upon dissociation allowing for full control over the interferometer dynamics.

Molecule production

The starting point for the interferometer experiments is a Bose-Einstein condensate with $\sim 2 \times 10^5$ Cs atoms. As described in Sec. 3.6 we use for the preparation of the atomic condensate the dipole trap setup 1. In particular the BEC is magnetically levitated and confined in the crossed-beam dipole trap generated by the 1064nm fiber laser beams (see Sec. 3.6.2). The BEC allows us to efficiently produce molecules on the narrow Feshbach resonance at 19.84 G using an optimized switching scheme [Mar05] similar to the one described in Sec. 4.1. With an efficiency of typically 25% we produce a pure molecular ensemble with up to 2.5×10^4 ultracold molecules all in state $|g\rangle$, initially close to quantum degeneracy [Her03].

Because of the problem of increased molecule losses induced by the 1064nm trapping light (cf. Sec. 3.1) the following experiments are performed on the molecular ensemble in free fall. We release the atomic sample from the trap when starting the molecule production at the Feshbach resonance. Simultaneously the magnetic leviation field is switched off to cancel the magnetic field spread across the sample. This is crucial for the performance and precision of the molecule interferometer experiments as we will see later. During the initial expansion to a $1/e$-diameter of about $28\,\mu$m along the radial and about $46\,\mu$m along the axial direction the peak density is reduced to $1 \times 10^{11}\,\mathrm{cm}^{-3}$ so that molecule-molecule interactions [Chi05b] can be neglected on the timescale of the experiment.

Molecule transfer

As described in Sec. 4.2, after production the molecules can be transferred to any one of the molecular states shown in Fig. 6.1 with near 100% efficiency by controlled 'jumping' or adiabatic following at the various crossings. When the magnetic field strength is decreased, the molecules first encounter the crossing at 13.6 G. At all ramp rates used in this experiment the passage through this crossing takes place in a fully adiabatic way. The molecules are thus transferred from $|g\rangle$ to $|g'\rangle$ along the upper branch of the crossing. They then encounter the next crossing at a magnetic field of $B_c \approx 11.4\,\mathrm{G}$ [1].

This crossing between $|g'\rangle$ and $|l\rangle$ is the central piece of the present experiment. It can be used as a tunable 'beam splitter', which allows adiabatic transfer, coherent splitting (as will be shown below), or diabatic transfer for the molecular states involved, depending on the chosen magnetic ramp rate near the crossing. As shown in Fig. 5.5 of Sec. 5.1.2 we find that a critical ramp speed of $r_c \approx 14\,\mathrm{G/ms}$ leads to a 50/50-splitting into $|g'\rangle$

[1] We accidentally found this weak crossing in our previous magnetic moment measurements [Chi05b]. This allowed the identification of the l-wave state $|l\rangle$ [Tie07].

and $|l\rangle$. Using the Landau-Zener formula and an estimate for the difference in magnetic moments for states $|g'\rangle$ and $|l\rangle$ [Tie07], we determine the coupling strength V between $|g'\rangle$ and $|l\rangle$ to be $\sim h\times 16(3)\,\mathrm{kHz}$.

Molecule detection

We state-selectively detect the molecules by ramping up the magnetic field to bring the molecules above the threshold for dissociation (see Sec. 4.3). For state $|g\rangle$ dissociation is observed for magnetic fields above the 19.84 G position of the corresponding Feshbach resonance. Fig. 6.1 (b) shows a typical absorption image of the resulting atom cloud [Her03]. For state $|l\rangle$ dissociation is observed above 16.5 G.

The molecular states can thus be easily discriminated by the different magnetic field values needed for dissociation. Moreover, the expansion pattern is qualitatively different from the one connected to state $|g\rangle$. The absorption image in Fig. 6.1 (c) shows an expanding 'bubble' of atoms with a relatively large kinetic energy of about $k_B\times 20\,\mu\mathrm{K}$ per atom. We find that significant dissociation occurs only when the state $|l\rangle$ couples to a quasi-bound g-wave state about $h\times 0.7\,\mathrm{MHz}$ above threshold [Kno08b]. The resulting bubble is not fully spherically symmetric, which indicates higher partial-wave contributions [Dür04b]. The different absorption patterns allow us to clearly distinguish between the two different dissociation channels in a single absorption picture when the magnetic field is ramped up to $\sim 22\,\mathrm{G}$. These dissociation channels serve as the interferometer 'output ports'.

6.3. Internal-state interferometry

The interferometer is based on two subsequent passages through the crossing following the scheme illustrated in Fig. 6.2. For an initial magnetic field above the crossing a downward magnetic-field ramp brings the initial molecular state into a coherent superposition of $|g'\rangle$ and $|l\rangle$. After the ramp the field is kept constant at a hold field B_0 below the crossing for a variable hold time τ. The total molecule wave function evolves in time according to

$$\Psi(\tau) \propto C_{g'}|g'\rangle + C_l e^{-\frac{i}{\hbar}(E_l - E_{g'})\tau}|l\rangle, \tag{6.1}$$

where $C_{g'}$ and C_l are the amplitudes and $E_{g'}$ and E_l are the binding energies of the molecular states $|g'\rangle$ and $|l\rangle$, respectively. With increasing time τ a differential phase $\phi = \frac{E_l - E_{g'}}{\hbar}\tau$ is accumulated between the two components of Eq. (6.1) which linearly

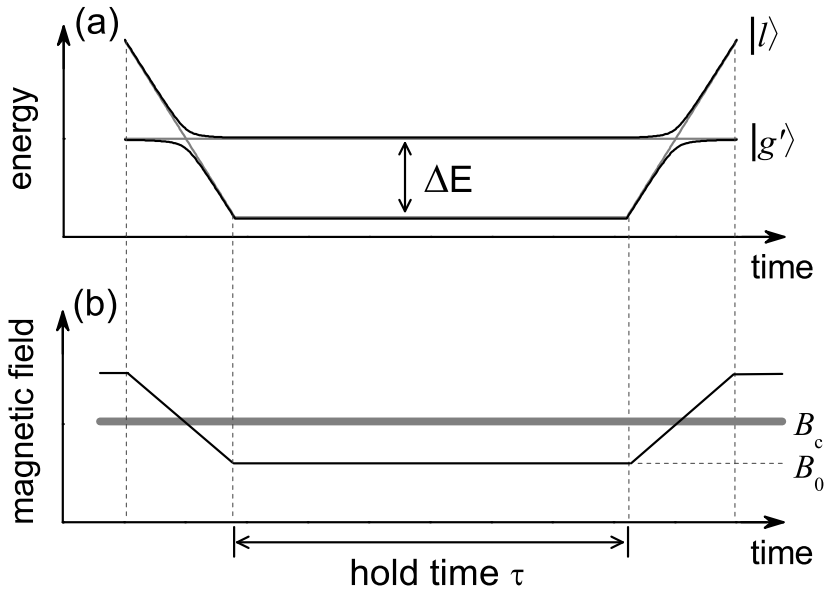

Figure 6.2.:
(a) Scheme of the 'Stückelberg interferometer'. By ramping the magnetic field over the avoided crossing at B_c at a rate near the critical ramp rate r_c the population in the initial molecular state is coherently split. ΔE is the binding energy difference at the given hold field B_0. After the hold time τ a reverse ramp coherently recombines the two populations. The populations in the two 'output ports' are then determined as a function of acquired phase difference $\phi \propto \Delta E \times \tau$. (b) Corresponding magnetic field ramp.

increases with the product of the binding energy difference $\Delta E = E_l - E_{g'}$ and the hold time τ.

After a variable hold time the magnetic field is ramped back up, and the second passage through the avoided crossing creates a new superposition state depending on ϕ. For a 50/50-splitting ratio, this can lead to complete destructive or constructive interference in the two output ports and thus to high-contrast fringes as a function of τ or ΔE. These fringes, resulting from two passages through the same crossing, are analogous to the well-known Stückelberg oscillations in collision physics [Stü32, Nik84] or in the physics with Rydberg atoms [Bar92, Yoa92]. Note that our realization of a 'Stückelberg interferometer' gives full control over the interferometer dynamics by appropriate choice of ramp rates and magnetic offset fields[2].

A typical ramp sequence, as shown in Fig. 6.2 (b), starts with a sample of $|g'\rangle$ molecules at a magnetic field of 11.6 G, about 250 mG above the crossing. At the critical ramp rate r_c we ramp the magnetic field within about 50 μs to a hold field B_0 below the crossing. After the variable hold time τ we reverse the ramp and transverse the crossing a second time at the critical ramp rate. The output of the interferometer is detected by rapidly ramping the magnetic field up to 22 G and by imaging the pattern of dissociating $|l\rangle$ and $|g\rangle$ molecules.

The molecule preparation close to the avoided crossing and the detection of the molecules via reverse magnetic field ramps is performed by using our standard magnetic field coils. For the interferometer ramp sequence we use the single booster coil which is described in Sec. 3.3. The ramping is controlled by a frequency generator programmed for a single ramp sequence and externally triggered. The duration τ between the forward and backward ramp can be adjusted within nanosecond precision.

Interferometer performance

The series of absorption images shown in Fig. 6.3 demonstrates the dependence of the dissociation pattern of the molecules on the hold time τ for one oscillation period. The hold time is increased in steps of 1 μs while the entire preparation, ramping, and detection procedure is repeated for each experimental cycle, lasting about 20 s. The molecular population oscillates from being predominantly l-wave to predominantly g-wave and back. For a quantitative analysis of the molecular population in each output port we fit the images with a simple model function (see App. C) and extract the fraction of molecules in each of the two output ports.

[2] For precise interferometer oscillations it is crucial that the magnetic offset field is precise and the same for all molecules. Magnetic field noise or an inhomogeneous magnetic field across the molecular sample limits the interferometer performance.

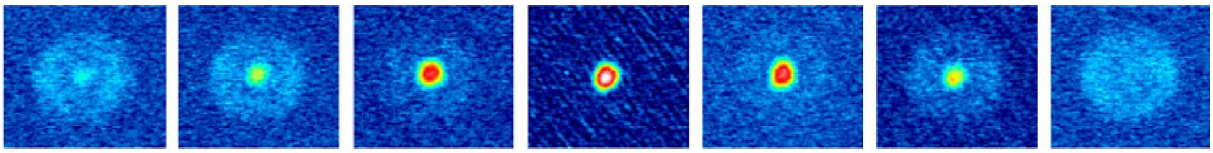

Figure 6.3.:
Series of dissociation patterns of molecules showing about one oscillation period with $\Delta E/h = 155\,\mathrm{kHz}$ at a hold field of $B_0 = 11.19\,\mathrm{G}$. From one picture to the next the hold time τ is increased by $1\,\mu\mathrm{s}$. The first and the last of the absorption images mainly show dissociation of l-wave molecules, whereas the central image shows predominant dissociation of g-wave molecules.

Figure 6.4 shows the g-wave molecular population as a function of hold time τ for various hold fields B_0 corresponding to different ΔE. The existence of these Stückelberg oscillations confirms that coherence is preserved by the molecular beam splitter. Note that the peak-to-peak amplitude for the oscillations shown in Fig. 6.4 (a) is nearly unity while it is reduced to about 0.75 in Fig. 6.4 (b) and (c). This reduction is the result of forward and backward ramp rates being slightly different from r_c, preventing an exact 50/50 splitting. However, sinusoidal fits to the data allow for an accurate determination of the oscillation frequency and hence of ΔE.

6.4. New tool for precision measurements

As a first application of our molecular interferometer we mapped the position of the avoided crossing and measured the coupling strength at the crossing. Figure 6.5 shows ΔE as a function of magnetic field strength near the avoided crossing. For magnetic fields below the crossing we obtain ΔE as described before. For magnetic fields above the crossing, we invert the interferometric scheme. Molecules are first transferred from $|g'\rangle$ into $|l\rangle$ using a slow adiabatic ramp. The field is then ramped up above the crossing with a rate near r_c, kept constant for the variable time τ at the hold field B_0 and then ramped down to close the interferometer. An adiabatic ramp through the crossing maps population in $|g'\rangle$ onto $|l\rangle$ and vice versa. Detection then proceeds as before.

For both realizations of the interferometer we obtain high-contrast fringes even when it is not operated in the Landau-Zener regime and the fast ramps are stopped right at the crossing as shown in the inset of Fig. 6.5. This allows us to measure ΔE in the crossing region. A fit to the data with the hyperbolic fit function

$$\Delta E = \sqrt{(\Delta\mu)^2(B - B_c)^2 + 4V^2} \tag{6.2}$$

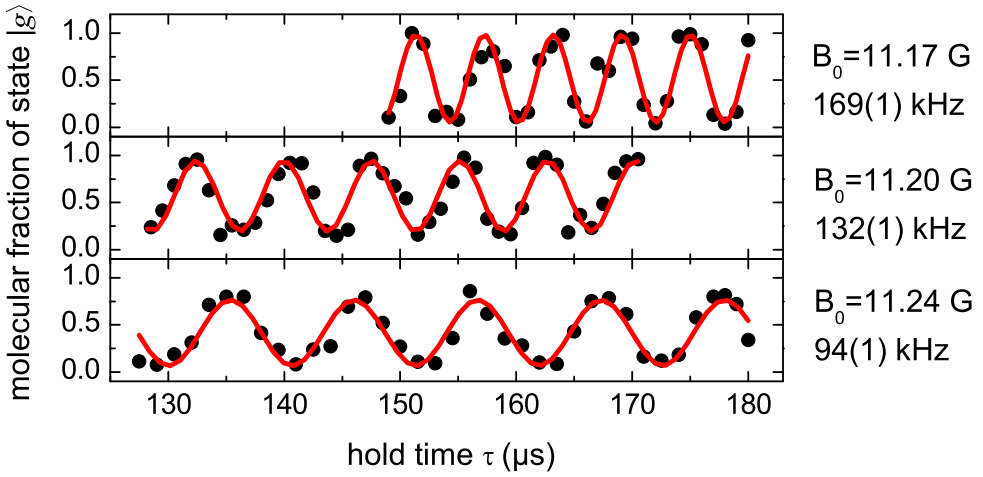

Figure 6.4.:
Interferometer fringes for magnetic hold fields B_0 below the crossing of $|g'\rangle$ and $|l\rangle$. The g-wave molecular fraction is plotted as a function of the hold time τ. Sinusoidal fits give the oscillation frequency as indicated.

according to the standard Landau-Zener model (cf. Sec. 5.1.2) yields $B_c = 11.339(1)\,\mathrm{G}$ for the position of the crossing, $\Delta\mu = 0.730(6)\,\mu_B$ for the difference in magnetic moment of the two states $|g'\rangle$ and $|l\rangle$, and $V = h \times 14(1)\,\mathrm{kHz}$ for the coupling strength. While the measured $\Delta\mu$ agrees reasonably well with the result from an advanced theoretical model of the Cs_2 dimer [Tie07], B_c and V cannot be obtained from these calculations with sufficient accuracy.

Current limitations

The present interferometer allows us to observe up to 100 oscillations at a frequency of 200 kHz. Shot-to-shot fluctuations increasingly scramble the phase of the oscillations for longer hold times ($> 200\,\mu\mathrm{s}$) until the phase appears to be fully randomized, although large amplitude variations for the molecular populations persist. The peak-to-peak amplitude of these fluctuations decays slowly and is still 50% of the initial contrast after 1 ms. We attribute this phase scrambling to magnetic field noise that causes shot-to-shot variations of ΔE, which are however the same for each molecule. The large amplitude of these fluctuations indicates that phase coherence is preserved within the molecular sample. We attribute the gradual loss of peak-to-peak amplitude to spatial magnetic field inhomogeneities. The single booster coil used for fast magnetic ramping produces

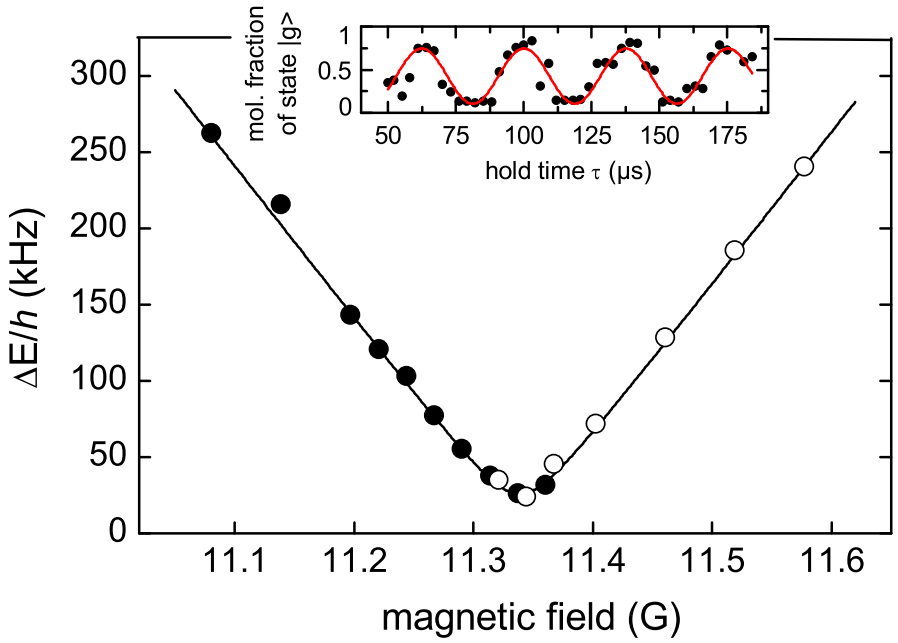

Figure 6.5.:
Interferometrically measured binding energy difference ΔE in the region of the crossing between states $|g'\rangle$ and $|l\rangle$ as a function of magnetic field. Solid circles: Standard ramp sequence of the interferometer. Open circles: Inverted scheme for field values above the crossing. The one-sigma statistical error from the sinusoidal fit is less than the size of the symbols. The solid curve is a hyperbolic fit to the experimental data. Inset: Oscillation at 26.6(3) kHz for a hold field $B_0 = 11.34\,\mathrm{G}$ right on the crossing.

a vertical magnetic field gradient of 1.04 G/cm at the position of the molecular cloud. The spatial distribution of the molecular ensemble is converted into an inhomogeneous distribution for ΔE and hence for the oscillation frequencies. Our observations agree well with simulations of the interferometer.

Improvements and perspectives

The interferometer can be used as a spectroscopic tool as it allows precise measurements of differential binding energies of molecular states. We expect that applying the interferometer to trapped molecular samples together with straightforward technical improvements regarding the magnetic field stability and homogeneity will allow us to extend the hold times far into the millisecond range. It will then be possible to measure ultraweak crossings with coupling strengths well below $h \times 1\,\mathrm{kHz}$.

In the future, this interferometer technique might be employed to measure feeble interactions between molecular states, e. g. parity non-conserving interactions [Com99]. In view of the rapid progress in experiments with cold molecular samples, new tools for precision measurements, such as our Stückelberg interferometer, will open up exciting avenues for future research.

7. Outlook

7.1. Metastable Feshbach molecules

As described earlier in Sec. 5.1, we have mapped out the molecular energy structure below threshold using the magnetic moment spectroscopy technique. With the same technique we have been able to extend our spectroscopy above threshold for molecular l-wave states. In particular, the spectroscopy measurements have been applied on the states $6l(4)$ and $6l(5)$. As an example, Fig. 7.1 shows our results from the measurements for the $6l(4)$ state.

The observed metastable character of the l-wave states is a result of their high angular momentum of $\ell = 8$. Their associated centrifugal barrier ($h \times 150$ MHz) suppresses tunneling to the l-wave scattering continuum. Moreover, coupling of these molecules to low angular momentum scattering waves is extremely weak. Subsequent lifetime measurements of the $6l(4)$ state have shown dissociation rates on the order of 1 Hz up to an energy of $h \times 3$ MHz above the atomic scattering continuum, thereby confirming the extremely weak coupling. For sufficiently large magnetic fields we have found a sharp onset of dissociation of the dimers into outgoing s- and d-wave states. This abrupt onset can be explained by the presence of the avoided crossing between the $6l(4)$ and $6g(5)$ states at about 28 G, see Fig. 7.1. Similar to the case of the $6l(3)$ state used for internal state interferometry as reported in Chap. 6, the avoided crossing above the threshold mediates a coupling from the l-wave to the s-wave continuum via the g-wave state. In this case the crossing is above the d-wave centrifugal barrier ($h \times 3.7$ MHz) and also d-wave scattering partial waves are populated. For a detailed report on our observations see Ref. [Kno08b].

One of the current research interests is focused on the producion of deeply bound molecules, aiming for possibly ground state molecular samples. However, investigations on molecules that exist above their threshold have so far attracted very few attention. In view of the rapid progress on Feshbach molecule studies, new applications arising from the meta-stable character of molecules might be advantageous. As an example, the dissociation of molecules triggered in a controlled way through a well-defined magnetic field could be used.

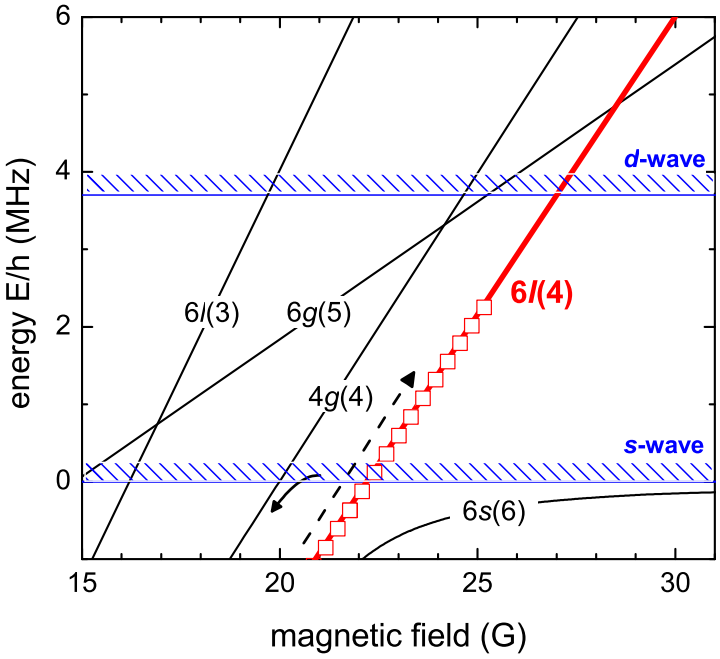

Figure 7.1.:
Energy structure of the Cs_2 dimer states in the magnetic field range 15 - 30 G, concentrating on the $6l(4)$ state above the s-wave scattering threshold ($E = 0$). The height of the d-wave centrifugal barrier at 3.7 MHz is also indicated. The open squares represent data obtained from magnetic moment spectroscopy measurements of the $6l(4)$ state. The thin arrows indicate the population pathway (see Sec. 4.2).

7.2. Few-body scattering phenomena

When we produced Feshbach molecules in our lab for the first time, one of the immediate questions has been related to the collisional stability of the weakly bound dimers. In general, very little is known on the collisional properties of bosonic Feshbach molecules and on a possible dependence on the scattering length. Both, atom-dimer and dimer-dimer collisions are theoretically very difficult to address as they represent three- and four-body scattering problems, respectively. However, few-body scattering phenomena such as dimer-dimer resonances have been observed experimentally [Chi05b] and make the creation of more complex objects feasible. In this context, one of the long standing goals is the experimental confirmation of predictions associated with three-body Efimov physics [Efi71]. The Efimov scenario is directly related to the long-range nature of weakly bound diatomic halo states. Therefore Feshbach molecules are good candidates to serve for a

deeper understanding of Efimov's effect. In addition, the finding of inelastic scattering resonances among cold atom-dimer mixtures may allow for a direct association of bound trimer states, similar to the production of dimers via Feshbach resonances [Kra06a].

As a consequence, collisional studies on molecules have become our main research topic. Experimentally the door for extensive collision measurements was opened the first time by the setup of the non-levitated CO_2-laser trap (cf. Sec. 3.1). Hence preliminary results on molecule-molecule and atom-molecule interactions could be obtained. Yet, limited by the attainable temperature of the molecules and possible corrugations in the optical trap, we have recently set up a new optical trapping scheme. The new scheme features our current requirements for the designated studies on Cs molecules [Sch07].

Our latest results from measurements on dimer-dimer and atom-dimer collisions are briefly presented in the following. In current studies we concentrate on investigations of the $6s$ molecules that are prepared via the 48 G Feshbach resonance. This state features to some extend 'halo-molecule' character. Within the magnetic field of 17 - 48 G, collision measurements are possible in a scattering length range from 0 to almost $1000\,a_0$. A detailed discussion on our findings related to dimer-dimer interactions will be given in Ref. [Fer08], measurements on interactions between atoms and dimers will be presented in Ref. [Kno08a].

7.2.1. Dimer-Dimer interactions

In the new optical dipole trap as introduced above a pure ensemble of $6s$ molecules is prepared similarly to the description given in Sec. 4.1 [Sch07]. We have measured the lifetime of the molecular sample for different magnetic field values and for various molecule temperatures. From each decay curve we obtain a loss rate due to the inelastic molecule collisions. Figure 7.2 shows the resulting loss rates for several sets of molecule temperatures as a function of the magnetic field and the scattering length, respectively. The loss rates are clearly depending on the scattering length and show a minimum around $500\,a_0$. For comparison we have measured loss rates for higher order molecules such as $4g(4)$ or $6g(6)$ dimers, but constant rates have been observed. The reason for the minimum is yet not fully understood. A possible interpretation in the context of universal behavior of the s-wave dimers is very difficult since the region of scattering lengths does not strictly fulfill $a \gg \overline{a}$ (cf. Sec.2.2). Thus also the connection to Efimov physics is challenging.

In addition to the rate measurements we have found several narrow collision resonances at different magnetic field values for both the s-wave and g-wave molecular states. Although the analysis is difficult, these resonances could indicate the existence of bound

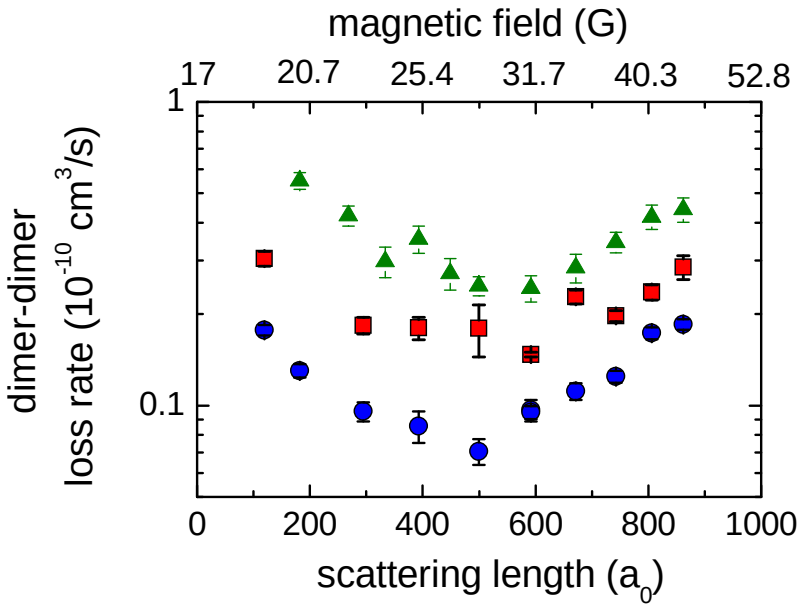

Figure 7.2.:
Loss rates of $6s$ dimers as a function of the two-body scattering length for different temperatures, (triangles) 190 nK, (squares) 80 nK, and (circles) 40 nK. Each temperature-set reveals a similar shape with a minimum around 500 a_0. The minimum tends to shift from larger to lower scattering length with decreasing temperature.

four-body molecular states [Chi05b]. Nevertheless it was not possible so far to observe the appearance of tetramer molecules directly.

7.2.2. Atom-dimer collision resonances

The preparation of trapped mixtures of ultracold molecules and atoms is rather easy as the preparation procedure can be operated without the blast pulse that removes the atoms. A simultaneous trapping of atoms and molecules in thermal equilibrium is possible for various molecular states and in a large magnetic field range if no magnetic field gradient is present. Conversely, for detection and analysis a spatial separation of atoms and molecules is required. This can be achieved by applying a small magnetic field gradient shortly before imaging. Therefore collisions between dimers and atoms can be investigated, independent on the molecular (or atomic) state and the magnetic field position.

Similar to the dimer-dimer research, we have performed lifetime measurements of the

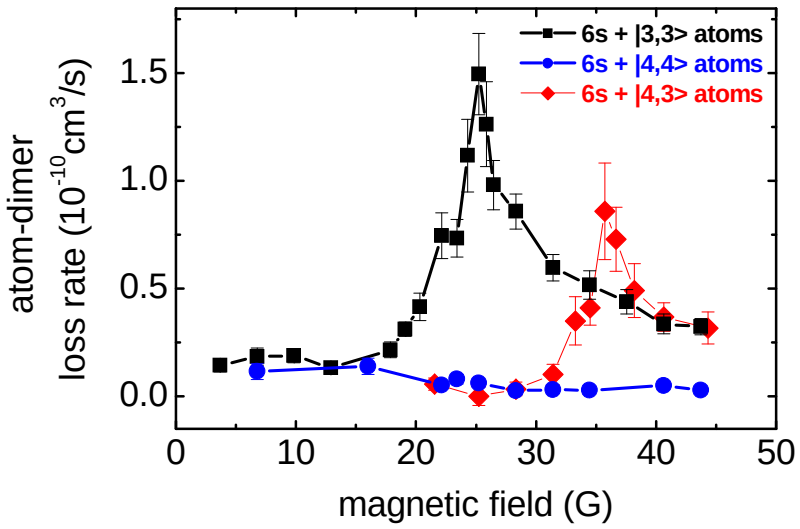

Figure 7.3.:
Loss rates of $6s$ molecules in mixtures with atoms in various hyperfine states $|F, m_F\rangle$ as a function of the magnetic field. We find a broad loss resonance at about 25 G for the molecules in combination with $|3, 3\rangle$ atoms. The position of this resonance corresponds to a scattering length value of $\sim 400\,a_0$. In addition we find for the mixture with $|4, 4\rangle$ atoms a smaller resonance at ~ 38 G. No magnetic field dependence is found for the mixture with atoms in the $|4, 3\rangle$ state.

trapped $6s$ molecules in mixtures with atomic samples from which we obtain the corresponding loss rates. Initially our collision studies were focused on mixtures with atoms prepared in their "original" hyperfine states $|F = 3, m_F = 3\rangle$. Recently the collision studies could be extended by developing a technique that changes the atomic hyperfine state into $|F = 4, m_F = 4\rangle$ or $|F = 4, m_F = 3\rangle$ while the initial molecular state is unaffected. The loss rates from our investigations are presented in Fig. 7.3. We find two loss resonances, a prominent resonance for the mixture of $6s$ dimers and $|3, 3\rangle$ atoms (squares) and a smaller one for a mixture with $|4, 3\rangle$ atoms (diamonds). The magnetic field position of the two resonances is about 25 G and 38 G, respectively. By contrast there is no resonance found for the $6s$ - $|4, 4\rangle$ mixture (circles).

The atom-dimer resonances might be a signature for the existence of bound trimer states. At the resonance positions, a weakly bound trimer state could couple to its threshold. This scenario would be an analog to the appearance of the Feshbach resonance between a bound dimer state and an atomic scattering state.

To further investigate both, the atom-dimer and the dimer-dimer loss resonances, the

experiment has now been equipped to allow driving magnetic field oscillations in the few-hundred kHz-range. As reported in Ref. [Don02], this technique was successfully used to populate dimer states from trapped atomic samples. Applying this method to a trapped molecular sample seems to be a promising route to prove the existence of a trimer state. Maybe the identification of an Efimov trimer state is possible. Similarly, in the vicinity of loss resonances in pure dimer samples, the existence of weakly bound tetramer states could be observed.

A. Magnetic field: setup and parameters

Overview and summary of coil parameters

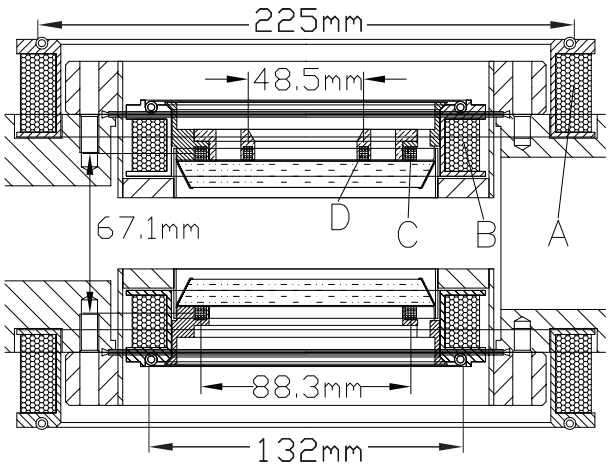

Figure A.1.:
Cut through the main experimental chamber. The various coil setups are labelled by A and B for the water-cooled ones and by C and D for the air-cooled coils. Table A.1 provides the detailed configurations and corresponding parameters.

Figure A.1 shows an overview of the main coil-setups mounted on the central experimental chamber. The coils are used to produce various magnetic fields. A summary how the individual coils are used is presented in Table A.1. In addition, the technical parameters are listed in the table for each magnetic field setup.

A elaborate description of the complete magnetic field setup including the compensation field along the horizontal directions is given in the thesis of Jens Herbig [Her05]. For further information, particularly for the home-made servo-loop controllers, we refer to Tobias Kraemer's thesis [Kra06a].

coil-setup	**A**		**B**		**C**	**D**
# single coils per side	6		3		1	1
mean radius (mm)	112.5		66		44.12	24.25
labeling	B_{bias}	B_{z}	B_{extraHH}	B_{grad}	B_{smallHH}	Booster-coil
max. fields	190 G	5.5 G	60 G	82 G/cm	10 G	7 G
windings per side	120 (5×24)	23	48	64 (2×32)	6	4
typ. switching times	3 ms	1 ms	1.5 ms	3 ms	300 μs	500 ns
current control	(a)	(b)	(c)	(a)	(c)	(d)
operation	dc	dc	dc	dc	dc	pulses, ≤ 1 ms
relative current stability	-	10^{-4}	$< 10^{-5}$	-	$< 10^{-5}$	$< 10^{-5}$
calibration value	1.909 G/A	0.557 G/V	6.158 G/V	0.836 G/cm/A	1.188 G/V	0.254 G/A
max. inputvalues	100 A	$\pm$10 V	10 V	100 A	8 V	3 V ($\equiv$ 30 A)

Table A.1.:
Summary of the magnetic field setup according to Fig. A.1: The setup of B_{bias} is to produce a large, but rather slow Helmholtz-field, B_{z} is for the vertical offset field, the field of B_{extraHH} is usually used for Feshbach tuning and molecule production. The magnetic gradient field for operating the MOT and the levitated dipole trap is realized by the B_{grad} coils in anti-Helmholtz configuration. B_{smallHH} and "Booster-coil" are mainly used to perform diabatic magnetic field ramps at molecular avoided level crossings since they can provide large ramp speeds of the magnetic field. The current control is performed by programable power supplies such as DELTA SM 30-100D labelled by (a) and HighFiness BCS 3/15 labelled by (b), while home-made servo-loop controllers are used for (c) and (d).

Electronic diagrams for booster coil control

Figure A.2 shows a block diagram of the control circuit for the booster coil. The circuit produces servo-loop controlled current pulses which drives the booster coil. For a current pulse, an amplitude of up to 30 A and a duration well below 1 μs can be achieved.

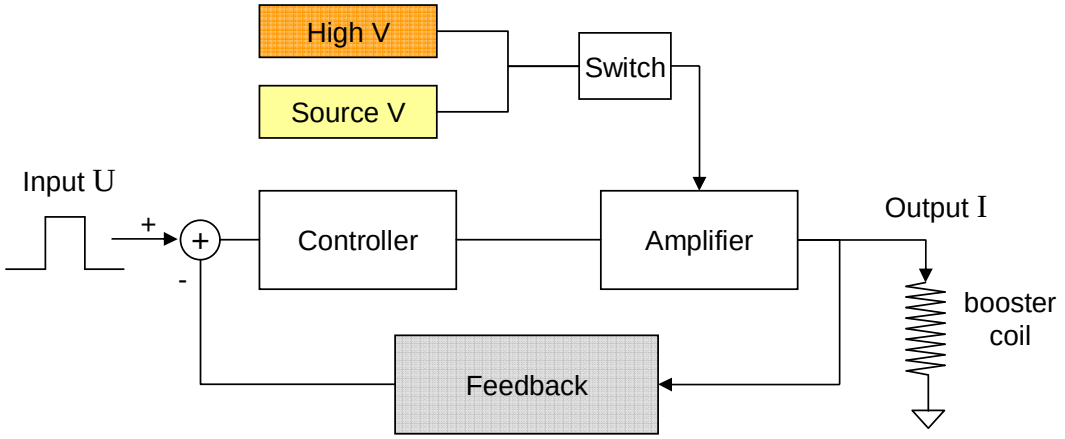

Figure A.2.:
Block diagram of the electronic circuit to control the booster coil. The maximum input voltage is 3 V which corresponds to a maximum available output current of 30 A. The longest pulse-durations are about 1 ms. The electronic diagrams of the individual blocks are shown in Fig. A.3 and Fig. A.4.

To achieve fast rise times of a current pulse, i. e. the output signal, generally high voltage is needed. This is a result of the inductive load from the coil which counteracts the rise time of the pulse. The high-voltage source 'High V' is realized by loading a high-voltage capacitor bench with constant current. The capacitors store the energy required for the fast rise times. After the switching-on process, the additional source-voltage 'Source V' is responsible to keep the adjusted current until the end of the pulse. In the experiment 'Source V' is a standard high-current supply. The switch-block manages the use of the two different sources when the pulse runs through the circuit. The controller block represents a PI-controller to counteract the differential action of the coil in the circuit. The controller allows to optimize the control deviation and the finally attainable rise time of the pulse. The amplifier uses the controlled signal and generates the current for the coil. Finally, the feedback closes the controlling loop.

The electronic diagrams of the complete controller circuit for the booster coil is illustrated in Fig. A.3 and Fig. A.4 where the dashed boxes indicate the corresponding circuit block.

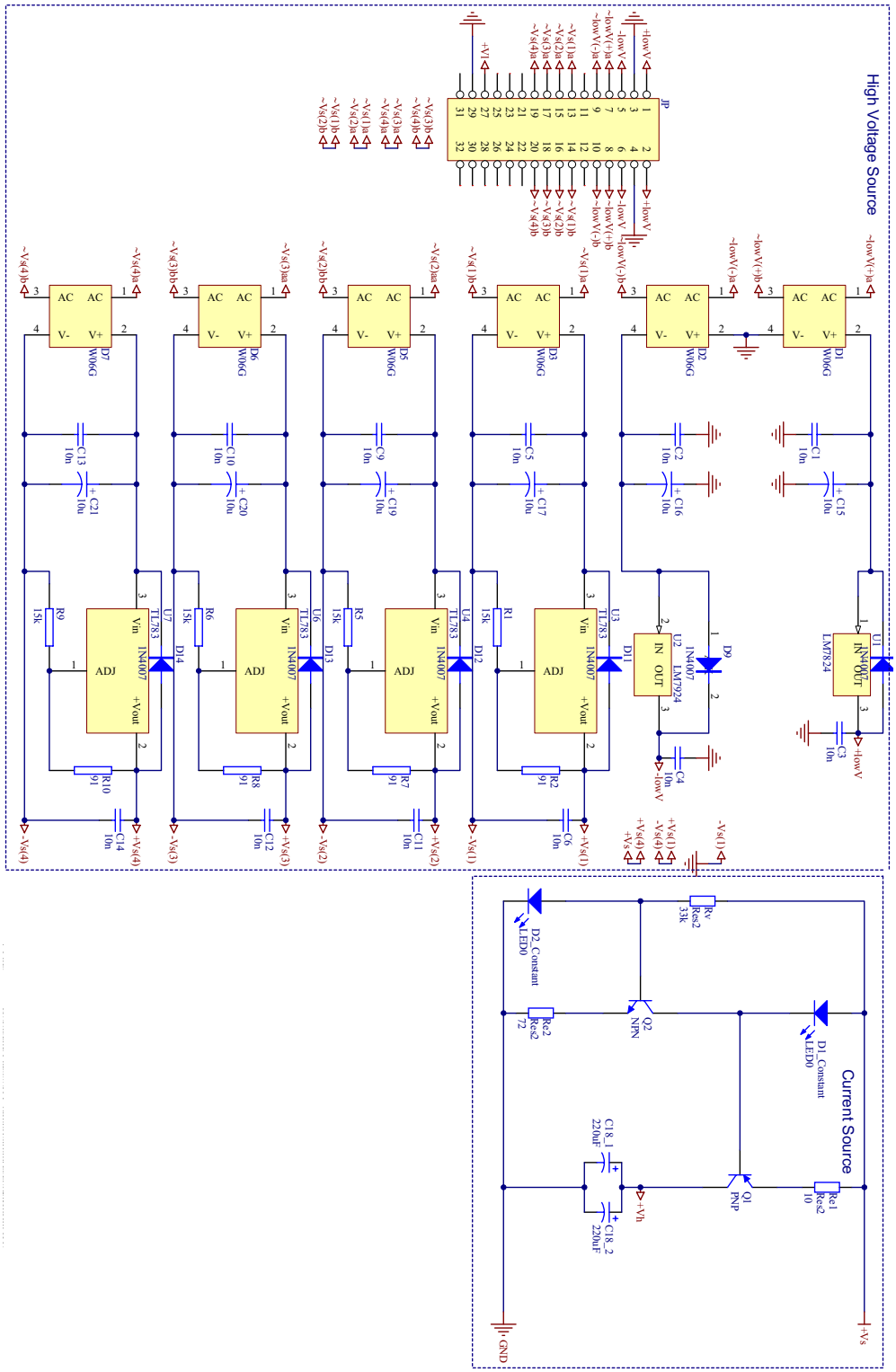

Figure A.3.:
Electronic diagram to realize the high-voltage source to achieve the fast rise time for the booster coil.

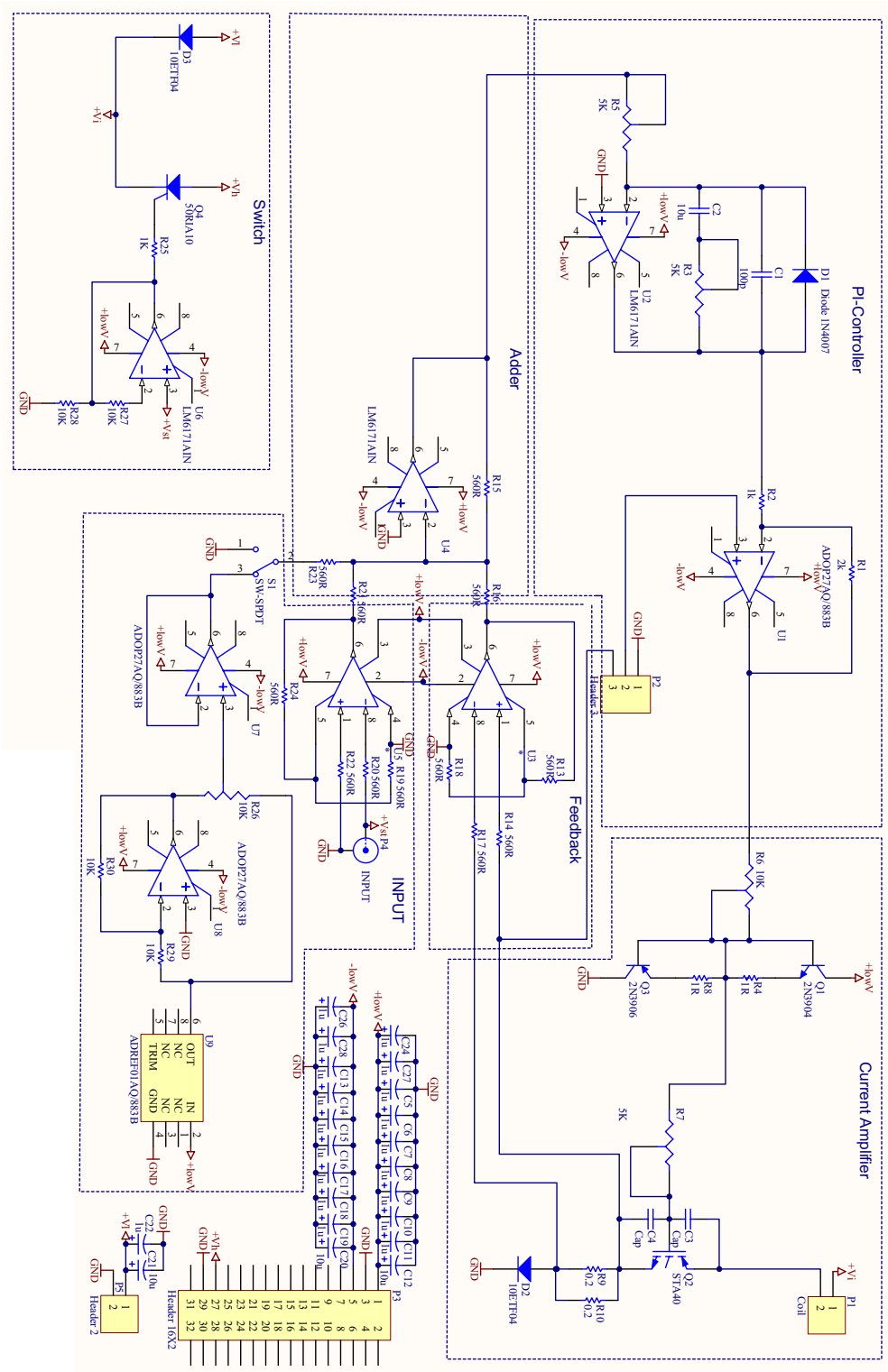

Figure A.4.:
Main Electronic diagram including the controller, the amplifier, the feedback and the switch circuit for the booster coil.

B. Analysis for magnetic field calibration

For the Zeeman shifts of state $|F = 4, m_F = 4\rangle$ with the g-factor for the total angular momentum $g_F = +\frac{1}{4}$ and of state $|F = 3, m_F = 3\rangle$ with $g_F = -\frac{1}{4}$ the Breit-Rabi formula reads:

$$E_{44} = -\frac{E_{\mathrm{hfs}}}{2(2I+1)} + g_I \mu_B 4B + \frac{E_{\mathrm{hfs}}}{2}\sqrt{1 + 4\frac{4x}{2I+1} + x^2} \tag{B.1}$$

$$E_{33} = -\frac{E_{\mathrm{hfs}}}{2(2I+1)} + g_I \mu_B 3B - \frac{E_{\mathrm{hfs}}}{2}\sqrt{1 + 4\frac{3x}{2I+1} + x^2} \tag{B.2}$$

where

$$E_{\mathrm{hfs}} = A_{\mathrm{hfs}}(I + 1/2) \qquad \text{and} \qquad x = (g_J - g_I)\mu_B \frac{B}{E_{\mathrm{hfs}}}.$$

E_{hfs} is the hyperfine splitting between the states $F = 3$ and $F = 4$ at zero magnetic field. With the nuclear spin of Cs of $I = 7/2$ and $A_{\mathrm{hfs}} = h \times 2.2981579425\,\mathrm{GHz}$ the splitting is $h \times 9.192631770\,\mathrm{GHz}$. The g-factors $g_I = -0.00039885395$ and $g_J = 2.00254032$ are the values of the nuclear spin and effectively of the electron spin (orbital angular momentum $L = 0$), respectively. Finally, $\mu_B = 1.399624624\,\mathrm{MHz/G}$ is the value used for Bohr's magneton.

The measured frequency ν_a from the microwave spectrum corresponds to

$$\nu_a = (E_{44} - E_{33} - E_{\mathrm{hfs}})/h + \nu_0 \tag{B.3}$$

from which the magnetic field value can be derived. In the formula, $\nu_0 = 42.629735\,\mathrm{MHz}$ is the frequency offset which has to be mixed with the PLDRO frequency of 9.150002 GHz to generate the transition frequency E_{hfs}/h at zero magnetic field.

C. Model functions to analyze interferometer images

The central cloud of the dissociation pictures shows the dissociation of the g-wave molecules which decay into the s-wave continuum. Due to the fast decay we observe small clouds which are fitted best by a simple Gauss-function.

In contrast, we analyze the images of the l-wave molecules by treating the dissociation pattern as a superposition of the two lowest possible spherical harmonics, i. e. Y_{00} for the s-wave and Y_{20} for the d-wave contribution. The resulting model function reads in spherical coordinates

$$f(\theta,\phi) = \cos^2(\alpha) Y_{00}(\theta,\phi) + \sin^2(\alpha) e^{i\delta} Y_{20}(\theta,\phi) \tag{C.1}$$

where

$$Y_{00}(\theta,\phi) = \frac{1}{2\sqrt{\pi}} \qquad \text{and} \qquad Y_{20}(\theta,\phi) = \frac{1}{4}\sqrt{\frac{5}{\pi}}\left(3\cos^2(\theta) - 1\right)$$

In Eq. (C.1) the parameter α is used to adjust the relative amplitudes of the spherical harmonics and δ represents the phase relation between the two spherical harmonics. Note that the spherical harmonics are rotationally symmetric as they do not depend on ϕ.

The conversion of Eq. (C.1) to Cartesian coordinates according to $\theta = \arccos(z/r)$ and $r = \sqrt{x^2+y^2+z^2}$ leads to

$$f(x,y,z) = \frac{\cos^2(\alpha)}{2\sqrt{\pi}} + \frac{1}{4} e^{i\delta}\sqrt{\frac{5}{\pi}}\left(\frac{3z^2}{x^2+y^2+z^2} - 1\right)\sin^2(\alpha). \tag{C.2}$$

To exclude the inner part of our typical dissociation patterns, i. e. the g-wave molecules, we use a simple Heaviside function to describe a constant radial dependence between an inner radius r_i and an outer radius r_a.

$$g(r) = \Theta(r - r_i)\,\Theta(r_a - r) \tag{C.3}$$

Imaging integrates the x-axis and yields a 2-dimensional absorption image as

$$I(y,z) = \int_{-\infty}^{+\infty} gg^* \cdot ff^*\, dx = 2\int_{\sqrt{r_i^2-y^2-z^2}}^{\sqrt{r_a^2-y^2-z^2}} ff^* dx \tag{C.4}$$

The result of the integration in Eq. (C.4) gives

$$\begin{aligned} I(y,z) \;=\; & \frac{1}{32\pi}\left\{ -\left[-3z^2 A\cdot C\cdot \arctan\left(\frac{\sqrt{r_a^2-y^2-z^2}}{\sqrt{y^2+z^2}}\right) + \right.\right. \\ & \left. \sqrt{r_a^2-y^2-z^2}\left(B - 5\sin^4\alpha\left(2+\frac{9z^4}{r_a^2(y^2+z^2)}\right)\right)\right](r_a^2-y^2-z^2) + \\ & \left[-3z^2 A\cdot C\cdot \arctan\left(\frac{\sqrt{r_i^2-y^2-z^2}}{\sqrt{y^2+z^2}}\right) + \right. \\ & \left.\left. \sqrt{r_i^2-y^2-z^2}\left(B - 5\sin^4\alpha\left(2+\frac{9z^4}{r_i^2(y^2+z^2)}\right)\right)\right](r_i^2-y^2-z^2)\right\} \end{aligned}$$

where

$$\begin{aligned} A &= \sin^2\alpha\left(4\sqrt{5}(1+e^{2i\delta})(y^2+z^2)\cos^2\alpha - 5e^{i\delta}(4y^2+z^2)\sin^2\alpha\right) \\ B &= -8\cos^4\alpha + \frac{4\sqrt{5}(1+e^{2i\delta})\cos^2\alpha\sin^2\alpha}{e^{i\delta}} \\ C &= \frac{1}{e^{i\delta}(y^2+z^2)^{3/2}} \end{aligned}$$

This expression is used to fit the "outer" part of the absorption images representing the l-wave molecules.

For the analysis of the pictures we manually define the region of g-wave molecules and l-wave molecules, respectively. By applying the corresponding fitting functions the fraction of particles in each state is obtained.

The used `matlab` files `fitpic.m`, `harmonics_fit.m` and `Y0020_xint.m` can be found on the Q-disk of the group, see `Q:\Cs_LEVT\PRL_interferometer`.

D. Publications

The following articles have been published in the framework of this PhD thesis and are attached in the following order:

1. S. Knoop, M. Mark, F. Ferlaino, J. G. Danzl, T. Kraemer, H.-C. Nägerl, and R. Grimm.
   Metastable Feshbach molecules in high rotational states.
   Phys. Rev. Lett. **100**, 083002 (2008).

2. M. Mark, F. Ferlaino, S. Knoop, J. G. Danzl, T. Kraemer, C. Chin, H.-C. Nägerl, and R. Grimm.
   Spectroscopy of ultracold trapped cesium Feshbach molecules.
   Phys. Rev. A **76**, 042514 (2007).

3. M. Mark, T. Kraemer, P. Waldburger, J. Herbig, C. Chin, H.-C. Nägerl, and R. Grimm
   'Stückelberg interferometry' with ultracold molecules.
   Phys. Rev. Lett. **99**, 113201 (2007).

4. T. Kraemer, M. Mark, P. Waldburger, J. G. Danzl, C. Chin, B. Engeser, A. D. Lange, K. Pilch, A. Jaakkola, H.-C. Nägerl, and R. Grimm.
   Evidence for Efimov quantum states in an ultracold gas of caesium atoms.
   Nature **440**, 315 (2006).

5. C. Chin, T. Kraemer, M. Mark, J. Herbig, P. Waldburger, H.-C. Nägerl, and R. Grimm.
   Observation of Feshbach-like resonances in collisions between ultracold molecules.
   Phys. Rev. Lett. **94**, 123201 (2005).

6. M. Mark, T. Kraemer, J. Herbig, C. Chin, H.-C. Nägerl, and R. Grimm.
   Efficient creation of molecules from a cesium Bose-Einstein condensate.
   Europhys. Lett. **69**, 706 (2005).

7. T. Kraemer, J. Herbig, M. Mark, T. Weber, C. Chin, H.-C. Nägerl, and R. Grimm.
Optimized production of a cesium Bose-Einstein condensate.
Appl. Phys. B **79**, 1013 (2004).

8. J. Herbig, T. Kraemer, M. Mark, T. Weber, C. Chin, H.-C. Nägerl, and R. Grimm.
Preparation of a Pure Molecular Quantum Gas.
Science **301**, 1510 (2003).

Metastable Feshbach Molecules in High Rotational States

S. Knoop,[1] M. Mark,[1] F. Ferlaino,[1,2] J. G. Danzl,[1] T. Kraemer,[1] H.-C. Nägerl,[1] and R. Grimm[1,3]

[1]*Institut für Experimentalphysik and Forschungszentrum für Quantenphysik, Universität Innsbruck, 6020 Innsbruck, Austria*

[2]*LENS and Dipartimento di Fisica, Università di Firenze, Firenze, Italy*

[3]*Institut für Quantenoptik und Quanteninformation, Österreichische Akademie der Wissenschaften, 6020 Innsbruck, Austria*

(Received 22 October 2007; published 29 February 2008)

We experimentally demonstrate Cs_2 Feshbach molecules well above the dissociation threshold, which are stable against spontaneous decay on the time scale of 1 s. An optically trapped sample of ultracold dimers is prepared in a high rotational state and magnetically tuned into a region with a negative binding energy. The metastable character of these molecules arises from the large centrifugal barrier in combination with negligible coupling to states with low rotational angular momentum. A sharp onset of dissociation with increasing magnetic field is mediated by a crossing with a lower rotational dimer state and facilitates dissociation on demand with a well-defined energy.

DOI: 10.1103/PhysRevLett.100.083002 PACS numbers: 33.15.Fm, 33.20.Sn, 33.80.Be, 37.10.Pq

Metastability is at the heart of many phenomena in physics. Energy barriers or conservation laws can efficiently prevent a system from decaying into lower-lying states. In the field of ultracold quantum gases, metastability is ubiquitous. Bose-Einstein condensates in dilute alkali vapors are intrinsically metastable, as the absolute ground state of the system is just a tiny piece of metal. Further prominent examples for the important role of metastability in ultracold gases can be found in Bose-Einstein condensates with attractive interactions [1,2], vortices in rotating superfluids [3,4], dark solitons [5,6], and repulsively bound atom pairs in optical lattices [7].

The association of Feshbach molecules in ultracold quantum gases [8] has opened up many new opportunities in the field, e.g., for experiments on quantum states with strong pair correlations. It has become experimentally routine to produce dimers in a binding energy range of typically 100 kHz up to a few 10 MHz below the atomic threshold. Considerable effort is in progress to extend the energy range of ultracold molecules initially prepared by Feshbach association to larger binding energies [9,10], ultimately with the goal to produce quantum-degenerate molecular samples in the rovibrational ground state.

In this Letter, we explore ultracold molecules in a new energy regime. We create metastable dimers *above* the threshold for spontaneous dissociation into free atoms, i.e., dimers with *negative* binding energies. In many experiments, the fast dissociation of Feshbach molecules above threshold on the time scale of microseconds [11,12] is used for detection purposes by imaging the resulting atoms. Feshbach molecules with energetically open channels for spontaneous dissociation were investigated in two previous experiments. Lifetimes of up to a few tens of milliseconds were demonstrated in an *s*-wave halo state of $^{85}Rb_2$ [13] and, more recently, $^{40}K_2$ *p*-wave molecules above threshold behind a centrifugal barrier were observed with lifetimes of a few hundreds of microseconds [14]. In contrast to these rather limited lifetimes, we demonstrate above-threshold molecules that are stable against dissociative decay on the time scale of a second; this can be considered infinitely long for experimental purposes. The basic idea to achieve such metastability is the transfer of the dimers to a high rotational state where a large centrifugal barrier in combination with a weak coupling to low partial-wave scattering states strongly suppresses spontaneous decay; see illustration in Fig. 1. Our experiments are performed on ultracold, trapped Cs_2 dimers transferred into a state with rotational quantum number $\ell = 8$, i.e., into an *l*-wave state [15]; here the centrifugal energy barrier is as high as $h \times 150$ MHz.

The two-body scattering properties of Cs and the underlying molecular structure have been thoroughly investigated in previous work [16,17]. Feshbach resonances up to *g*-wave character have been found. The underlying

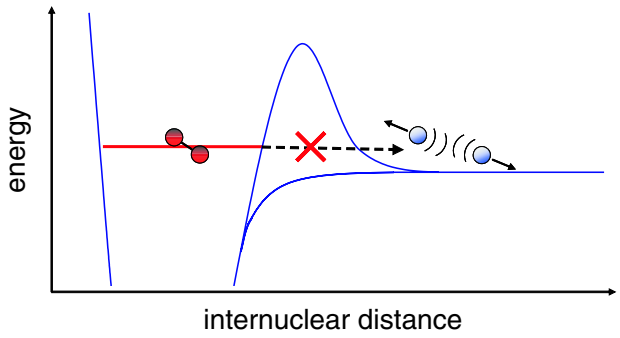

FIG. 1 (color online). Illustration of the basic idea of a long-lived metastable Feshbach molecule in a high rotational state. The solid lines illustrate two molecular potential curves, with high rotational angular momentum and with zero rotation. Direct dissociation through the large centrifugal barrier is strongly suppressed. Indirect dissociation by coupling at short distances to a partial wave with low angular momentum is negligible because of the large difference in the rotational quantum numbers.

coupling of the s-wave scattering continuum to g-wave molecular states is special to cesium because of relatively strong indirect spin-spin coupling [18]. This second-order interaction in general allows coupling between different partial-wave states with a difference $\Delta\ell$ in rotational quantum numbers up to $|\Delta\ell| = 4$. The Cs dimer energy structure in the relevant range is shown in Fig. 2. The s-wave threshold corresponds to two free atoms in the lowest hyperfine ground state sublevel $|F, m_F\rangle = |3, 3\rangle$ with zero kinetic energy. The notation $f\ell(m_f)$ for molecular states was introduced in Ref. [17]; the symbols f and m_f represent the quantum numbers for the total internal angular momentum and its projection.

The Cs_2 spectrum provides several accessible l-wave states, which have been identified in Refs. [17,19,20]. Remarkably, these states do not manifest themselves in observable Feshbach resonances in the scattering of atoms, which is a consequence of the negligible coupling to the scattering continuum for $|\Delta\ell| > 4$. The l-wave states can nevertheless be populated efficiently by using coherent state-transfer at avoided level crossings [17], where each step obeys the selection rule $\Delta\ell \leq 4$ for the rotational angular momentum.

In this work, the state $6l(4)$ serves as a model system for metastable dimers in high rotational states above the dissociation threshold. The starting point for our experiments is a sample of typically 1×10^4 l-wave dimers prepared in a crossed-beam CO_2 laser trap at a temperature of $T =$ 250(50) nK; the mean trap frequency is $\bar{\omega} = 2\pi \times 41(1)$ Hz. The experimental procedures have been developed earlier [17]. In brief, molecules are first created by Feshbach association in the state $4g(4)$ using the 19.84-G resonance, followed by transfer into $6l(4)$ via an intermediate state $6g(6)$; the latter state has a binding energy of about $h \times 5$ MHz and is out of the energy range displayed in Fig. 2. The state $6l(4)$ has a magnetic moment of $0.96(1)\mu_B$ and crosses the dissociation threshold at a magnetic field of 22.0(2) G. We have spectroscopically investigated this state by extending magnetic-moment measurements [17] into energy regions above threshold; see open squares in Fig. 2.

To measure the lifetime of the l-wave state, we hold the sample at magnetic fields corresponding to energies above and below the dissociation threshold. After variable storage times of up to 0.4 s, the remaining molecules are quickly (within typically 10 ms) subjected to the reverse transfer route and dissociated at the g-wave Feshbach resonance at 19.84 G. Standard absorption imaging is finally applied to the resulting atom sample [21].

In Fig. 3, we show typical decay measurements. Just below threshold ($B = 21.6$ G, closed squares), we observe a nonexponential decay of the molecular sample on a time scale of 100 ms, which is a result of inelastic two-body collisions. For an energy of $h \times 2$ MHz above threshold (24.7 G, open triangles), the behavior is very similar with a slightly faster decay. Only at magnetic fields around 27 G we observe a much faster loss of molecules. We analyze the decay measurements using the rate equation

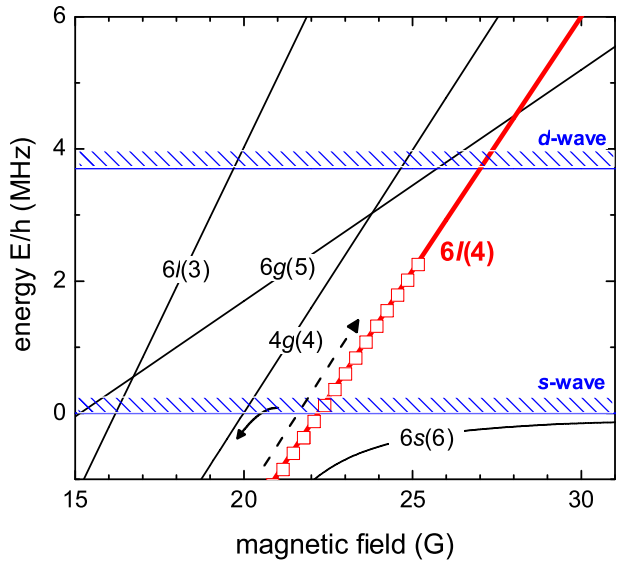

FIG. 2 (color online). Energy curves of the relevant Cs_2 dimer states as function of the magnetic field [16,17]. The s-wave threshold ($E = 0$) and the height of the d-wave centrifugal barrier ($E = h \times 3.7$ MHz) are indicated. The quantum state relevant for this work is labeled with $6l(4)$. The open squares represent spectroscopic data on this state obtained from measuring its magnetic moment, and the arrows indicate the path for preparation of the dimers (for details see text).

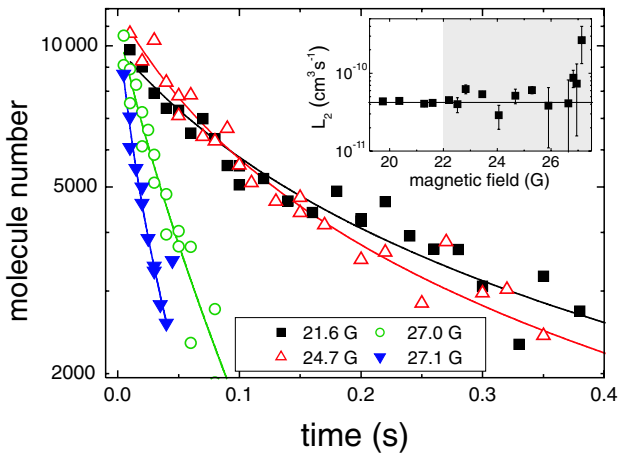

FIG. 3 (color online). Loss measurements of the $6l(4)$ molecular sample for different magnetic fields. One set of data is taken below the dissociation threshold ($B = 21.6$ G); three further sets (24.7, 27.0, 27.1 G) refer to situations above threshold. The lines are fits to the measurements including two-body and one-body decay. The inset shows the resulting two-body loss coefficient L_2, where the shaded region indicates the magnetic field region above threshold. The horizontal line indicates the average L_2 below threshold.

$\dot{N}/N = -\alpha - L_2\bar{n}$, where L_2 is the loss coefficient that describes two-body decay resulting from inelastic dimer-dimer collisions. The parameter α represents the rate of spontaneous dissociation as the dominant one-body decay process of the dimers. The mean molecular density $\bar{n}$ is related to the molecule number N by $\bar{n} = [m\bar{\omega}^2/(2\pi k_B T)]^{3/2} N$, where m is the mass of a Cs atom. Below threshold the loss of molecules is solely determined by inelastic two-body decay and the one-body decay term can be omitted. Other loss sources, such as light-induced dissociation and background collisions, can be neglected under our experimental conditions.

The fit results for L_2 as a function of the magnetic field are shown in the inset of Fig. 3. Below threshold no magnetic field dependence is observed. Here L_2 has a value of $4.2(0.2)_{\mathrm{stat}}(1.4)_{\mathrm{syst}} \times 10^{-11}$ cm^3 s^{-1}, similar to the values for Cs_2 found in other quantum states [19,22]. The systematic error is based on the uncertainty in the temperature and the trap frequency measurements. Above threshold α is a free parameter in the fit procedure and the competition between one-body and two-body decay introduces a large error. The values obtained for L_2 above threshold scatter around the value obtained below threshold with a trend to somewhat higher values.

The results for the dissociation rate α are shown in Fig. 4 (closed symbols). We also apply a constrained fit, in which L_2 is fixed to its constant value below threshold. The results of this constrained fit (open symbols) give an upper limit for the dissociation rates under the plausible assumption that collisional decay does not decrease above threshold. Below 26 G, i.e., up to 4 G above threshold, the dissociation rates remain close to zero. Around 27 G, however, an increase is observed, which is most clearly seen from the constrained fit. One-body lifetimes for spontaneous dissociation in the regime of negative binding energies above threshold are obtained by inverting the dissociation rates and are shown in the inset of Fig. 4 as function of the energy above threshold. The one-body lifetimes up to 26 G ($h \times 3$ MHz) are at least 1 s, which highlights the long-lived metastable character of the l-wave Feshbach molecules. Beyond this time scale, we cannot rule out a very slow dissociative decay, e.g., by a high-order coupling to the s-wave scattering continuum.

The increase of the dissociation rate around 27 G shows that a new dissociation channel opens up. This behavior cannot be explained by tunneling through the l-wave centrifugal barrier, as the estimated rate for this process is 4 orders of magnitude smaller than observed here experimentally. We explain the onset of dissociation by coupling to a g-wave state, which mediates the dissociation [23]. The $6l(4)$ state crosses a state $6g(5)$ at about 28 G (see Fig. 2). When the crossing is approached, a g-wave component starts to mix in. This increasing admixture then allows decay into s- and d-waves without the requirement of any higher-order coupling beyond the indirect spin-spin interaction.

To investigate the dissociation process around 27 G in more detail, we directly image the resulting atoms [14,24], without the reverse transfer route and dissociation at 19.84 G. In Fig. 5, we show the number of dissociated molecules as function of the magnetic field. Here the images are taken 5 ms after reaching the final magnetic field value in a fast ramp. Below 26 G no dissociated molecules are observed, while in the region of 27–28 G a rapid appearance is seen. The inset of Fig. 5 shows an absorption image at 27.8 G. The dissociation pattern is

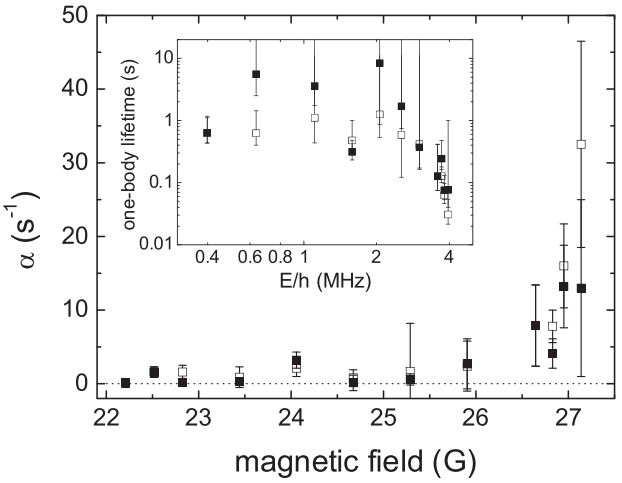

FIG. 4. Dissociation rate α for the $6l(4)$ state as function of magnetic field obtained from an unconstrained fit (closed squares) and a constrained fit, fixing L_2 to its value below threshold (open squares). The inset shows the corresponding one-body lifetime as function of energy above threshold.

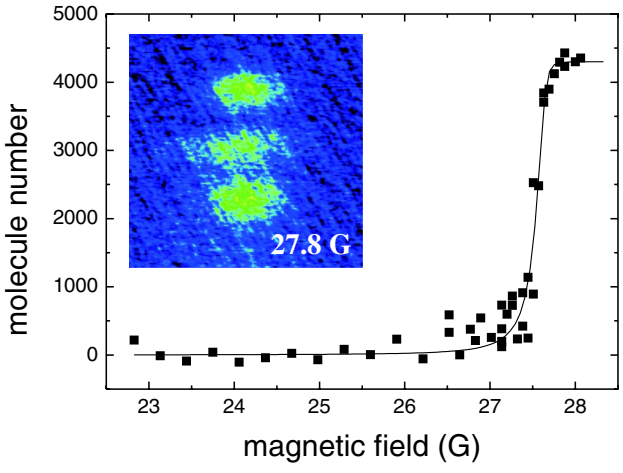

FIG. 5 (color online). The number of dissociated molecules as function of the magnetic field. The curve is a fit, based on modeling the amount of g-wave character around the crossing between the $6l(4)$ state and the $6g(5)$ state. The inset shows an absorption image of rapid dissociated $6l(4)$ dimers at a magnetic field of 27.8 G (averaged over 16 shots).

consistent with an interference between s and d waves. The presence of d-waves is expected as the dissociation occurs above the d-wave centrifugal barrier.

We use a simple two-channel avoided crossing approach to model the magnetic field dependence of the dissociation rate. Near the crossing, we describe the molecular state as a superposition of the l- and g-wave states. The g-wave amplitude determines the dissociation rate and increases smoothly from zero to one when the avoided crossing of quasibound states is followed from below. A fit based on this model is shown by the solid line in Fig. 5. The model allows us to determine the position of the crossing within an uncertainty of 0.1 G. We obtain a value of 27.7 G, which is consistent with our previous knowledge of the molecular spectrum [17].

The dissociation mechanism discussed for the $6l(4)$ state also agrees with observations in further experiments on the two other neighboring l-wave states $6l(3)$ and $6l(5)$. The latter state crosses the atomic threshold at 35.0(2) G and has a first avoided crossing with a g-wave state only around $h \times 12$ MHz (not shown in Fig. 2). Here we explored magnetic fields up to 48 G and corresponding energies up to $h \times 8$ MHz without finding any significant decay, even far above the d-wave centrifugal barrier [26]. In contrast, the $6l(3)$ state shows significant dissociation already at a relatively small energy of $h \times 0.7$ MHz above threshold [20]. This is explained by the presence of a crossing with the $6g(5)$ state, which is found at a magnetic field only 0.5 G higher than the intersection of the $6l(3)$ state with the s-wave threshold (see Fig. 2).

To conclude, we have demonstrated the metastable character of ultracold dimers in a high rotational state above the dissociation threshold, where the binding energy is negative. In our experiments, we observed Cs_2 Feshbach molecules in an l-wave state to be stable against dissociative decay on a time scale of at least 1 s. The large centrifugal barrier suppresses tunneling to the l-wave scattering continuum while the coupling to lower partial waves is extremely small. The metastable region and onset of dissociation for the l-wave states depends on the location of the first crossing with a g-wave state, which mediates dissociative decay.

In future work, shielding the dimers against collisional decay can be achieved by trapping in an optical lattice [27]. In such a periodic environment one may also create a Mott-like state with exactly one molecule per lattice site [28]. This opens up the possibility to create novel metastable quantum states with strong pair correlations. The possibility to achieve dissociative decay on demand with a well-defined energy by switching the magnetic field to particular values opens up further possibilities, e.g., for a controlled collective decay of the inverted medium in analogy to superradiance.

We thank S. Dürr and T. Volz for fruitful discussions. We acknowledge support by the Austrian Science Fund (FWF) within No. SFB 15 (project part 16). S. K. is supported within the Marie Curie Intra-European Program of the European Commission. F. F. is supported within the Lise Meitner program of the FWF.

[1] C. C. Bradley, C. A. Sackett, and R. G. Hulet, Phys. Rev. Lett. **78**, 985 (1997).
[2] J. L. Roberts *et al.*, Phys. Rev. Lett. **86**, 4211 (2001).
[3] K. W. Madison *et al.*, Phys. Rev. Lett. **84**, 806 (2000).
[4] M. W. Zwierlein *et al.*, Nature (London) **435**, 1047 (2005).
[5] S. Burger *et al.*, Phys. Rev. Lett. **83**, 5198 (1999).
[6] J. Denschlag *et al.*, Science **287**, 97 (2000).
[7] K. Winkler *et al.*, Nature (London) **441**, 853 (2006).
[8] T. Köhler, K. Góral, and P. S. Julienne, Rev. Mod. Phys. **78**, 1311 (2006).
[9] K. Winkler *et al.*, Phys. Rev. Lett. **98**, 043201 (2007).
[10] F. Lang *et al.*, arXiv:0708.3958 [Nature Phys. (to be published)].
[11] T. Mukaiyama *et al.*, Phys. Rev. Lett. **92**, 180402 (2004).
[12] S. Dürr, T. Volz, and G. Rempe, Phys. Rev. A **70**, 031601(R) (2004).
[13] S. T. Thompson, E. Hodby, and C. E. Wieman, Phys. Rev. Lett. **94**, 020401 (2005).
[14] J. P. Gaebler *et al.*, Phys. Rev. Lett. **98**, 200403 (2007).
[15] H. N. Russell, A. G. Shenstone, and L. A. Turner, Phys. Rev. **33**, 900 (1929).
[16] C. Chin *et al.*, Phys. Rev. A **70**, 032701 (2004).
[17] M. Mark *et al.*, Phys. Rev. A **76**, 042514 (2007).
[18] P. J. Leo, C. J. Williams, and P. S. Julienne, Phys. Rev. Lett. **85**, 2721 (2000).
[19] C. Chin *et al.*, Phys. Rev. Lett. **94**, 123201 (2005).
[20] M. Mark *et al.*, Phys. Rev. Lett. **99**, 113201 (2007).
[21] J. Herbig *et al.*, Science **301**, 1510 (2003).
[22] N. Zahzam *et al.*, Phys. Rev. Lett. **96**, 023202 (2006).
[23] The enhancement of dissociation at a certain magnetic field above threshold appears similar to previous observations on $^{87}Rb_2$ dimers [24,25]. In the latter work, however, the underlying mechanism is tunneling through the centrifugal barrier when the dimer in a closed channel couples to a shape resonance in an open channel. In our work, the g-wave state mediates coupling of the l-wave dimer to a low partial-wave scattering state (superposition of s and d waves) without the necessity to tunnel through a centrifugal barrier.
[24] T. Volz *et al.*, Phys. Rev. A **72**, 010704(R) (2005).
[25] S. Dürr *et al.*, Phys. Rev. A **72**, 052707 (2005).
[26] The $6l(5)$ state shows even more favorable conditions regarding metastability compared to the $6l(4)$ state. However, we focus on the $6l(4)$ state in this paper, as the production and detection of $6l(5)$ state is more difficult.
[27] G. Thalhammer *et al.*, Phys. Rev. Lett. **96**, 050402 (2006).
[28] T. Volz *et al.*, Nature Phys. **2**, 692 (2006).

Spectroscopy of ultracold trapped cesium Feshbach molecules

M. Mark,[1] F. Ferlaino,[1,2] S. Knoop,[1] J. G. Danzl,[1] T. Kraemer,[1] C. Chin,[3] H.-C. Nägerl,[1] and R. Grimm[1,4]
[1]*Institut für Experimentalphysik and Forschungszentrum für Quantenphysik, Universität Innsbruck, 6020 Innsbruck, Austria*
[2]*LENS and Dipartimento di Fisica, Università di Firenze, Firenze, Italy*
[3]*Physics Department and James Franck Institute, University of Chicago, Chicago, Illinois 60637, USA*
[4]*Institut für Quantenoptik und Quanteninformation, Österreichische Akademie der Wissenschaften, 6020 Innsbruck, Austria*
(Received 7 June 2007; published 25 October 2007)

We explore the rich internal structure of Cs_2 Feshbach molecules. Pure ultracold molecular samples are prepared in a CO_2-laser trap, and a multitude of weakly bound states is populated by elaborate magnetic-field ramping techniques. Our methods use different Feshbach resonances as input ports and various internal level crossings for controlled state transfer. We populate higher partial-wave states of up to eight units of rotational angular momentum (*l*-wave states). We investigate the molecular structure by measurements of the magnetic moments for various states. Avoided level crossings between different molecular states are characterized through the changes in magnetic moment and by a Landau-Zener tunneling method. Based on microwave spectroscopy, we present a precise measurement of the magnetic-field-dependent binding energy of the weakly bound *s*-wave state that is responsible for the large background scattering length of Cs. This state is of particular interest because of its quantum-halo character.

DOI: 10.1103/PhysRevA.76.042514 PACS number(s): 33.20.−t, 33.80.Ps, 34.50.−s, 05.30.Jp

I. INTRODUCTION

The possibility to associate molecules via Feshbach resonances in ultracold gases [1] has opened up new avenues of research. The demonstration of coherent atom-molecule coupling [2], the creation of pure molecular samples from atomic Bose-Einstein condensates [3–5], and the formation of ultracold molecules from atomic Fermi gases [6–9] paved the way for spectacular achievements. Prominent examples are the observation of molecular Bose-Einstein condensation [10–12] and the creation of strongly interacting superfluids in atomic Fermi gases [13]. Ultracold molecules have also opened up new ways to study few-body physics with ultracold atoms [14,15]. In optical lattices, controlled molecule formation [16–18] has been the experimental key to create correlated states in a crystal-like environment [19,20].

A Feshbach resonance [21,22] arises when a bound molecular dimer state is magnetically tuned near a two-atom scattering state, leading to resonant atom-molecule coupling. The molecular structure and in particular the molecular state that interacts with the atomic threshold determine the character of a particular Feshbach resonance [1]. The rotational angular momentum of the molecular state, characterized by the rotational quantum number ℓ, plays a central role. Various types of Feshbach molecules ranging from dimers in *s*-wave states ($\ell=0$) to dimers in *g*-wave states ($\ell=4$) have been realized [1].

For experiments with molecular quantum gases, cesium is particularly rich as it offers a unique variety of different Feshbach resonances and molecular states [23]. Pronounced relativistic effects lead to strong higher-order coupling between atom pairs and molecules and between different molecular states. For achieving Bose-Einstein condensation in cesium [24], the detailed understanding of the complex molecular structure was a crucial factor. The interaction properties of cesium atoms were characterized by Feshbach spectroscopy in a series of atom scattering experiments performed at Stanford University [23,25,26]. In these experiments the magnetic-field positions of many Feshbach resonances up to *g*-wave character were measured. This provided the necessary experimental input for theoretical calculations of the molecular energy structure [23,27], performed at the National Institute of Standards and Technology (NIST). In the following, we will refer to the cesium molecular structure as presented in Ref. [23] as the "NIST model." It represents the current knowledge of the structure of weakly bound molecular states, and thus constitutes the theoretical basis for the experiments discussed in this work.

In this paper, we report on a thorough investigation of the energy structure of weakly bound Cs_2 Feshbach molecules. Our experiments are performed on ultracold molecular samples confined in a CO_2-laser trap [14,28–30] and extend previous work [23] in three important ways. First, we show how any of the weakly bound molecular states can be populated based on elaborate time-dependent magnetic-field control. Spectroscopy performed on various molecular states confirms the main predictions of the NIST model and provides input for further refinements of the model. Second, we demonstrate how one can indirectly populate states with high rotational angular momentum of $\ell=8$ (*l*-wave states) by taking advantage of avoided level crossings with $\ell=4$ (*g*-wave) states. For these *l*-wave states, direct Feshbach association is not feasible because of negligible coupling with the atomic scattering continuum. Third, spectroscopy on avoided crossings between bound states yields precise information about the coupling strengths between molecular states.

In Sec. II, we first review the energy structure of weakly bound Cs_2 dimers. In Sec. III, we address the preparation of molecular samples, detail our techniques to transfer molecular samples to various internal states, and present the methods for molecule detection. In Sec. IV, we report on spectroscopic measurements using magnetic moment and microwave techniques.

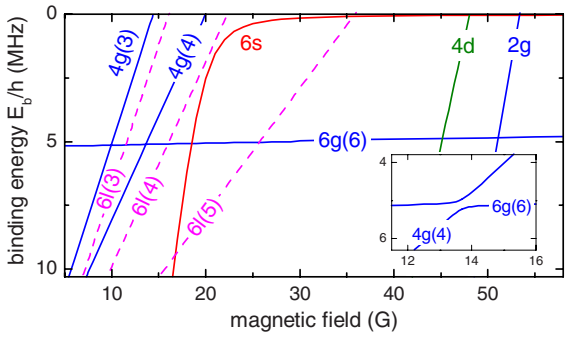

FIG. 1. (Color online) Molecular energy structure below the threshold of two free Cs atoms in the absolute ground state $|F=3,m_F=3\rangle$. Molecular state labeling is according to the quantum numbers $f\ell(m_f)$, $m_\ell=6-m_f$. The quantum number m_f is omitted for states with $m_f=f$ and $m_\ell=\ell$. The solid lines represent the *s*-, *d*-, and *g*-wave states included in the NIST model [23]. The intersections of the *d*- and *g*-wave states with the threshold cause narrow Feshbach resonances that can be used for molecule production. The curvature of the 6*s* state arises from a large avoided crossing between two states of the same $f\ell$ quantum numbers. The NIST model does not take into account weak avoided crossings between bound molecular states mediated by the relativistic spin-spin dipole and second-order spin-orbit interactions. If these interactions are taken into account, the crossings between bound molecular states become avoided as illustrated in the inset for the example of the $4g(4)/6g(6)$ crossing. The dashed lines represent *l*-wave states ($\ell=8$) obtained from extended calculations based on the NIST model.

II. ENERGY STRUCTURE OF WEAKLY BOUND CESIUM DIMERS

Figure 1 gives an overview of the molecular states relevant to the present work, covering the magnetic-field region up to 55 G and binding energies up to $h\times 10$ MHz, where h is Planck's constant. Zero energy corresponds to the dissociation threshold into two Cs atoms in the absolute hyperfine ground-state sublevel $|F=3,m_F=3\rangle$. Each intersection of the atomic threshold with a molecular state corresponds to a Feshbach resonance. The rotational angular momentum associated with a molecular state is denoted by the quantum number ℓ. We follow the convention of labeling states with $\ell=0,2,4,6,8,\ldots$ as $s,d,g,i,l,\ldots$-wave states [31] and the associated Feshbach resonances as $s,d,g,i,l,\ldots$-wave resonances. As a consequence of the bosonic nature of Cs atoms, only even values of ℓ occur. The solid lines in Fig. 1 represent states resulting from the NIST model [23], including *s*-, *d*-, and *g*-wave states. For two interacting Cs atoms, relativistic spin-spin dipole and second-order spin-orbit interactions are particularly important [27]. Therefore, in Cs not only *s*- and *d*-wave states but also *g*-wave states couple sufficiently to the atomic threshold to produce experimentally observable Feshbach resonances. The magnetic-field positions of these Feshbach resonances were determined experimentally in an optically confined atomic Cs gas [23,25,26]. The NIST predictions for the weakly bound molecular structure result from a theoretical model of the energy spectrum with parameters adjusted to reproduce the measured magnetic-field positions of the Feshbach resonances.

TABLE I. List of angular momentum quantum numbers for the relevant molecular states. Each state is represented by four quantum numbers: the total internal angular momentum f and the rotational angular momentum ℓ with m_f and m_ℓ as the respective projections along the quantization axis.

Label of state	$6s$	$4d$	$2g$	$4g(3)$	$4g(4)$	$6g(6)$	$6l(3)$	$6l(4)$	$6l(5)$
f,m_f	6,6	4,4	2,2	4,3	4,4	6,6	6,3	6,4	6,5
ℓ,m_ℓ	0,0	2,2	4,4	4,3	4,2	4,0	8,3	8,2	8,1

Cs molecular states near threshold are for the most part sufficiently well characterized by the quantum numbers $|f,m_f;\ell,m_\ell\rangle$ [1], where f represents the sum of the total atomic spins $F_{1,2}$ of the individual atoms, and ℓ is the nuclear mechanical angular momentum quantum number. The respective projection quantum numbers are given by m_f and m_ℓ. In special cases the quantum numbers F_1 and F_2 also must be specified. To account for the molecular structure below threshold, not only the exchange and van der Waals interaction, the atomic hyperfine structure, and the Zeeman energy, but also the weaker relativistic spin-spin dipole and second-order spin-orbit interactions must be considered [23,32]. The exchange and van der Waals interactions conserve ℓ and f, whereas the two relativistic interactions weakly mix states with different ℓ and f. The complete interaction Hamiltonian conserves the total angular momentum $f+\ell$ at zero magnetic field. More importantly, it always conserves the projection of the total angular momentum m_f+m_ℓ. In our experiments, we start with an ultracold, spin-polarized atomic sample of Cs atoms in their hyperfine ground state $|F=3,m_F=3\rangle$. At ultralow scattering energies only incoming *s* waves ($\ell=0$) need to be considered. The atomic scattering state is hence $|f=6,m_f=6;\ell=0,m_\ell=0\rangle$. Consequently all molecular states relevant to the present work obey $m_f+m_\ell=6$.

To label molecular states we use the three quantum numbers $f\ell(m_f)$. For states with $m_f=f$ and $m_\ell=\ell$, we only use f and ℓ for brevity. Table I gives the full set of angular momentum quantum numbers for all molecular states relevant to the present work.

Coupling between molecular states with the same f and ℓ in general leads to very broad avoided crossings between molecular states. The strong curvature of the 6*s* state in Fig. 1 is a result of such a crossing. In this case, a weakly bound 6*s* state with $F_1=3$ and $F_2=3$ happens to couple to a 6*s* state with $F_1=4$ and $F_2=4$. Narrow avoided crossings arise when molecular states of different f and ℓ intersect. These narrow crossings are mediated by the spin-spin dipole and second-order spin-orbit interactions. In the NIST model, narrow avoided crossings were only taken into account for special cases where it was necessary to assign the experimentally observed Feshbach resonances. Consequently, the molecular states in Fig. 1 are shown as intersecting lines. Nevertheless, the existence of avoided crossings between molecular states of different $f\ell$ is crucial for the present work as it allows the transfer of molecules from one state to another. As an example, the inset in Fig. 1 schematically illustrates the

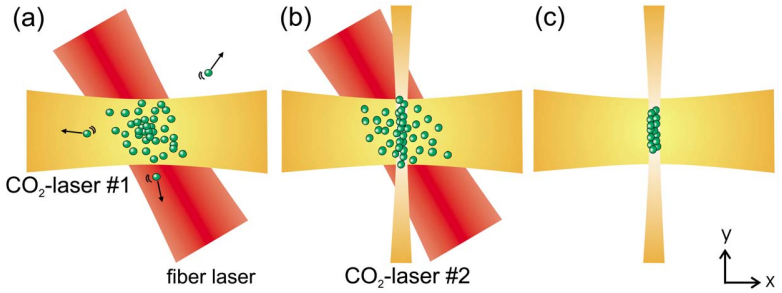

FIG. 2. (Color online) Successive stages of optical dipole traps. (a) We first realize a large volume "reservoir" trap by crossing a CO_2-laser beam and a 1070 nm fiber-laser beam in the presence of a levitating gradient. (b) We ramp up a tightly focused CO_2-laser beam, (c) switch off the 1070 nm reservoir beam, and then evaporate along the vertical direction (z axis) by lowering the gradient. We obtain typically 4×10^5 Cs atoms at a temperature of 200 nK.

avoided crossing between the $4g(4)$ state and the $6g(6)$ state at $\sim$13.5 G.

The dashed lines in Fig. 1 represent l-wave states. As states with higher angular momentum ($\ell>4$) do not couple to the s-wave scattering continuum, the l-wave states cannot be observed by Feshbach spectroscopy in an ultracold atomic gas. Consequently, no experimental input for higher angular momentum states was available for the NIST model. It is not a surprise, however, that for Cs l-wave states exist in the low magnetic-field region. This follows from a general property of the asymptotic van der Waals potential [33]. In the case of an s state being close to threshold, angular momentum states with $\ell=4,8,\ldots$ should also occur near threshold. The observation of both g- and l-wave states in a system with near-resonant s-wave background scattering properties nicely illustrates this general property. When the NIST model is extended to states with higher angular momentum it indeed predicts l-wave states in the low-field region [34]. The calculations are expected to accurately predict the magnetic moments, i.e., the slopes, of these states but they leave some uncertainty concerning the exact binding energies [34]. The l-wave states shown in Fig. 1 result from the extended NIST model, but they are energetically adjusted to the experimental observations (Sec. IV) by equally down-shifting all three states by about $h\times2$ MHz.

III. PREPARATION OF Cs_2 MOLECULES IN VARIOUS INTERNAL STATES

In this section, we present our basic methods to prepare Cs_2 Feshbach molecules in various internal states. The starting point for all the experiments is an optically trapped ensemble of Cs atoms, the preparation of which is briefly summarized in Sec. III A. We then describe the creation of optically trapped Cs molecules based on different Feshbach resonances (Sec. III B). These resonances serve as "entrance doors" into the rich molecular structure near threshold. In Sec. III C, we discuss our techniques to transfer molecules to various internal states by application of elaborate time variations of the magnetic field. We make use of the possibility of adiabatic or diabatic passages through avoided crossings. In Sec. III D we discuss the methods to detect the molecular samples through controlled dissociation.

A. Atomic sample preparation

The setup used for the present experiments is optimized for molecule trapping and molecular state manipulation, and not for Bose-Einstein condensation (BEC) as in our previous work [3,24,35]. Here we start with an atomic sample near degeneracy, for which we obtain sufficient efficiencies for molecule formation.

For the present experiments we use a sequence of three dipole traps in the cooling and sample preparation process as shown in Fig. 2. The final dipole trap for molecule experiments is realized by crossing two CO_2-laser beams. The far-infrared CO_2-laser trap avoids the use of near-infrared radiation. In previous experiments we used the 1064 nm broadband radiation from a Yb fiber laser in the final trapping stage, and we observed strong light-induced trap losses for the Feshbach molecules, presumably as a result of excitation of molecular bound-bound transitions. The CO_2 light is sufficiently off resonance and it thus allows for long molecule trapping times [14,29,30] and facilitates efficient in-trap production of molecules. One of the important features in our previous experiments on Cs BEC and the production of Feshbach molecules is the ability to levitate the atoms and molecules against gravity using a magnetic-field gradient [14,24]. However, for the preparation of molecular samples in various states the requirement of magnetic-field gradients is problematic, because molecules can have widely different magnetic moments and thus require different levitation gradients. By using a relatively tight focus of one of the trapping CO_2-laser beams, we can hold the molecules against gravity without the levitation gradient field.

The cooling and trapping procedure for the atoms is similar to the techniques described in Ref. [35]. In brief, we first load a magneto-optical trap (MOT) followed by a short optical molasses phase to compress and further cool the atomic sample. Using the technique of Raman sideband cooling in an optical lattice [36] the atoms are then cooled and simultaneously polarized into the lowest hyperfine state $|F=3,m_F=3\rangle$. We typically obtain 2×10^7 atoms at a temperature of $\sim$700 nK.

The polarized sample is adiabatically released from the lattice into a large volume dipole trap. This "reservoir trap" is realized by two crossed laser beams. As illustrated in Fig.

2(a), we use a CO_2 laser and a Yb fiber laser for the reservoir with wavelengths of 10.6 μm and 1070 nm, respectively. For each laser the beam waist is around 650 μm. This shallow reservoir trap cannot hold the atoms against gravity. Therefore we apply magnetic levitation at this stage [24,35]. The resulting effective trap depth is about 7 μK. After releasing the atoms from the optical lattice used for Raman sideband cooling into the reservoir trap, 2 s of plain evaporation are necessary to thermalize the sample in the trap. The thermalization is performed at a magnetic field of 75 G, corresponding to a scattering length of about $1200a_0$, where a_0 denotes Bohr's radius. We measure about 4×10^6 atoms at a temperature of ~1 μK [35], the phase-space density is $\sim1/1000$.

After thermalization, the reservoir trap is crossed with a tightly focused CO_2-laser beam as shown in Fig. 2(b). The waist of this "CO_2 dimple" is about 80 μm. This value is diffraction limited by the aperture of the window of the vacuum chamber. We linearly ramp up the power of the beam within 2.8 s to $\sim$2.5 W corresponding to a trap depth of about 17 μK. Simultaneously the magnetic field is ramped down to 35 G, corresponding to a scattering length of $700a_0$. This procedure provides efficient collisional loading of the CO_2 dimple [35]. The remaining atoms in the reservoir trap are released by switching off the Yb fiber-laser beam. In the crossed CO_2-laser trap [see Fig. 2(c)] we measure typically 1×10^6 atoms at a temperature of 1 μK.

We then apply forced evaporative cooling by exponentially lowering the magnetic-field gradient within 6.3 s to 0. Atoms thus mainly escape from the trap along the vertical direction. Simultaneously, we adjust the scattering length by decreasing the magnetic field to a final value of $\sim$22 G to minimize three-body losses [37]. As we also slightly decrease the power of the CO_2 dimple to 2 W, the effective trap depth without levitation is ~2 μK.

We finally obtain $\sim4\times10^5$ Cs atoms at a temperature of about 200 nK in the crossed CO_2-laser trap. The trap frequencies of the final configuration without magnetic-field gradient are measured to be 84(1) Hz and 10(1) Hz in the horizontal plane, and 80(1) Hz in the vertical direction. The resulting peak density of the atoms is $\sim1\times10^{13}$ cm^{-3}, and the phase-space density is about 0.4. The total time to prepare the atomic sample is about 17 s.

B. Molecule production through Feshbach resonances

We magnetically associate ultracold cesium atoms to dimers on Feshbach resonances [1,3–5]. In this work we use *three different* resonances, the two g-wave resonances at $B=19.8$ G and 53.4 G and the d-wave resonance at 47.9 G, see Fig. 3. The width of the g-wave resonances is only a few mG, the d-wave resonance is about 200 mG wide. While the molecule formation at the 19.8 G g-wave resonance results in g-wave molecules, the association at the 47.9 G d-wave resonance leads in practice to s-wave molecules. This is a consequence of an avoided level crossing close to threshold between the states $4d$ and $6s$, see Fig. 3. Similarly, the association at the 53.4 G g-wave resonance results in d-wave molecules.

For molecule creation two different techniques are used. Depending on the character of the Feshbach resonance, we apply a ramping or a switching scheme to produce dimers [38]. The switching scheme works particularly well at the narrow g-wave Feshbach resonances. We set the magnetic field typically 0.5 G above the resonance. The field is then suddenly changed to the resonance position and kept there for $\sim$5 ms. In contrast, at the much broader 47.9 G d-wave Feshbach resonance we find superior efficiency by applying a linear magnetic-field ramp (ramping scheme). We start typically 350 mG above the resonance and linearly ramp the magnetic field within 5 ms to about 350 mG below the resonance. The efficiencies for molecule production range from a few percent up to 20%. Starting from 4×10^5 atoms we typically obtain 15 000 molecules, see Table II.

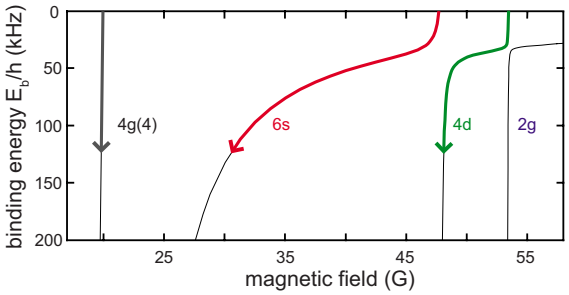

FIG. 3. (Color online) The molecular energy structure for very small binding energies in the region of the 19.8, 47.9, and 53.4 G Feshbach resonances, not resolved in Fig. 1. Above 45 G two avoided crossings are present in the energy structure. We use all three Feshbach resonances to associate molecules by ramping or switching the magnetic field. The arrows indicate the pathway after molecule association as the magnetic field is ramped down to allow for the optical removal of the atoms from the molecules. For details see the text.

To prepare a maximum number of molecules in the trap, it is necessary to separate atoms and molecules as fast as possible, since atom-dimer collisions dramatically reduce the lifetime of the molecular sample [39]. We remove the atoms from the dipole trap using a blast technique similar to Ref. [5]. First, the atoms are pumped out of the $|3,3\rangle$ state by light close to the $F=3\rightarrow F'=3$ transition. The blast pulse is tuned to the closed optical transition $|F=4,m_F=4\rangle\rightarrow|F'=5,m_{F'}=5\rangle$, which we also use for imaging. The optical cleaning process causes some unwanted loss and heating of the molecules. Particularly if the molecules are very weakly bound ($\lesssim h\times1$ MHz) or the blast duration is too long

TABLE II. Parameters for molecule production using three different Feshbach resonances. B_r is the field value at which the atoms are removed with the blast technique.

Feshbach resonance position (G)	19.8	47.9	53.4
Entrance state	$4g(4)$	$4d$	$2g$
Ramp speed (G/s)		140	
State at B_r	$4g(4)$	$6s$	$4d$
B_r (G)	14.5	19.7	45
Time to reach B_r (ms)	0.4	3	1
Number of molecules	19000	9000	15000

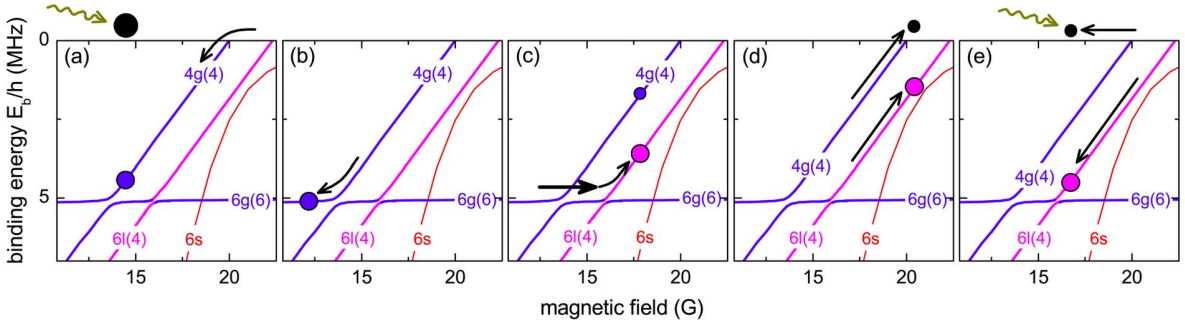

FIG. 4. (Color online) Illustration of the experimental toolbox for the preparation of molecules in various internal states. As an example the creation of molecules in the $6l(4)$ state is shown. (a) First, we produce $4g(4)$ molecules at the g-wave Feshbach resonance at 19.8 G and remove the remaining atoms by a short blast pulse, indicated by the rippled arrow. (b) The $4g(4)$ state is transferred into state $6g(6)$ by slowly lowering the magnetic field. (c) To overcome the avoided level crossing between state $4g(4)$ and $6g(6)$ a very fast magnetic-field ramp is applied. The target state $6l(4)$ is then accessed by using a second adiabatic ramp. (d) To remove the residual $4g(4)$ molecules from the $6l(4)$ dimers we ramp the magnetic field slightly above 20 G, dissociating the $4g(4)$ molecules into atoms while not affecting the l-wave molecules. (e) The magnetic field is lowered again to increase the binding energy of the target state molecules. A second blast pulse removes the remaining atoms.

($\gtrsim$1 ms) these effects are not negligible. Therefore immediately after the association we rapidly ramp the magnetic field further down. When the binding energy of the molecular state is on the order of $h\times 5$ MHz the molecules are much less affected by the blast light. When using the 19.8 G resonance the magnetic field must be ramped down only a few Gauss to reach such a binding energy. In the case of the 47.9 G resonance (53.4 G resonance) the lowering of the magnetic field transfers the molecules into the $6s$ state ($4d$ state) through the present avoided crossings, see Fig. 3. Therefore, to reach a sufficiently large binding energy a larger change in the magnetic field is required, resulting in a longer time to reach the field. However, with a typical blast duration of 400 μs we achieve a sufficient removal of the atoms from the trap while keeping the blast-induced molecule losses small ($\sim$10%–15%).

The precise timing for molecule production, the magnetic field for the purification, and the obtained number of molecules strongly depend on the particular Feshbach resonance. Table II summarizes the relevant experimental parameters of our molecule production. We measure a typical temperature of 250 nK for the molecular samples. This is slightly higher than the temperature of the atoms, presumably because of the effects of the blast cleaning technique. The corresponding peak density of the molecules is $\sim 7\times 10^{11}$ cm^{-3}.

C. Molecular state transfer

Other molecular states than the ones that we can directly access through the Feshbach creation schemes can be populated by controlled state transfer. The experimental key is the precise control of Landau-Zener tunneling at avoided crossings through elaborate magnetic-field ramps. By means of the ramp speed we can choose whether a crossing is followed adiabatically (slow ramp) or jumped diabatically (fast ramp). An important application of controlled ramps through avoided crossings is the coherent splitting of the molecular wave function for intermediate ramp speeds, as reported in Ref. [40].

Within the Landau-Zener model [41,42] an avoided level crossing is characterized by two parameters, the coupling strength and the differential slope of the states. For the coupling strength we introduce the parameter V as one-half the energy splitting between the two states at the crossing point. To characterize the slope we use $\Delta\mu$ as the magnetic moment difference between the two states. With these two parameters one commonly defines a critical ramp speed

$$r_c = \frac{2\pi V^2}{\hbar \Delta\mu}. \tag{1}$$

For fast ramps with ramp speed $\dot{B} \gg r_c$, the passage through the crossing is diabatic and the molecules stay in the same bare state. For slow ramps ($\dot{B} \ll r_c$), an adiabatic transfer into the other molecular state takes place. For Cs Feshbach dimers the typical coupling strengths for crossings between states of different $f\ell$ (see Sec. II) are such that the critical ramp speeds are found in a range convenient for experiments. Full control ranging from completely diabatic Landau-Zener tunneling to full adiabatic transfer can be achieved for most crossings (see Sec. IV A 2).

To illustrate the experimental procedure for transferring molecules into different states, we now consider the preparation of a molecular sample in a selected "target" state. As an example we discuss the population of the target state $6l(4)$ in detail. As the state transfer strongly relies on the technical performance of the setup for magnetic-field control, we give a detailed description of the setup in the Appendix.

As shown in Fig. 4(a), we first create $4g(4)$ molecules at the 19.8 G Feshbach resonance. We then lower the magnetic field to about 14.5 G and remove the remaining atoms with the blast pulse. In a second step, see Fig. 4(b), we lower the magnetic field to $\sim$12 G within a few ms. Consequently, we pass the avoided crossing between the two states $4g(4)$ and $6g(6)$ at about 13.5 G. For this crossing the critical ramp speed, given by Eq. (1), is $r_c \sim 1100$ G/ms as the coupling strength is $V \simeq h\times 150$ kHz [14]. With the applied ramp

speed of ~2 G/ms the transfer into state $6g(6)$ is therefore fully adiabatic. Figure 4(c) illustrates the transfer of the $6g(6)$ molecules to the target state $6l(4)$. First we apply a fast magnetic-field ramp to overcome the $4g(4)/6g(6)$ crossing, indicated by the straight arrow. The high ramp speed required is accomplished by a specially designed "booster" coil, described in the Appendix. With a maximum possible ramp speed of 7500 G/ms we achieve a transfer efficiency of typically 70%. After the jump we enter the target state $6l(4)$ by adiabatically following the next avoided crossing between state $6g(6)$ and $6l(4)$ at ~15.5 G. For this crossing we find a fully adiabatic transfer when ramping the magnetic field from 15 G to ~17 G within a few ms. In the fourth step, illustrated in Fig. 4(d), we prepare the cleaning of the sample from the residual $4g(4)$ molecules. The magnetic field is ramped up to ~20 G and kept constant for a few ms. While the remaining $4g(4)$ molecules break up into atoms, the $6l(4)$ molecules are not affected as their dissociation threshold is higher. Finally, we ramp down the magnetic field to $B \simeq 16$ G where the target molecules are well below threshold, see Fig. 4(e). Again we remove the residual atoms using a blast pulse. As a result, we obtain a pure molecular sample in the state $6l(4)$.

In analogous ways, we apply these techniques to populate any of the states shown in Fig. 1. The time to prepare the molecular sample together with the duration of all subsequent measurements is about 20 ms to 25 ms. Molecule-molecule collisions [14,30] are not relevant on this time scale for the given molecular densities.

D. Molecule detection

The standard detection scheme for Feshbach molecules relies on the controlled dissociation by reverse magnetic-field ramps [3,43]. When ramping the magnetic field above the dissociation threshold, the molecules become quasibound and decay into the atomic scattering continuum. The resulting atom cloud can then be detected using standard absorption imaging.

Magnetic dissociation by inverse magnetic-field ramps is straightforward for states with large coupling to the scattering continuum, and hence any of the Feshbach resonances up to g wave can be used. We ramp the magnetic field typically 2 G above threshold and wait a few ms at the dissociation field before the image is taken. l-wave molecules do not sufficiently couple to the atomic continuum and significant dissociation is prevented. One way to detect l-wave dimers is to transfer these molecules into one of the s-, d-, or g-wave states which allow for dissociation and hence for detection.

To illustrate the detection by controlled dissociation, we resume our previous example of Sec. III C, where we have described the preparation of a molecular sample in the $6l(4)$ state. Figure 5 shows the detection scheme that we use for this state. First the molecular sample is adiabatically transferred to the state $4g(4)$ via the state $6g(6)$ by lowering the magnetic field to about 12.5 G, see Fig. 5(a). We then perform a diabatic state transfer over the avoided crossing at ~14 G as indicated in Fig. 5(b). Finally, we ramp the magnetic field up to ~21 G, which is well above the dissociation threshold of the $4g(4)$ state.

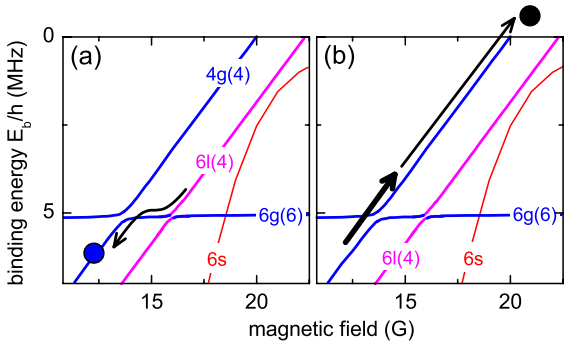

FIG. 5. (Color online) Example of a detection scheme for l-wave molecules. (a) First the $6l(4)$ molecules are adiabatically transferred into the state $4g(4)$ via the state $6g(6)$ by ramping down the magnetic field. (b) The avoided crossing at 13.6 G is passed by using a fast magnetic-field ramp. When ramping up to a field of ~21 G, the molecules are brought above threshold and dissociate. The resulting atom cloud is detected using the standard absorption imaging technique.

An alternative method for the detection of l-wave molecules relies on the particular energy structure of Cs atoms above the dissociation threshold. We find that the decay of metastable l-wave dimers can be mediated by coupling to a quasibound g-wave molecular state above threshold. Such a coupling with $\Delta\ell=4$ is sufficiently strong. We have previously used this process for the detection of l-wave molecules in the state $6l(3)$ in Ref. [40]. A more detailed analysis of this dissociation mechanism will be presented elsewhere [44].

For imaging of the resulting atomic cloud, the atoms are first pumped to the $|4,4\rangle$ state using light close to the $F=3 \rightarrow F'=3$ transition. The imaging light is resonantly tuned to the closed $|F=4,m_F=4\rangle \rightarrow |F'=5,m_F'=5\rangle$ optical transition, taking the Zeeman shift at the imaging magnetic field into account.

IV. FESHBACH MOLECULE SPECTROSCOPY

The rich energy structure of Cs_2 Feshbach molecules requires flexible methods for determining the molecular energy spectrum. Previous studies on Feshbach molecules have mostly addressed the last, most weakly bound state responsible for the respective Feshbach resonance. Molecular binding energies have been measured by applying various methods either to atomic [2,18,45,46] or to molecular samples [6,14,40,47].

In this section, we present our results on spectroscopy of weakly bound trapped molecules. We use two different techniques to measure the binding energies. Both techniques are suitable for probing weakly as well as deeply bound molecular states.

The first method (Sec. IV A) is based on a measurement of the molecular magnetic moment [14]. Magnetic moment spectroscopy is a very general method, independent of selection rules and wave-function overlap requirements. It can be

applied to any molecular state and thus is an important tool for molecular state identification. The method in particular allows us to follow and investigate the avoided level crossings between different molecular states. Transfers between different molecular states are observed as sudden changes of the magnetic moment. In this way, we are able to completely map out the molecular spectrum below the atomic scattering continuum, including three l-wave states, two of which had so far not been discovered.

The second method (Sec. IV B) uses microwave radiation to measure binding energies of trapped molecules with very high precision. We use a microwave pulse to drive a hyperfine transition from a molecular bound state to a higher molecular bound state that is associated with another channel of the electronic ground-state manifold. Rapid spontaneous dissociation loss [48] provides the spectroscopic signal.

A. Magnetic moment spectroscopy

1. Bare energy levels

We measure the molecular magnetic moment using the Stern-Gerlach effect. Optically trapped molecules are initially prepared in a single quantum state at a certain magnetic field B by following the procedure described in Sec. III. The molecular sample is then released from the trap. It starts to expand while simultaneously a vertical magnetic-field gradient $B'=\partial B/\partial z$ of typically 13 G/cm is turned on. During the time of flight, both the gravitational and the magnetic force displace the center-of-mass position of the molecular cloud along the vertical direction. The magnetic force acting on the molecules is given by

$$F_z = \mu_{\mathrm{mol}} B', \tag{2}$$

where μ_{mol} is the molecular magnetic moment. The vertical relative displacement Δz_{mol} of the molecular cloud with respect to the position after expansion at zero magnetic gradient is proportional to μ_{mol},

$$\Delta z_{\mathrm{mol}} = \frac{1}{2}\frac{\mu_{\mathrm{mol}} B'}{m_{\mathrm{mol}}} t_{\mathrm{SG}}^2, \tag{3}$$

where $m_{\mathrm{mol}}=2m_{\mathrm{at}}$ is the molecular mass and t_{SG} is the time spent by the molecules in the magnetic-field gradient during the Stern-Gerlach procedure.

To minimize uncertainties resulting from B', t_{SG}, and the spatial calibration of the imaging system, it is convenient to measure μ_{mol} relative to the well-known magnetic moment μ_{at} of the atoms. Consequently, μ_{mol} can be written as

$$\mu_{\mathrm{mol}} = \frac{\Delta z_{\mathrm{mol}}}{\Delta z_{\mathrm{at}}} 2\mu_{\mathrm{at}}, \tag{4}$$

where Δz_{at} is the measured displacement of atoms for the same B' and t_{SG}.

In previous experiments, we have determined μ_{mol} by measuring the magnetic-field gradient needed to levitate the molecules against gravity [3,14]. For each magnetic-field value B, the value of B' was adjusted to maintain the levitation condition. This method is not practical when B is changed over a wide range. In the present experiments, we measure the displacement of the molecular gas for a fixed B' and for $B'=0$.

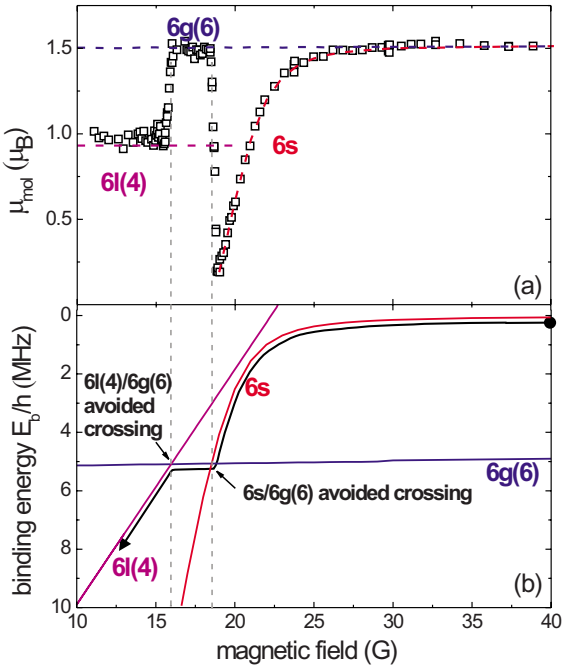

FIG. 6. (Color online) Magnetic moment of Cs dimers across the $6s$–$6g(6)$–$6l(4)$ molecular path. (a) The measured magnetic moments (open squares) are compared to the NIST calculations (dashed lines). The fast changes of the magnetic moment at 18.5 and 16 G result from the $6l(4)/6g(6)$ and $6s/6g(6)$ avoided crossings, respectively. (b) Molecular binding energies of the $6s$, $6g(6)$, and $6l(4)$ levels calculated from the NIST model; see also Fig. 1. The molecular path followed in the measurement is indicated by the black arrow.

Once the magnetic moment μ_{mol} is known as a function of B, the molecular binding energy E_b is calculated by integrating

$$\frac{\partial E_b}{\partial B} = 2\mu_{\mathrm{at}} - \mu_{\mathrm{mol}}. \tag{5}$$

The integration constant is fixed by the atomic scattering threshold where $E_b=0$. Equation (5) establishes a one-to-one correspondence between μ_{mol} and E_b at each magnetic field.

An example of a magnetic moment measurement is shown in Fig. 6. We produce $6s$ molecules from the 47.9 G resonance, as discussed in Sec. III B. We then follow the path indicated by the arrow in Fig. 6(b) and measure the molecular magnetic moment at different values of B. We observe a strong magnetic-field dependence of the magnetic moment of $6s$ molecules. Above 30 G, where the $6s$ level runs almost parallel to the atomic threshold [see Fig. 6(b)], μ_{mol} is nearly constant with a value close to $2\mu_{\mathrm{at}}$ ($=1.5\mu_B$, with Bohr's magneton μ_B, for which $\mu_B/h \approx 1.400$ MHz/G). When lowering B below 30 G, we start to observe a decrease of μ_{mol}, which drops to one-tenth of the initial value within a magnetic-field range of about 10 G. This behavior is ex-

TABLE III. Measured magnetic moment μ_{mol} of Cs_2 molecules in different internal states with the corresponding magnetic-field range. The error of μ_{mol} accounts for the statistical error and a slight change of μ_{mol} in the range considered. For each state also the theoretical magnetic moment from the NIST model is listed.

Molecular state	B (G)	μ_{mol}/μ_B Measured	μ_{mol}/μ_B NIST model
$6l(3)$	4–9	0.75(4)	0.702
	12–16	0.75(2)	0.702
$4g(4)$	5.5–12	0.95(4)	0.912
	15.5–20	0.949(6)	0.932
$6l(4)$	11–15	0.98(3)	0.931
	16–24	0.96(1)	0.931
$6s$	19	0.192	0.191
	45	1.519	1.515
$6l(5)$	15.5–23.5	1.15(3)	1.155
	26–37	1.15(2)	1.155
$4d$	41–43.2	0.39(1)	0.310
	45.5–47.1	0.36(2)	0.310
$2g$	51.7–52.2	0.05(3)	0.001
$6g(6)$	19–24	1.49(1)	1.503
	26–40	1.5(1)	1.503

plained by the strong coupling between two different $6s$ states. When further lowering the magnetic field, μ_{mol} suddenly changes from $0.19\mu_B$ to $1.5\mu_B$ as the molecules are transferred to the $6g(6)$ state via the $6s/6g(6)$ avoided crossing. The $6g(6)$ state has a nearly constant magnetic moment, slightly less than $1.5\mu_B$. Upon further lowering of B the next avoided crossing [to the state $4g(4)$, see Fig. 1] would be expected at 13.6 G [14,40]. However, μ_{mol} undergoes a rapid change to a value of about $1\mu_B$ at $\approx$16 G. This indicates the presence of a new avoided crossing and hence the presence of a new state. The existence of this state cannot be explained within the original NIST model [23,27], which includes molecular states only up to g waves. The extension of the model to higher order molecular states (Sec. II) identifies this state as a $6l(4)$ state [34].

Our method generally works well when the magnetic moment is constant. The typical error resulting from the determination of the cloud position is less than $0.03\mu_B$. Systematic errors are the result of some magnetic-field curvature. For nonconstant magnetic moment, e.g., near avoided crossings, systematic errors are introduced as a result of the cloud expansion and fall in the magnetic gradient field. The limitations are briefly discussed below.

Similar measurements have been performed for most of the molecular states in the magnetic-field range from 5 to 55 G. The results of our magnetic moment spectroscopy are summarized in Table III and the molecular energy spectrum derived using Eq. (5) is shown in Fig. 7 (open circles) along with the results of the extended NIST model (solid lines). We detect all of the s-, d-, g-, and l-wave states in the range of interest. Note that there are no i-wave states in this range. All d-, g-, and l-wave states exhibit a rather constant magnetic moment. Consequently, we find a nearly linear dependence of the binding energy on B, as shown in Fig. 7.

In Table III and Fig. 7 we compare our results with the NIST model. In general, we find good agreement with the theoretical predictions for the binding energies and magnetic moments of the s-, d-, and g-wave states. The small discrepancies observed for the lower branch of the $4g(4)$ state and for the $4d$ state probably reflect the systematic errors in de-

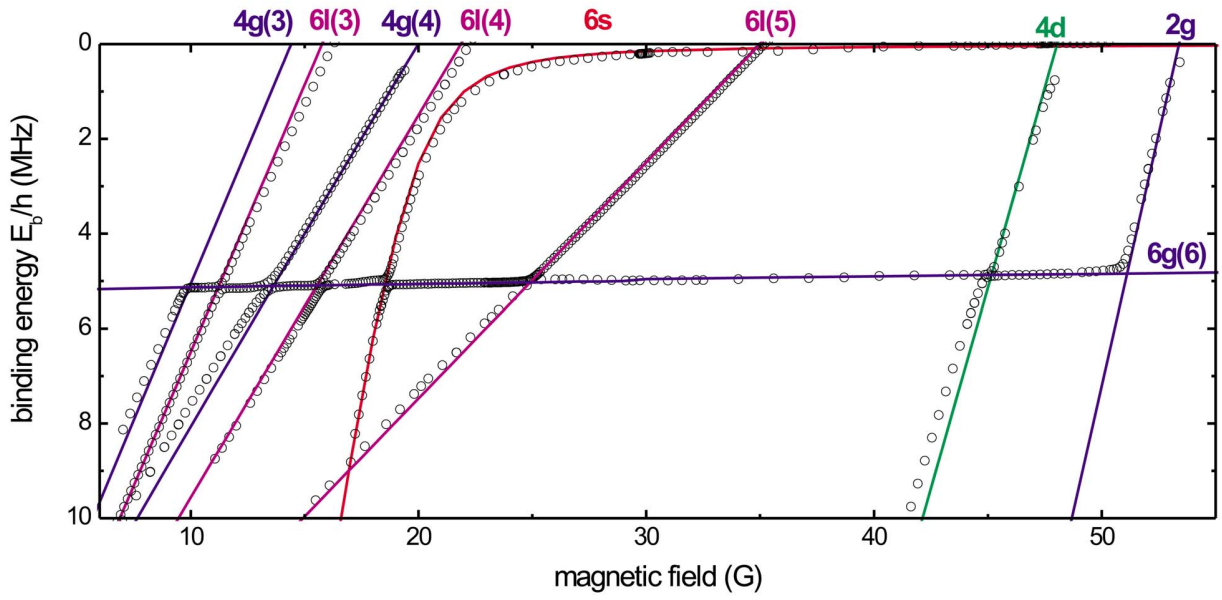

FIG. 7. (Color online) Energy spectrum of weakly bound Cs molecules as a function of the magnetic field. The binding energies for the different molecular states are derived from magnetic moment spectroscopy (open circles). The solid lines are the molecular binding energies resulting from the extended NIST model (for details see Sec. II).

termining the magnetic moment on the narrow avoided crossings.

An important result of the magnetic moment spectroscopy is the detection and characterization of three l-wave states, the states $6l(3)$, $6l(4)$, and $6l(5)$. Recently, signatures of the $6l(3)$ state have been reported in Ref. [40], whereas the other two states had so far not been discovered. In contrast to the s-, d-, and g-wave states, the l-wave states do not reveal themselves via Feshbach resonances in atomic scattering as the coupling to the atomic scattering state is too weak. Therefore, these states had previously not been included in the NIST model. The extended NIST model shows the existence of these three l-wave states and predicts their magnetic moments. Despite the accuracy for these predictions, the model is not able to precisely determine the binding energies. Our measurements now completely characterize the three l-wave states and in particular give a value for the binding energy at zero magnetic field where all three states are degenerate. We find the binding energy of the $6l$ manifold of states at zero magnetic field to be 17.61(9) MHz. In Fig. 1 and in Fig. 7 we have down-shifted the NIST prediction of the $6l$ states by $\approx$2.25 MHz to match the experimentally obtained binding energies. The measurements also locate the magnetic-field positions where the three $6l$ states intersect the atomic scattering continuum. We find the crossing positions for the $6l(3)$, $6l(4)$, and $6l(5)$ states at 16.1(2) G, 22.0(2) G, and 35.0(2) G, respectively.

2. Avoided crossings

Magnetic moment spectroscopy also allows a direct observation of the avoided crossings between different molecular states. As is well known, the coupling V between two generic molecular states, state 1 and state 2, modifies the bare energies E_1 and E_2 by opening an energy gap $2V$ at the crossing position. In the limit of a coupling strength V that is small compared to the energy separation to all other states, the avoided crossings can be studied within a simple two-state model. This model takes the two interacting bound states into account while both the couplings with the scattering continuum and with other molecular states are neglected. The coupled energy levels are given by

$$E_{\pm} = \frac{(E_1 + E_2) \pm \sqrt{(E_1 - E_2)^2 + 4V^2}}{2}. \tag{6}$$

The energies E_+ and E_- refer to the upper and lower adiabatic levels of the avoided crossing. The derivatives $-\partial E_{\pm}/\partial B$ correspond to the magnetic moments μ_+ and μ_- of the coupled states with

$$\mu_{\pm} = \frac{1}{2}(\mu_1 + \mu_2) \mp \frac{1}{2}\frac{(\mu_2 - \mu_1)^2(B - B_0)}{\sqrt{(\mu_2 - \mu_1)^2(B - B_0)^2 + 4V^2}}. \tag{7}$$

Here, B_0 is the magnetic field at the avoided-crossing position, and μ_1 and μ_2 are the magnetic moments of the two bare molecular states.

In the following we focus on the avoided crossings between the $6g(6)$ state and the other $f\ell(m_f)$ states. Figure 8 shows the magnetic moments μ_+ (circles) and μ_- (triangles) across the $6g(6)/4g(4)$ avoided crossing. To derive the coupling strength between these two states, we fit our data using Eq. (7) by leaving μ_1, μ_2, B_0, and V as free parameters. The same procedure is adopted to analyze the other crossings. The coupling strengths and the avoided crossing positions are listed in Table IV. For comparison, we include in Table IV measurements of V obtained with other techniques, such as the Landau-Zener method discussed below, a magnetic levitation method [14], and an interferometric method [40].

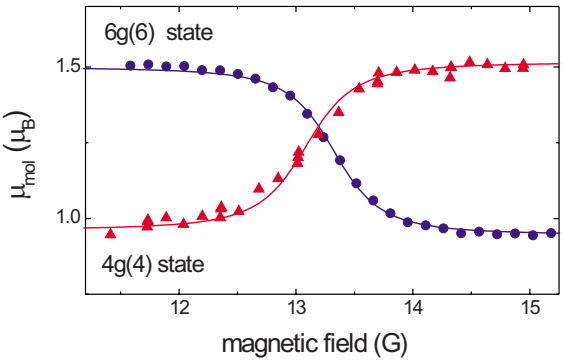

FIG. 8. (Color online) Magnetic moments of Cs dimers across the $6g(6)/4g(4)$ avoided crossing. Both the change in magnetic moment from the $6g(6)$ to the $4g(4)$ state (circles) and the one from the $4g(4)$ to the $6g(6)$ state (triangles) are shown. The measured magnetic moments are fitted using Eq. (7) (solid lines).

In Fig. 9 we plot the measured coupling strengths V between the $6g(6)$ state and the other intersecting states as a function of the difference in orbital angular momentum $|\Delta\ell|$. While the $6g(6)/4g(4)$ and the $6g(6)/4d$ crossings are the result of the first-order spin-spin dipole interaction, the crossings with the l-wave states are second order. As a general trend, crossings with larger $|\Delta\ell|$ tend to have a weaker coupling.

Systematic errors in our avoided crossing measurements stem from the finite size of the molecular cloud and the change of μ_{mol} during the freefall and expansion in the presence of the magnetic-field gradient. This effect causes a smoothening of the rapid magnetic moment changes (see

TABLE IV. Avoided crossing positions B_0 and coupling strengths V/h between the $6g(6)$ state and the intersecting $f\ell(m_f)$ molecular states obtained by fitting the measured magnetic moments with Eq. (7). The errors are the 1σ statistical uncertainties. V/h measured with different techniques are also reported (see table footnotes).

$f\ell(m_f)$	B_0 (G)	V/h (kHz)	
$6l(3)$	11.22(2)		16(3)[a], 14(1)[b]
$4g(4)$	13.29(4)	164(30)	150(10)[c]
$6l(4)$	15.50(3)	64(13)[d]	
$6l(5)$	25.3(1)	63(22)[d]	
$4d$	45.15(4)	120(21)	

[a]Landau-Zener method.
[b]Interferometric method [40].
[c]Magnetic levitation method [14].
[d]The values should be considered as upper limits.

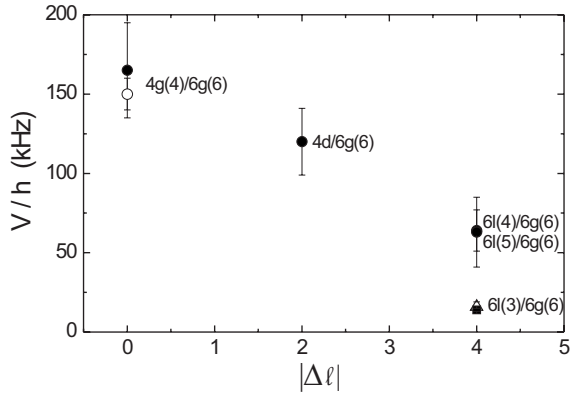

FIG. 9. Coupling strengths V/h between the $6g(6)$ state and the intersecting $f\ell(m_f)$ molecular states as a function of the difference of their orbital angular momentum quantum numbers, $|\Delta\ell|$. The data refer to the values obtained via the magnetic moment spectroscopy (filled circles), a magnetic levitation method (empty circle) [14], an interferometer method (square) [40], and the Landau-Zener method (triangle).

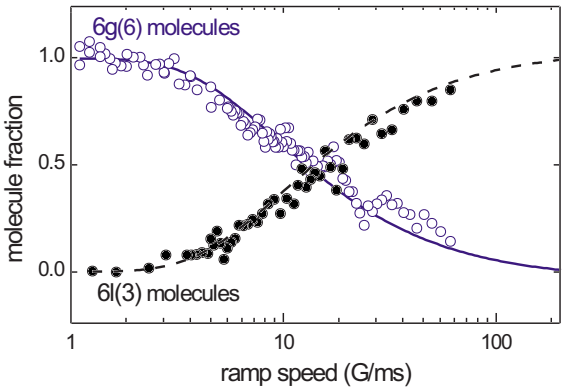

FIG. 10. (Color online) Conversion efficiency on the $6g(6)/6l(3)$ avoided crossing as a function of the ramp speed. A pure sample of $6l(3)$ molecules is partially transferred into the $6g(6)$ state at different ramp speeds. We measure either the fraction of transferred $6g(6)$ molecules (open circles) or the fraction of nonconverted $6l(3)$ molecules (filled circles). The solid line refers to the Landau-Zener formula for p given by Eq. (8), while the dashed line is $1-p$.

Fig. 6) and hence an apparent broadening of the avoided crossings and leads to an overestimation of the coupling strengths, in particular for the narrower crossings. We find a limit on the minimum coupling strength that can be extracted with reasonable precision. We estimate from simulations that coupling strengths below $h\times 50$ kHz can no longer be sensitively measured with our present method.

An alternative method to determine the coupling strengths of avoided crossings is based on the Landau-Zener tunneling model [41,42,49], already discussed in Sec. III C. Equation (1) shows a quadratic dependence of the critical ramp speed r_c on the coupling strength V. The probability to transfer molecules from one bare state to the next in a single passage through the avoided crossing is given by the well-known Landau-Zener formula [41,42]

$$p = 1 - \exp(-r_c/\dot{B}), \tag{8}$$

where $\dot{B}$ is the ramp speed.

As an example, we apply this method to the $6g(6)/6l(3)$ avoided crossing. We measure the conversion efficiency of molecules from the $6l(3)$ state below the crossing to the $6g(6)$ state by sweeping the magnetic field across the $6g(6)/6l(3)$ crossing at various ramp speeds $\dot{B}$. The results are shown in Fig. 10. For $\dot{B}\ll r_c$, the molecules are adiabatically transferred to the $6g(6)$ state (open circles) whereas, for $\dot{B}\gg r_c$, they end up in the $6l(3)$ state above the crossing. The conversion efficiency is measured by detecting the $6g(6)$ molecules (open circles) and also by detecting the $6l(3)$ molecules (filled circles). By fitting our data with Eq. (8), we estimate the coupling strength of the $6l(3)/6g(6)$ crossing to be $V=h\times 16(3)$ kHz. This value is consistent with the result of 14(1) kHz obtained in Ref. [40] using a more precise interferometric technique.

B. Microwave spectroscopy

Molecules in the $6s$ state (see Fig. 1) are of particular interest as *quantum-halo* states [50]. Halo states are extremely weakly bound dimers characterized by a large interatomic separation that greatly exceeds the van der Waals length r_0 (for Cs, $r_0\simeq 101a_0$) and by a binding energy much smaller than the van der Waals energy (for Cs, $\hbar^2/mr_0^2\approx h\times 2.708$ MHz) [1]. These states are universal in the sense that they are fully characterized by a large atomic s-wave scattering length a. In particular, the wave function does not depend on the microscopic details of the scattering potential. The precise knowledge of the $6s$ state is crucial for understanding universal two-body physics and for studying universal three-body Efimov-type states [15].

We detect molecular transitions induced by microwave radiation to probe the binding energy of the $6s$ molecules. The relevant atomic states are the lowest hyperfine state $|F=3,m_F=3\rangle$ and the doubly polarized state $|F=4,m_F=4\rangle$. Figure 11(a) shows the energy level structure of the two scattering channels $|F=3,m_F=3\rangle+|F=3,m_F=3\rangle$ and $|F=3,m_F=3\rangle+|F=4,m_F=4\rangle$. The bound states involved in the molecular transition are the $6s$ state and a $7s$ state that lies slightly below the atomic scattering channel $|F=3,m_F=3\rangle+|F=4,m_F=4\rangle$.

The weakly bound $7s$ state is directly related to the large triplet scattering length a_T that dominates the $|F=3,m_F=3\rangle+|F=4,m_F=4\rangle$ scattering channel. The Cs triplet scattering length, predicted by the NIST model, is $(2400\pm 100)a_0$, and consequently the $7s$ state has a small binding energy of $E_b'=\hbar^2/ma_T^2\approx h\times 5$ kHz.

We map out the binding energy of the $6s$ molecules by measuring the transition frequency ν_{mol} from the $6s$ to the $7s$ state as a function of B. The binding energy is then given by

$$E_b(B) = h[\nu_{\mathrm{mol}}(B) - \nu_{\mathrm{at}}(B)] + E_b', \tag{9}$$

where $\nu_{\mathrm{at}}(B)$ is the $|F=3,m_F=3\rangle\rightarrow|F=4,m_F=4\rangle$ atomic transition, which follows the Breit-Rabi formula and is used

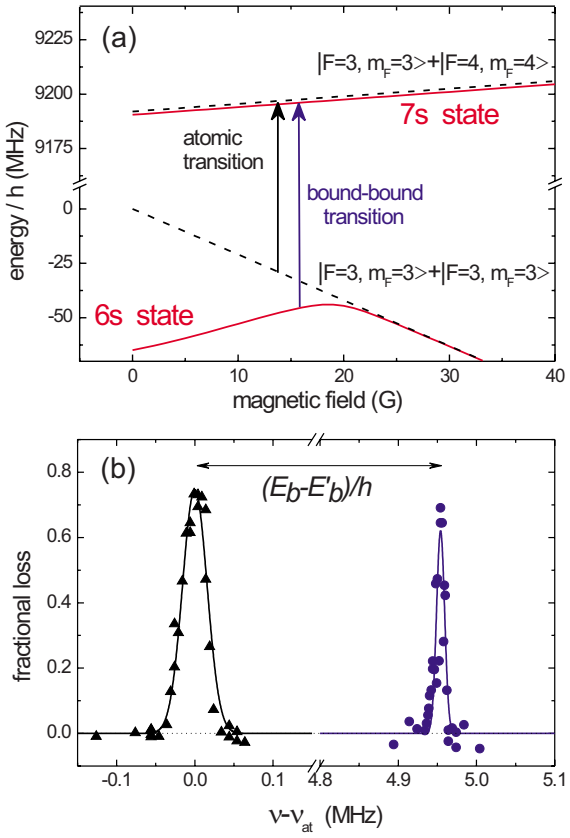

FIG. 11. (Color online) Microwave spectroscopy of Cs dimers. (a) A bound-bound transition is driven from the $6s$ state to a $7s$ state slightly below the $|F=3,m_F=3\rangle+|F=4,m_F=4\rangle$ scattering channel, as illustrated by the longer arrow. The $7s$ state is offset from the scattering channel for clarity. The frequency corresponding to the $|F=3,m_F=3\rangle\rightarrow|F=4,m_F=4\rangle$ atomic transition at zero field is $\nu_{\mathrm{at}}\approx 9.193$ G Hz. (b) Microwave spectrum of atoms (triangles) and $6s$ molecules (dots) at $B\approx 18.7$ G as a function of the frequency offset $\nu-\nu_{\mathrm{at}}$. The molecular transition corresponds to a sharp loss resonance. We determine the center position to be 4.9545(3) MHz and the resonance width to 12(3) kHz from a Gaussian fit (solid line).

here as a frequency reference. In our experiment, we again start with optically trapped $6s$ molecules at some magnetic field B. A microwave pulse of typically 5 ms duration drives the bound-bound transition, and partially transfers molecules from the $6s$ state to the $7s$ state. We then hold the sample in the trap for 10 ms and we detect the total number of remaining molecules using the techniques described in Sec. III D. We perform similar measurements at different magnetic fields to recover E_b within the magnetic-field range of investigation.

As a frequency reference, we measure $\nu_{\mathrm{at}}(B)$ on a trapped sample of 4×10^5 Cs atoms at $T\approx 200$ nK, initially prepared in the hyperfine ground state $|F=3,m_F=3\rangle$. For each B, we apply a microwave pulse resonant to the $|F=3,m_F=3\rangle\rightarrow|F=4,m_F=4\rangle$ hyperfine transition. The atoms are then detected after a holding time in the trap of typically 100 ms. The microwave excitation results in resonant loss from the atomic sample.

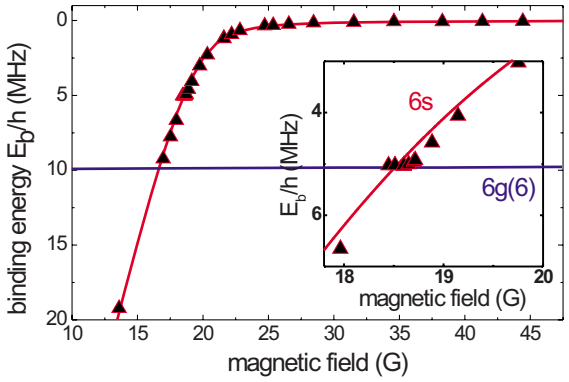

FIG. 12. (Color online) Binding energy of the $6s$ molecules as a function of the magnetic field (triangles). The binding energies correspond to the measured frequency shift from the expected $|F=3,m_F=3\rangle\rightarrow|F=4,m_F=4\rangle$ atomic transition [see Eq. (9)]. The statistical errors are about 1 kHz, i.e., much smaller than the data symbol size. The solid line is the result of the NIST model. The inset is an expanded view of the binding energy in the proximity of the $6s/6g(6)$ avoided crossing.

The particle losses observed in both the atomic and the molecular sample are the result of hyperfine spin relaxation [48,51]. In the atomic case, the relaxation is driven by the binary collision of two free atoms, while in the molecular case it can be considered as being driven by a collision within the molecule [51], leading to spontaneous dissociation. In any case, one of the atoms is subject to a spin flip, releasing the hyperfine energy that greatly exceeds the trap depth and leading to trap loss. According to the NIST model, the $7s$ state is coupled to several possible decay channels, causing a decay width of the state of $\sim 2\pi\times 70$ Hz [34]. We in fact observe a decay of $7s$ molecules on a time scale of a few ms. In the case of Cs atoms in the $|F=3,m_F=3\rangle+|F=4,m_F=4\rangle$ scattering channel, we measure a lifetime of ~ 50 ms consistent with the predicted two-body loss coefficient of 5×10^{-12} cm^3/s [34].

A typical microwave spectrum for both atoms and molecules is shown in Fig. 11(b). The resonant frequencies and the linewidths are determined by fitting the data with Gaussian profiles. The molecular transition shows a narrow and symmetric loss resonance. From the fit, we find a linewidth of 12(3) kHz. This value is close to our experimental resolution of ~ 10 kHz, essentially resulting from magnetic-field fluctuations. As demonstrated in Refs. [47,52], the symmetry of line shape indicates that a bound-bound transition occurs, even in the presence of magnetic-field broadening. We cannot distinguish bound-bound from possible bound-free transitions due to the small energy difference between the $|F=3,m_F=3\rangle+|F=4,m_F=4\rangle$ scattering channel and the $7s$ state. However, we believe that the bound-bound transition dominates as the transition probability for a bound-free transition is expected to be much weaker due to the smaller Franck-Condon overlap between the initial and final state [52].

Figure 12 shows the binding energies of $6s$ molecules in a magnetic-field range from 12 to 45 G together with the predictions from the NIST model. The inset shows an expanded

view of the binding energy in the proximity of the $6s/6g(6)$ avoided crossing at around 18.5 G. We observe an increase of the microwave power needed to drive the bound-bound transition when the avoided crossing is approached. The $6s$ and $6g(6)$ states couple and the molecules are in a dressed state. A microwave pulse can drive molecular transitions that change the total angular momentum f and its projection m_f, while the orbital momentum ℓ must be conserved. The bound-bound transition between the $6g(6)$ and the $7s$ state with $\Delta\ell=4$ is hence forbidden.

The microwave measurements on the $6s$ state provide precise binding energies of up to about $h\times 20$ MHz. Higher binding energies can in principle be accessed by further lowering the magnetic field. The comparison between our results and the NIST model generally shows very good agreement. We have observed small deviations between theory and experiment when the $6s$ state starts to bend toward larger binding energies (see inset of Fig. 12). This deviation suggests that the $6s$ state is perturbed by the coupling to other molecular states. Our data provide high precision input for further refinements of the NIST model.

V. CONCLUSION

We have explored the rich internal structure of weakly bound Cs_2 Feshbach molecules, prepared in a CO_2-laser trap. Magnetically induced association based on three different Feshbach resonances served as the entrance door into the manifold of molecular states. We have developed a set of methods to transfer molecules to various internal states, to clean the population in the optical trap from remaining atoms and from molecules in unwanted states, and to detect the molecular population via controlled dissociation. In particular, we have investigated so far unexplored l-wave states, for which direct Feshbach association is not possible because of negligible coupling to atomic scattering states.

We have determined the binding energy spectrum using two different techniques. Magnetic moment spectroscopy has been demonstrated as a versatile and sensitive method to detect molecular states. It shows avoided crossings between different molecular states and reveals the presence of higher partial-wave states. Using this technique we have mapped out the molecular spectrum up to binding energies of $E_b/h=10$ MHz and in a magnetic-field range from 5 to 55 G. Using microwave spectroscopy, we have performed highly precise measurements of the binding energy of a particularly important s-wave state above 13 G, where $E_b/h<20$ MHz. The results show how this state, which essentially determines the s-wave scattering length, evolves into a weakly bound state with quantum-halo character. These results are important for applications of this s-wave state to universal few-body quantum physics, such as the exploration of Efimov states.

Our measurements provide a sensitive test for the theoretical NIST model, which was developed to describe quantum scattering phenomena of Cs atoms. We could confirm the basic predictions of this model on the weakly bound molecular structure. The exploration of l-wave states and highly precise measurements on a weakly bound s-wave state provide experimental input for further refinements of the NIST model.

In a broader perspective, our work demonstrates general ways to manipulate Feshbach molecules through elaborate magnetic-field control. This extends the experimental toolbox available for the preparation of homonuclear and heteronuclear ultracold molecules in desired internal states.

ACKNOWLEDGMENTS

The authors thank E. Tiesinga, P. Julienne, and C. Williams for providing invaluable theoretical input and J. Hutson and A. Simoni for helpful discussions. The authors acknowledge support by the Austrian Science Fund (FWF) within SFB 15 (project part 16) and by the European Union within the Cold Molecules TMR Network under Contract No. HPRN-CT-2002-00290. One of the authors (M.M.) acknowledges support within the Ph.D. program DOC of the Austrian Academy of Sciences, and two of the authors (F.F., C.C.) acknowledge support within the Lise Meitner program of the FWF. One of the authors (S.K.) is supported by the European Community, Marie Curie Intra-European program.

APPENDIX: MAGNETIC-FIELD SETUP AND CALIBRATION

The experiments with ultracold Cs molecules are performed in a 12-sided polygonal stainless-steel vacuum chamber with large reentrant viewports on top and bottom for maximum optical access along the vertical axis [53]. The CO_2-laser light is brought in along the horizontal plane through special ZnSe viewports. On the 12 sides of the polygon, there are in total four pairwise opposite viewports for the CO_2-laser light and six pairwise opposite viewports for the near-infrared laser cooling and trapping light, and for imaging. The two remaining opposite openings are reserved for the atomic beam, the Zeeman slowing laser beam, and the vacuum pumps. The total magnetic field is produced by several sets of coils, some mounted on the steel chamber, others placed inside the reentrant viewports closer to the trap center, but still outside the vacuum. The presence of the metal limits the magnetic-field switching times as a result of eddy currents. Nevertheless, we achieve a maximum of experimental flexibility by combining the larger fields of the bigger coils with the more rapidly switchable fields of the smaller coils inside the viewports.

1. Bias field

The vertical offset field for molecule production and manipulation is created by a pair of water cooled coils with a mean radius of 66 mm in approximate Helmholtz configuration. The coils are placed inside the reentrant viewports along the rim of the windows. They allow a magnetic field of up to 60 G for dc operation with a typical $1/e$ switching time of 1.5 ms. The current from a programmable power supply is servo-loop controlled. A second pair of large coils with a mean radius of 112.5 mm is attached to the outside of the flanges that hold the reentrant viewports and can provide an additional dc field of up to 200 G.

For the molecule transfer schemes as described in Sec. III, one further set of air cooled coils and a single "booster-coil" are used inside the reentrant viewport: A pair of coils in approximate Helmholtz configuration with a radius of 44 mm is mounted on plastic holders near the vacuum window as close to the trap center as possible. The coils with a servo-loop controlled current produce a magnetic field of up to 10 G, while the $1/e$ switching time is $\sim 300\ \mu$s. As a result, ramp speeds in the range of 30 G/ms can be achieved. The fastest magnetic-field changes are realized by a small, single "booster" coil with only four windings and a radius of 24 mm at a distance of ~ 30 mm to the trap center placed inside the top reentrant viewport. Using a capacitor bench and servo-loop control for the current we achieve magnetic-field pulses with amplitudes of up to 7 G. The maximum pulse duration of 1 ms is sufficiently long to adjust the offset field of the other coils within this time. With a typical switching time of 400 ns we achieve ramp speeds of up to 17 000 G/ms. To change the ramp speed we vary the pulse amplitude as the rise-time cannot be adjusted. The coupling of ramp speed and pulse amplitude is somewhat problematic. It limits the possible ramp speeds at certain avoided crossings, because too large pulse amplitudes can produce uncontrolled ramps over other avoided crossings nearby. Note that the booster coil also produces a magnetic-field gradient. However, this gradient is irrelevant for the experiments reported here.

The relative stability of the servo-loop controllers is about 10^{-5} and thus well below the ambient magnetic line noise (~ 10 mG).

2. Gradient field

The magnetic gradient field is produced by a pair of water cooled coils in approximate anti-Helmholtz configuration. These coils with a radius of 66 mm are also placed inside the reentrant viewports. They allow a dc-gradient field of up to 80 G/cm. Large field gradients can be switched within ~ 3 ms, limited by eddy currents. For small gradients such as 13 G/cm, as used in the magnetic moment spectroscopy measurements, we measure somewhat lower magnetic switching times of ~ 1 ms.

3. Magnetic-field calibration

To calibrate the magnetic field we use the microwave technique on a trapped atomic sample as described in Sec. IV B. We use the Breit-Rabi formula to determine the magnetic-field value from a measurement of the atomic hyperfine transition frequency between the states $|F=3, m_F=3\rangle \rightarrow |F=4, m_F=4\rangle$. Line noise limits the stability of the magnetic field to about 10 mG for typical integration times.

[1] T. Köhler, K. Góral, and P. S. Julienne, Rev. Mod. Phys. **78**, 1311 (2006).

[2] E. A. Donley, N. R. Clausen, S. T. Thompson, and C. E. Wieman, Nature (London) **417**, 529 (2002).

[3] J. Herbig, T. Kraemer, M. Mark, T. Weber, C. Chin, H.-C. Nägerl, and R. Grimm, Science **301**, 1510 (2003).

[4] S. Dürr, T. Volz, A. Marte, and G. Rempe, Phys. Rev. Lett. **92**, 020406 (2004).

[5] K. Xu, T. Mukaiyama, J. R. Abo-Shaeer, J. K. Chin, D. E. Miller, and W. Ketterle, Phys. Rev. Lett. **91**, 210402 (2003).

[6] C. A. Regal, C. Ticknor, J. L. Bohn, and D. S. Jin, Nature (London) **424**, 47 (2003).

[7] K. E. Strecker, G. B. Partridge, and R. G. Hulet, Phys. Rev. Lett. **91**, 080406 (2003).

[8] J. Cubizolles, T. Bourdel, S. J. J. M. F. Kokkelmans, G. V. Shlyapnikov, and C. Salomon, Phys. Rev. Lett. **91**, 240401 (2003).

[9] S. Jochim, M. Bartenstein, A. Altmeyer, G. Hendl, C. Chin, J. H. Denschlag, and R. Grimm, Phys. Rev. Lett. **91**, 240402 (2003).

[10] S. Jochim, M. Bartenstein, A. Altmeyer, G. Hendl, S. Riedl, C. Chin, J. H. Denschlag, and R. Grimm, Science **302**, 2101 (2003).

[11] M. Greiner, C. A. Regal, and D. S. Jin, Nature (London) **426**, 537 (2003).

[12] M. W. Zwierlein, C. A. Stan, C. H. Schunck, S. M. F. Raupach, S. Gupta, Z. Hadzibabic, and W. Ketterle, Phys. Rev. Lett. **91**, 250401 (2003).

[13] *Ultracold Fermi Gases*, edited by M. Inguscio, W. Ketterle, and C. Salomon, Proceedings of the International School of Physics "Enrico Fermi," Course CLXIV, Varenna, 2006 (IOS, Amsterdam, 2007).

[14] C. Chin, T. Kraemer, M. Mark, J. Herbig, P. Waldburger, H.-C. Nägerl, and R. Grimm, Phys. Rev. Lett. **94**, 123201 (2005).

[15] T. Kraemer *et al.*, Nature (London) **440**, 315 (2006).

[16] T. Stöferle, H. Moritz, K. Günter, M. Köhl, and T. Esslinger, Phys. Rev. Lett. **96**, 030401 (2006).

[17] G. Thalhammer, K. Winkler, F. Lang, S. Schmid, R. Grimm, and J. H. Denschlag, Phys. Rev. Lett. **96**, 050402 (2006).

[18] C. Ospelkaus, S. Ospelkaus, L. Humbert, P. Ernst, K. Sengstock, and K. Bongs, Phys. Rev. Lett. **97**, 120402 (2006).

[19] K. Winkler, G. Thalhammer, F. Lang, R. Grimm, J. Hecker Denschlag, A. J. Daley, A. Kantian, H. P. Büchler, and P. Zoller, Nature (London) **441**, 853 (2006).

[20] T. Volz, N. Syassen, D. Bauer, E. Hansis, S. Dürr, and G. Rempe, Nat. Phys. **2**, 692 (2006).

[21] E. Tiesinga, B. J. Verhaar, and H. T. C. Stoof, Phys. Rev. A **47**, 4114 (1993).

[22] S. Inouye, M. R. Andrews, J. Stenger, H.-J. Miesner, S. M. Stamper-Kurn, and W. Ketterle, Nature (London) **392**, 151 (1998).

[23] C. Chin, V. Vuletic, A. J. Kerman, S. Chu, E. Tiesinga, P. J. Leo, and C. J. Williams, Phys. Rev. A **70**, 032701 (2004).

[24] T. Weber, J. Herbig, M. Mark, H.-C. Nägerl, and R. Grimm, Science **299**, 232 (2003).

[25] V. Vuletić, A. J. Kerman, C. Chin, and S. Chu, Phys. Rev. Lett. **82**, 1406 (1999).

[26] C. Chin, V. Vuletić, A. J. Kerman, and S. Chu, Phys. Rev. Lett.

85, 2717 (2000).
[27] P. J. Leo, C. J. Williams, and P. S. Julienne, Phys. Rev. Lett. **85**, 2721 (2000).
[28] T. Takekoshi, B. M. Patterson, and R. J. Knize, Phys. Rev. Lett. **81**, 5105 (1998).
[29] P. Staanum, S. D. Kraft, J. Lange, R. Wester, and M. Weidemüller, Phys. Rev. Lett. **96**, 023201 (2006).
[30] N. Zahzam, T. Vogt, M. Mudrich, D. Comparat, and P. Pillet, Phys. Rev. Lett. **96**, 023202 (2006).
[31] H. N. Russell, A. G. Shenstone, and L. A. Turner, Phys. Rev. **33**, 900 (1929).
[32] F. H. Mies, C. J. Williams, P. S. Julienne, and M. Krauss, J. Res. Natl. Inst. Stand. Technol. **101**, 521 (1996).
[33] B. Gao, Phys. Rev. A **62**, 050702(R) (2000).
[34] E. Tiesinga and P. S. Julienne (private communication).
[35] T. Kraemer, J. Herbig, M. Mark, T. Weber, C. Chin, H.-C. Nägerl, and R. Grimm, Appl. Phys. B: Lasers Opt. **B79**, 1013 (2004).
[36] P. Treutlein, K. Y. Chung, and S. Chu, Phys. Rev. A **63**, 051401(R) (2001).
[37] T. Weber, J. Herbig, M. Mark, H.-C. Nägerl, and R. Grimm, Phys. Rev. Lett. **91**, 123201 (2003).
[38] M. Mark, T. Kraemer, J. Herbig, C. Chin, H.-C. Nägerl, and R. Grimm, Europhys. Lett. **69**, 706 (2005).
[39] T. Mukaiyama, J. R. Abo-Shaeer, K. Xu, J. K. Chin, and W. Ketterle, Phys. Rev. Lett. **92**, 180402 (2004).
[40] M. Mark, T. Kraemer, P. Waldburger, J. Herbig, C. Chin, H.-C. Nägerl, and R. Grimm, Phys. Rev. Lett. **99**, 113201 (2007).
[41] L. Landau, Phys. Z. Sowjetunion **2**, 46 (1932).
[42] C. Zener, Proc. R. Soc. London, Ser. A **137**, 696 (1932).
[43] S. Dürr, T. Volz, and G. Rempe, Phys. Rev. A **70**, 031601(R) (2004).
[44] S. Knoop, M. Mark, F. Ferlaino, J. G. Danzl, T. Kraemer, H.-C. Nägerl, and R. Grimm (unpublished).
[45] N. R. Claussen, S. J. J. M. F. Kokkelmans, S. T. Thompson, E. A. Donley, E. Hodby, and C. E. Wieman, Phys. Rev. A **67**, 060701(R) (2003).
[46] S. T. Thompson, E. Hodby, and C. E. Wieman, Phys. Rev. Lett. **95**, 190404 (2005).
[47] M. Bartenstein, A. Altmeyer, S. Riedl, R. Geursen, S. Jochim, C. Chin, J. H. Denschlag, R. Grimm, A. Simoni, E. Tiesinga, C. J. Williams, and P. S. Julienne, Phys. Rev. Lett. **94**, 103201 (2005).
[48] S. T. Thompson, E. Hodby, and C. E. Wieman, Phys. Rev. Lett. **94**, 020401 (2005).
[49] P. S. Julienne, E. Tiesinga, and T. Köhler, J. Mod. Opt. **513**, 1787 (2004).
[50] A. S. Jensen, K. Riisager, D. V. Fedorov, and E. Garrido, Rev. Mod. Phys. **76**, 215 (2004).
[51] T. Köhler, E. Tiesinga, and P. S. Julienne, Phys. Rev. Lett. **94**, 020402 (2005).
[52] C. Chin and P. S. Julienne, Phys. Rev. A **71**, 012713 (2005).
[53] T. Weber, Ph.D. thesis, University of Innsbruck, 2003, www.ultracold.at/theses

"Stückelberg Interferometry" with Ultracold Molecules

M. Mark,[1] T. Kraemer,[1] P. Waldburger,[1] J. Herbig,[1] C. Chin,[1,3] H.-C. Nägerl,[1] and R. Grimm[1,2]

[1]*Institut für Experimentalphysik und Forschungszentrum für Quantenphysik, Universität Innsbruck, 6020 Innsbruck, Austria*
[2]*Institut für Quantenoptik und Quanteninformation, Österreichische Akademie der Wissenschaften, 6020 Innsbruck, Austria*
[3]*Physics Department and James Franck Institute, University of Chicago, Chicago, Illinois 60637, USA*

(Received 4 April 2007; published 11 September 2007)

We report on the realization of a time-domain ''Stückelberg interferometer'', which is based on the internal-state structure of ultracold Feshbach molecules. Two subsequent passages through a weak avoided crossing between two different orbital angular momentum states in combination with a variable hold time lead to high-contrast population oscillations. This allows for a precise determination of the energy difference between the two molecular states. We demonstrate a high degree of control over the interferometer dynamics. The interferometric scheme provides new possibilities for precision measurements with ultracold molecules.

DOI: 10.1103/PhysRevLett.99.113201 PACS numbers: 34.50.−s, 05.30.Jp, 32.80.Pj, 67.40.Hf

The creation of molecules on Feshbach resonances in atomic quantum gases has opened up a new chapter in the field of ultracold matter [1]. Molecular quantum gases are now readily available in the lab for various applications. Prominent examples are given by the creation of strongly interacting many-body systems based on molecular Bose-Einstein condensates [2], experiments on few-body collision physics [3], the realization of molecular matter-wave optics [4], and by the demonstration of exotic pairs in optical lattices [5]. Recent experimental progress has shown that full control over all degrees of freedom can be expected for such molecules [6–8]. Ultracold molecular samples with very low thermal spread and long interaction times could greatly increase the sensitivity in measurements of fundamental physical properties such as the existence of an electron dipole moment [9] and a possible time variation of the fine-structure constant [10,11].

Most of today's most accurate and precise measurements rely on interferometric techniques applied to ultracold atomic systems. For example, long coherence times in atomic fountains or in optical lattices allow ultraprecise frequency metrology [12,13]. Molecules, given their rich internal structure, greatly extend the scope of possible precision measurements. Molecular clocks, for example, may provide novel access to fundamental constants and interaction effects, different from atomic clocks. The fast progress in preparing cold molecular samples thus opens up fascinating perspectives for precision interferometry. Recently, the technique of Stark deceleration has allowed a demonstration of Ramsey interferometry with a cold and slowed molecular beam [10]. Ultracold trapped molecular ensembles are expected to further enhance the range of possible measurements.

In this Letter, we report on the realization of an internal-state interferometer with ultracold Cs_2 molecules. A weak avoided crossing is used as a ''beam splitter'' for molecular states as a result of partial Landau-Zener tunneling when it is traversed by means of an appropriately chosen magnetic-field ramp. Using the avoided crossing twice, first for splitting, and then for recombination of molecular states, leads to the well-known Stückelberg oscillations [14]. We thus call our scheme a Stückelberg interferometer. Our realization of this interferometer allows full control over the interferometer dynamics. In particular, the hold time between splitting and recombination can be freely chosen. In analogy to the well-known Ramsey interferometer [15] the acquired interferometer phase is mapped onto the relative populations of the two output states that can be well discriminated upon molecular dissociation. To demonstrate the performance of the Stückelberg interferometer we use it for precision molecular spectroscopy to determine the position and coupling strength of the avoided crossing.

The energy structure of weakly bound Cs_2 dimers in the relevant range of low magnetic-field strength is shown in Fig. 1 [16]. Zero binding energy corresponds to the threshold of dissociation into two free Cs atoms in the lowest hyperfine sublevel $|F = 3, m_F = 3\rangle$ and thus to the zero-energy collision limit of two atoms. The states relevant for this work are labeled by $|g\rangle$, $|g'\rangle$, and $|l\rangle$ [17]. While $|g\rangle$ and $|g'\rangle$ are g-wave states with orbital angular momentum $\ell = 4$, the state $|l\rangle$ is an l-wave state with a high orbital angular momentum of $\ell = 8$ [18]. Coupling with $\Delta\ell = 4$ between s-wave atoms and g-wave molecules and between g- and l-wave states is a result of the strong indirect spin-spin interaction between two Cs atoms [16].

The starting point for our experiments is a Bose-Einstein condensate (BEC) with $\sim 2 \times 10^5$ Cs atoms in the $|F = 3, m_F = 3\rangle$ ground state confined in a crossed-beam dipole trap generated by a broadband fiber laser with a wavelength near 1064 nm [19,20]. The BEC allows us to efficiently produce molecules on a narrow Feshbach resonance at 19.84 G [21] in an optimized scheme as described in Ref. [22]. With an efficiency of typically 25% we produce a pure molecular ensemble with up to 2.5×10^4 ultracold molecules all in state $|g\rangle$, initially close to quantum degeneracy [21]. The following experiments are performed on the molecular ensemble in free fall. During the

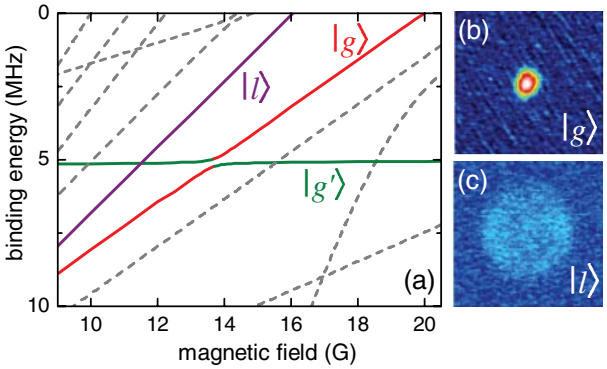

FIG. 1 (color online). (a) Molecular energy structure below the dissociation threshold showing all molecular states up $\ell = 8$. The relevant states for the present experiment (solid lines) are labeled $|g\rangle$, $|g'\rangle$, and $|l\rangle$. Molecules in state $|g\rangle$ or $|l\rangle$ are detected upon dissociation as shown in (b) and (c). The crossing used for the interferometer is the one between $|g'\rangle$ and $|l\rangle$ near 11.4 G. Initially, ultracold molecules are generated in state $|g\rangle$ on the Feshbach resonance at 19.8 G.

initial expansion to a $1/e$-diameter of about 28 μm along the radial and about 46 μm along the axial direction, the peak density is reduced to 1×10^{11} cm^{-3} so that molecule-molecule interactions [3] can be neglected on the time scale of the experiment.

The molecules can now be transferred to any one of the molecular states shown in Fig. 1 with near 100% efficiency by controlled "jumping" or adiabatic following at the various crossings [23]. When the magnetic-field strength is decreased, the molecules first encounter the crossing at 13.6 G. At all ramp rates used in our present experiments the passage through this crossing takes place in a fully adiabatic way. The molecules are thus transferred from $|g\rangle$ to $|g'\rangle$ along the upper branch of the crossing. They then encounter the next crossing at a magnetic field of $B_c \approx 11.4$ G. We accidentally found this weak crossing in our previous magnetic moment measurements [3,23]. This allowed the identification of the l-wave state $|l\rangle$ [18].

This crossing between $|g'\rangle$ and $|l\rangle$ plays a central role in the present experiment. It can be used as a tunable "beam splitter", which allows adiabatic transfer, coherent splitting, as will be shown below, or diabatic transfer for the molecular states involved, depending on the chosen magnetic ramp rate near the crossing. We find that a critical ramp rate of $R_c \approx 14$ G/ms leads to a 50/50-splitting into $|g'\rangle$ and $|l\rangle$ [23]. Using the well-known Landau-Zener formula and an estimate for the difference in magnetic moment for states $|g'\rangle$ and $|l\rangle$ [18] we determine the coupling strength V between $|g'\rangle$ and $|l\rangle$, defined as half the energy splitting, to $\sim h \times 15$ kHz.

We state-selectively detect the molecules by ramping up the magnetic field to bring the molecules above the threshold for dissociation. There the quasibound molecules decay into the atomic scattering continuum. For state $|g\rangle$, dissociation is observed for magnetic fields above the 19.84 G position of the corresponding Feshbach resonance. Figure 1(b) shows a typical absorption image of the resulting atom cloud [21]. For state $|l\rangle$ dissociation is observed above 16.5 G. The molecular states can thus be easily discriminated by the different magnetic-field values needed for dissociation. Moreover, the expansion pattern is qualitatively different from the one connected to state $|g\rangle$. The absorption image in Fig. 1(c) shows an expanding "bubble" of atoms with a relatively large kinetic energy of about $k_B \times 20$ μK per atom. Here, k_B is Boltzmann's constant. We find that significant dissociation occurs only when the state $|l\rangle$ couples to a quasibound g-wave state about $h \times 0.7$ MHz above threshold [24]. The resulting bubble is not fully spherically symmetric, which indicates higher partial-wave contributions [25]. The different absorption patterns allow us to clearly distinguish between the two different dissociation channels in a single absorption picture when the magnetic field is ramped up to $\sim$22 G. These dissociation channels serve as the interferometer "output ports."

The interferometer is based on two subsequent passages through the crossing following the scheme illustrated in Fig. 2. For an initial magnetic field above the crossing a downward magnetic-field ramp brings the initial molecular state into a coherent superposition of $|g'\rangle$ and $|l\rangle$. After the ramp the field is kept constant at a hold field B_0 below the crossing for a variable hold time τ. A differential phase ϕ is then accumulated between the two components, which linearly increases with the product of the binding energy difference ΔE and the hold time τ. The magnetic field is then ramped back up, and the second passage creates a new superposition state depending on ϕ. For a 50/50-splitting ratio, this can lead to complete destructive or constructive interference in the two output ports and thus to high-

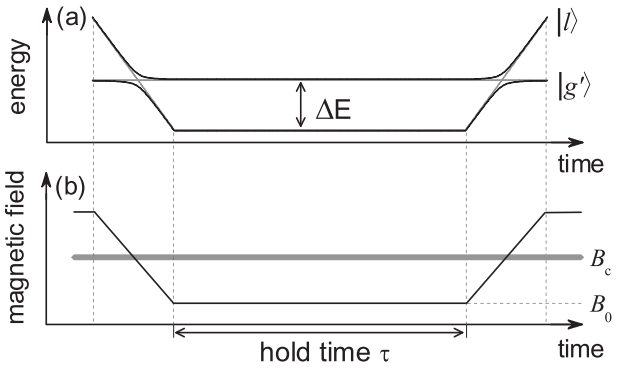

FIG. 2. (a) Scheme of the Stückelberg interferometer. By ramping the magnetic field over the avoided crossing at B_c at a rate near the critical ramp rate R_c the population in the initial molecular state is coherently split. ΔE is the binding energy difference at the given hold field B_0. After the hold time τ a reverse ramp coherently recombines the two populations. The populations in the two "output ports" are then determined as a function of acquired phase difference $\phi \propto \Delta E \times \tau$. (b) Corresponding magnetic-field ramp.

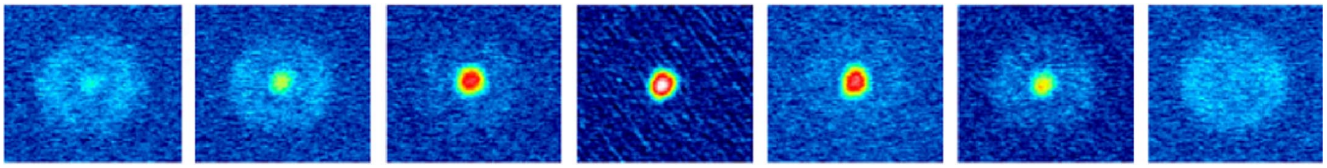

FIG. 3 (color online). Series of dissociation patterns showing about one oscillation period with $\Delta E/h = 155$ kHz at a hold field of 11.19 G. From one picture to the next the hold time τ is increased by 1 μs. The first and the last of the absorption images mainly show dissociation of l-wave molecules, whereas the central image shows predominant dissociation of g-wave molecules.

contrast fringes as a function of τ or ΔE. These fringes, resulting from two passages through the same crossing, are analogous to the well-known Stückelberg oscillations in collision physics [14,26] or in the physics with Rydberg atoms [27,28]. Note that our realization of a Stückelberg interferometer gives full control over the interferometer dynamics by appropriate choice of ramp rates and magnetic offset fields.

A typical ramp sequence, as shown in Fig. 2(b), starts with a sample of $|g'\rangle$ molecules at a magnetic field of 11.6 G about 250 mG above the crossing. At the critical ramp rate R_c we ramp the magnetic field within about 50 μs to a hold field B_0 below the crossing. After the variable hold time τ we reverse the ramp and transverse the crossing a second time at the critical ramp rate. The output of the interferometer is detected by rapidly ramping the magnetic field up to 22 G and by imaging the pattern of dissociating $|l\rangle$ and $|g\rangle$ molecules.

For one period of oscillation the dependence of the dissociation pattern on the hold time τ is demonstrated by the series of absorption images shown in Fig. 3. The hold time is increased in steps of 1 μs while the entire preparation, ramping, and detection procedure is repeated for each experimental cycle, lasting about 20 s. The molecular population oscillates from being predominantly l-wave to predominantly g- wave and back. For a quantitative analysis of the molecular population in each output port we fit the images with a simple model function [29] and extract the fraction of molecules in each of the two output ports. Figure 4 shows the g-wave molecular population as a function of hold time τ for various hold fields B_0

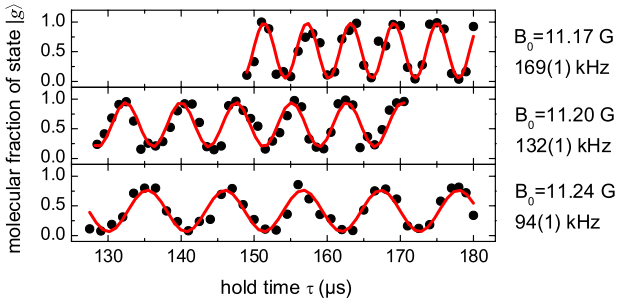

FIG. 4 (color online). Interferometer fringes for magnetic hold fields B_0 below the crossing of $|g'\rangle$ and $|l\rangle$. The g-wave molecular fraction is plotted as a function of the hold time τ. Sinusoidal fits give the oscillation frequency as indicated.

corresponding to different ΔE. The existence of these Stückelberg oscillations confirms that coherence is preserved by the molecular beam splitter. Their high-contrast ratio shows that near 50/50-splitting is achieved. Sinusoidal fits to the data allow for an accurate determination of the oscillation frequency and hence of ΔE.

Figure 5 shows ΔE as a function of magnetic-field strength near the avoided crossing. For magnetic fields below the crossing we obtain ΔE as described before. For magnetic fields above the crossing, we invert the interferometric scheme. Molecules are first transferred from $|g'\rangle$ into $|l\rangle$ using a slow adiabatic ramp. The field is then ramped up above the crossing with a rate near R_c, kept constant for the variable time τ at the hold field B_0 and then ramped down to close the interferometer. An adiabatic ramp through the crossing maps population in $|g'\rangle$ onto $|l\rangle$ and vice versa. Detection then proceeds as before.

For both realizations of the interferometer we obtain high-contrast fringes even when it is not operated in the Landau-Zener regime and the fast ramps are stopped right at the crossing (see inset to Fig. 5). This allows us to measure ΔE in the crossing region. A fit to the data with

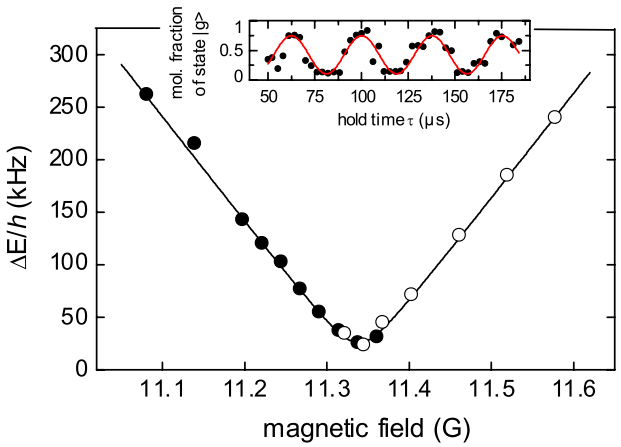

FIG. 5 (color online). Interferometrically measured binding energy difference ΔE in the region of the crossing between states $|g'\rangle$ and $|l\rangle$ as a function of magnetic field. Solid circles: Standard ramp sequence of the interferometer. Open circles: Inverted scheme for field values above the crossing. The one-sigma statistical error from the sinusoidal fit is less than the size of the symbols. The solid curve is a hyperbolic fit to the experimental data. Inset: Oscillation at 26.6(3) kHz for a hold field $B_0 = 11.34$ G right on the crossing.

a hyperbolic fit function according to the standard Landau-Zener model yields $B_c = 11.339(1)$ G for the position of the crossing, $\Delta\mu = 0.730(6)\mu_B$ for the difference in magnetic moment of the two states involved (μ_B is Bohr's magneton), and $V = h \times 14(1)$ kHz for the coupling strength. While the measured $\Delta\mu$ agrees reasonably well with the result from an advanced theoretical model of the Cs_2 dimer [18], B_c and V cannot be obtained from these calculations with sufficient accuracy.

The present interferometer allows us to observe up to 100 oscillations at 200 kHz. Shot-to-shot fluctuations increasingly scramble the phase of the oscillations for longer hold times until the phase appears to be fully randomized while large amplitude variations for the molecular populations persist. The peak-to-peak amplitude of these fluctuations decays slowly and is still 50% of the initial contrast after 1 ms. We attribute this phase scrambling to magnetic-field noise that causes shot-to-shot variations of ΔE, the same, however, for each molecule. The large amplitude of these fluctuations indicates that phase coherence is preserved within the molecular sample. We attribute the gradual loss of peak-to-peak amplitude to spatial magnetic-field inhomogeneities. We expect that straightforward technical improvements regarding the magnetic-field stability and homogeneity and applying the interferometer to trapped molecular samples will allow us to extend the hold times far into the millisecond range. It will then be possible to measure ultraweak crossings with coupling strengths well below $h \times 1$ kHz.

We have demonstrated a molecular Stückelberg interferometer with full control over the interferometer dynamics. The interferometer allows precise measurements of binding energy differences of molecular states and of the positions of avoided crossings, independent of a precise knowledge of the ramp rate through the crossing. In the future, the technique might be employed to measure feeble interactions between molecular states, such as parity nonconserving interactions [30]. In general, ultralow molecular temperatures combined with long storage times in optical traps [3] or lattices [5–7] may allow us to study interaction phenomena on the $h \times 1$ Hz scale. In view of the rapid progress in various preparation methods for cold molecular samples, new tools for precision measurements on molecular samples, such as our Stückelberg interferometer, will open up exciting avenues for future research.

We thank E. Tiesinga for discussions and for theoretical support. We acknowledge financial support by the Austrian Science Fund (FWF) within SFB 15 (project part 16) and by the EU within the Cold Molecules TMR Network under Contract No. HPRN-CT-2002-00290. M. M. and C. C. acknowledge support by DOC [PhD-Program of the Austrian Academy of Science] and the FWF Lise-Meitner program, respectively.

[1] For a review, see T. Köhler, K. Góral, and P. S. Julienne, Rev. Mod. Phys. **78**, 1311 (2006).
[2] See, e.g., *Ultracold Fermi Gases, Proceedings of the International School of Physics "Enrico Fermi", Course CLXIV, Varenna, 20-30 June 2006*, edited by M. Inguscio, W. Ketterle, and C. Salomon (to be published).
[3] C. Chin *et al.*, Phys. Rev. Lett. **94**, 123201 (2005).
[4] J. R. Abo-Shaeer *et al.* Phys. Rev. Lett. **94**, 040405 (2005).
[5] K. Winkler *et al.*, Nature (London) **441**, 853 (2006).
[6] G. Thalhammer *et al.*, Phys. Rev. Lett. **96**, 050402 (2006).
[7] T. Volz *et al.*, Nature Phys. **2**, 692 (2006).
[8] K. Winkler *et al.*, Phys. Rev. Lett. **98**, 043201 (2007).
[9] J. J. Hudson, B. E. Sauer, M. R. Tarbutt, and E. A. Hinds, Phys. Rev. Lett. **89**, 023003 (2002).
[10] E. R. Hudson, H. J. Lewandowski, B. C. Sawyer, and J. Ye, Phys. Rev. Lett. **96**, 143004 (2006).
[11] C. Chin and V. V. Flambaum, Phys. Rev. Lett. **96**, 230801 (2006).
[12] S. Bize *et al.*, J. Phys. B **38**, S449 (2005).
[13] M. M. Boyd *et al.*, Phys. Rev. Lett. **98**, 083002 (2007).
[14] E. C. G. Stückelberg, Helv. Phys. Acta **5**, 369 (1932).
[15] N. F. Ramsey, *Molecular Beams* (Oxford University, London, 1956).
[16] C. Chin *et al.*, Phys. Rev. A **70**, 032701 (2004).
[17] Using the notation $|f, m_f; l, m_l\rangle$ of Ref. [16], the three states $|g\rangle$, $|g'\rangle$, and $|l\rangle$ correspond to $|4, 4; 4, 2\rangle$, $|6, 6; 4, 0\rangle$, and $|6, 3; 8, 3\rangle$, respectively.
[18] E. Tiesinga (private communication).
[19] T. Kraemer *et al.*, Appl. Phys. B **79**, 1013 (2004).
[20] T. Weber *et al.*, Science **299**, 232 (2003).
[21] J. Herbig *et al.*, Science **301**, 1510 (2003).
[22] M. Mark *et al.*, Europhys. Lett. **69**, 706 (2005).
[23] M. Mark *et al.*, arXiv:0706.1041.
[24] S. Knoop *et al.* (to be published).
[25] S. Dürr, T. Volz, and G. Rempe, Phys. Rev. A **70**, 031601(R) (2004).
[26] E. E. Nikitin and S. Ya. Umanskii, *Theory of Slow Atomic Collisions* (Springer, Berlin, 1984).
[27] M. C. Baruch and T. F. Gallagher, Phys. Rev. Lett. **68**, 3515 (1992).
[28] S. Yoakum, L. Sirko, and P. M. Koch, Phys. Rev. Lett. **69**, 1919 (1992).
[29] We model the dissociation pattern with appropriately chosen spherical harmonic functions to account for the angular distribution [25].
[30] E. D. Commins, Adv. At. Mol. Opt. Phys. **40**, 1 (1999).

LETTERS

Evidence for Efimov quantum states in an ultracold gas of caesium atoms

T. Kraemer[1], M. Mark[1], P. Waldburger[1], J. G. Danzl[1], C. Chin[1,2], B. Engeser[1], A. D. Lange[1], K. Pilch[1], A. Jaakkola[1], H.-C. Nägerl[1] & R. Grimm[1,3]

Systems of three interacting particles are notorious for their complex physical behaviour. A landmark theoretical result in few-body quantum physics is Efimov's prediction[1,2] of a universal set of bound trimer states appearing for three identical bosons with a resonant two-body interaction. Counterintuitively, these states even exist in the absence of a corresponding two-body bound state. Since the formulation of Efimov's problem in the context of nuclear physics 35 years ago, it has attracted great interest in many areas of physics[3–8]. However, the observation of Efimov quantum states has remained an elusive goal[3,5]. Here we report the observation of an Efimov resonance in an ultracold gas of caesium atoms. The resonance occurs in the range of large negative two-body scattering lengths, arising from the coupling of three free atoms to an Efimov trimer. Experimentally, we observe its signature as a giant three-body recombination loss[9,10] when the strength of the two-body interaction is varied. We also detect a minimum[9,11,12] in the recombination loss for positive scattering lengths, indicating destructive interference of decay pathways. Our results confirm central theoretical predictions of Efimov physics and represent a starting point with which to explore the universal properties of resonantly interacting few-body systems[7]. While Feshbach resonances[13,14] have provided the key to control quantum-mechanical interactions on the two-body level, Efimov resonances connect ultracold matter[15] to the world of few-body quantum phenomena.

Efimov's treatment of three identical bosons[1,2] is closely linked to the concept of universality[7] in systems with a resonant two-body interaction, where the *s*-wave scattering length a fully characterizes the two-body physics. When $|a|$ greatly exceeds the characteristic range ℓ of the two-body interaction potential, details of the short-range interaction become irrelevant because of the long-range nature of the wavefunction. Universality then leads to a generic behaviour in three-body physics, reflected in the energy spectrum of weakly bound Efimov trimer states. Up to now, in spite of their great fundamental importance, these states could not be observed experimentally. An observation in the realm of nuclear physics, as originally proposed by Efimov, is hampered by the presence of the Coulomb interaction, and only two-neutron halo systems with a spinless core are likely to feature Efimov states[3]. In molecular physics, the helium trimer is predicted to have an excited state with Efimov character[4]. The existence of this state could not be confirmed[5]. A different approach to experimentally studying the physics of Efimov states is based on the unique properties of ultracold atomic quantum gases. Such systems[15] provide an unprecedented level of control, enabling the investigation of interacting quantum systems. The ultralow collision energies allow us to explore the zero-energy quantum limit. Moreover, two-body interactions can be precisely tuned on the basis of Feshbach resonances[13,14].

Efimov's scenario[1,2,7] can be illustrated by the energy spectrum of the three-body system as a function of the inverse scattering length $1/a$ (Fig. 1). Let us first consider the well-known weakly bound dimer state, which only exists for large positive a. In the resonance regime, its binding energy is given by the universal expression $E_b = -\hbar^2/(ma^2)$, where m is the atomic mass and $\hbar$ is Planck's constant divided by 2π. In Fig. 1, where the resonance limit corresponds to $1/a \rightarrow 0$, the dimer energy E_b is represented by a parabola for $a > 0$. If we now add one more atom with zero energy, a natural continuum threshold for the bound three-body system (hatched line in Fig. 1) is given by the three-atom threshold ($E = 0$) for negative a and by the dimer-atom threshold (E_b) for positive a. Energy states below the continuum threshold are necessarily three-body bound states. When $1/a$ approaches the resonance from the negative-a side, a first Efimov trimer state appears in a range where a weakly bound two-body state does not exist. When passing through the resonance the state connects to the positive-a side, where it finally intersects with the dimer-atom threshold. An infinite series of such Efimov states is found when scattering lengths are increased and binding energies are decreased in powers of universal scaling

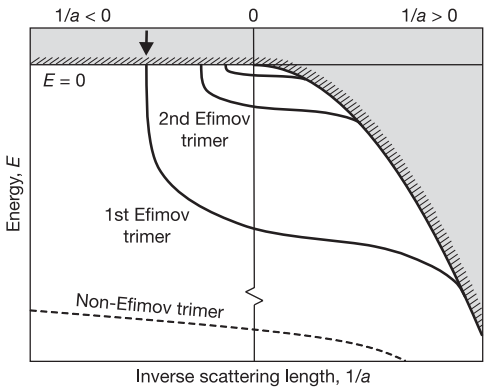

Figure 1 | Efimov's scenario. Appearance of an infinite series of weakly bound Efimov trimer states for resonant two-body interaction. The binding energy is plotted as a function of the inverse two-body scattering length $1/a$. The shaded region indicates the scattering continuum for three atoms ($a < 0$) and for an atom and a dimer ($a > 0$). The arrow marks the intersection of the first Efimov trimer with the three-atom threshold. To illustrate the series of Efimov states, we have artificially reduced the universal scaling factor from 22.7 to 2. For comparison, the dashed line indicates a tightly bound non-Efimov trimer[30], which does not interact with the scattering continuum.

[1]Institut für Experimentalphysik, Universität Innsbruck, Technikerstraße 25, A-6020 Innsbruck, Austria. [2]James Franck Institute, Physics Department of the University of Chicago, 5640 S. Ellis Avenue Chicago, Illinois 60637, USA. [3]Institut für Quantenoptik und Quanteninformation der Österreichischen Akademie der Wissenschaften, Otto-Hittmair-Platz 1, A-6020 Innsbruck, Austria.

factors[1,2,7] $e^{\pi/s_0} \approx 22.7$ and $e^{-2\pi/s_0} \approx 1/515$ (where $s_0 = 1.00624$), respectively.

Resonant scattering phenomena arise as a natural consequence of Efimov's scenario[16]. When an Efimov state intersects with the continuum threshold at negative scattering lengths a, three free atoms in the ultracold limit resonantly couple to a trimer. This results in a triatomic Efimov resonance. At finite collision energies, the phenomenon evolves into a triatomic continuum resonance[17]. Another type of Efimov resonance[18] is found at positive values of a for collisions between a free atom and a dimer, when Efimov states intersect with the dimer–atom threshold. While the latter type of Efimov resonance corresponds to Feshbach resonances in collisions between atoms and dimers[18], triatomic Efimov resonances can be interpreted as a three-body generalization to Feshbach resonances[8].

Striking manifestations of Efimov physics have been predicted for three-body recombination processes in ultracold gases with tunable two-body interactions[7,9–12,19]. Three-body recombination leads to losses from a trapped gas with a rate proportional to the third power of the atomic number density. These losses are commonly described[20] in terms of a loss rate coefficient L_3. In the resonant case ($|a| \gg \ell$), it is convenient to express this coefficient in the form $L_3 = 3C(a)\hbar a^4/m$, separating a general a^4-scaling[20,21] from an additional dependence[9,10,12] $C(a)$. Efimov physics is reflected in a logarithmically periodic behaviour $C(22.7a) = C(a)$, corresponding to the scaling of the infinite series of weakly bound trimer states. For negative scattering lengths, the resonant coupling of three atoms to an Efimov state opens up fast decay channels into deeply bound dimer states plus a free atom.

Triatomic Efimov resonances thus show up in giant recombination loss. This striking phenomenon was first identified in numerical solutions to the adiabatic hyperspherical approximation of the three-body Schrödinger equation, assuming simple model potentials and interpreted in terms of tunnelling through a potential barrier in the three-body entrance channel[9]. A different theoretical approach[7,10], based on effective field theory, provides the analytic expression $C(a) = 4,590\sinh(2\eta_-)/(\sin^2[s_0\ln(|a|/a_-)] + \sinh^2\eta_-)$. The free parameter a_- for the resonance positions at a_-, 22.7 a_-,… depends on the short-range part of the effective three-body interaction and is thus not determined in the frame of the universal long-range theory. As a second free parameter, the dimensionless quantity η_- describes the unknown decay rate of Efimov states into deeply bound dimer states plus a free atom, and thus characterizes the resonance width.

Our measurements are based on the magnetically tunable interaction properties of caesium atoms[22] in the lowest internal state. By applying fields between 0 and 150 G, we varied the s-wave scattering length a in a range between $-2,500a_0$ to $1,600a_0$, where a_0 is Bohr's radius. Accurate three-body loss measurements are facilitated by the fact that inelastic two-body loss is energetically forbidden[20]. The characteristic range of the two-body potential is given by the van der Waals length[23], which for caesium is $\ell \approx 100a_0$. This leaves us with enough room to study the universal regime requiring $|a| \gg \ell$. For negative a, a maximum value of 25 is attainable for $|a|/\ell$. Efimov's estimate $\frac{1}{\pi}\ln(|a|/\ell)$ for the number of weakly bound trimer states[2] suggests the presence of one Efimov resonance in the accessible range of negative scattering lengths.

Our experimental results (Fig. 2), obtained with optically trapped thermal samples of caesium atoms in two different set-ups (see Methods), indeed show a giant loss feature marking the expected resonance. We present our data in terms of a recombination length[9] $\rho_3 = [2m/(\sqrt{3}\hbar)L_3]^{1/4}$, which leads to the simple relation $\rho_3/a = 1.36C^{1/4}$. Note that the general a^4-scaling corresponds to a linear behaviour in $\rho_3(a)$ (straight lines in Fig. 2). A fit of the analytic theory[7,10] to our experimental data taken for negative a at temperatures $T \approx 10$ nK shows a remarkable agreement and determines the resonance position to $a_- = -850(20)a_0$ and the decay parameter to $\eta_- = 0.06(1)$. The pronounced resonance behaviour with a small value for the decay parameter ($\eta_- \ll 1$) demonstrates a sufficiently long lifetime of Efimov trimers to allow their observation as distinct quantum states.

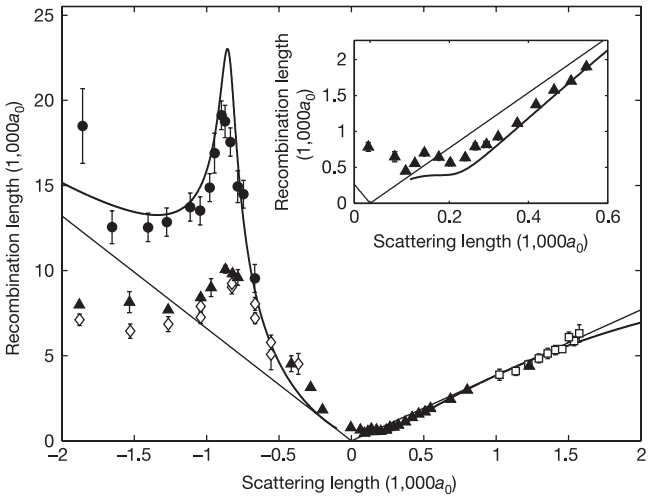

Figure 2 | Observation of the Efimov resonance in measurements of three-body recombination. The recombination length $\rho_3 \propto L_3^{1/4}$ is plotted as a function of the scattering length a. The dots and the filled triangles show the experimental data from set-up A for initial temperatures around 10 nK and 200 nK, respectively. The open diamonds are from set-up B at temperatures of 250 nK. The open squares are previous data[20] at initial temperatures between 250 and 450 nK. The solid curve represents the analytic model from effective field theory[7] with $a_- = -850a_0$, $a_+ = 1,060a_0$, and $\eta_- = \eta_+ = 0.06$. The straight lines result from setting the $\sin^2$ and $\cos^2$-terms in the analytic theory to 1, which gives a lower recombination limit for $a < 0$ and an upper limit for $a > 0$. The inset shows an expanded view for small positive scattering lengths with a minimum for $C(a) \propto (\rho_3/a)^4$ near $210a_0$. The displayed error bars refer to statistical uncertainties only. Uncertainties in the determination of the atomic number densities may lead to additional calibration errors for ρ_3 of up to 20%.

All the results discussed so far are valid in the zero-energy collision limit of sufficiently low temperatures. For ultralow but non-zero temperatures the recombination length is unitarity limited[19] to $5.2\hbar(mk_BT)^{-1/2}$. For $T = 10$ nK this limit corresponds to about $60,000a_0$ and our sample is thus cold enough to justify the zero-temperature limit. For 250 nK, however, unitarity limits the recombination length to about $12,000a_0$. The Efimov resonance is still visible at temperatures of 200 and 250 nK (filled triangles and open diamonds in Fig. 2). The slight shift to lower values of $|a|$ suggests the evolution of the zero-energy Efimov resonance into a triatomic continuum resonance[17]. In further experiments at higher temperatures (data not shown) we observed the resonance to disappear above ~500 nK.

For positive scattering lengths, we found three-body losses to be typically much weaker than for negative values. Our measurements are consistent with a maximum recombination loss of $C(a) \approx 70$, or equivalently $\rho_3 \approx 3.9a$, as predicted by different theories[9,11,12] (straight line for $a > 0$ in Fig. 2). For a below $600a_0$ the measured recombination length significantly drops below this upper limit (inset in Fig. 2). The analytic expression from effective field theory[7,12] for $a > 0$ reads $C(a) = 67.1e^{-2\eta_+}(\cos^2[s_0\ln(a/a_+)] + \sinh^2\eta_+) + 16.8(1 - e^{-4\eta_+})$ with the two free parameters a_+ and η_+. The first term describes recombination into the weakly bound dimer state with an oscillatory behaviour that is due to an interference effect between two different pathways[9,11]. The second term results from decay into deeply bound states. We use this expression to fit our data points with $a > 5\ell \approx 500a_0$. This somewhat arbitrary condition is introduced as a reasonable choice to satisfy $a \gg \ell$ for the validity of the universal theory. The fit is quite insensitive to the value of the decay parameter and yields $\eta_+ < 0.2$. This result is consistent with the theoretical assumption[10] of the same value for the decay

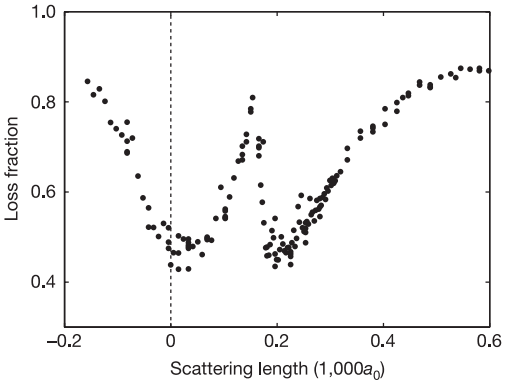

Figure 3 | Atom loss for small scattering lengths. Besides a minimum near zero scattering length, we identify a minimum of recombination loss at $\sim 210a_0$, which can be attributed to a predicted destructive interference effect[9,11,12].

parameter for positive and negative a, which in our case is $\eta_+ = \eta_- = 0.06$. For maximum $C(a)$, we obtain $a_+ = 1{,}060(70)a_0$. According to theory[7], the trimer state hits the dimer–atom threshold at $a = 1.1a_+ \approx 1{,}170a_0$. The logarithmic periodicity of the Efimov scenario suggests that adjacent loss minima occur at $\sqrt{22.7} \times 1{,}060a_0 \approx 5{,}000a_0$ and at $1{,}060a_0/\sqrt{22.7} \approx 220a_0$. While the former value is out of our accessible range, the latter value ($a \approx 2\ell$) is too small to strictly justify universal behaviour in the resonance limit ($a \gg \ell$). Nevertheless, our experimental results (inset to Fig. 2) indicate a minimum at $a \approx 210a_0$ and the analytic expression for $C(a)$ is found to describe our data quite well down to this minimum.

The occurrence of the interference minimum in three-body loss is demonstrated more clearly in another set of experiments (Fig. 3), where we simply measured the loss of atoms after a fixed storage time in the optical trap. This minimum is located at $a = 210(10)a_0$ in addition to a second minimum close to zero scattering length. We point out that the existence of the minimum at $210a_0$ is very advantageous for efficient evaporative cooling of caesium as it combines a large scattering cross-section with very low loss. Inadvertently, we have already benefited from this loss minimum for the optimized production of a Bose–Einstein condensate of caesium[24].

The comparison of our experimental results to available three–body theory shows remarkable agreement, although the collision physics of caesium is in general a very complicated multi-channel scattering problem. We believe that the particular nature of the broad, "open-channel dominated" Feshbach resonance[25] that underlies the tunability of our system plays a crucial role. For such a resonance, the two-body scattering problem can be described in terms of an effective single-channel model. It is very interesting to investigate to what degree this great simplification of the two-body physics extends to the three-body problem. Here we particularly wonder how the regions of positive and negative scattering lengths are connected in our experiment, where a is changed through a zero crossing—that is, through a non-universal region, and not across the universal resonance region.

In our case, there is no obvious connection between the Efimov state that leads to the observed resonance for $a < 0$ and the states responsible for the behaviour for $a > 0$. In our analysis of the experimental data, we have thus independently fitted the data sets for negative and positive a. Nevertheless, the resulting values for the two independent fit parameters a_- and a_+ do suggest a connection: for the ratio $a_+/|a_-|$ our experiment yields 1.25(9), whereas universal theory[7] predicts 0.96(3). These numbers are quite close in view of the Efimov factor of 22.7. If it is not an accidental coincidence, we speculate that the apparent relation between a_+ and a_- may be a further consequence of universality in a system where the resonant two-body interaction can be modelled in terms of a single scattering channel. In general, the multi-channel nature of three-body collisions near Feshbach resonances[26,27] leads to further interesting questions, such as whether there may be resonance effects beyond the Efimov scenario. Advances in three-body theory are necessary to answer these questions and to provide a complete interpretation of our present observations.

In the past few years, applications of Feshbach resonances in ultracold gases and the resulting ability to create dimer states have set the stage for many new developments in matter-wave quantum physics. The observation of an Efimov resonance now confirms the existence of weakly bound trimer states and opens up new ways[6,8] of experimentally exploring the intriguing physics of few-body quantum systems.

METHODS

Magnetic tuning of the two-body interaction. For Cs atoms in their energetically lowest state (quantum numbers $F = 3$ for the total spin and $m_F = 3$ for its projection) the s-wave scattering length a varies strongly with the magnetic field[22]. Between 0 and 150 G the dependence can in general be well approximated by the fitting formula:

$$a(B)/a_0 = (1{,}722 + 1.52B/\mathrm{G})\left(1 - \frac{28.72}{B/\mathrm{G} + 11.74}\right)$$

except for a few narrow Feshbach resonances[22]. The smooth variation of the scattering length in the low-field region results from a broad Feshbach resonance centred at about -12 G (equivalent to $+12$ G in the state $F = 3, m_F = -3$). In all our measurements we excluded the magnetic field regions where the narrow Feshbach resonances influence the scattering behaviour through coupling to other molecular potentials. The Efimov resonance is centred at 7.5 G.

Trap set-ups and preparation of the Cs gases. All measurements were performed with trapped thermal samples of caesium atoms at temperatures T ranging from 10 to 250 nK. We used two different experimental set-ups, which have been described elsewhere[24,28].

In set-up A we first produced an essentially pure Bose–Einstein condensate with up to 250,000 atoms in a far-detuned crossed optical dipole trap generated by two 1,060-nm Yb-doped fibre laser beams[24]. We then ramped the magnetic field to 16.2 G, where the scattering length is negative with a value of $-50a_0$, thus inducing a collapse of the condensate[29]. After an equilibration time of 1 s we were left with a thermal sample at typically $T = 10$ nK containing up to 20,000 atoms at peak densities ranging from $n_0 = 3 \times 10^{11}\,\mathrm{cm}^{-3}$ to $3 \times 10^{12}\,\mathrm{cm}^{-3}$. Alternatively, we interrupted the evaporation process before condensation to produce thermal samples at $T \approx 200$ nK in a crossed dipole trap generated by one of the 1,060-nm beams and a 10.6-μm CO_2 laser beam. After recompression of the trap this produced typical densities of $n_0 = 5 \times 10^{13}\,\mathrm{cm}^{-3}$. The measurements in the region of the loss minima as displayed in Fig. 3 were taken after a storage time of 200 ms at initial densities of $n_0 = 6 \times 10^{13}\,\mathrm{cm}^{-3}$.

In set-up B we used an optical surface trap[28] in which we prepared a thermal sample of 10,000 atoms at $T \approx 250$ nK via forced evaporation at a density of $n_0 = 1.0 \times 10^{12}\,\mathrm{cm}^{-3}$. The dipole trap was formed by a repulsive evanescent laser wave on top of a horizontal glass prism in combination with a single horizontally confining 1,060-nm laser beam propagating along the vertical direction.

Determination of three-body loss rate coefficients. We measured three-body loss rates in set-up A by recording the time evolution of the atom number N and the temperature T. A detailed description of this procedure has been given in ref. 20. In brief, the process of three-body recombination not only leads to a loss of atoms, but also induces 'anti-evaporation' and recombination heating. The first effect is present at any value of the scattering length a. The second effect occurs for positive values of a when the recombination products remain trapped. Atom loss and temperature rise are modelled by a set of two coupled nonlinear differential equations. We used numerical solutions to this set of equations to fit our experimental data. From these fits, together with measurements of the trapping parameters, we obtained the rate coefficient L_3. In set-up B we recorded the loss at decay times sufficiently short to make sure that heating is negligible.

Received 12 December 2005; accepted 2 February 2006.

1. Efimov, V. Energy levels arising from resonant two-body forces in a three-body system. *Phys. Lett. B.* **33,** 563–564 (1970).
2. Efimov, V. Weakly-bound states of three resonantly-interacting particles. *Sov. J. Nucl. Phys.* **12,** 589–595 (1971).
3. Jensen, A. S., Riisager, K., Fedorov, D. V. & Garrido, E. Structure and reactions of quantum halos. *Rev. Mod. Phys.* **76,** 215–261 (2004).

4. Lim, T. K., Duffy, K. & Damer, W. C. Efimov state in the ^{4}He trimer. *Phys. Rev. Lett.* **38,** 341–343 (1977).
5. Brühl, R. *et al.* Matter wave diffraction from an inclined transmission grating: Searching for the elusive ^{4}He trimer Efimov state. *Phys. Rev. Lett.* **95,** 063002 (2005).
6. Braaten, E., Hammer, H.-W. & Kusunoki, M. Efimov states in a Bose-Einstein condensate near a Feshbach resonance. *Phys. Rev. Lett.* **90,** 170402 (2003).
7. Braaten, E. & Hammer, H.-W. Universality in few-body systems with large scattering length. Preprint at ⟨http://arXiv.org/abs/cond-mat/0410417⟩ (2004).
8. Stoll, M. & Köhler, T. Production of three-body Efimov molecules in an optical lattice. *Phys. Rev. A* **72,** 022714 (2005).
9. Esry, B. D., Greene, C. H. & Burke, J. P. Jr Recombination of three atoms in the ultracold limit. *Phys. Rev. Lett.* **83,** 1751–1754 (1999).
10. Braaten, E. & Hammer, H.-W. Three-body recombination into deep bound states in a Bose gas with large scattering length. *Phys. Rev. Lett.* **87,** 160407 (2001).
11. Nielsen, E. & Macek, J. H. Low-energy recombination of identical bosons by three-body collisions. *Phys. Rev. Lett.* **83,** 1566–1569 (1999).
12. Bedaque, P. F., Braaten, E. & Hammer, H.-W. Three-body recombination in Bose gases with large scattering length. *Phys. Rev. Lett.* **85,** 908–911 (2000).
13. Tiesinga, E., Verhaar, B. J. & Stoof, H. T. C. Threshold and resonance phenomena in ultracold ground-state collisions. *Phys. Rev. A* **47,** 4114–4122 (1993).
14. Inouye, S. *et al.* Observation of Feshbach resonances in a Bose–Einstein condensate. *Nature* **392,** 151–154 (1998).
15. Southwell, K. (ed.) *Ultracold matter Nature* (Insight) **416**, 205–246 (2002).
16. Efimov, V. Low-energy properties of three resonantly interacting particles. *Sov. J. Nucl. Phys.* **29,** 546–553 (1979).
17. Bringas, F., Yamashita, M. T. & Frederico, T. Triatomic continuum resonances for large negative scattering lengths. *Phys. Rev. A* **69,** 040702(R) (2004).
18. Nielsen, E., Suno, H. & Esry, B. D. Efimov resonances in atom-diatom scattering. *Phys. Rev. A* **66,** 012705 (2002).
19. D'Incao, J. P., Suno, H. & Esry, B. D. Limits on universality in ultracold three-boson recombination. *Phys. Rev. Lett.* **93,** 123201 (2004).
20. Weber, T., Herbig, J., Mark, M., Nägerl, H.-C. & Grimm, R. Three-body recombination at large scattering lengths in an ultracold atomic gas. *Phys. Rev. Lett.* **91,** 123201 (2003).
21. Fedichev, P. O., Reynolds, M. W. & Shlyapnikov, G. V. Three-body recombination of ultracold atoms to a weakly bound *s* level. *Phys. Rev. Lett.* **77,** 2921–2924 (1996).
22. Chin, C. *et al.* Precision Feshbach spectroscopy of ultracold Cs_2. *Phys. Rev. A* **70,** 032701 (2004).
23. Bolda, E. L., Tiesinga, E. & Julienne, P. S. Effective-scattering-length model of ultracold atomic collisions and Feshbach resonances in tight harmonic traps. *Phys. Rev. A* **66,** 013403 (2002).
24. Kraemer, T. *et al.* Optimized production of a cesium Bose-Einstein condensate. *Appl. Phys. B* **79,** 1013–1019 (2004).
25. Köhler, T., Goral, K. & Julienne, P. S. Production of cold molecules via magnetically tunable Feshbach resonances. Preprint at ⟨http://arxiv.org/abs/cond-mat/0601420⟩ (2006).
26. Kartavtsev, O. I. & Macek, J. H. Low-energy three-body recombination near a Feshbach resonance. *Few-Body Syst.* **31,** 249–254 (2002).
27. Petrov, D. S. Three-boson problem near a narrow Feshbach resonance. *Phys. Rev. Lett.* **93,** 143201 (2004).
28. Rychtarik, D., Engeser, B., Nägerl, H.-C. & Grimm, R. Two-dimensional Bose-Einstein condensate in an optical surface trap. *Phys. Rev. Lett.* **92,** 173003 (2004).
29. Donley, E. A. *et al.* Dynamics of collapsing and exploding Bose–Einstein condensates. *Nature* **412,** 295–299 (2001).
30. Thomas, L. H. The interaction between a neutron and a proton and the structure of H^3. *Phys. Rev.* **47,** 903–909 (1935).

Acknowledgements We thank E. Braaten, C. Greene, B. Esry, H. Hammer and T. Köhler for many discussions and E. Kneringer for support regarding the data analysis. We acknowledge support by the Austrian Science Fund (FWF) within Spezialforschungsbereich 15 and within the Lise Meitner programme, and by the European Union in the frame of the TMR networks 'Cold Molecules' and 'FASTNet'. M.M. is supported within the Doktorandenprogramm of the Austrian Academy of Sciences.

Author Information Reprints and permissions information is available at npg.nature.com/reprintsandpermissions. The authors declare no competing financial interests. Correspondence and requests for materials should be addressed to H.-C.N. (christoph.naegerl@ultracold.at).

Observation of Feshbach-Like Resonances in Collisions between Ultracold Molecules

C. Chin,[1,*] T. Kraemer,[1] M. Mark,[1] J. Herbig,[1] P. Waldburger,[1] H.-C. Nägerl,[1] and R. Grimm[1,2]
[1]*Institut für Experimentalphysik, Universität Innsbruck, Technikerstraße 25, 6020 Innsbruck, Austria*
[2]*Institut für Quantenoptik und Quanteninformation, Österreichische Akademie der Wissenschaften, 6020 Innsbruck, Austria*
(Received 10 November 2004; published 1 April 2005)

We observe magnetically tuned collision resonances for ultracold Cs_2 molecules stored in a CO_2-laser trap. By magnetically levitating the molecules against gravity, we precisely measure their magnetic moment. We find an avoided level crossing which allows us to transfer the molecules into another state. In the new state, two Feshbach-like collision resonances show up as strong inelastic loss features. We interpret these resonances as being induced by Cs_4 bound states near the molecular scattering continuum. The tunability of the interactions between molecules opens up novel applications such as controlled chemical reactions and synthesis of ultracold complex molecules.

DOI: 10.1103/PhysRevLett.94.123201 PACS numbers: 34.50.–s, 05.30.Jp, 32.80.Pj, 67.40.Hf

The synthesis of ultracold molecules from ultracold atoms has opened up new possibilities for studies on molecular matter waves [1–3], strongly interacting superfluids [4], high-precision molecular spectroscopy [5] and coherent molecular optics [6]. In all these experiments, control of the interatomic interaction by magnetic fields plays an essential role in the association process. When a two-atom bound state is magnetically tuned near the quantum state of two scattering atoms, coupling from the atomic to the molecular state can be resonantly enhanced. This is commonly referred to as a Feshbach resonance [7].

The success in controlling the interaction of ultracold atoms raises the question whether a similar level of control can be achieved for ultracold molecules. Resonant interactions between molecules may lead to synthesis of complex objects beyond atomic dimers. Furthermore, scattering processes for molecules involve many novel reactive channels in comparison to the atomic counterpart, e.g., collision induced dissociation, rearrangement, or displacement chemical reactions. Magnetic tunability of the molecular interactions, similar to that resulting from atomic Feshbach resonances, will lead to exciting perspectives for investigating these chemical processes in regimes where quantum statistics and quantum coherence play an important role.

In this Letter, we report the observation of magnetically tuned collision resonances in an ultracold gas of Cs_2 molecules. The ultracold dimers are created from an atomic Bose-Einstein condensate (BEC) by use of a Feshbach ramp [1] and are trapped in a CO_2-laser trap. We precisely measure the magnetic moment of the molecules and observe an avoided crossing [8] which allows us to transfer the molecules into another state. In the new state, we discover two narrow inelastic collision resonances. The resonance structure suggests that bound states of two cesium molecules, or equivalently Cs_4 states, induce the resonant scattering of molecules. These resonances, which we interpret as Feshbach resonances for ultracold molecules, may open the door to the synthesis of more complex molecules and to the control of their chemical reactions.

The relevant molecular energy structure shown in Fig. 1 is based on calculations done at NIST [9,10]. The dissociation threshold, providing the energy reference $E_b = 0$, is associated with two Cs atoms in the lowest ground state sublevel $|F = 3, m_F = 3\rangle$, where F and m_F are the quantum number of the atomic angular momentum and its projection, respectively. As a result of the strong indirect spin-spin interaction of Cs atoms [11], coupling to molecular states with large orbital angular momentum $l = 4$ [10,12] leads to the complexity of the energy structure shown in Fig. 1. This type of coupling is generally referred to as g-wave Feshbach coupling.

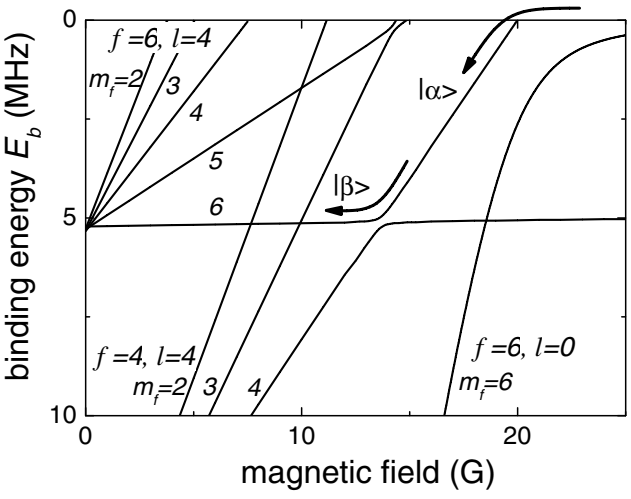

FIG. 1. Molecular energy structure below the scattering continuum of two cesium atoms in the $|F = 3, m_F = 3\rangle$ state. The energy of the dissociation threshold corresponds to $E_b = 0$. The arrows mark the paths to the molecular states we explore, which include the creation of the molecules in $|\alpha\rangle$ via the atomic Feshbach resonance at 19.84 G [1,19] and an avoided crossing to $|\beta\rangle$ at ~13.6 G. Included are only molecular states which can couple to the continuum via Feshbach couplings up to g-wave interaction ($l \leq 4$, $m_f + m_l = 6$ and $m_f \geq 2$).

We create the molecules in the bound state $|\alpha\rangle \equiv |f = 4, m_f = 4; l = 4, m_l = 2\rangle$ via g-wave Feshbach coupling at 19.84 G [1]; see Fig. 1. Here, f is the internal angular momentum of the molecule, and m_f and m_l are the projections of f and l, respectively. The molecular state $|\alpha\rangle$ is stable against spontaneous dissociation for magnetic fields below 19.84 G and acquires larger binding energies at lower magnetic fields. This is due to the small magnetic momentum of $\sim 0.95\mu_B$ of this state as compared to the atomic scattering continuum with $\sim 1.5\mu_B$. At about 14 G, an avoided crossing to another state $|\beta\rangle \equiv |f = 6, m_f = 6; l = 4, m_l = 0\rangle$ is induced by the indirect spin-spin coupling. In this work, we ramp the magnetic field adiabatically and explore the upper branch of the avoided crossing.

Our experiment starts with an essentially pure atomic BEC with up to 2.2×10^5 atoms in a crossed dipole trap formed by two CO_2 laser beams [13,14]. We apply a magnetic field of 20 G, slightly above the Feshbach resonance, and a magnetic field gradient of 31 G/cm to levitate the atoms [15]. The CO_2-laser trap is roughly spherically symmetric with a trapping frequency of $\omega \approx 2\pi \times 20$ Hz and a trap depth of 7 μK. The atomic density is 6×10^{13} cm^{-3} and the chemical potential is $k_B \times 20$ nK, where k_B is Boltzmann's constant.

To create the molecules, we first ramp the magnetic field from 20.0 to 19.5 G in 8 ms and then quickly change the field to 17 G to decouple the molecules from the atoms. Simultaneously, we ramp the magnetic field gradient from 31 up to 50 G/cm. The latter field gradient levitates the molecules [1] and removes all the atoms from the trap in 3 ms. As a consequence, we obtain a pure molecular sample in the CO_2-laser trap with typically 10^4 molecules. The magnetic field ramping process also leads to a small momentum kick on the molecules, which start oscillating in the trap. After ~ 100 ms, the oscillations are damped out and the sample comes to a new equilibrium at a temperature of 250 nK with a peak density of 5×10^{10} cm^{-3} and a phase space density of 10^{-2} to 10^{-3}. To measure the molecule number, we dissociate the molecules into free atoms by reversely ramping the magnetic field back above the resonance to 21 G. We then image the resulting atoms [1].

A key parameter for a perfect levitation of the Cs_2 molecules is the precise value of their magnetic moment [1]. The levitation field is crucial because the gravitational force is much stronger than the trapping force of the CO_2 lasers. In contrast to ground state atoms with only slow-varying magnetic moment, the magnetic moment of the molecules can sensitively depend on the magnetic field as a result of the complex interactions between molecular states; see Fig. 1. Therefore, the prerequisite to perform Cs_2 molecule experiments at different magnetic fields is the knowledge of the molecular magnetic moment for an accurate setting of the levitation field.

We map out the magnetic moment of the molecules over the range of 11.5 to 19.8 G. This is realized by a two-step process: First, we slowly tune the magnetic field in 60 ms to a desired value and find a corresponding magnetic field gradient which can approximately keep the molecules near the center of the CO_2-laser trap. Second, after a hold time of 500 ms needed for the ensemble to come to an equilibrium, we measure the position of the cloud. The location of the molecular cloud provides a very sensitive probe to the residual imbalance of the magnetic force and gravity. Given a small vertical displacement of the molecules relative to the trap center δz for a local magnetic field B and a field gradient B', the magnetic moment is then $\mu(B) = (2m\omega^2\delta z + 2mg)/B'$. Here $2m$ is the molecular mass, and g is the gravitational acceleration. Independent measurements based on releasing the molecules into free space [1] confirm the accuracy of the above method to $0.01\mu_B$.

The measured magnetic moments of the molecules show the expected behavior in the range of 11.5 to 19.8 G; see Fig. 2. We find that the magnetic moment slowly decreases from $0.98\mu_B$ to $0.93\mu_B$ as the magnetic field is lowered from 19.8 G. For magnetic fields below ~ 14 G, the magnetic moment quickly rises and levels off at $1.5\mu_B$. This behavior is readily explained by the avoided crossing at 13.6 G (Figs. 1 and 2), which transfers the molecules from state $|\alpha\rangle$ with $\mu \approx 0.9\mu_B$ to $|\beta\rangle$ with $\mu \approx 1.5\mu_B$. Below 11.5 G, a new avoided crossing to a very weakly coupled $l = 8$ molecular state occurs [16]. We observe fast loss of the molecules since our current apparatus cannot produce a sufficient levitation field to support the molecules against gravity in this new state.

Our measurement agrees excellently with the NIST calculation [9,10] within the 200 mG uncertainty from the multichannel calculation; see Fig. 2. We evaluate the

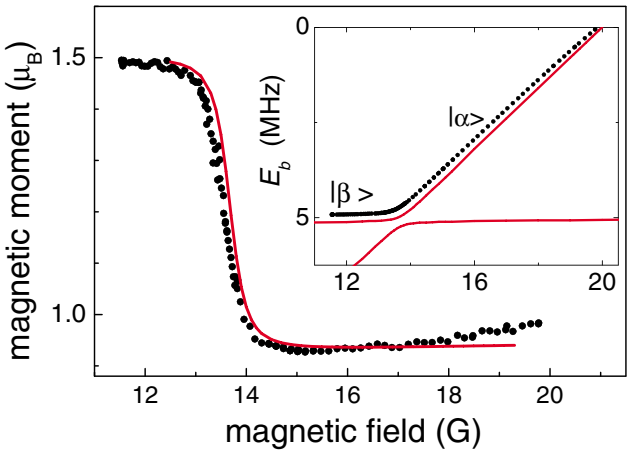

FIG. 2 (color online). Magnetic moment of the Cs_2 molecules. The measured magnetic moment (solid circles) is compared to the NIST calculation (solid line). The fast change at ~ 13.6 G is associated with an avoided crossing. In the inset, we derive the molecular binding energy (solid circles) by integrating the measured magnetic moment. Binding energies from the NIST calculation (solid lines) for both branches of the avoided crossing between state $|\alpha\rangle$ and state $|\beta\rangle$ are shown; see also Fig. 1.

molecular binding energy based on integrating the measured magnetic moments. Here the integration constant is fixed by the fact that the molecular binding energy is zero at the atomic Feshbach resonance $B = 19.84$ G. The result shown in the inset of Fig. 2 gives very good agreement with the theoretical calculation within the energy uncertainty of 0.25 MHz [9]. By fitting our binding energies to a simple avoided crossing model, we determine the crossing to be $B_{\mathrm{cross}} = 13.55(4)$ G and the coupling strength, half the energy splitting between the two eigenstates at B_{cross}, to be $h \times 150(10)$ kHz. Here h is Planck's constant.

To investigate the interactions between molecules, we measure the inelastic collision loss after a trapping time of 300 ms (Fig. 3). For molecules in state $|\alpha\rangle$ ($14\ \mathrm{G} < B < 19.8$ G), the fractional loss is about ~40%. In this molecular state, we do not see any strong magnetic field dependence. When the magnetic field is tuned near the Feshbach resonance at 19.8 G, molecules dissociate into free atoms, which leave the trap.

In state $|\beta\rangle$ ($11.5\ \mathrm{G} < B < 13.6$ G), the behavior of the molecules is strikingly different. We observe a weaker background loss of ~20% and two pronounced resonances with a fractional loss of up to 60%. An expanded view in the inset of Fig. 3 shows that the "double peak" structure can be well fit by a sum of two Lorentzian profiles. From the fit, we determine the resonance positions to be 12.72(1) and 13.15(2) G with full widths of 0.25 and 0.24 G, respectively. Note that due to the levitation gradient field, the inhomogeneity across the molecular sample is as large as 0.15 G in state $|\beta\rangle$, which suggests that the intrinsic widths of these resonances are less than the observed values.

The observed resonances cannot be explained by single-molecule effects based on the Cs_2 energy structure, which is precisely known to very high partial waves [9,10]. Beyond single-molecule effects, the observed resonance structure strongly suggests that bound states of two Cs_2 molecules (Cs_4 tetramer states) are tuned in resonance with the scattering state of the molecules and induce Feshbach-like couplings to inelastic decay channels. Other possible scattering processes, e.g., direct coupling to a trimer and an atom or a dimer and two atoms, should result in a threshold behavior in the loss spectrum instead of the observed resonance structure. For Cs_2 molecules, the appearance of Cs_4 bound states near the scattering continuum is not surprising considering the complexity of interaction between Cs atoms and the additional rotational and vibrational degrees of freedom.

To confirm that the loss is indeed due to collisions between molecules, we observe the decay of the molecular population in the CO_2-laser trap. Starting with 11 000 molecules prepared at different magnetic fields, we record the molecule number after various wait times, as shown in Fig. 4. Three magnetic field values are chosen here: 15.4 G where the molecules are in state $|\alpha\rangle$, 12.1 G where the molecules are in state $|\beta\rangle$ and are away from the resonance, and 12.7 G where the molecules are on the strong molecular resonance; see Fig. 4. The number of trapped molecules shows a nonexponential decay, which provides a clear signature of the density-dependent processes.

To further investigate the underlying molecular collision processes, we model the loss based on a two-body or a three-body loss equation. Assuming a Gaussian distribution for the thermal ensemble in a harmonic trap with a constant temperature and that the collision loss rate is slow compared to the thermalization rate, we fit the measured molecule numbers to the two-body and three-body decay equation; see in Fig. 4. For 15.4 and 12.1 G, we find that the two-body equation provides excellent fits. The two-body

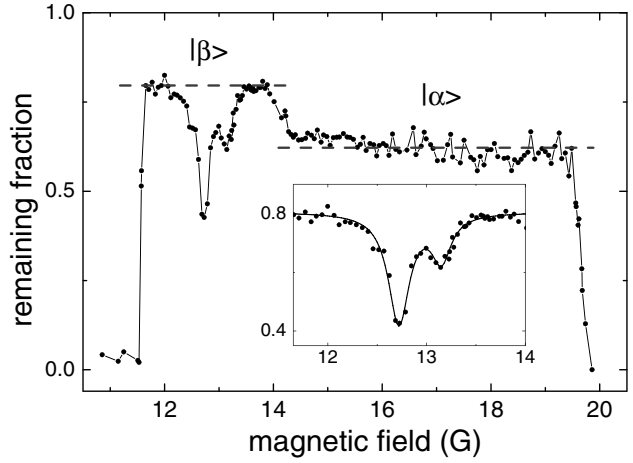

FIG. 3. Remaining fraction of optically trapped molecules after a storage time of 300 ms. Initially, there are 11 000 molecules at a peak density of 6×10^{10} cm^{-3} and a temperature of 250 nK. The dashed lines mark the background loss rates in state $|\alpha\rangle$ and in state $|\beta\rangle$. The two loss resonances for $|\beta\rangle$ are fit by a sum of two Lorentzian profiles (inset).

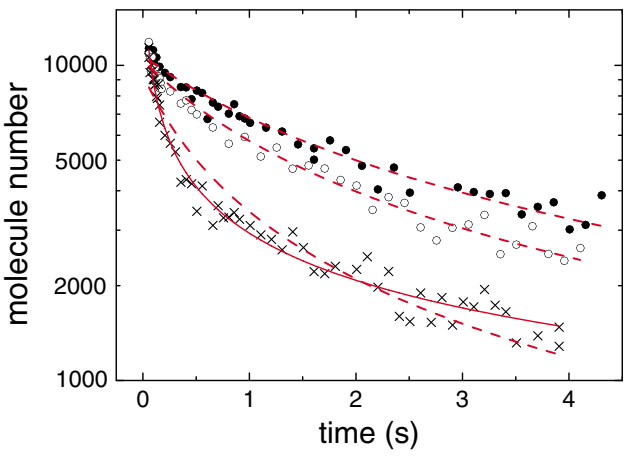

FIG. 4 (color online). Time evolution of the molecule number in the CO_2-laser trap for molecules in state $|\alpha\rangle$ at 15.4 G (open circles), in state $|\beta\rangle$ at 12.1 G (off resonance, solid circles) and at 12.7 G (on resonance, crosses). Fits based on two-body loss (dashed lines) work well for 15.4 and 12.1 G. A fit based on three-body loss (solid line) works better for 12.7 G.

coefficients are 5×10^{-11} cm^3/s at 15.4 G and 3×10^{-11} cm^3/s at 12.1 G. We cannot, however, rule out the possibility that three-body processes also play a role. The measured collision rate coefficients are similar to the measurements from the MIT group on Na_2 [17], and are an order of magnitude below the unitarity limit of $2h/mk = 4 \times 10^{-10}$ cm^3/s, where k is the characteristic collision wave number associated with the temperature of the sample.

At 12.7 G, where the molecules are on the strong resonance, we find that the three-body equation actually provides a better fit than the two-body fit with a three-body loss coefficient at 6×10^{-20} cm^6/s; see Fig. 4. This value, however, is much too high compared to the three-body unitarity limit of $96\pi h/mk^4 = 2 \times 10^{-23}$ cm^6/s [18]. One alternative explanation is that on resonance, the fast collision loss rate might leave the molecules insufficient time to reach thermal equilibrium. By fitting the resonance data in the first 200 ms with the two-body loss model, we determine the two-body loss coefficient to be 2×10^{-10} cm^3/s, which indeed approaches the unitarity limit of 4×10^{-10} cm^3/s.

In conclusion, we have observed magnetically tuned collision resonances in a trapped ultracold sample of Cs_2 dimers. The density-dependent inelastic decay and the resonance structure strongly suggest a resonant coupling to Cs_4 tetramer states. Our observations are reminiscent of Feshbach resonances in atom-atom scattering. The controlled use of such resonances for interaction tuning and molecule formation in atomic ensembles has opened up new avenues in research on ultracold quantum gases. Our observation of magnetically tuned Feshbach-like resonances in molecule-molecule scattering brings in fascinating prospects for a controlled synthesis of ultracold tetramers in a single four-body quantum state in analogy to the formation of ultracold dimers near atomic Feshbach resonances. The tunability of the interactions in molecular quantum gases can potentially open up the door to few-body physics beyond simple atoms and diatomic molecules and to a new ultracold chemistry.

We greatly thank E. Tiesinga and P. S. Julienne for stimulating discussions, and, in particular, for providing us with the theoretical calculation on the Cs_2 energy structure. We acknowledge support by the Austrian Science Fund (FWF) within SFB 15 and the Lise Meitner program, and by the European Union in the frame of the Cold Molecules TMR Network under Contract No. HPRN-CT-2002-00290. M. M. is supported by DOC [Doktorandenprogramm der Österreichischen Akademie der Wissenschaften].

*Present address: Department of Physics and James Franck Institute, University of Chicago, Chicago, IL 60637, USA.

[1] J. Herbig, T. Kraemer, M. Mark, T. Weber, C. Chin, H.-C. Nägerl, and R. Grimm, Science **301**, 1510 (2003).

[2] K. Xu, T. Mukaiyama, J. R. Abo-Shaeer, J. K. Chin, D. E. Miller, and W. Ketterle, Phys. Rev. Lett. **91**, 210402 (2003).

[3] S. Jochim, M. Bartenstein, A. Altmeyer, G. Hendl, S. Riedl, C. Chin, J. Hecker Denschlag, and R. Grimm, Science **302**, 2101 (2003); M. Greiner, C. A. Regal, and D. S. Jin, Nature (London) **426**, 537 (2003); M. W. Zwierlein, C. A. Stan, C. H. Schunck, S. M. F. Raupach, S. Gupta, Z. Hadzibabic, and W. Ketterle, Phys. Rev. Lett. **91**, 250401 (2003).

[4] M. Bartenstein, A. Altmeyer, S. Riedl, S. Jochim, C. Chin, J. Hecker Denschlag, and R. Grimm, Phys. Rev. Lett. **92**, 120401 (2004); C. A. Regal, M. Greiner, and D. S. Jin, Phys. Rev. Lett. **92**, 040403 (2004); M. W. Zwierlein, C. A. Stan, C. H. Schunck, S. M. F. Raupach, A. J. Kerman, and W. Ketterle, Phys. Rev. Lett. **92**, 120403 (2004); T. Bourdel, L. Khaykovich, J. Cubizolles, J. Zhang, F. Chevy, M. Teichmann, L. Tarruell, S. J. J. M. F. Kokkelmans, and C. Salomon, Phys. Rev. Lett. **93**, 050401 (2004).

[5] M. Bartenstein, A. Altmeyer, S. Riedl, R. Geursen, S. Jochim, C. Chin, J. Hecker Denschlag, R. Grimm, A. Simoni, E. Tiesinga, C. J. Williams, and P. S. Julienne, Phys. Rev. Lett. **94**, 103201 (2005); cond-mat/0408673.

[6] J. R. Abo-Shaeer, D. E. Miller, J. K. Chin, K. Xu, T. Mukaiyama, and W. Ketterle, Phys. Rev. Lett. **94**, 040405 (2005).

[7] E. Tiesinga, B. J. Verhaar, and H. T. C. Stoof, Phys. Rev. A **47**, 4114 (1993); S. Inouye, M. Andrews, J. Stenger, H.-J. Miesner, S. Stamper-Kurn, and W. Ketterle, Nature (London) **392**, 151 (1998).

[8] S. Dürr, T. Volz, A. Marte, and G. Rempe, Phys. Rev. Lett. **92**, 020406 (2004).

[9] E. Tiesinga and P. S. Julienne (private communication).

[10] C. Chin, V. Vuletić, A. J. Kerman, S. Chu, E. Tiesinga, P. J. Leo, and C. J. Williams, Phys. Rev. A **70**, 032701 (2004).

[11] F. H. Mies, C. J. Williams, P. S. Julienne, and M. Krauss, J. Res. Natl. Inst. Stand. Technol. **101**, 521 (1996).

[12] C. Chin, A. J. Kerman, V. Vuletić, and S. Chu, Phys. Rev. Lett. **90**, 033201 (2003).

[13] T. Kraemer, J. Herbig, M. Mark, T. Weber, C. Chin, H.-C. Nägerl, R. Grimm, Appl. Phys. B **79**, 1013 (2004).

[14] We adiabatically transfer the atomic BEC from a near-infrared laser trap, where the atomic BEC is formed [13], to the CO_2-laser trap by simultaneously reducing the near-infrared laser power to zero and ramping the CO_2 lasers to full power in 1 s.

[15] T. Weber, J. Herbig, M. Mark, H.-C. Nägerl, and R. Grimm, Science **299**, 232 (2003).

[16] This $l = 8$ state, not shown in Fig. 1, is very weakly coupled to the state $|\beta\rangle$. Investigations on this state are currently in progress.

[17] T. Mukaiyama, J. R. Abo-Shaeer, K. Xu, J. K. Chin, and W. Ketterle, Phys. Rev. Lett. **92**, 180402 (2004).

[18] H. Suno, B. D. Esry, and C. H. Greene, Phys. Rev. Lett. **90**, 053202 (2003).

[19] M. Mark, T. Kraemer, J. Herbig, C. Chin, H.-C. Nägerl, and R. Grimm, Europhys. Lett. **69**, 706 (2005); cond-mat/0409737.

EUROPHYSICS LETTERS 1 March 2005

Europhys. Lett., **69** (5), pp. 706–712 (2005)
DOI: 10.1209/epl/i2004-10427-7

Efficient creation of molecules from a cesium Bose-Einstein condensate

M. Mark[1], T. Kraemer[1], J. Herbig[1], C. Chin[1]
, H.-C. Nägerl[1] and R. Grimm[1,2]

[1] *Institut für Experimentalphysik, Universität Innsbruck*
Technikerstraße 25, 6020 Innsbruck, Austria
[2] *Institut für Quantenoptik und Quanteninformation*
Österreichische Akademie der Wissenschaften - 6020 Innsbruck, Austria

received 29 September 2004; accepted in final form 12 January 2005
published online 2 February 2005

PACS. 03.75.-b – Matter waves.
PACS. 34.50.-s – Scattering of atoms and molecules.
PACS. 32.80.Pj – Optical cooling of atoms; trapping.

Abstract. – We report a new scheme to create weakly bound Cs_2 molecules from an atomic Bose-Einstein condensate. The method is based on switching the magnetic field to a narrow Feshbach resonance and yields a high atom-molecule conversion efficiency of more than 30%, a factor of three higher than obtained with conventional magnetic-field ramps. The Cs_2 molecules are created in a single g-wave rotational quantum state. The observed dependence of the conversion efficiency on the magnetic field and atom density shows scattering processes beyond two-body coupling to occur in the vicinity of the Feshbach resonance.

The newly emerging field of quantum-degenerate molecules provides intriguing possibilities for controlled studies of multicomponent matter-wave systems. Chemical reactions are expected to show effects of coherence, matter-wave interference, quantum tunneling, and bosonic stimulation. Recently, coherent atom-molecule couplings [1] have been observed in a Bose-Einstein condensate (BEC), and molecular quantum gases [2,3] and molecular BECs [4] have been realized. The key ingredient in these experiments has been the presence of magnetically induced Feshbach resonances [5]. These resonances provide the variable coupling between atoms and molecules as a function of an external magnetic field and allow the conversion of atoms to molecules and vice versa.

In the previous experiments on the creation of ultracold Cs_2, Na_2 and Rb_2 molecules from the corresponding atomic BECs [2, 3, 6] the molecules are formed by ramping the magnetic field through a Feshbach resonance; see illustration in fig. 1. It is expected that during the ramping process the ground-state atom population in the trap is adiabatically and efficiently converted into molecules in a weakly bound state [7]. However, the reported efficiencies using this method are relatively low: Typically 5%–10% are observed, whereas up to 50% to 70% of the atoms are lost during the ramping process. The missing fraction, the lost atoms which are not converted into weakly bound molecules, is generally believed to result from the creation

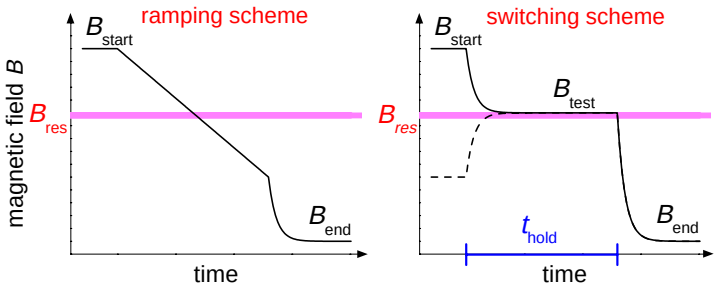

Fig. 1 – Schemes for molecule creation near a Feshbach resonance, located at $B_{\rm res}$. In the ramping scheme, we linearly ramp the magnetic field from $B_{\rm start}$, well above the resonance, to some value well below the resonance, and then quickly to $B_{\rm end}$. In the switching scheme, we first switch from $B_{\rm start}$ to $B_{\rm test}$. After a hold time $t_{\rm hold}$, we switch the field to $B_{\rm end}$. The switching scheme also works for $B_{\rm start}$ below the resonance (dashed line). The finite response time of the magnetic field in our experiment is due to eddy currents in the stainless-steel vacuum chamber.

of molecules in states which cannot be detected by the conventional imaging method, or to consist of "hot" atoms which quickly leave the trap [2,8].

In this paper, we report a high atom-molecule conversion efficiency in excess of 30% from an atomic BEC based on a novel switching scheme. This scheme is illustrated in fig. 1. The magnetic field is quickly switched from an off-resonant value $B_{\rm start}$ to a field $B_{\rm test}$, near the resonance position $B_{\rm res}$. After a variable hold time $t_{\rm hold}$, the magnetic field is quickly lowered well below the resonance $B_{\rm end}$, where atoms and molecules decouple and can be independently measured. Our new scheme works for initial magnetic fields $B_{\rm start}$ both well above or well below the resonance. In the latter case, the creation of molecules cannot be explained in terms of the two-body adiabatic conversion picture [7]. An investigation on the atom loss and molecule creation efficiencies suggests that different scattering processes are involved near the narrow Feshbach resonance.

The cesium molecules we create are of special interest since they have a large orbital angular momentum ($l = 4$). Coupling from ultracold atoms in an s-wave scattering state to the g-wave molecular states is observed only for cesium atoms due to the large indirect spin-spin coupling [9]. Many narrow Feshbach resonances of this kind were observed at low magnetic fields for cesium atoms polarized in the lowest internal state $|F = 3, m_F = 3\rangle$ [10], where F is the total angular momentum and m_F is the magnetic quantum number. Based on these narrow resonances, the formation of thermal molecules was investigated [11] and a pure molecular quantum gas was created from an atomic BEC [2].

Our experiments start with a pure BEC of cesium with up to 2.2×10^5 atoms in the ground state $|F = 3, m_F = 3\rangle$ [12,13]. The magnetic field is set to 21 G, corresponding to an atomic scattering length of $210a_0$, where a_0 is the Bohr radius. The magnetic field gradient is set to 31.3 G/cm for levitation of the atoms [12]. The condensate is confined in a crossed dipole trap formed by two horizontally intersecting laser beams, which are derived from a broad-band Yb fiber laser at 1064 nm. One tightly focused beam with a waist of 35 μm and a power of 0.5 mW essentially provides the radial confinement; the other beam with a waist of 300 μm and power of 350 mW essentially provides the axial confinement. The radial and axial trap frequencies are $\omega_r/2\pi = 17.5$ Hz and $\omega_z/2\pi = 4.7$ Hz, respectively. The chemical potential is $k_{\rm B} \times 11$ nK, where $k_{\rm B}$ is Boltzmann's constant.

Before we start the molecule creation, we first compress the condensate by adiabatically increasing the power of the tightly focused laser in 0.7 s to 40 mW. The higher laser power provides a stronger trapping force and allows us to turn off the levitation field. The absence

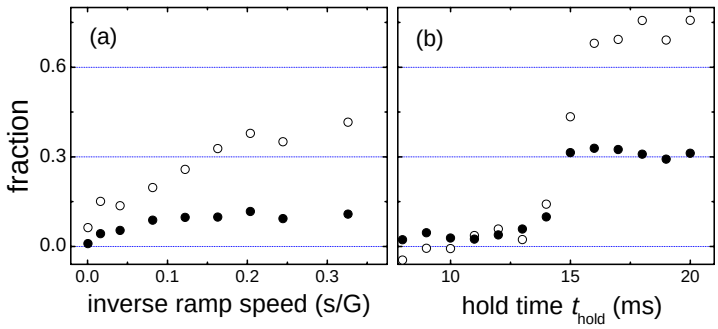

Fig. 2 – Comparison of the two schemes of molecule creation. Molecule fraction (solid circles) and atom loss fraction (open circles) are shown for (a) the ramping scheme, where the fractions are measured for different ramp speeds, and for (b) the switching scheme for different hold times $t_{\rm hold}$. In (b), $B_{\rm test}$ is set right on resonance.

of the magnetic field gradient is crucial to ensure that all atoms experience the same magnetic field and can simultaneously participate in the molecule formation process. In the compressed trap, the trap frequencies are $\omega_r/2\pi = 170\,\mathrm{Hz}$ and $\omega_z/2\pi = 6.5\,\mathrm{Hz}$, the chemical potential is $k_{\rm B} \times 86\,\mathrm{nK}$ and the peak density is $1.7 \times 10^{14}\,\mathrm{cm}^{-3}$. We then slowly change the magnetic field in 200 ms to a starting value of $B_{\rm start}$, typically 0.5 G above the Feshbach resonance $B_{\rm res}$. Note that this 0.5 G offset is much larger than the resonance width of a few mG. The condensate at $B_{\rm start}$ is not influenced by the resonance. We then switch off the dipole trap and release the atoms into free space and, at the same time, tune the magnetic field toward the Feshbach resonance to create molecules. At the end of the molecule formation phase, we quickly lower the magnetic field down to $B_{\rm end} \approx 18\,\mathrm{G}$ to decouple the molecules and atoms.

The resulting molecule and atom numbers can be determined independently by absorption imaging [2]. The atoms are directly imaged at 18 G. We verify that the molecules are insensitive to the imaging beam at this magnetic field. To detect the molecules, we first blast away the atoms at 18 G with a resonant beam [3], and then ramp the magnetic field back above the resonance to 21 G. The weakly bound molecular state is then above the continuum and the molecules quickly dissociate into free atoms [14]. By imaging the cloud of the resulting atoms, we can determine the molecule number. We define the corresponding molecule fraction as the number of atoms detected after dissociation normalized to the initial atom number. This is then, by definition, equal to the atom-molecule conversion efficiency.

We employ both the ramping scheme and the switching scheme for molecule production (see fig. 1) and compare their performances. In the ramping scheme, we tune the magnetic field across the resonance with a constant ramping speed. Based on the resulting molecule number and the loss in atomic number, we calculate the conversion fractions, shown in fig. 2(a). A maximum molecule fraction of 10% is observed when the ramps are slower than 10 G/s. The atom loss for these ramps is about 40%, which indicates a missing fraction of about 30%. This result is similar to all previous experiments using the same method [2, 3, 6]. For the switching scheme, we quickly tune the magnetic field onto the Feshbach resonance $B_{\rm test} \approx B_{\rm res}$, wait for various hold times $t_{\rm hold}$, and quickly lower the magnetic field to $B_{\rm end} = 18\,\mathrm{G}$. Due to the finite response time of the magnetic field, the field approaches the Feshbach resonance after about 12 ms [15]. At this time, the peak density of the expanding condensate reduces to $1.1 \times 10^{12}\,\mathrm{cm}^{-3}$ [16]. For hold times $t_{\rm hold} > 15\,\mathrm{ms}$, molecule fractions of $30 \sim 35\%$ and atom loss fractions of $\sim 70\%$ are reached as shown in fig. 2(b). The conversion efficiency is by more than a factor of three higher than obtained from the ramping scheme. Note that in order

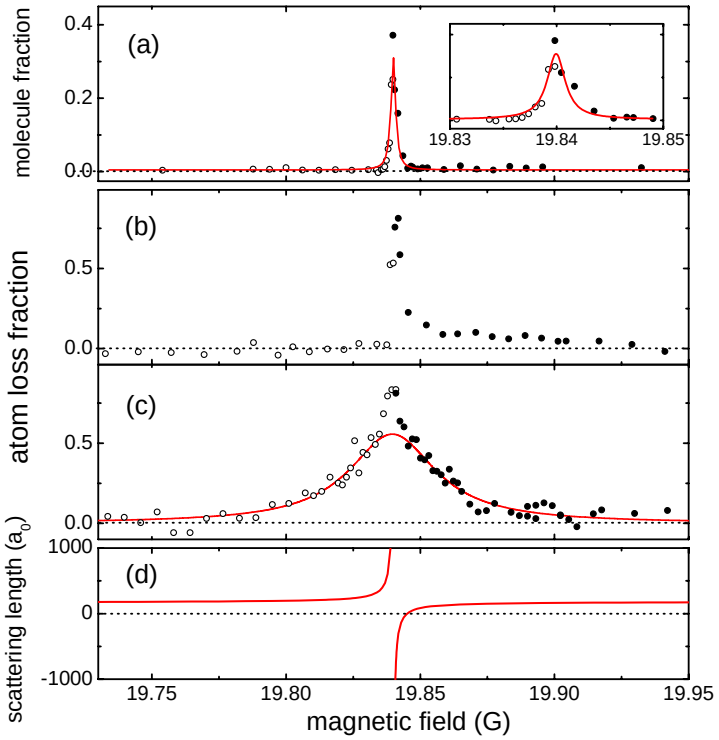

Fig. 3 – Molecule creation and atom loss near the Feshbach resonance. Based on the switching scheme, molecule increase in $t_{\rm hold} = 18\,{\rm ms}$ (a) and atom loss in 18 ms (b) are measured for various test fields $B_{\rm test}$. The inset shows the expanded view of the molecule signal. For comparison, the atom trap loss in the compressed trap is shown in (c). The scattering length is shown in (d) for reference. Solid circles (open circles) show the measurements above (below) the resonance. In (a), a Lorentzian fit (solid line) yields a width of 2.1 mG and the resonance position of $B_{\rm res} = 19.840\,{\rm G}$, subject to a calibration uncertainty of 4 mG. Fitting both wings in (c) gives a Lorentzian width of 40(2) mG.

to precisely set the magnetic field right on the narrow Feshbach resonance, we synchronize the experiment with the 50 Hz line voltage to reduce the effects of the ambient magnetic-field ripple, for which we measure an amplitude of 4 mG. This suppresses uncontrolled magnetic-field variations to about 1 mG.

To understand the different performance of the two schemes, we study the atom loss and molecule increase at different magnetic fields $B_{\rm test}$ based on the switching scheme, see fig. 3(a) and (b). For comparison, we also show the atom loss in the compressed trap in fig. 3(c), where the initial peak density is $1.9 \times 10^{14}\,{\rm cm}^{-3}$ [17]. The calculated scattering length is shown in fig. 3(d) [18]. For all measurements with $B_{\rm test}$ above the resonance, we prepare the condensate as previously described at $B_{\rm start} = B_{\rm res} + 0.5\,{\rm G}$. For $B_{\rm test}$ below the resonance, we prepare the condensate at a magnetic field below the resonance by quickly switching the magnetic field from the initial value to $B_{\rm res} - 0.5\,{\rm G}$. No appreciable atom loss, molecule formation or condensate excitation is observed in this process. We then follow the same experimental procedure, but approach the resonance from below. These two different preparation procedures for magnetic fields above and below the resonance are necessary to avoid a slow field-sweep across the resonance, which can lead to systematic atom loss or molecule increase.

In the molecule creation spectrum (fig. 3(a)) we observe a very narrow linewidth of 2.1 mG, which is consistent with the predicted resonance width. Notably, our molecule creation scheme also works for $B_{\rm start}$ below the resonance, which suggests that coupling beyond the adiabatic

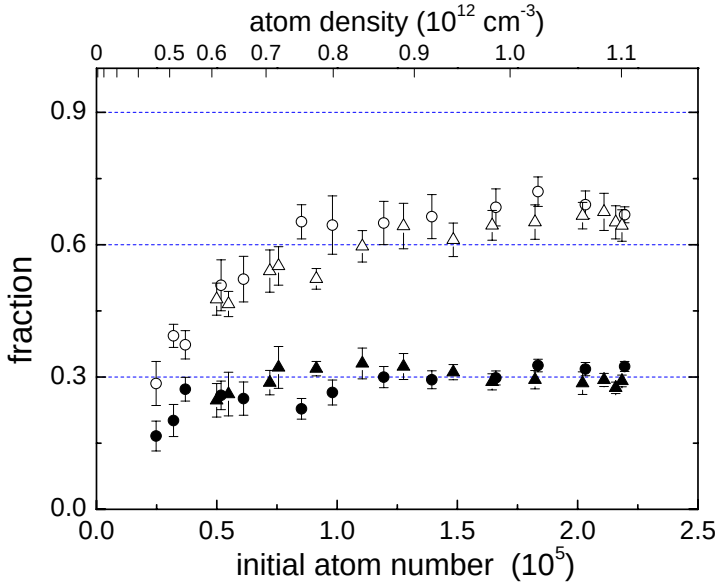

Fig. 4 – Density dependence of the atom loss fraction (open symbols) and molecule fraction (solid symbols). The atom number in the BEC is varied by either adjusting optical cooling efficiencies (solid and open circles) or the loading efficiencies into the crossed dipole trap (solid and open triangles). The corresponding atomic density of the sample right before the molecule formation (after 12 ms expansion in free space) is given on the top axis.

conversion model plays an important role in the creation process. In the adiabatic passage picture, molecules cannot be created when the creation field is below the resonance. The atom loss, shown in fig. 3(b), is asymmetric and seems to include two components, a narrow peak on resonance and a much broader and weaker loss feature for magnetic fields above the resonance. The narrow peak has a similar width as in the molecule production spectrum in fig. 3(a), and is clearly related to the observed molecule formation. The broad and weak feature on the high magnetic-field side has a width of 80(20) mG as determined from a one-sided Lorentzian fit. To obtain further information about the atom loss process, we measure the atom loss in the compressed trap, where the atom density is higher by a factor of ~ 170 than in fig. 3(a) and (b). The result shown in fig. 3(c) displays a wide and symmetric loss feature. By fitting the two wings to a Lorentzian profile, we find a width of 40(2) mG.

The different lineshapes suggest that different scattering processes are involved near the Feshbach resonance. The molecule formation width is close to the predicted width of the Feshbach resonance and can be interpreted in terms of the two-body Feshbach coupling. The asymmetric loss feature in fig. 3(b) and the trap loss may be due to three-body recombination or many-body effects. These broad atom loss features are puzzling, since they are a factor of 20 or more wider than the Feshbach resonance width of 2 mG. The physical origin of the associated loss mechanisms requires further investigation.

The large width of the atom loss feature, however, does provide a qualitative explanation why the switching scheme is more efficient than the ramping scheme. In a linear ramp, atoms sample all magnetic fields near the resonance which, for a large fraction of time, leads to atom loss without molecule increase. With the switching scheme, the atoms spend more time in the magnetic-field range where the molecules can be created.

To further investigate and differentiate the physical mechanisms that are responsible for the missing fraction and for the molecule increase, we measure the dependence of the atom loss

fraction and molecule fraction on the atom number in the condensate, as shown in fig. 4. Atom numbers ranging from 2.5×10^4 to 2.2×10^5 correspond to peak densities of $7.9 \times 10^{13}\,\mathrm{cm}^{-3}$ to $1.9 \times 10^{14}\,\mathrm{cm}^{-3}$ in the compressed trap and to $4.6 \times 10^{11}\,\mathrm{cm}^{-3}$ to $1.1 \times 10^{12}\,\mathrm{cm}^{-3}$ in free space at the moment the molecules are created. For the calculation of the densities in free space, we take into account the 12 ms expansion of the condensate in the Thomas-Fermi regime after the dipole trap is turned off.

Several interesting features show up in the density dependence. The molecule fraction grows and saturates to $\sim 30\%$ at densities higher than $5 \times 10^{11}\,\mathrm{cm}^{-3}$. The saturation of the molecule fraction resembles observations in a thermal gas [11,19], where a thermal equilibrium is reached with a constant molecule fraction in the sample [20]. The missing fraction is very small at low densities and continues to grow up to a density of $8 \times 10^{12}\,\mathrm{cm}^{-3}$. The stronger density dependence of the missing fraction suggests that scattering processes involved in the atom loss are of higher order than for the molecule increase. Similar enhancement of the collision loss near the Feshbach resonance was also observed in a ^{85}Rb condensate [21] and in a thermal Cs gas [22]. A further analysis on the scattering dynamics and the possible thermal equilibrium condition is necessary.

In conclusion, we show that an atom-molecule conversion fraction of more than 30% can be reached based on a magnetic-field switching scheme. The performance of this scheme is superior to the conventional linear magnetic-field ramping scheme since the molecules are created only within the narrow Feshbach resonance width of 2 mG, while the atoms are lost over a much large range of ~ 40 mG. The density dependence of both the missing fraction and the molecule fraction suggests that in our scheme the molecules are created via Feshbach coupling, while the missing fraction comes from higher-order scattering processes. Based on the new creation scheme, we are now able to obtain samples with up to 40000 ultracold molecules. This provides a good starting point to investigate the trapping, the interactions, and the matter-wave nature of ultracold molecules.

* * *

We acknowledge support by the Austrian Science Fund (FWF) within SFB 15 (project part 16) and by the European Union in the frame of the Cold Molecules TMR Network under Contract No. HPRN-CT-2002-00290. MM is supported by DOC (Doktorandenprogramm der Österreichischen Akademie der Wissenschaften). CC is a Lise-Meitner research fellow of the FWF.

REFERENCES

[1] Donley E. A., Claussen N. R., Thompson S. T. and Wieman C., *Nature*, **412** (2002) 295.
[2] Herbig J., Kraemer T., Mark M., Weber T., Chin C., Nägerl H.-C. and Grimm R., *Science*, **301** (2003) 1510.
[3] Xu K., Mukaiyama T., Abo-Shaeer J. R., Chin J. K., Miller D. E. and Ketterle W., *Phys. Rev. Lett.*, **91** (2003) 210402.
[4] Jochim S., Bartenstein M., Altmeyer A., Hendl G., Riedl S., Chin C., Hecker Denschlag J. and Grimm R., *Science*, **302** (2003) 2101; published online November 13, 2003 (10.1126/science.1093280); Greiner M., Regal C. A. and Jin D. S., *Nature*, **426** (2003) 537; Zwierlein M. W., Stan C. A., Schunck C. H., Raupach S. M. F., Gupta S., Hadzibabic Z. and Ketterle W., *Phys. Rev. Lett.*, **91** (2003) 250401.
[5] Tiesinga E., Verhaar B. J. and Stoof H. T. C., *Phys. Rev. A*, **47** (1993) 4114; Inouye S., Andrews M., Stenger J., Miesner H.-J., Stamper-Kurn S. and Ketterle W., *Nature*, **392** (1998) 151.

[6] Dürr S., Volz T., Marte A. and Rempe G., *Phys. Rev. Lett.*, **92** (2004) 020406.
[7] Kokkelmans S. J. J. M. F., Vissers H. M. J. and Verhaar B. J., *Phys. Rev. A*, **63** (2001) 031601(R); van Abeelen F. A. and Verhaar B. J., *Phys. Rev. Lett.*, **83** (1999) 1550; Tiesinga E., Williams C. J., Mies F. H. and Julienne P. S., *Phys. Rev. A*, **61** (2000) 063416.
[8] Regal C. A., Ticknor C., Bohn J. L. and Jin D. S., *Nature*, **424** (2003) 47.
[9] Mies F. H., Williams C. J., Julienne P. S. and Krauss M., *J. Res. Natl. Inst. Stand. Technol.*, **101** (1996) 521.
[10] Chin C., Vuletić V., Kerman A. J., Chu S., Tiesinga E., Leo P. and Williams C. J., *Phys. Rev. A*, **70** (2004) 032701.
[11] Chin C., Vuletić V., Kerman A. J. and Chu S., *Phys. Rev. Lett.*, **90** (2003) 033201.
[12] Weber T., Herbig J., Mark M., Nägerl H.-C. and Grimm R., *Science*, **299** (2003) 232.
[13] Kraemer T., Herbig J., Mark M., Weber T., Chin C., Nägerl H.-C. and Grimm R., *Appl. Phys. B*, **79** (2004) 1013. For the present experiment, we have improved the atom number in the BEC by another factor two using the higher power from a new Yb fiber laser.
[14] Mukaiyama T., Abo-Shaeer J. R., Xu K., Chin J. K. and Ketterle W., *Phys. Rev. Lett.*, **92** (2004) 180402; Dürr S., Volz T. and Rempe G., *Phys. Rev. A*, **70** (2004) 031601(R).
[15] The response time of $t_{1/e} = 1.54\,\mathrm{ms}$ for the magnetic field is limited by the eddy currents from the vacuum chamber. Starting from 500 mG above the resonance, we estimate the magnetic field will take $\ln(500\,\mathrm{mG}/2\,\mathrm{mG})t_{1/e} \approx 9\,\mathrm{ms}$ to settle within the resonance width. This result is close to the measured delay time of 12 ms.
[16] We observe that the expansion rate of the molecules is very close to that of the expanding condensate.
[17] This value is slightly higher than the value given before because of the reduced scattering length.
[18] The calculated resonance position is 20.1 G. To reflect the correct resonance position, we shift the numerical data by centering the resonance at our observed value of 19.84 G.
[19] Jochim S., Bartenstein M., Altmeyer A., Hendl G., Chin C., Hecker Denschlag J. and Grimm R., *Phys. Rev. Lett.*, **91** (2003) 240402.
[20] Chin C. and Grimm R., *Phys. Rev. A*, **69** (2004) 033612.
[21] Roberts J. L., Claussen N. R., Cornish S. L. and Wieman C. E., *Phys. Rev. Lett.*, **85** (2000) 728.
[22] Weber T., Herbig J., Mark M., Nägerl H.-C. and Grimm R., *Phys. Rev. Lett.*, **91** (2003) 123201.

Appl. Phys. B 79, 1013–1019 (2004)
DOI: 10.1007/s00340-004-1657-5

Applied Physics B
Lasers and Optics

T. KRAEMER[1]
J. HERBIG[1]
M. MARK[1]
T. WEBER[1]
C. CHIN[1]
H.-C. NÄGERL[1,✉]
R. GRIMM[1,2]

Optimized production of a cesium Bose–Einstein condensate

[1] Institut für Experimentalphysik, Universität Innsbruck, Technikerstraße 25, 6020 Innsbruck, Austria
[2] Institut für Quantenoptik und Quanteninformation, Österreichische Akademie der Wissenschaften, 6020 Innsbruck, Austria

Received: 11 August 2004
Published online: 6 October 2004 •

ABSTRACT We report on the optimized production of a Bose–Einstein condensate of cesium atoms using an optical trapping approach. Based on an improved trap loading and evaporation scheme we obtain more than 10^5 atoms in the condensed phase. To test the tunability of the interaction in the condensate we study the expansion of the condensate as a function of scattering length. We further excite strong oscillations of the trapped condensate by rapidly varying the interaction strength.

PACS 03.75.Kk; 32.80.Pj

1 Introduction

Much of the present work in the field of quantum gases relies on optical trapping techniques and on the ability to tune atomic interactions. Optical approaches have been recently employed in several atomic Bose–Einstein condensation experiments [1–5] and in experiments on the production of ultracold molecular samples [6–10] and on molecular Bose–Einstein condensates [11, 12]. The major advantages in optical traps are the possibility to trap atoms in any sublevel of the electronic ground state and the ease to adjust the interaction strength using magnetically induced Feshbach resonances.

The cesium atom is very attractive for experiments with tunable atomic interactions. The lowest internal quantum state of Cs features a unique combination of wide and narrow Feshbach resonances which are easily accessible at low magnetic fields [13]. This results in a great flexibility for tuning the atomic scattering properties. In particular, magnetic tuning of the interaction strength has recently allowed the first realization of a Bose–Einstein condensate (BEC) with Cs atoms [4] and the realization of a two-dimensional condensate very close to a dielectric surface [5]. The tunability of the atomic interaction can be exploited in experiments where one might wish to adjust or to dynamically change the mean-field interaction of the condensate. Also, the Feshbach resonances can be used to produce molecules from an atomic BEC [8–10, 14] and to study the transition from an atomic BEC to a molecular BEC. In this context, a quantum phase transition with an essentially topological character has been predicted [15, 16]. For such and many other intriguing experiments it is desirable to have a large BEC of Cs atoms as a starting point.

In this paper we report on the optimized production of an essentially pure Cs BEC in the lowest internal quantum state with more than 10^5 atoms. Since this state cannot be trapped by purely magnetic means, the path to condensation relies on a sequence of optical traps. We discuss the loading and transfer from one trap to the next and give a detailed description of the evaporation path and of the resulting condensate. As a demonstration for tunability, we measure the expansion energy as a function of scattering length in time-of-flight experiments. In particular, we show the ultra-slow expansion of the condensate after release from the trap for nearly vanishing scattering length. The release energy corresponds to ~ 50 pK. Finally, we present first results when the scattering length is suddenly stepped and the condensate then starts to oscillate freely in the trap.

2 Cesium scattering properties and Feshbach resonances

Early experiments [17, 18] towards condensation of cesium focused on samples in magnetic traps polarized either in the upper hyperfine ground state $F = 4$, magnetic sublevel $m_F = 4$, or in the lower hyperfine state $F = 3$, $m_F = -3$. Here, F denotes the total angular momentum and m_F the magnetic quantum number. The spin relaxation rates were measured to be several orders of magnitude higher than expected [19–21]. It was later understood that this is caused by the dipolar relaxation process induced by the second-order spin–orbit interaction [22]. The maximum phase-space density in a small sample of Cs atoms was a factor of about four away from condensation [23].

The problem of the strong inelastic two-body losses can be overcome by using the lowest internal state of cesium, $F = 3$, $m_F = 3$ [24–27]. In this state, all inelastic two-body processes are endothermic and are thus fully suppressed at sufficiently low temperature. This state requires optical trapping since it cannot be captured in a magnetic trap. Optically trapped atoms can only be efficiently evaporated by lowering the total potential depth. This process weakens the confine-

✉ Fax: +43-512-507-2921, E-mail: christoph.naegerl@uibk.ac.at

ment of the trapped sample and thus makes it difficult to achieve sufficiently high elastic collision rates for effective evaporation. Hence, adjustability of the collisional properties is very helpful for a fast evaporation strategy.

The success in condensing Cs [4] largely relies on the fact that the s-wave scattering length for the $F = 3, m_F = 3$ state can be tuned to moderate and positive values by the application of relatively low dc magnetic fields [13]. As Fig. 1 shows, an external magnetic field allows for precise tuning of the atomic scattering length a from negative to positive values. Positive scattering lengths in the range between zero and one thousand a_0 are attained for magnetic fields of a few ten Gauss; a_0 denotes Bohr's radius. In particular, there is a gentle zero-crossing of the scattering length near 17 G [25]. Here, the interaction of atoms in a BEC is effectively switched off. Several narrow higher-order Feshbach resonances [13], caused by coupling to d- and g-wave molecular states, enable very rapid control of the atomic scattering properties. With the magnetic field being a free parameter in our optical trapping approach, we can take full advantage of this tunability of the s-wave scattering length.

For Cs in the $F = 3, m_F = 3$ ground state the process of three-body recombination is the dominant loss and heating mechanism [28]. In a recombination process, three atoms collide, two of them form a molecule, and the third atom takes away two thirds of the binding energy according to energy and momentum conservation. The atoms that form the molecule are usually lost, and the third atom is either lost or it deposits its share of the binding energy in the sample. Heating of the sample is the combination of "anti-evaporation" and recombination heating [28]. To a good approximation, the three-body recombination rate scales with the fourth power of the scattering length. Unfortunately, the prefactor in this scaling law is measured to be relatively large [28]. To minimize this heating, the recombination products should be removed quickly from the trap. It is thus important to assure that the sample is not operated too deeply in the hydrodynamic regime and that the evaporation is efficient in all directions. Arbitrarily increasing the scattering length to speed up the forced evaporation is therefore not possible without sacrificing cooling efficiency. Within these limits, tuning the scattering length allows for an optimization of the evaporation for given trap parameters. For example, for the low initial densities in a large reservoir trap the evaporation may be sped up by increasing the scattering length. In a later trapping stage with a higher atomic density the scattering length should be reduced to optimize the ratio of good to bad collisions.

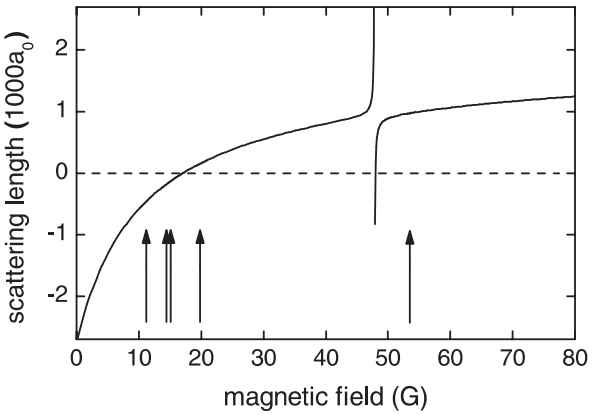

FIGURE 1 Scattering length as a function of magnetic field for the state $F = 3, m_F = 3$. There is a relatively broad Feshbach resonance at 48.0 G due to coupling to a d-wave molecular state. The *arrows* indicate several very narrow resonances at 11.0, 14.4, 15.0, 19.9 and 53.5 G, which result from coupling to g-wave molecular states. The data are taken from [13]

3 BEC production

3.1 *Overview of experimental strategy*

For producing large condensates in optical dipole traps, it is necessary to independently optimize both trap loading and evaporative cooling. For initial loading of as many atoms as possible, an optical trap with large volume is needed which, in view of limited laser power, implies a shallow trapping potential. For subsequent forced evaporative cooling, however, high densities and fast elastic collisions require much tighter confinement. These two requirements in general demand dynamical changes of the trapping potential. A possible way to implement this is a spatial compression of the optical trap using e.g., a zoom-lens system [29]. Our approach is based on an alternative way where a sequence of optical trapping schemes is used to provide optimized loading together with optimized evaporative cooling.

We first use a shallow, large volume CO_2-laser trap as a "reservoir" for collecting the atoms before forced evaporative cooling is implemented in a tighter trap. The reservoir trap can be efficiently loaded with atoms that are precooled by Raman-sideband cooling [30]. This approach allows for the collection of atoms at moderate densities with little loss from three-body collisions and with negligible heating from either photon scattering or trap vibrations. It serves as a good starting point for the final transfer into a tighter optical trap. The tighter trap is adiabatically increased and adds a "dimple" to the trapping potential of the reservoir. Collisional loading of this dimple already yields a significant enhancement of the local number and phase-space density [31]. After turning off the reservoir trap excellent conditions for further forced evaporative cooling are obtained.

The different trap stages of optical trapping used in our experiments are illustrated in Fig. 2. An overview of the evolution of phase-space density and particle number for the various trapping stages is shown in Fig. 3.

The use of relatively weak optical trapping necessitates the implementation of magnetic "levitation" where a magnetic field gradient along the vertical direction compensates for the gravitational force. This levitation turns out to be very useful in two ways: First, in the limit of very weak optical trapping only one spin state is held in the trap. This assures perfect spin polarization of the sample[1]. Further, efficient evaporation can be performed without the effect of gravitational sag in the trap. The dc magnetic field offset remains a free parameter for flexible tuning of the scattering length.

[1] This Stern–Gerlach separation technique also allows for radio-frequency evaporation along the vertical direction. Although one-dimensional, this type of evaporation has been applied to produce ultracold Cs atoms for studying three-body collisions [28].

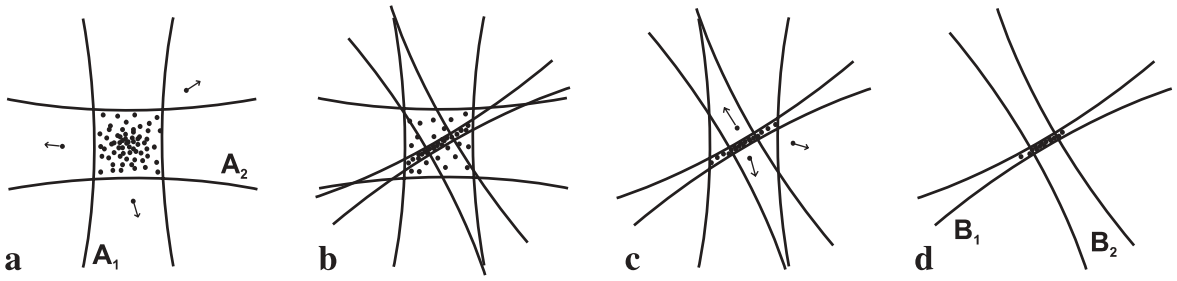

FIGURE 2 Illustration of the various stages of trap loading and evaporative cooling as seen from above. (**a**) Plain evaporation in a crossed CO_2-laser trap generated by beams A_1 and A_2 at a scattering length of $a = 1215\,a_0$. (**b**) 1.5 s of ramping and collisional loading into a crossed 1064-nm fibre laser trap generated by beams B_1 and B_2 with a final scattering length $a = 210\,a_0$. (**c**) Forced evaporative cooling after switching off CO_2-laser beam A_2. The power of all remaining lasers is ramped down, and the power in CO_2-laser beam A_1 is reduced to zero. (**d**) Final configuration of the crossed 1064-nm trap. Imaging is done in the horizontal plane at an angle of 30° with respect to the long axis of the cigar-shaped atomic cloud

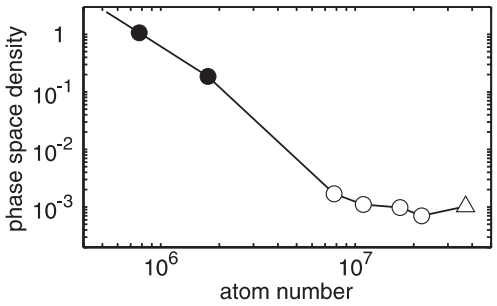

FIGURE 3 Peak phase space density as function of atom number. The path of evaporation proceeds from right to left. The *triangle* shows the atomic ensemble immediately after lattice cooling. The *open circles* show the ensemble in the reservoir trap after 0.08, 0.22, 0.64, and 2.0 s. The *filled circles* correspond to the sample in dimple trap right after loading and after 1.5 s of evaporation. The phase transition occurs after 2 s of forced evaporation with $\sim 5 \times 10^5$ atoms left in the dimple trap

3.2 *Laser cooling*

The initial collection and cooling of Cs atoms is achieved by conventional techniques. In a stainless steel vacuum chamber [32] atoms are loaded into a magneto-optical trap (MOT) from a Zeeman slowed atomic beam with up to 3×10^8 atoms after about 6 s. The MOT is operated on the $6^2S_{1/2}$, $F = 4$ to $6^2P_{3/2}$, $F' = 5$ transition. The ultra-high vacuum of less than 1×10^{-11} mbar gives 200 s for the 1/e-lifetime of the MOT. The MOT light is derived from a high power laser diode[2] referenced via beat-lock to a grating-stabilized master diode laser. Standard absorption imaging is used to determine particle numbers and temperatures.

We compress the atomic cloud by ramping up the magnetic field gradient in the MOT by a factor of five to 33 G/cm within 40 ms. Simultaneously we linearly change the detuning of the MOT laser from around 10 MHz to 30 MHz. At the end of the ramp, we switch off the MOT light and the magnetic field gradient. To cool the compressed cloud, we then apply degenerate Raman-sideband cooling [30] in an optical lattice to further cool and to polarize the atoms in the desired $F = 3, m_F = 3$ state. We have adapted the technique as described in [33] to our setup. This cooling scheme is particularly suited for polarizing atoms in the $F = 3, m_F = 3$ state because this is a dark state for which photon scattering is suppressed. Four laser beams derived from an injection locked slave laser resonant with the $F = 4$ to $F' = 4$ transition produce a three-dimensional optical lattice, drive Raman-sideband transitions and repump out of the $F = 4$ ground state manifold. The total power of all the four beams is 65 mW and their $1/e^2$-beam radii are about 1 mm. The oscillation frequency in the lattice is on the order of 100 kHz. A small magnetic field offset of several hundred mG is applied to induce the Raman-sideband cooling. We succeed in polarizing 90% of the atoms. The ensemble is then adiabatically released from the lattice after 6 ms of cooling time. If the atomic cloud is released into free space, the temperature of the ensemble with up to 4×10^7 atoms is about 0.7 μK. For our typical atomic densities this corresponds to a phase space density of 1×10^{-3}.

3.3 *Reservoir trap*

We generate the large reservoir trap by horizontally crossing two CO_2-laser beams A_1 and A_2 at right angles as shown in Fig. 2a. At the same time we apply a magnetic gradient field in the vertical direction to levitate the atoms against gravity. The delivered powers in laser beams A_1 and A_2 are 90 W and 65 W, respectively. The light comes from two separate, highly stable linearly polarized single-frequency CO_2-lasers[3]. Switching of the beams is done by external acousto-optical modulators[4] (AOMs). A_1 is downshifted in frequency by 40 MHz, whereas A_2 is upshifted by 40 MHz to prevent any interference. To avoid mode-hops the cooling water for the lasers needs to be stabilized to better than ±20 mK. Still, a slow mode drift changes the power of the lasers by a few percent over the time scale of minutes. At the crossing point the $1/e^2$-beam radii of the two lasers are (605 ± 35) μm and (690 ± 35) μm.

The magnetic fields for levitation and for Feshbach tuning are generated by two pairs of coils aligned with their axes parallel to the vertical direction. One pair in anti-Helmholtz configuration produces the vertical magnetic field gradient near 31.3 G/cm to levitate the atoms in the $F = 3, m_F = 3$ state. Another pair in Helmholtz configuration provides a variable bias field B_0 of up to 200 G. The combined field results in a weak outward directed force $F(\varrho) = m\alpha^2\varrho$ depend-

[2] SDL-5712-H1

[3] Coherent-DEOS GEM-100L

[4] Intraaction AGM-408BB1M

ing on the horizontal distance ϱ from the vertical symmetry axis. For perfect levitation of our atoms the constant $\alpha = g\sqrt{m/(3\mu_B B_0)}$ describes the curvature of the parabolic anti-trapping potential. The levitation field thus slightly reduces the trap depth along the horizontal direction. Here, m is the mass of Cs, g is the gravitational acceleration, and μ_B is Bohr's magneton. At $B_0 = 17$ G we have $\alpha = 2\pi \times 3.4$ Hz. The horizontal trap frequencies $\omega_{x,y}$ are reduced according to $\omega'_{x,y} = \sqrt{\omega^2_{x,y} - \alpha^2}$. This is usually a very small effect for all but the lowest trap frequencies. Note that levitation also affects the horizontal motion of free atoms after the optical trap is shut off. The horizontal motion follows $\varrho(t) = \varrho_0 \cosh(\alpha t) + \alpha^{-1} v_0 \sinh(\alpha t)$ for initial position ϱ_0 and initial velocity v_0. The vertical motion is not affected.

We excite vertical trap oscillations by briefly changing the vertical magnetic field gradient and hence tilting the trap. For exciting horizontal trap oscillations we shift the equilibrium position of the atoms by adding a horizontal magnetic field component. In both cases we monitor the center-of-mass oscillation of the atomic cloud after 50 ms time-of-flight. The geometrically averaged trap frequency $\bar{\nu}$ is calculated to be (12.6 ± 1.5) Hz which is in good agreement with the experimental value of (13.2 ± 0.2) Hz. Together with the levitation and the magnetic bias field the lasers provide an effective trap depth of about $k_B \times 7$ μK. This trap depth is given by the weaker of the two CO_2-lasers as the atoms can escape along the direction of the stronger beam.

For transfer of the precooled atoms into the reservoir trap, we leave the light of the two CO_2-lasers on during the entire pre-cooling phase. This is because the CO_2-lasers show strong variations in beam pointing and beam shape as a function of radio-frequency power to the AOMs. We have checked that the small light shift introduced by the lasers does not affect the initial loading and cooling efficiency. The reservoir trap is then activated by ramping up the magnetic field and its gradient. The 1/e-rise time of the magnetic fields is limited to 1.5 ms because of eddy currents in the stainless steel chamber. We, therefore, do not expect the transfer to be fully adiabatic.

We find that the atoms are heated to about 2.2 μK by the transfer into the reservoir trap. A clear measurement on the trapped sample is only possible after about 50 ms since the system initially is not in thermal equilibrium and since the untrapped atoms need to disappear from the field of view. We largely attribute the heating to imperfect phase space matching. In fact, the atomic cloud after Raman-sideband cooling to 0.7 μK has a 1/e-radius of ~ 350 μm. In comparison, an equilibrium distribution in the reservoir trap at 0.7 μK would have a 1/e-radius of ~ 100 μm. Potential energy is thus gained which is then turned into kinetic energy, effectively heating the cloud of atoms. Subsequently, the hot atoms evaporate out of the trap. For this phase of plain evaporation we set the magnetic bias field to 73.5 G. The scattering length is then 1215 a_0. The temperature is reduced to less than 1 μK within 10 s. After this time, we measure more than 4×10^6 atoms, corresponding to a peak phase space density of 2×10^{-3}.

3.4 *Dimple trap*

We proceed with loading of the dimple trap after 2 s of plain evaporation in the reservoir trap. At this point the atom number is 7.8×10^6 and the phase space density is 1.7×10^{-3} (see Fig. 3). The dimple trap is generated by horizontally intersecting one tightly focused laser beam B_1 with 34-μm waist and another less focused beam B_2 with 260-μm waist at right angles, rotated by 30° in the horizontal plane with respect to the CO_2-laser beams as shown in Fig. 2d. This is different from our earlier work [4] where we have used CO_2-laser beam A_2 for axial confinement. We introduce the B_2 beam because some weak back reflections of the CO_2-laser beams led to a slight undesirable corrugation of the optical potential. This complicated the quantitative analysis of the BEC. Beams B_1 and B_2 are derived from a broadband fiber laser[5] at 1064 nm. The powers in these beams are ramped up within 1.5 s to a maximum power of 70 mW for B_1 and 270 mW for B_2. The trapping in the dimple is now briefly done by all four laser beams with B_1 providing most of the radial and A_1 most of the axial confinement. After switching off beam A_2, we measure the radial and axial trap frequencies in the dimple to (221.2 ± 1.6) Hz and (14.2 ± 0.1) Hz, respectively. During the ramping up phase of B_1 and B_2 we reduce the magnetic field offset to 23 G and thus the scattering length to 300 a_0 in order to reduce losses from three-body recombination [28]. The trap now contains about 1.7×10^6 atoms at a peak phase space density of approximately 0.13.

3.5 *Forced evaporation towards BEC*

We start forced evaporative cooling by ramping down the power in all three remaining beams. Simultaneously we remove the reservoir by switching off the CO_2-laser A_2 that is not responsible for axial confinement. To assure a well-defined ramp over a large intensity range we control the light power of the near-infrared beam B_1 by means of a logarithmic photodiode and a servo loop. The power in CO_2-laser beam A_1 is ramped to zero within 5.5 s so that B_2 at the end of evaporation exclusively assures axial confinement. The change in beam pointing for A_2 does not affect the evaporation. For B_1 we approximately follow an exponential ramp over 5.5 s. The power in beam B_2 is only slightly reduced. The final power in B_1 and B_2 is 0.5 mW and 220 mW. We find and optimize this ramp by extending the ramp in discrete time steps of a few hundred milliseconds at the beginning and up to one second towards the end of the ramp.

At each step we search for a maximum in evaporation efficiency $\gamma = \log(D'/D)/\log(N/N')$ as a function of the trap depth and scattering length [34]. Here, D and D' are the phase-space densities at the beginning and end of each step, N and N' denote the respective particle numbers. Maximizing γ at each step results in an overall optimization of the evaporation path. We find that a magnetic field value of 21 G with scattering length $a = 210\,a_0$ is optimal during the forced evaporation phase. As can be seen from Fig. 3 the efficiency γ lies around 3 during the forced evaporation ramp. We attribute this high efficiency to the fact that atoms can escape the trap into almost all directions because of the levitation field.

We observe the phase transition after 2 s of forced evaporative cooling with about 5×10^5 atoms at a temperature of (200 ± 10) nK. At this point the power in beams B_1 and B_2 is

[5] IPG Laser PYL-10

8.7 mW and 250 mW. The duration of the ramp is relatively short. Our evaporation proceeds close to the hydrodynamic regime. Thus, significant improvement of the evaporation is not to be expected.

Further evaporation leaves a cigar-shaped condensate with the long axis in the horizontal plane. In Fig. 4 we show vertical density profiles of expanding condensates. The tunability of the scattering length allows us to explore different regimes of expansion. For Fig. 4a we expand the condensate at the creation scattering length of $210\,a_0$. This is the usual type of self-similar expansion in which the condensate in the Thomas–Fermi regime retains its parabolic shape [35]. For Fig. 4b we step the scattering length to zero at the moment of release from the trap. The mean-field interaction thus vanishes and the rate of expansion is greatly reduced. This exposes a small thermal component, for which a bimodal fit reveals a temperature of around 10 nK. The critical temperature at these trapping conditions is 24 nK; therefore, the expected condensate fraction agrees well with the measured value of 91%. From the fit to the data in Fig. 4 we obtain that there are up to 1.1×10^5 atoms in the condensate with a 20% calibration error. The error does not come from the fit but from the overall uncertainty in determining the atom number. Usually, the error from absorption imaging alone is around 50%, but we can calibrate the atom number from measurements on the chemical potential, see Sect. 4.1. For this particular experiment we measure the final trap frequencies to (4.3 ± 0.2) Hz and (21.1 ± 0.2) Hz along the axial and radial direction, respectively. We thus infer for the initial Thomas–Fermi sizes $R_{\rm r}^{\rm TF} = (8.7 \pm 0.3)$ μm and $R_{\rm a}^{\rm TF} = (42.5 \pm 1.2)$ μm along the radial and axial directions at a scattering length of $a = 210\,a_0$. The peak density of the condensate is $n_0 = (2.1 \pm 0.1)\,10^{13}\,{\rm cm}^{-3}$.

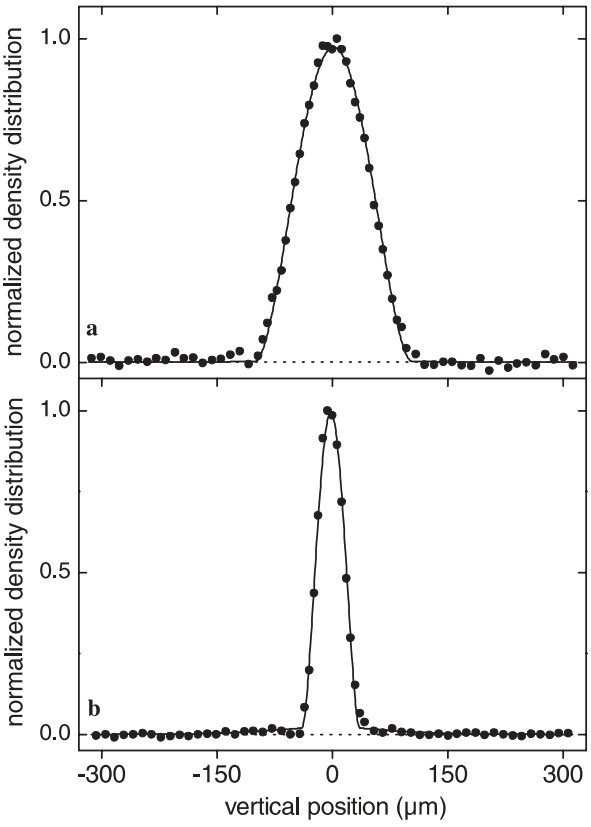

FIGURE 4 Vertical density profiles of Cs condensates after 100 ms of free expansion in the levitation field. The *solid curves* are fits to the data for the Thomas–Fermi profiles which include possible thermal components. For better distinction the baseline is dashed. (**a**) Expansion with no change in scattering length. The total number of atoms in the condensate is $N = 1.1 \times 10^5$. (**b**) Expansion near zero scattering length under the same conditions reveals a small thermal component with a temperature of about 10 nK

4 Tunable quantum gas

We now test the tunability of the condensate interaction. We first study the condensate expansion as a function of scattering length [36] in two different ways. We then specialize to the case when the interaction energy is switched off and present improved results on the ultra-slow expansion of the condensate in comparison with earlier measurements in [4]. Finally, we excite compression oscillations of the trapped condensate by suddenly stepping the scattering length to a lower value.

4.1 *Expansion energy as a function of scattering length*

We measure the release energy of the condensate for slow and fast changes of the scattering length. When we slowly vary the scattering length the wave function of the trapped condensate can follow adiabatically and the condensate remains in equilibrium. The release energy is proportional to the chemical potential of the condensate at the given value of the scattering length. The situation is different when we rapidly switch the scattering length at the moment of condensate release. The condensate then expands from a non-equilibrium state because the wave function has not had time to adjust to the change in interaction energy. This leads to strong changes for the rate of condensate expansion in comparison to the expansion from equilibrium.

We first consider a condensate in the Thomas–Fermi regime for which we adiabatically ramp the scattering length to a new value. For such a condensate, the release energy $E_{\rm rel}$ directly corresponds to the chemical potential $\mu_{\rm TF}$ through $\frac{7}{2} E_{\rm rel} = \mu_{\rm TF}$ [35], which is given by

$$\mu_{\rm TF} = \frac{h\bar{\nu}}{2} \left(\frac{15N}{a_{\rm ho}} \right)^{2/5} a^{2/5}. \qquad (1)$$

Here, $\bar{\nu}$ is the geometric average of the trap frequencies, N is the particle number in the condensate, and $a_{\rm ho} = \sqrt{\hbar/(m2\pi\bar{\nu})}$ is the oscillator length. For the experiment we produce a condensate with $N = 8.5 \times 10^4$ atoms at a creation scattering length of $a_{\rm c} = 210\,a_0$. We then slowly ramp the magnetic field to values between 20 and 35 G, setting the scattering length to a value between about 200 and $700\,a_0$. The slow ramping excludes values below the Feshbach resonance at 19.9 and above the one at 48.0 G because of strong loss[6]. The condensate is then released from the trap and we measure the release energy. The results are shown in Fig. 5. Here we assume that the magnetic field strength translates into scattering length according to Fig. 1. The data is well fit by a function of the

[6] A combination of slow ramping and quick jumping at the Feshbach resonances would allow access to the full range of values for the scattering length.

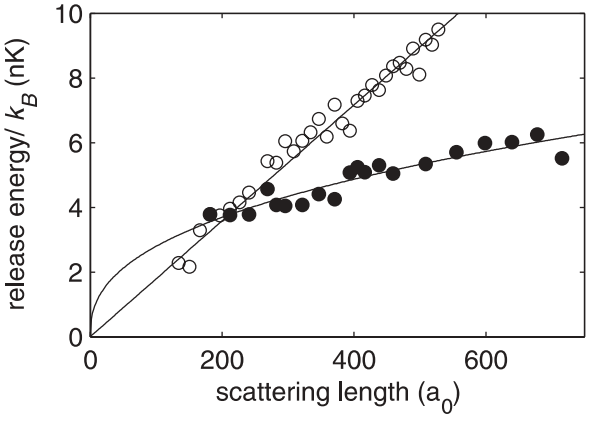

FIGURE 5 Release energy of the condensate as a function of scattering length a. The *filled circles* represent experimental data for the case of adiabatic ramping of a trapped condensate. The data, corresponding to 2/7 of the chemical potential at a given value of the scattering length, are fit by $C\,a^{2/5}$. The *open circles* represent data for rapid switching at the moment of condensate release. As discussed in the text, the straight line is not a fit. It connects the origin with the fitted value of the release energy at the creation scattering length

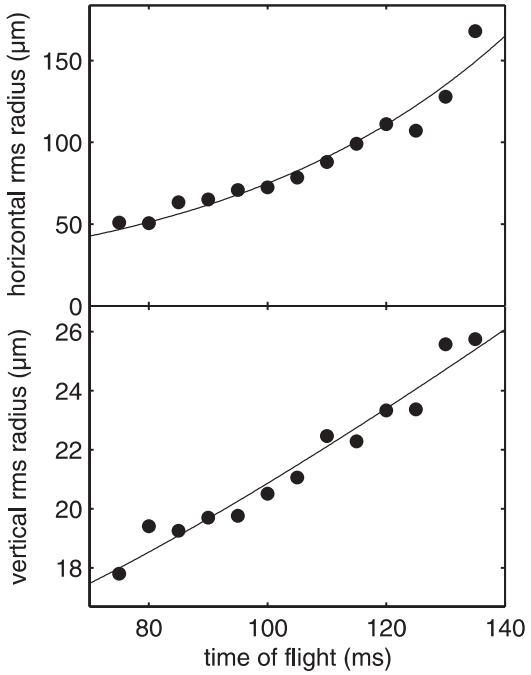

FIGURE 6 Expansion of the non-interacting condensate. The data points show the horizontal (above) and vertical (below) rms radius of the BEC as a function of expansion time near the zero crossing of scattering length. Note the different scales. The fit to the residual vertical expansion reveals a release energy of $k_B \times (51 \pm 3)$ pK. For the horizontal expansion the data are fit by $A \cosh(\alpha t)$ with $\alpha = 2\pi \times (3.20 \pm 0.23)$ Hz

form $Ca^{2/5}$ according to (1). From the fit parameter C we can deduce an independent estimate of the particle number $N = (8.2 \pm 1.3) \times 10^4$. The error is dominated by the error in determining the trap frequencies.

For a sudden change of the scattering length the condensate wave function has no time to react. For example, for an increase of the scattering length the density distribution is too narrow in comparison to the equilibrium density distribution at the new value of the scattering length. The condensate thus expands more rapidly than a condensate in equilibrium at this new value. Since the mean-field interaction energy of the condensate scales linearly with the scattering length for a given density profile [35], we expect a linear behavior of the release energy as a function of the final scattering length a. In Fig. 5 we thus compare the data for the measured release energy to a straight line $Ca_c^{2/5} a/a_c$ given by the origin and the fitted value of the release energy at the creation scattering length $a_c = 210\,a_0$. We find good agreement with the linear dependence.

4.2 *Ultra-slow condensate expansion*

We now study the expansion of the condensate near the zero-crossing of the scattering length. At the moment of condensate release, we rapidly switch the magnetic field from the creation field near 20 G to (17.17 ± 0.05) G, corresponding to $a = (3.4 \pm 3.0)\,a_0$. The error in determining the precise magnetic field at the position of condensate requires that we choose a slightly positive value of the scattering length to assure that no weakly attractive interactions modify the condensate expansion. The levitation field remains on, allowing for an extended observation period because the atoms then do not fall under gravity. Figure 6 shows the vertical and horizontal extent of a BEC with 1.2×10^5 atoms as a function of time after release from the trap. We only show the data after 75 ms of expansion when the optical density of the atomic cloud is sufficiently reduced to allow for reliable absorption imaging. The horizontal expansion is dominated by the magnetic anti-trapping potential which derives from the presence of the levitation field and which magnifies the atomic cloud according to the cosine hyperbolicus function, see Sect. 3.3. The measured rate of expansion $2\pi \times (3.20 \pm 0.23)$ Hz agrees reasonably well with the expected rate constant $\alpha = 2\pi \times 3.4$ Hz. The vertical expansion corresponds to a release energy of $k_B \times (51 \pm 3)$ pK. Note that this is much lower than the kinetic energy of the ground state $\hbar\omega_r/4 = k_B \times 253$ pK given by a radial trap frequency of $\omega_r = 2\pi \times 21.1$ Hz. It is remarkable that the release energy is less than the zero-point energy of the ground state. Since the spatial extent of the condensate is much larger than the size of the ground state wave function of the harmonic oscillator, the momentum spread, limited by the uncertainty of the wave function of the initial condensate, is lower than that of the ground state.

4.3 *Condensate oscillations*

By rapidly ramping the scattering length it is possible to excite oscillations of the condensate in the trap [37]. In fact, in the limit of a cigar shaped condensate one expects radial "compression" or "expansion oscillations" at twice the trap frequency. Compression oscillations can be seen in Fig. 7 where we plot the vertical radius of the released condensate as a function of hold time t_h in the trap. To excite the oscillation we step the scattering length from a value of $a = 363\,a_0$ ($B = 24.4$ G) to $a = 25\,a_0$ ($B = 17.6$ G) at time t_0. The condensate is then allowed to oscillate in the trap for a variable hold time t_h at the final value of the scattering length. We release the condensate at time $t_0 + t_h$ and take an image after 80 ms of free expansion. We fit the data

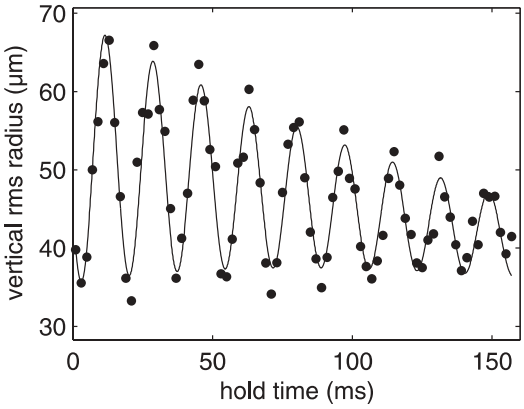

FIGURE 7 Condensate oscillations after rapid switching of the scattering length. The *filled circles* show the vertical rms radius of an expanding BEC with 7×10^4 atoms after 80 ms of free expansion as a function of hold time in the trap. The scattering length has been switched rapidly from $363\,a_0$ to $25\,a_0$. The *solid curve* is a fit to the data giving an oscillation frequency of (58.3 ± 0.2) Hz. We independently measure the radial trap frequency to (28 ± 1) Hz

by a sinusoidal function. The measured compression oscillation frequency of (58.3 ± 0.2) Hz agrees well with twice the radial trap frequency of $2 \times (28 \pm 1)$ Hz at the given trapping power. To account for the damping we have to introduce an exponential decay of the amplitude and of the offset value. The damping of the amplitude has a time constant of 126 ms. We have not yet identified the origin of this damping. Possibly the BEC samples different trapping frequencies due to the large amplitude of the oscillation, which would lead to an apparent damping. Also, damping might be caused by the interaction with a residual thermal cloud or by parametric processes [38].

5 Conclusion

We have shown that essentially pure Cs condensates can be produced with more than 10^5 atoms. In our optical trap it is possible to flexibly change the atomic scattering properties. The atomic condensate can now be used as the starting point for experiments where a tuning and ramping of the scattering properties can be exploited. It will be interesting to study the case of a non-interacting condensate at the zero-crossing of the scattering length. Such a condensate might be used in atom interferometers where one wishes to suppress any mean-field effects [39]. On the other hand, tuning to large values of the scattering length might allow the investigation of effects beyond the mean-field approximation [35]. Also, modulation of the scattering length could be used as an alternative tool to probe the excitation spectrum of the condensate. Finally, ultracold Cs_2 molecules can be created by ramping across one of the Feshbach resonances [8] and the transition from an atomic to a molecular condensate could then be studied.

ACKNOWLEDGEMENTS This work is supported by the Austrian "Fonds zur Förderung der wissenschaftlichen Forschung" (FWF) within SFB 15 (project part 16) and by the European Union in the frame of the Cold Molecules TMR Network under Contract No. HPRN-CT-2002-00290. M.M. is supported by DOC [Doktorandenprogramm der Österreichischen Akademie der Wissenschaften]. C.C. is supported by a Lise-Meitner-Fellowship from the FWF.

REFERENCES

1 M. Barrett, J. Sauer, M. Chapman: Phys. Rev. Lett. **87**, 010404 (2001)
2 Y. Takasu, K. Maki, K. Komori, T. Takano, K. Honda, M. Kumakura, T. Yabuzaki, Y. Takahashi: Phys. Rev. Lett. **91**, 040404 (2003)
3 G. Cennini, G. Ritt, C. Geckeler, M. Weitz: Phys. Rev. Lett. **91**, 240408 (2003)
4 T. Weber, J. Herbig, M. Mark, H.-C. Nägerl, R. Grimm: Science **299**, 232 (2003)
5 D. Rychtarik, B. Engeser, H.-C. Nägerl, R. Grimm: Phys. Rev. Lett. **92**, 173003 (2004)
6 C. Chin, A.J. Kerman, V. Vuletic, S. Chu: Phys. Rev. Lett. **90**, 033201 (2003)
7 C.A. Regal, C. Ticknor, J.L. Bohn, D.S. Jin: Nature **424**, 47 (2003)
8 J. Herbig, T. Kraemer, M. Mark, T. Weber, C. Chin, H.-C. Nägerl, R. Grimm: Science **301**, 1510 (2003)
9 S. Dürr, T. Volz, A. Marte, G. Rempe: Phys. Rev. Lett. **92**, 020406 (2004)
10 K. Xu, T. Mukaiyama, J.R. Abo-Shaeer, J.K. Chin, D.E. Miller, W. Ketterle: Phys. Rev. Lett. **91**, 210402 (2003)
11 S. Jochim, M. Bartenstein, A. Altmeyer, G. Hendl, S. Riedl, C. Chin, J. Hecker Denschlag, R. Grimm: Science **302**, 2101 (2003)
12 M. Greiner, C.A. Regal, D.S. Jin: Nature **426**, 537 (2003)
13 C. Chin, V. Vuletic, A.J. Kerman, S. Chu, E. Tiesinga, P.J. Leo, C.J. Williams: Phys. Rev. A **70**, 032701 (2004)
14 E.A. Donley, N.R. Claussen, S.T. Thomson, C.E. Wieman: Nature **417**, 529 (2002)
15 L. Radzihovsky, J. Park, P.B. Weichman: Phys. Rev. Lett. **92**, 160402 (2004)
16 M.W.J. Romans, R.A. Duine, S. Sachdev, H.T.C. Stoof: Phys. Rev. Lett. **93**, 020405 (2004)
17 J. Söding, D. Guéry-Odelin, P. Desbiolles, G. Ferrari, J. Dalibard: Phys. Rev. Lett. **80**, 1869 (1998)
18 J. Arlt, P. Bance, S. Hopkins, J. Martin, S. Webster, A. Wilson, K. Zetie, C.J. Foot: J. Phys. B **31**, L321 (1998)
19 D. Guéry-Odelin, J. Söding, P. Desbiolles, J. Dalibard: Europhys. Lett. **44**, 26 (1998)
20 D. Guéry-Odelin, J. Söding, P. Desbiolles, J. Dalibard: Optics Express **2**, 323 (1998)
21 S.A. Hopkins, S. Webster, J. Arlt, P. Bance, S. Cornish, O. Maragò, C.J. Foot: Phys. Rev. A. **61**, 032707 (2000)
22 P.J. Leo, E. Tiesinga, P.S. Julienne, D.K. Walter, S. Kadlecek, T.G. Walker: Phys. Rev. Lett. **81**, 1389 (1998)
23 A.M. Thomas, S. Hopkins, S.L. Cornish, C.J. Foot: J. Opt. B **5**, S107 (2003)
24 H. Perrin, A. Kuhn, I. Bouchoule, C. Salomon: Europhys. Lett. **42**, 395 (1998)
25 V. Vuletić, A.J. Kerman, C. Chin, S. Chu: Phys. Rev. Lett. **82**, 1406 (1999)
26 M. Hammes, D. Rychtarik, V. Druzhinina, U. Moslener, I. Manek-Hönninger, R. Grimm: J. Mod. Opt. **47**, 2755 (2000)
27 D.-J. Han, M.T. DePue, D.S. Weiss: Phys. Rev. A **63**, 023405 (2001)
28 T. Weber, J. Herbig, M. Mark, H.-C. Nägerl, R. Grimm: Phys. Rev. Lett. **91**, 123201 (2003)
29 D.-J. Han, M.T. DePue, D.S. Weiss: Phys. Rev. A **63**, 023405 (2001)
30 A.J. Kerman, V. Vuletić, C. Chin, S. Chu: Phys. Rev. Lett. **84**, 439 (2000)
31 D.M. Stamper-Kurn, H.-J. Miesner, A.P. Chikkatur, S. Inouye, J. Stenger, W. Ketterle: Phys. Rev. Lett. **81**, 2194 (1998)
32 T. Weber: PhD thesis, Univ. Innsbruck 2003
33 P. Treutlein, K.Y. Chung, S. Chu: Phys. Rev. A **63**, 051401 (2001)
34 W. Ketterle, N.J. Van Druten: Adv. At. Mol. Opt. Phys. **37**, 181 (1996)
35 L. Pitaevskii, S. Stringari: *Bose–Einstein Condensation* (Clarendon Press, Oxford 2003)
36 S.L. Cornish, N.R. Claussen, J.L. Roberts, E.A. Cornell, C.E. Wieman: Phys. Rev. Lett. **85**, 1795 (2000)
37 Y. Kagan, E.L. Surkov, G.V. Shlyapnikov: Phys. Rev. Lett. **79**, 2604 (2001)
38 F. Chevy, V. Bretin, P. Rosenbusch, K.W. Madison, J. Dalibard: Phys. Rev. Lett. **88**, 250402 (2002)
39 S. Gupta, K. Dieckmann, Z. Hadzibabic, D.E. Pritchard: Phys. Rev. Lett. **89**, 140401 (2002)

One additional correction that cannot be added as a σ in quadrature is the LMC rotation. Several young and intermediate-age kinematic tracers have been measured in the LMC, including HII regions, PN, CH stars, Miras, and carbon stars. In the inner regions of the LMC bar, these populations are rotating as a solid body, with 25 km/s per kpc. For a scale of 1 kpc = 1.2°, our fields should not show a rotation component larger than 10 km/s.

In addition, a correction for rotation may not be necessary for the RR Lyrae population, because there is no evidence that this old population follows the LMC rotation. On the basis of the Milky Way RR Lyrae, one might suspect that the LMC RR Lyrae do not rotate like the rest of the stars. However, a composite RR Lyrae population may be present. For example, earlier interpretation of the RR Lyrae number counts indicated an exponential disk distribution (*31*). Multiple components (halo plus thick disk) cannot be ruled out without rotation measurements. Our fields are not spread out enough to measure the rotation. In order to measure the systemic rotation of the RR Lyrae population, one would need to observe $N \cong 50$ stars per field in fields located >3° away on opposite sides of the bar. We estimate the correction in two ways: with the use of the velocities from HI maps (*32*) and with the use of the mean rotation fits of the disk (*22*, *24*). This correction does not change at all the LMC RR Lyrae velocity dispersion.

The large RR Lyrae velocity dispersion $\sigma_{true} = 53$ km/s implies that metal-poor old stars are distributed in a halo population. The velocity dispersion for the old RR Lyrae stars is higher than that for the old LMC clusters, although there are too few old clusters to measure the kinematics in the LMC. The presence of a kinematically hot, old, and metal-poor halo in the LMC suggests that galaxies like the Milky Way and small galaxies like the LMC have similar early formation histories (*33*).

The stellar halo traced by the RR Lyrae amounts only to 2% of the mass of the LMC, which is akin to the Milky Way halo (*1*, *22*). Consequently, its contribution to the microlensing optical depth should not be important (*26*, *34*). The ongoing Supermacho experiment will discover an order of magnitude more microlensing events toward the LMC (*35*), allowing us to test this prediction.

References and Notes

1. T. D. Kinman *et al.*, *Publ. Astron. Soc. Pac.* **103**, 1279 (1991).
2. M. Feast, in *Variable Stars and Galaxies*, Brian Warner, Ed. [Astronomical Society of the Pacific (ASP) Conference Series 30, San Francisco, 1992], p. 143.
3. E. W. Olszewski, N. B. Suntzeff, M. Mateo, *Annual Rev. Astron. Astrophys.* **34**, 511 (1996).
4. D. Minniti, *Astrophys. J.* **459**, 175 (1996).
5. A. Layden, in *Galactic Halos*, D. Zaritsky, Ed. (ASP Conference Series 136, San Francisco, 1998), p.14.
6. L. Searle, R. Zinn, *Astrophys. J.* **225**, 358 (1978).
7. O. Eggen, D. Lynden-Bell, A. Sandage, *Astrophys. J.* **136**, 748 (1962).
8. D. Minniti, A. A. Zijlstra, *Astrophys. J.* **467**, L13 (1996).
9. D. R. Alves, M. Rejkuba, D. Minniti, K. H. Cook, *Astrophys. J.* **573**, L51 (2002).
10. K. C. Freeman, G. Illingworth, A. Oemler, *Astrophys. J.* **272**, 488 (1983).
11. R. A. Schommer, E. W. Olszewski, N. B. Suntzeff, H. C. Harris, *Astron. J.* **103**, 447 (1992).
12. C. Alcock *et al.*, *Astrophys. J.* **490**, L59 (1997).
13. C. Alcock *et al.*, *Astrophys. J.* **482**, 89 (1997).
14. C. Alcock *et al.*, *Astrophys. J.* **542**, 257 (2000).
15. The MACHO RR Lyrae data are available online at the MACHO Project home page (www.macho.mcmaster.ca/). These RR Lyrae are classified on the basis of the MACHO light curves, with RRab being fundamental pulsators; RRc, first overtones; and RRe, double mode pulsators.
16. H. A. Smith, *The RR Lyrae Stars* (Cambridge Univ. Press, Cambridge, 1995).
17. C. M. Clement *et al.*, *Astron. J.* **122**, 2587 (2001).
18. M. Mayor *et al.*, *Astron. Astrophys.* **114**, 1087 (1997).
19. J. Kaluzny *et al.*, *Astron. Astrophys. Suppl. Ser.* **122**, 471 (1997).
20. J. E. Norris, K. C. Freeman, M. Mayor, P. Seitzer, *Astrophys. J.* **487**, 187 (1997).
21. D. S. Graff, A. Gould, N. B. Suntzeff, R. Schommer, E. Hardy, *Astrophys. J.* **540**, 211 (2000).
22. D. R. Alves, C. A. Nelson, *Astrophys. J.* **542**, 789 (2001).
23. E. Hardy, D. R. Alves, D. S. Graff, N. B. Suntzeff, R. A. Schommer, *Astrophys. J. Suppl. Ser.* **277**, 471 (2001).
24. R. P. van der Marel, D. R. Alves, E. Hardy, N. B. Suntzeff, *Astron. J.* **124**, 2639 (2002).
25. S. M. G. Hughes, P. R. Wood, I. N. Reid, *Astron. J.* **101**, 1304 (1991).
26. G. Gyuk, N. Dalal, K. Griest, *Astrophys. J.* **535**, 90 (2000).
27. We eliminated a low-velocity star, discrepant by more than 4σ from the mean, which could be a misidentified foreground star.
28. G. Clementini, R. Megighi, C. Cacciari, C. Gouiffes, *Mon. Not. R. Astron. Soc.* **267**, 83 (1994).
29. I. Skillen, J. A. Fernley, R. S. Stobie, R. F. Jameson, *Mon. Not. R. Astron. Soc.* **265**, 301 (1993).
30. We adopt a conservative error of 10 km/s for this quantity on the basis of uncertainties in the control samples.
31. C. Alcock *et al.*, *Astron. J.* **119**, 2194 (2000).
32. K. Rohlfs, J. Kreitschmann, B. C. Siegman, J. V. Feitzinger, *Astron. Astrophys.* **137**, 343 (1984).
33. The sample is not large enough and the velocities are not accurate enough to (i) detect tidal streams in front or behind the LMC and (ii) measure the systemic rotation of the halo RR Lyrae population. However, from a sample of this size, and with velocities measured to this accuracy, there is no difficulty in measuring the velocity dispersion and thus distinguishing a disk population from a halo population in the LMC.
34. C. Alcock *et al.*, *Astrophys. J.* **542**, 281 (2000).
35. C. Stubbs, in *The Galactic Halo*, B. K. Gibson, T. S. Axelrod, M. E. Putman, Eds. (ASP Conference Series 165, San Francisco, 2000), p. 503.

36. We gratefully acknowledge suggestions from E. Olszewski, A. Drake, M. Catelan, and C. Alcock and support by the Fondap Center for Astrophysics 15010003; by the U.S. Department of Energy National Nuclear Security Administration to University of California's Lawrence Livermore National Laboratory under contract W-7405-Eng-48; and by the Bilateral Science and Technology Program of the Australian Department of Industry, Technology, and Regional Development; and by ESO Program 70.B-0547.

27 June 2003; accepted 11 August 2003

Preparation of a Pure Molecular Quantum Gas

Jens Herbig, Tobias Kraemer, Michael Mark, Tino Weber, Cheng Chin, Hanns-Christoph Nägerl, Rudolf Grimm*

An ultracold molecular quantum gas is created by application of a magnetic field sweep across a Feshbach resonance to a Bose-Einstein condensate of cesium atoms. The ability to separate the molecules from the atoms permits direct imaging of the pure molecular sample. Magnetic levitation enables study of the dynamics of the ensemble on extended time scales. We measured ultralow expansion energies in the range of a few nanokelvin for a sample of 3000 molecules. Our observations are consistent with the presence of a macroscopic molecular matter wave.

Rapid progress in controlling ultracold atomic gases, culminating in the creation of atomic Bose-Einstein condensates (BECs) and opening the door to the realm of coherent matter-wave physics (*1*–*3*), has raised the question of whether a similar level of control is possible with molecular samples. Molecules, in contrast to atoms, have a much richer internal structure and can possess permanent vector or tensor properties, such as electric dipole moments, rotational angular momentum, and even chirality. Molecule-atom and molecule-molecule interactions are at least three- and four-body processes in nature, posing new challenges to our theoretical understanding. Exquisite control over the internal and external degrees of freedom of molecules could allow the experimental study of a new coherent chemistry (*4*), where matter-wave interference, quantum tunneling, and bosonic stimulation dominate the dynamics and where the interaction properties can be externally controlled and engineered with electromagnetic fields. Quantum degenerate molecular gases with permanent dipole moments are also prime candidates for the precise investigation of strongly correlated quantum

Institut für Experimentalphysik, Universität Innsbruck, Technikerstraβe 25, 6020 Innsbruck, Austria.

*To whom correspondence should be addressed. E-mail: rudolf.grimm@uibk.ac.at

systems and for the study of novel quantum phase transitions (*5*).

Several avenues have been investigated to cool and trap molecules. Slowing of a supersonic jet of polar molecules in time-varying electric fields (*6*) and buffer gas loading and trapping (*7*) in either electrostatic or magnetic traps both permit large molecular populations with temperatures in the mK range. Alternatively, creation of molecules by photoassociation of precooled atoms has led to molecular samples with temperatures in the μK range (*8*). For all these techniques, however, the resulting molecular phase-space density is still many orders of magnitude away from quantum degeneracy.

Starting with a sample of ultracold atoms, controlled production of molecules can be realized by the coherent coupling of an atom pair state to a molecular state. For example, a two-photon Raman transition has successfully been applied to produce molecules within an atomic BEC (*9*). Similarly, the coherent nature of atomic scattering can be exploited on a Feshbach resonance to transfer colliding atoms into molecules, which has been predicted to convert an atomic BEC into a molecular BEC (*10*–*12*). A Feshbach resonance occurs when the energy of the atomic scattering state is tuned into degeneracy with that of a bound molecular state (*13*). Experimentally, Feshbach resonances can be induced by an external magnetic field when both states feature different Zeeman shifts. Consequently, the atom-molecule coupling can be resonantly enhanced at a particular magnetic field value, and a sweep of the field near or across the resonance can convert the atoms into molecules in a single molecular quantum state. Existence of molecules created through atomic Feshbach resonances has been reported previously in a BEC of ^{85}Rb atoms (*14*), in thermal samples of ^{133}Cs (*15*), and in degenerate Fermi gases of ^{40}K (*16*) and ^{6}Li (*17*). These studies demonstrate the quantum coherence of the Feshbach coupling (*14*) and the ability to detect molecules within the atomic sample by means of laser-induced (*15*) or radiofrequency-induced (*16*) dissociation. However, the resulting molecular samples could not be spatially distinguished from the atoms, nor could the molecular clouds be directly imaged and analyzed. Here, we report the observation of pure molecular quantum matter, achieved by applying a Feshbach sweep to an atomic Cs BEC (*18*) with immediate spatial Stern-Gerlach separation of the two species. By monitoring the evolution of the coupled-out molecular cloud, we measure ultralow kinetic expansion energies that are consistent with the presence of a coherent molecular matter wave.

The starting point of our experiment was a pure BEC of up to 6×10^4 Cs atoms in an optical trap (*19*) with a radial Thomas-Fermi radius of 8.6 μm and an axial Thomas-Fermi radius of 26.5 μm. The atoms were in the hyperfine ground state with total angular momentum $F = 3$ and magnetic quantum number $m_F = 3$. As the optical trap was by far too weak to support the atoms against gravity during the evaporative cooling process, a magnetic field gradient of 30.9 G/cm was applied to levitate the atoms (*20*). This levitation is very sensitive to the magnetic moment of the trapped particles, and a small change of 1% in either the gradient or in the magnetic moment of the trapped particles is sufficient to render the trap unstable. The state $F = 3$, $m_F = 3$ features a narrow Feshbach resonance near 20 G (*21*) with an estimated resonance width of 5 mG (*22*). According to an analysis of the Cs scattering properties (*23*, *24*), the corresponding molecular state (*25*) has a predicted magnetic moment of $\mu = 0.93\ \mu_B$, where μ_B is Bohr's magneton, with a small magnetic field dependence (*22*). We produced molecules from the atomic BEC by sweeping the magnetic field across the resonance from a higher field value with a constant rate of typically 50 G/s (Fig. 1). The duration of the sweep was 3 ms. To turn off the Feshbach coupling, the field was then quickly lowered to a hold field at 17 G for a variable hold time while the optical trap was shut off (*20*). Because of the large magnetic field gradient along the vertical direction and the narrow resonance width of 5 mG, the Feshbach resonance occurred only within a 2-μm-thin horizontal layer. The conversion zone swept through the condensate from below at a speed of 15 μm/ms, or equivalently, in 1.3 ms. The newly created molecules immediately started falling with an acceleration of $0.38g$ due to their reduced magnetic moment. The molecular cloud was then completely separated from the atoms within 3 ms. By raising the magnetic field gradient quickly at the end of the sweep to about 50 G/cm, we levitated the molecules. In this case, the atoms accelerated upward at $0.61g$. Rapid molecule-atom separation and subsequent levitation permit long observation times for studying the dynamics of the molecular sample.

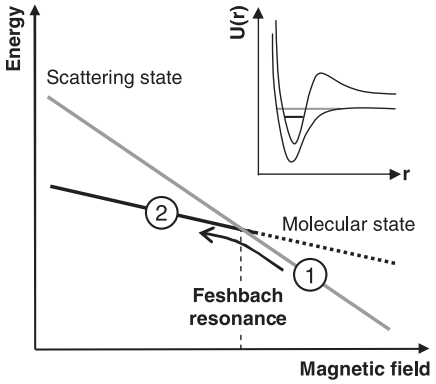

Fig. 1. Energy diagram for the atomic scattering state and the molecular bound state. The Feshbach resonance condition occurs near 20 G, where the Zeeman energy of the atomic scattering state becomes equal to that of a molecular bound state because of the difference in magnetic moments. Molecules at (2) are created from the BEC at (1) by a downward sweep of the magnetic field across the resonance. For detection, a reversed sweep brings the molecules above the dissociation limit. The inset schematically shows the molecular potential that corresponds to the open channel (lower curve) and the molecular potential that supports the bound state (upper curve). U, potential energy; r, interatomic distance.

To image the molecular cloud, we applied a reversed field sweep across the Feshbach resonance. The reversed sweep brought the molecules above the scattering continuum, and they quickly dissociated into free atoms. An immediate absorption image of the reconverted atoms thus reveals the spatial distribution of the molecules. A resolution limit of about 10 μm was caused by an energy on the order of $k_B \times 1$ μK released in the dissociation process (*20*), where k_B is the Boltzmann constant. We applied a fit to the image to determine the center position, the size of the spatial distribution, and the number of molecules. The evolution of the molecular cloud was recorded by variation of the hold time.

The complete atom-molecule separation is clearly visible in absorption images (Fig. 2). For reference, the image of a levitated BEC after 12 ms of expansion time is given in Fig. 2A. In Fig. 2, B and C, a Feshbach sweep has been applied to the BEC. In Fig. 2B, a coupled-out molecular cloud with ~3000 molecules can be seen below the atomic BEC. The number of atoms in the remaining BEC is reduced by 50% from those shown in Fig. 2A, to ~25,000. The molecular cloud is falling, because the magnetic field gradient needed to levitate the atoms was maintained. For Fig. 2C, the magnetic field gradient was

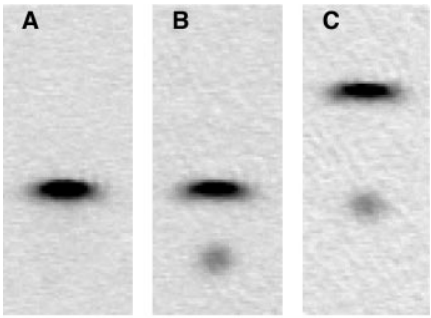

Fig. 2. Absorption images of (**A**) the levitated BEC without the Feshbach sweep, (**B**) the levitated BEC after the Feshbach sweep with a falling molecular cloud below, and (**C**) the levitated molecular cloud with an upward-rising BEC above. In (B) and (C), 3000 molecules are produced at a sweep rate of 50 G/s. The separation between the atoms and the molecules is 150 μm in (B) and 240 μm in (C).

raised after the Feshbach sweep in order to levitate the molecules. Hence, the atomic BEC accelerates upward and can be seen at the top of the image above the molecules. Careful adjustment of the magnetic field gradient to null the molecular acceleration allowed a precise determination of the molecular magnetic moment. We find that $\mu = 0.930(5)\ \mu_B$ (*20*), which is in good agreement with the theoretical calculation (*22*).

We investigated the atom-molecule conversion as a function of the end value B_f of the creation ramp. The ramp speed was kept constant at 50 G/s by variation of B_f together with the duration of the ramp. We have checked that for final values of B_f well above the resonance, the rapid jump over the resonance to the hold field after the end of the creation ramp did not produce any molecules. As Fig. 3 shows, molecules were created in a steplike manner. Simultaneously, the atomic population in the BEC is reduced. The transition value agrees well with the resonance position of 19.83(2) G as determined from three-body recombination loss measurements (*26*). From the plot of the atom number, it can be seen that up to 50% of the atoms were lost from the condensate, corresponding to ~25,000 atoms for this experiment. Hence, for a detected number of 3000 molecules, only about 24% of the lost atoms reappeared as partners in molecule formation. Also, we varied the speed of the downward magnetic field ramp across the Feshbach resonance and found that for decreasing ramp speed, the number of detected molecules saturated at a value of ~3000 molecules for speeds less than 50 G/s. The missing atoms and the saturation suggest that collisional relaxation into other molecular states occurs during the creation phase (*27*). After separation from the atoms, however, we did not detect any substantial loss.

We observed ultralow expansion energies for the molecular cloud in both the vertical and the horizontal directions. This was done in time-of-flight expansion measurements by variation of the hold time and hence the total expansion time. We plotted the vertical and horizontal root-mean-square (rms) widths of the reconverted atomic cloud as a function of total expansion time (Fig. 4, A and B). An apparent anisotropy of the expansion can be seen. The faster vertical expansion corresponds to a mean kinetic energy of $E_z = \frac{1}{2}\ k_B \times (40 \pm 3 \pm 2)$ nK (*20*), where the first one-standard-deviation error is statistical and the second one is systematic. The origin of this vertical energy was identified as the velocity dispersion of the molecules during the creation phase. The dispersion was caused by the fact that the conversion zone passes through the condensate at a finite speed from below. Hence, molecules created earlier acquire a larger velocity, and those created later acquire a smaller velocity, as a result of the gravity pulling. When the size of the BEC was taken into account, the vertical expansion energy as a result of the velocity dispersion was calculated to be about $\frac{1}{2}\ k_B \times 30$ nK for the molecular cloud, largely explaining the observed energy. In fact, vertical compression of the BEC did lead to a smaller vertical energy spread. By increasing the dipole trap depth to decrease the vertical extent of the BEC by a factor of 1.3, we found that the measured molecular kinetic energy was reduced in the expected way to a value of $E_z = \frac{1}{2}\ k_B \times (19 \pm 2 \pm 1)$ nK.

The horizontal expansion shown in Fig. 4B was unaffected by the velocity dispersion effect. However, a repulsive force due to the curvature of the levitation field acted on the molecules. This force resulted in an expansion of the cloud that follows a cosine hyperbolicus function and has been characterized previously (*18*). When the resolution limit due to the dissociation and the cosine hyperbolicus expansion dynamics (*20*) is incorporated, the fit in Fig. 4B yields an extremely low kinetic energy of $E_x = \frac{1}{2}\ k_B \times (2 \pm 2 \pm 3)$ nK in the horizontal direction.

The slow expansion of the molecules is consistent with the behavior of a macroscopic matter wave, as the horizontal expansion showed vanishing release energy and the vertical expansion was dominated by the dispersive gravity pulling effect, which is coherent in its nature. In view of a possible quantum degeneracy of the molecular ensemble, we first estimated the peak molecular density right after creation to $1 \times 10^{12}\ \mathrm{cm}^{-3}$, assuming 3000 molecules with a spatial density profile that reflects that of the atomic BEC (*28*). Given the free-space degeneracy condition, the critical temperature is 6 nK. Comparing this value to the observed horizontal energy spread that corresponds to (2 ± 2 ± 3) nK, we raise the question whether a molecular cloud with macroscopic coherence has been created. Our capability to monitor the spatial distribution of the molecules should allow us to detect interference patterns (*29*) and thus to investigate the macroscopic coherence of the molecular matter wave.

To create molecules coherently with high efficiency, it will be advantageous to load the atomic BEC into an optical lattice (*30*), which allows the preparation of a Mott insulator phase (*31*) with exactly two atoms per lattice site. Molecules created by a subsequent Feshbach sweep will therefore be individually isolated and immune to collisional losses. After the creation of a pure molecular matter wave, one might be able to coherently transfer the molecules to low-lying molecular states by two-photon Raman transitions. Hence, a complete and coherent control over the dynamics of molecular quantum matter can be envisaged.

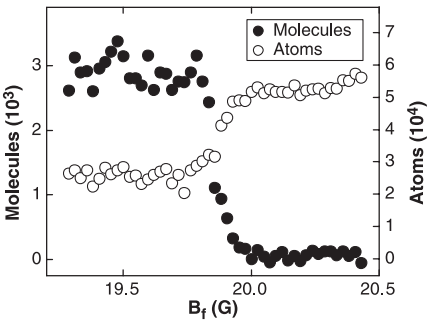

Fig. 3. Creation of molecules (solid circles) and simultaneous loss of atoms (open circles) as a function of the final value of the magnetic field ramp B_f for a fixed ramp speed of 50 G/s.

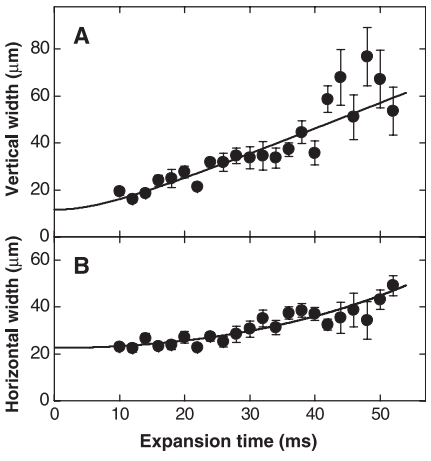

Fig. 4. (**A**) Vertical rms width and (**B**) horizontal rms width of the molecular cloud as a function of expansion time. From (A), a vertical expansion energy of $E_z = 1/2\ k_B \times (40 \pm 3 \pm 2)$ nK and an imaging resolution of 11(3) μm is obtained. The fit in (B) then yields an initial horizontal expansion energy of $E_x = 1/2\ k_B \times (2 \pm 2 \pm 3)$ nK.

References and Notes

1. E. A. Cornell, C. E. Wieman, *Rev. Mod. Phys.* **74**, 875 (2002).
2. W. Ketterle, *Rev. Mod. Phys.* **74**, 1131 (2002).
3. Nature Insight on Ultracold Matter, *Nature* **416**, 205 (2002).
4. D. J. Heinzen, R. Wynar, P. D. Drummond, K. V. Kheruntsyan, *Phys. Rev. Lett.* **84**, 5029 (2000).
5. K. Góral, L. Santos, M. Lewenstein, *Phys. Rev. Lett.* **88**, 170406 (2002).
6. H. L. Bethlem *et al.*, *Nature* **406**, 491 (2000).
7. J. D. Weinstein, R. deCarvalho, T. Guillet, B. Friedrich, J. M. Doyle, *Nature* **395**, 148 (1998).
8. N. Vanhaecke, W. de Souza Melo, B. L. Tolra, D. Comparat, P. Pillet, *Phys. Rev. Lett.* **89**, 063001 (2002).
9. R. Wynar, R. S. Freeland, D. J. Han, C. Ryu, D. J. Heinzen, *Science* **287**, 1016 (2000).
10. F. A. van Abeelen, B. J. Verhaar, *Phys. Rev. Lett.* **83**, 1550 (1999).
11. E. Timmermans, P. Tommasini, M. Hussein, A. Kerman, *Phys. Rep.* **315**, 199 (1999).
12. F. H. Mies, E. Tiesinga, P. S. Julienne, *Phys. Rev. A* **61**, 022721 (2000).
13. S. Inouye *et al.*, *Nature* **392**, 151 (1998).
14. E. A. Donley, N. R. Claussen, S. T. Thompson, C. E. Wieman, *Nature* **417**, 529 (2002).
15. C. Chin, A. J. Kerman, V. Vuletić, S. Chu, *Phys. Rev. Lett.* **90**, 033201 (2003).
16. C. A. Regal, C. Ticknor, J. L. Bohn, D. S. Jin, *Nature* **424**, 47 (2003).

17. C. Salomon, talk presented at the Quantum Electronics and Laser Science Conference, Baltimore, MD, 5 June 2003.
18. T. Weber, J. Herbig, M. Mark, H.-C. Nägerl, R. Grimm, *Science* **299**, 232 (2003); published online 5 Dec 2002 (10.1126/science.1079699).
19. The optical trap has a depth of $k_B \times 45$ nK with a radial trap frequency of 18 Hz and an axial trap frequency of 6 Hz. The axial direction of the BEC is oriented in the horizontal plane. At 20 G, the Cs scattering length is $a = 163\ a_0$, with a_0 denoting Bohr's radius. The resulting chemical potential for the BEC is $k_B \times 7$ nK.
20. Materials and methods are available as supporting material on *Science* Online.
21. V. Vuletić, C. Chin, A. J. Kerman, S. Chu, *Phys. Rev. Lett.* **83**, 943 (1999).
22. P. S. Julienne, E. Tiesinga, private communication (2003).
23. C. Chin, V. Vuletić, A. J. Kerman, S. Chu, *Phys. Rev. Lett.* **85**, 2717 (2000).
24. P. J. Leo, C. J. Williams, P. S. Julienne, *Phys. Rev. Lett.* **85**, 2721 (2000).
25. The molecular state was identified as a high-lying rovibrational state with internal angular momentum $f = 4$, magnetic quantum number $m_f = 4$, molecular orbital angular momentum $L = 4$, and angular momentum projection $m_L = 2$.
26. T. Weber, J. Herbig, M. Mark, H.-C. Nägerl, R. Grimm, *Phys. Rev. Lett.*, in press (available at http://arXiv.org/abs/physics/0304052).
27. V. A. Yurovsky, A. Ben-Reuven, P. S. Julienne, C. J. Williams, *Phys. Rev. A* **62**, 043605 (2000).
28. This is a reasonable assumption, because no molecules can be created in the absence of atoms.
29. M. R. Andrews *et al.*, *Science* **275**, 637 (1997).
30. D. Jaksch, V. Venturi, J. I. Cirac, C. J. Williams, P. Zoller, *Phys. Rev. Lett.* **89**, 040402 (2002).
31. M. Greiner, O. Mandel, T. Esslinger, T. W. Hänsch, I. Bloch, *Nature* **415**, 39 (2002).
32. We thank P. S. Julienne for very helpful discussions. Supported by the Austrian Science Fund (FWF) within Spezialforschungsbereich 15 (project part 16) and by the European Union through the Cold Molecules Training and Mobility of Researchers Network under contract no. HPRN-CT-2002-00290.

Supporting Online Material
www.sciencemag.org/cgi/content/full/1088876/DC1
Materials and Methods
Figs. S1 to S3

7 July 2003; accepted 11 August 2003
Published online 21 August 2003;
10.1126/science.1088876
Include this information when citing this paper.

Cooling Bose-Einstein Condensates Below 500 Picokelvin

A. E. Leanhardt,* T. A. Pasquini, M. Saba, A. Schirotzek, Y. Shin, D. Kielpinski, D. E. Pritchard, W. Ketterle

Spin-polarized gaseous Bose-Einstein condensates were confined by a combination of gravitational and magnetic forces. The partially condensed atomic vapors were adiabatically decompressed by weakening the gravito-magnetic trap to a mean frequency of 1 hertz, then evaporatively reduced in size to 2500 atoms. This lowered the peak condensate density to 5×10^{10} atoms per cubic centimeter and cooled the entire cloud in all three dimensions to a kinetic temperature of 450 ± 80 picokelvin. Such spin-polarized, dilute, and ultracold gases are important for spectroscopy, metrology, and atom optics.

The pursuit of lower temperatures is motivated by the quest to observe phenomena that occur on very low energy scales, in particular, phase transitions to new forms of matter. The achievement of temperatures near 1 K in solids and in liquids led to the discoveries of superconductivity (*1*) and superfluidity (*2*), respectively. The advent of laser cooling resulted in microkelvin temperature atomic vapors (*3*–*5*), subsequently cooled to nanokelvin temperatures by evaporative cooling to form dilute Bose-Einstein condensates (*6*, *7*) and quantum degenerate Fermi gases (*8*). Collectively, these low-temperature systems have a host of applications, including superconducting quantum interference devices (SQUIDs) (*9*), superfluid gyroscopes (*10*, *11*), and atomic clocks (*12*).

Temperature is a quantity that parameterizes how energy is distributed across the available states of a system, and effective temperatures can be defined for decoupled degrees of freedom or subsets of particles. For example, nuclear spins isolated from the kinetic motion of their respective atoms have been cooled by adiabatic demagnetization to an effective temperature of 280 pK (*13*). Spin ensembles have a finite number of available states, such that a spin-polarized sample, as in our work, would be characterized by zero effective temperature. In contrast, the motion of free particles is subject to a continuum of states, and the kinetic temperature of an ensemble can only asymptotically approach absolute zero.

Effective temperatures in atomic vapors are defined by the widths of velocity distributions, which can be much smaller than the mean velocity of the sample. Raman cooling (*14*, *15*) and velocity-selective coherent population trapping (VSCPT) (*16*) have generated velocity distributions with very narrow peaks, corresponding to nanokelvin and picokelvin effective temperatures. However, these temperatures were associated with the motion of only a subset of the atoms in the cloud and/or with atomic motion in only one dimension.

For trapped, partially condensed atomic vapors, the condensate fraction has zero entropy and the kinetic temperature of the sample is determined by the velocity distribution of the thermal (noncondensed) component. When released, the condensate fraction expands more slowly than the thermal component and has been characterized by picokelvin effective temperatures for anisotropic (*17*) and noninteracting (*18*) gases.

Cooling the atomic motion of entire ensembles in all three dimensions has proven difficult. To date, kinetic temperatures of a few hundred nanokelvin have been achieved with adiabatic and optical cooling (*19*, *20*), and evaporative cooling techniques have produced condensates with temperatures of 3 nK (*21*). By adiabatic expansion and subsequent evaporation, we have cooled partially condensed atomic vapors to picokelvin kinetic temperatures.

Our thermometry is calibrated by the Bose-Einstein condensation (BEC) phase transition temperature, T_c, which in the thermodynamic limit for a harmonically trapped ideal Bose gas is (*22*)

$$k_B T_c = \hbar\bar{\omega}\left(\frac{N}{\zeta(3)}\right)^{1/3} \approx 0.94\hbar\bar{\omega}N^{1/3} \qquad (1)$$

where k_B is Boltzmann's constant, $\hbar$ is Planck's constant h divided by 2π, $\zeta(n)$ is the Riemann Zeta function, $\bar{\omega} = (\omega_x\omega_y\omega_z)^{1/3}$ is the geometric mean of the harmonic trap frequencies, and N is the total number of atoms, both condensed and noncondensed. Thus, the atom number and the trap frequencies set an upper limit for the temperature of a confined Bose-Einstein condensate. In our work, adiabatically weakening the trapping potential to a mean frequency of $\bar{\omega} = 2\pi \times (1.12 \pm 0.08)$ Hz guaranteed that partially condensed atomic vapors with $N \leq 8000$ atoms had picokelvin temperatures ($T_c \leq 1$ nK).

Bose-Einstein condensates containing more than 10^7 ^{23}Na atoms were created in the weak field seeking $|F = 1, m_F = -1\rangle$ state in a magnetic trap, captured in the focus of an optical tweezers laser beam, and transferred into an auxiliary "science" chamber as described in (*23*). In the science chamber, condensates containing 2×10^6 to 3×10^6 atoms were transferred from the optical tweezers into a gravito-magnetic trap (Fig. 1A). A small coil carrying current I_S generated a vertical bias field B_z and supported the condensates against gravity with a vertical magnetic field gradient, $B_z' = 2\ mg/$

Department of Physics, MIT-Harvard Center for Ultracold Atoms, and Research Laboratory of Electronics, Massachusetts Institute of Technology, Cambridge, MA 02139, USA.

*To whom correspondence should be addressed. E-mail: ael@mit.edu

Bibliography

[And95] M. H. Anderson, J. R. Ensher, M. R. Matthews, C. E. Wieman, and E. A. Cornell, *Observation of Bose-Einstein Condensation in a Dilute Atomic Vapor*, Science **269**, 198 (1995).

[And97] M. R. Andrews, C. G. Townsend, H.-J. Miesner, D. S. Durfee, D. M. Kurn, and W. Ketterle, *Observation of Interference Between Two Bose-Einstein Condensates*, Science **275**, 637 (1997).

[AS01] J. R. Abo-Shaeer, C. Raman, J. M. Vogels, and W. Ketterle, *Observation of Vortex Lattices in Bose-Einstein Condensates*, Science **292**, 476 (2001).

[AS05] J. R. Abo-Shaeer, D. E. Miller, J. K. Chin, K. Xu, T. Mukaiyama, and W. Ketterle, *Coherent molecular optics using ultracold sodium dimers*, Phys. Rev. Lett. **94**, 040405 (2005).

[Bar92] M. C. Baruch and T. F. Gallagher, *Ramsey interference fringes in single pulse microwave multiphoton transitions*, Phys. Rev. Lett. **68**, 3515 (1992).

[Bar04] M. Bartenstein, A. Altmeyer, S. Riedl, S. Jochim, C. Chin, J. H. Denschlag, and R. Grimm, *Crossover from a Molecular Bose-Einstein Condensate to a Degenerate Fermi Gas*, Phys. Rev. Lett. **92**, 120401 (2004).

[Bar05] M. Bartenstein, A. Altmeyer, S. Riedl, R. Geursen, S. Jochim, C. Chin, J. H. Denschlag, R. Grimm, A. Simoni, E. Tiesinga, C. J. Williams, and P. S. Julienne, *Precise Determination of ^{6}Li Cold Collision Parameters by Radio-Frequency Spectroscopy on Weakly Bound Molecules*, Phys. Rev. Lett. **94**, 103201 (2005).

[Bet00] H. L. Bethlem, G. Berden, F. M. H. Crompvoets, R. T. Jongma, A. J. A. van Roij, and G. Meijer, *Electrostatic trapping of ammonia molecules*, Nature **406**, 491 (2000).

[Biz05] S. Bize, P. Laurent, M. Abgrall, H. Marion, I. Maksimovic, L. Cacciapuoti, J. Grünert, C. Vian, F. P. dos Santos, P. Rosenbusch, P. Lemonde,

G. Santarelli, P. Wolf, A. Clairon, A. Luiten, M. Tobar, and C. Salomon, *Cold atom clocks and applications*, J. Phys. B: At. Mol. Opt. Phys. **38**, S449 (2005).

[Bly05] P. Blythe, B. Roth, U. Fröhlich, H. Wenz, and S. Schiller, *Production of Ultracold Trapped Molecular Hydrogen Ions*, Phys. Rev. Lett. **95**, 183002 (2005).

[Bos24] S. N. Bose, *Wärmegleichgewicht im Strahlungsfeld bei Anwesenheit von Materie*, Z. Phys. **26** (1924).

[Bra95] C. C. Bradley, C. A. Sackett, J. J. Tollett, and R. G. Hulet, *Evidence of Bose-Einstein Condensation in an Atomic Gas with Attractive Interactions*, Phys. Rev. Lett. **75**, 1687 (1995).

[Chi00] C. Chin, V. Vuletić, A. J. Kerman, and S. Chu, *High Resolution Feshbach Spectroscopy of Cesium*, Phys. Rev. Lett. **85**, 2717 (2000).

[Chi01] C. Chin, *Cooling, collisions and coherence of cold cesium atoms in a trap*, Ph.D. thesis, Stanford University (2001).

[Chi04a] C. Chin, M. Bartenstein, A. Altmeyer, S. Riedl, S. Jochim, J. H. Denschlag, and R. Grimm, *Observation of the pairing gap in a strongly interacting Fermi gas*, Science **305**, 1128 (2004).

[Chi04b] C. Chin, V. Vuletic, A. J. Kerman, S. Chu, E. Tiesinga, P. J. Leo, and C. J. Williams, *Precision Feshbach spectroscopy of ultracold Cs_2*, Phys. Rev. A **70**, 032701 (2004).

[Chi05a] C. Chin and P. S. Julienne, *Radio-frequency transitions on weakly bound ultracold molecules*, Phys. Rev. A **71**, 012713 (2005).

[Chi05b] C. Chin, T. Kraemer, M. Mark, J. Herbig, P. Waldburger, H.-C. Nägerl, and R. Grimm, *Observation of Feshbach-Like Resonances in Collisions between Ultracold Molecules*, Phys. Rev. Lett. **94**, 123201 (2005).

[Chi06] C. Chin and V. V. Flambaum, *Enhanced Sensitivity to Fundamental Constants In Ultracold Atomic and Molecular Systems near Feshbach Resonances*, Phys. Rev. Lett. **96**, 230801 (2006).

[Cla03] N. R. Claussen, S. J. J. M. F. Kokkelmans, S. T. Thompson, E. A. Donley, E. Hodby, and C. E. Wieman, *Very-high-precision bound-state spectroscopy near a ^{87}Rb Feshbach resonance*, Phys. Rev. A **67**, 060701(R) (2003).

[Com99] E. D. Commins, *Electric dipole moments of leptons*, Adv. At. Mol. Opt. Phys. **40**, 1 (1999).

[Cor02] E. A. Cornell and C. E. Wieman, *Nobel Lecture: Bose-Einstein condensation in a dilute gas, the first 70 years and some recent experiments*, Rev. Mod. Phys. **74**, 875 (2002).

[Cub03] J. Cubizolles, T. Bourdel, S. J. J. M. F. Kokkelmans, G. V. Shlyapnikov, and C. Salomon, *Production of Long-Lived Ultracold Li_2 Molecules from a Fermi Gas*, Phys. Rev. Lett. **91**, 240401 (2003).

[Dal99] J. Dalibard, *Collisional dynamics of ultra-cold atomic gases*, Proceedings of the International School of Physics Enrico Fermi, IOS Press, Amsterdam, 1999, course CXL, Varenna 1998.

[Dav95] K. B. Davis, M.-O. Mewes, M. R. Andrews, N. J. van Druten, D. Durfee, D. M. Kurn, and W. Ketterle, *Bose-Einstein Condensation in a Gas of Sodium Atoms*, Phys. Rev. Lett. **75**, 3969 (1995).

[Den00] J. Denschlag, J. E. Simsarian, D. L. Feder, C. W. Clark, L. A. Collins, J. Cubizolles, L. Deng, E. W. Hagley, K. H. W. P. Reinhardt, S. L. Rolston, B. I. Schneider, and W. D. Phillips, *Generating Solitons by Phase Engineering of a Bose-Einstein Condensate*, Science **287**, 97 (2000).

[Don02] E. A. Donley, N. R. Claussen, S. T. Thompson, and C. E. Wieman, *Atom-molecule coherence in a Bose-Einstein condensate*, Nature **417**, 529 (2002).

[Dür04a] S. Dürr, T. Volz, A. Marte, and G. Rempe, *Observation of Molecules Produced from a Bose-Einstein Condensate*, Phys. Rev. Lett. **92**, 020406 (2004).

[Dür04b] S. Dürr, T. Volz, and G. Rempe, *Dissociation of ultracold molecules with Feshbach resonances*, Phys. Rev. A **70**, 031601(R) (2004).

[Efi71] V. Efimov, *Weakly-bound states of three resonantly-interacting particles*, Sov. J. Nucl. Phys. **12**, 589 (1971).

[Ein25] A. Einstein, *Quantentheorie des einatomigen idealen Gases*, Zweite Abhandlung, Sitzungsber. Preuss. Akad. Wiss. 3 (1925).

[Fer08] F. Ferlaino, S. Knoop, M. Mark, M. Berninger, H. Schöbel, H.-C. Nägerl, and R. Grimm, *Collisional Behavior of Four-Boson Systems with Large Scattering Length*, manuscript in preparation (2008).

[Fes58] H. Feshbach, *Unified theory of nuclear reactions*, Ann. Phys. (N. Y.) **5**, 357 (1958).

[Fio98] A. Fioretti, D. Comparat, A. Crubellier, O. Dulieu, F. Masnou-Seeuws, and P. Pillet, *Formation of Cold Cs_2 Molecules through Photoassociation*, Phys. Rev. Lett. **80**, 4402 (1998).

[Gao00] B. Gao, *Zero-energy bound or quasibound states and their implications for diatomic systems with an asymptotic van der Waals interaction*, Phys. Rev. A **62**, 050702 (2000).

[Gre02] M. Greiner, O. Mandel, T. Esslinger, T. W. Hänsch, and I. Bloch, *Quantum phase transition from a superfluid to a Mott insulator in a gas of ultracold atoms*, Nature **415**, 39 (2002).

[Gre03] M. Greiner, C. A. Regal, and D. S. Jin, *Emergence of a molecular Bose-Einstein condensate from a Fermi gas*, Nature **426**, 537 (2003).

[Gri93] G. F. Gribakin and V. V. Flambaum, *Calculation of the scattering length in atomic collisions using the semiclassical approximation*, Phys. Rev. A **48**, 546 (1993).

[Gri00] R. Grimm, M. Weidemüller, and Y. Ovchinnikov, *Optical dipole traps for neutral atoms*, Adv. At. Mol. Opt. Phys. **42**, 95 (2000).

[Her03] J. Herbig, T. Kraemer, M. Mark, T. Weber, C. Chin, H.-C. Nägerl, and R. Grimm, *Preparation of a Pure Molecular Quantum Gas*, Science **301**, 1510 (2003).

[Her05] J. Herbig, *Quantum-Degenerate Cesium: Atoms and Molecules*, Ph.D. thesis, University of Innsbruck (2005).

[Hod05] E. Hodby, S. T. Thompson, C. A. Regal, M. Greiner, A. C. Wilson, D. S. Jin, E. A. Cornell, and C. E. Wieman, *Production efficiency of ultracold Feshbach molecules in Bosonic and Fermionic systems*, Phys. Rev. Lett. **94**, 120402 (2005).

[Hol05] L. Hollberg, C. W. Oates, G. Wilpers, C. W. Hoyt, Z. W. Barber, S. A. Diddams, W. Oskay, and J. C. Bergquist, *Optical frequency/wavelength references*, J. Phys. B: At. Mol. Opt. Phys. **38**, S469 (2005).

[Hud02] J. J. Hudson, B. E. Sauer, M. R. Tarbutt, and E. A. Hinds, *Measurement of the Electron Electric Dipole Moment Using YbF Molecules*, Phys. Rev. Lett. **89**, 023003 (2002).

[Hud06] E. R. Hudson, H. J. Lewandowski, B. C. Sawyer, and J. Ye, *Cold Molecule Spectroscopy for Constraining the Evolution of the Fine Structure Constant*, Phys. Rev. Lett. **96**, 143004 (2006).

[Ing99] M. Inguscio, S. Stringari, and C. E. Wieman (Eds.), *Bose-Einstein Condensation in Atomic Gases*, Proceedings of the International School of Physics Enrico Fermi, IOS Press, Amsterdam, 1999, 1999, course CXL, Varenna 1998.

[Ing06] M. Inguscio, W. Ketterle, and C. Salomon (Eds.), *Ultracold Fermi Gases*, Proceedings of the International School of Physics Enrico Ferm, IOS Press, Amsterdam, 2007, 2006, course CLXIV, Varenna 2006.

[Jak02] D. Jaksch, V. Venturi, J. I. Cirac, C. J. Williams, and P. Zoller, *Creation of a Molecular Condensate by Dynamically Melting a Mott Insulator*, Phys. Rev. Lett. **89**, 040402 (2002).

[Jen04] A. S. Jensen, K. Riisager, D. V. Fedorov, and E. Garrido, *Structure and reactions of quantum halos*, Rev. Mod. Phys. **76**, 215 (2004).

[Joc03a] S. Jochim, M. Bartenstein, A. Altmeyer, G. Hendl, S. Riedl, C. Chin, J. Hecker Denschlag, and R. Grimm, *Bose-Einstein condensation of molecules*, Science **302**, 2101 (2003).

[Joc03b] S. Jochim, M. Bartenstein, A. Altmeyer, G. Hendl, C. Chin, J. Hecker Denschlag, and R. Grimm, *Pure Gas of Optically Trapped Molecules Created from Fermionic Atoms*, Phys. Rev. Lett **91**, 240402 (2003).

[Jul04] P. S. Julienne, E. Tiesinga, and T. Köhler, *Making Cold Molecules by Time-dependent Feshbach Resonances*, J. Mod. Opt. **513**, 1787 (2004).

[Ker00] A. J. Kerman, V. Vuletić, C. Chin, and S. Chu, *Beyond Optical Molasses: 3D Raman Sideband Cooling of Atomic Cesium to High Phase-Space Density*, Phys. Rev. Lett. **84**, 439 (2000).

[Ket99] W. Ketterle, D. S. Durfee, and D. M. Stamper-Kurn, *Making, probing and understanding Bose-Einstein condensates*, Proceedings of the International School of Physics Enrico Fermi, IOS Press, Amsterdam, 1999, course CXL, Varenna 1998.

[Ket02] W. Ketterle, *Nobel lecture: When atoms behave as waves: Bose-Einstein condensation and the atom laser*, Rev. Mod. Phys. **74**, 1131 (2002).

[Kha02] L. Khaykovich, F. Schreck, G. Ferrari, T. Bourdel, J. Cubizolles, L. D. Carr, Y. Castin, and C. Salomon, *Formation of a Matter-Wave Bright Soliton*, Science **296**, 1290 (2002).

[Kno08a] S. Knoop, F. Ferlaino, M. Mark, M. Berninger, H. Schöbel, H.-C. Nägerl, and R. Grimm, *Observation of Resonant Enhancement in Ultracold Atom-Dimer Scattering*, manuscript in preparation (2008).

[Kno08b] S. Knoop, M. Mark, F. Ferlaino, J. G. Danzl, T. Kraemer, H.-C. Nägerl, and R. Grimm, *Metastable Feshbach Molecules in High Rotational States*, Phys. Rev. Lett. **100**, 083002 (2008).

[Köh05] T. Köhler, E. Tiesinga, and P. S. Julienne, *Spontaneous Dissociation of* ^{85}*Rb Feshbach Molecules*, Phys. Rev. Lett. **94**, 020402 (2005).

[Köh06] T. Köhler, K. Góral, and P. S. Julienne, *Production of cold molecules via magnetically tunable Feshbach resonances*, Rev. Mod. Phys. **78**, 1311 (2006).

[Kok01] S. J. J. M. F. Kokkelmans, H. M. J. Vissers, and B. J. Verhaar, *Formation of a Bose condensate of stable molecules via a Feshbach resonance*, Phys. Rev. A **63**, 031601 (2001).

[Kra04] T. Kraemer, J. Herbig, M. Mark, T. Weber, C. Chin, H.-C. Nägerl, and R. Grimm, *Optimized production of a cesium Bose-Einstein condensate*, Appl. Phys. B **79**, 1013 (2004).

[Kra06a] P. T. Kraemer, *Few-Body Interactions in an Ultracold Gas of Cesium Atoms*, Ph.D. thesis, University of Innsbruck (2006).

[Kra06b] T. Kraemer, M. Mark, P. Waldburger, J. G. Danzl, C. Chin, B. Engeser, A. D. Lange, K. Pilch, A. Jaakkola, H.-C. Nägerl, and R. Grimm, *Evidence for Efimov Quantum States in an Ultracold Gas of Cesium Atoms*, Nature **440**, 315 (2006).

[Lan32] L. Landau, Phys. Z. Sowjetunion **2**, 46 (1932).

[Lan77] L. D. Landau and E. M. Lifshitz, *Quantum Mechanics: Non-Relativistic Theory*, Pergamon Press, Oxford, 1977.

[Leo00] P. J. Leo, C. J. Williams, and P. S. Julienne, *Collision Properties of Ultracold ^{133}Cs Atoms*, Phys. Rev. Lett. **85**, 2721 (2000).

[Mad00] K. W. Madison, F. Chevy, W. Wohlleben, and J. Dalibard, *Vortex Formation in a Stirred Bose-Einstein Condensate*, Phys. Rev. Lett. **84**, 806 (2000).

[Mar03] M. Mark, *Bose-Einstein Kondensation von Cäsium*, Master's thesis, University of Innsbruck (2003).

[Mar05] M. Mark, T. Kraemer, J. Herbig, C. Chin, H.-C. Nägerl, and R. Grimm, *Efficient creation of molecules from a cesium Bose-Einstein condensate*, Europhys. Lett. **69**, 706 (2005).

[Mar07a] M. Mark, F. Ferlaino, S. Knoop, J. G. Danzl, T. Kraemer, C. Chin, H.-C. Nägerl, and R. Grimm, *Spectroscopy of ultracold trapped cesium Feshbach molecules*, Phys. Rev. A **76**, 042514 (2007).

[Mar07b] M. Mark, T. Kraemer, P. Waldburger, J. Herbig, C. Chin, H.-C. Nägerl, and R. Grimm, *"Stückelberg Interferometry" with Ultracold Molecules*, Phys. Rev. Lett. **99**, 113201 (2007).

[Mat99] M. R. Matthews, B. P. Anderson, P. C. Haljan, D. S. Hall, C. E. Wieman, and E. A. Cornell, *Vortices in a Bose-Einstein Condensate*, Phys. Rev. Lett. **83**, 2498 (1999).

[Met99] H. J. Metcalf and P. van der Straten, *Laser cooling and trapping*, Springer-Verlag, New York, 1999.

[Mie96] F. H. Mies, C. J. Williams, P. S. Julienne, and M. Krauss, *Estimating Bounds on Collisional Relaxation Rates of Spin-Polarized ^{87}Rb Atoms at Ultracold Temperatures*, J. Res. Natl. Inst. Stan. **101**, 521 (1996).

[MS01] F. Masnou-Seeuws and P. Pillet, *Formation of ultracold molecules via photoassociation in a gas of laser cooled atoms*, Adv. At. Mol. Opt. Phys. **47**, 53 (2001).

[Mud04] M. Mudrich, O. Bünermann, F. Stienkemeier, O. Dulieu, and M. Weidemüller, *Formation of cold bialkali dimers on helium nanodroplets*, Eur. Phys. J. D **31**, 291 (2004).

[Muk04] T. Mukaiyama, J. R. Abo-Shaeer, K. Xu, J. K. Chin, and W. Ketterle, *Dissociation and decay of ultracold sodium molecules*, Phys. Rev. Lett. **92**, 180402 (2004).

[Nik84] E. E. Nikitin and S. Y. Umanskii, *Theory of Slow Atomic Collisions*, Springer-Verlag, Berlin, 1984.

[Osp06] C. Ospelkaus, S. Ospelkaus, L. Humbert, P. Ernst, K. Sengstock, and K. Bongs, *Ultracold Heteronuclear Molecules in a 3D Optical Lattice*, Phys. Rev. Lett. **97** (2006).

[Pet04] D. S. Petrov, C. Salomon, and G. V. Shlyapnikov, *Weakly bound dimers of fermionic atoms*, Phys. Rev. Lett. **93**, 090404 (2004).

[Pit03] L. Pitaevskii and S. Stringari, *Bose-Einstein Condensation*, Oxford University Press, 2003.

[Ram56] N. Ramsey, *Molecular Beams*, Oxford University Press, London, 1956.

[Reg03] C. A. Regal, C. Ticknor, J. L. Bohn, and D. S. Jin, *Creation of ultracold molecules from a Fermi gas of atoms*, Nature **424**, 47 (2003).

[Reg04] C. A. Regal, M. Greiner, and D. S. Jin, *Observation of Resonance Condensation of Fermionic Atom Pairs*, Phys. Rev. Lett. **92**, 040403 (2004).

[Rie05] T. Rieger, T. Junglen, S. A. Rangwala, P. W. H. Pinkse, and G. Rempe, *Continuous Loading of an Electrostatic Trap for Polar Molecules*, Phys. Rev. Lett. **95**, 173002 (2005).

[Rom04] M. W. J. Romans, R. A. Duine, S. Sachdev, and H. T. C. Stoof, *Quantum phase transition in an atomic Bose gas with a Feshbach resonance*, Phys. Rev. Lett. **93**, 020405 (2004).

[Rus29] H. N. Russell, A. G. Shenstone, and L. A. Turner, Phys. Rev. **33**, 900 (1929).

[Sch94] W. Schöllkopf and J. P. Toennis, *Nondestructive Mass Selection of Small van der Waals Clusters*, Science **266**, 1345 (1994).

[Sch07] H. Schöbel, *Ultrakalte Cs_2-Moleküle in einer optischen Dipolfalle mit kontrollierbarer Elliptizität*, Master's thesis, University of Innsbruck (2007).

[Smi07] G. Smirne, R. M. Godun, D. Cassettari, V. Boyer, C. J. Foot, T. Volz, N. Syassen, S. Dürr, G. Rempe, M. D. Lee, K. Góral, and T. Köhler, *Collisional relaxation of Feshbach molecules and three-body recombination in ^{87}Rb Bose-Einstein condensates*, Phys. Rev. A **75**, 020702 (2007).

[Söd98] J. Söding, D. Guéry-Odelin, P. Desbiolles, G. Ferrari, and J. Dalibard, *Giant Spin Relaxation of an Ultracold Cesium Gas*, Phys. Rev. Lett. **80**, 1869 (1998).

[Sta06] P. Staanum, S. D. Kraft, J. Lange, R. Wester, and M. Weidemüller, *Experimental Investigation of Ultracold Atom-Molecule Collisions*, Phys. Rev. Lett. **96** (2006).

[Stö06] T. Stöferle, H. Moritz, K. Günter, M. Köhl, and T. Esslinger, *Molecules of Fermionic Atoms in an Optical Lattice*, Phys. Rev. Lett. **96** (2006).

[Str02] K. E. Strecker, G. B. Partridge, A. G. Truscott, and R. Hulet, *Formation and propagation of matter-wave soliton trains*, Nature **417**, 150 (2002).

[Str03] K. E. Strecker, G. B. Partridge, and R. G. Hulet, *Conversion of an Atomic Fermi Gas to a Long-Lived Molecular Bose Gas*, Phys. Rev. Lett. **91** (2003).

[Stü32] E. C. G. Stückelberg, Helv. Phys. Acta **5**, 369 (1932).

[Stw76] W. C. Stwalley, *Stability of Spin-Aligned Hydrogen at Low Temperatures and High Magnetic Fields: New Field-Dependent Scattering Resonances and Predissociations*, Phys. Rev. Lett. **37**, 1828 (1976).

[Sya06] N. Syassen, T. Volz, S. Teichmann, S. Dürr, and G. Rempe, *Collisional decay of ^{87}Rb Feshbach molecules at 1005.8 G*, Phys. Rev. A **74**, 062706 (2006).

[Tak98] T. Takekoshi, B. M. Patterson, and R. J. Knize, *Observation of Optically Trapped Cold Cesium Molecules*, Phys. Rev. Lett. **81**, 5105 (1998).

[Tha06] G. Thalhammer, K. Winkler, F. Lang, S. Schmid, R. Grimm, and J. Hecker Denschlag, *Long-Lived Feshbach Molecules in a Three-Dimensional Optical Lattice*, Phys. Rev. Lett. **96**, 050402 (2006).

[Tho05a] S. T. Thompson, E. Hodby, and C. E. Wieman, *Spontaneous Dissociation of ^{85}Rb Feshbach Molecules*, Phys. Rev. Lett. **94**, 020401 (2005).

[Tho05b] S. T. Thompson, E. Hodby, and C. E. Wieman, *Ultracold Molecule Production via a Resonant Oscillating Magnetic Field*, Phys. Rev. Lett. **95**, 190404 (2005).

[Tie93] E. Tiesinga, B. J. Verhaar, and H. T. C. Stoof, *Threshold and resonance phenomena in ultracold gound-state collisons*, Phys. Rev. A **47**, 4114 (1993).

[Tie07] E. Tiesinga and P. S. Julienne, private communication (2007).

[Tre01] P. Treutlein, K. Y. Chung, and S. Chu, *High-brightness atom source for atomic fountains*, Phys. Rev. A **63**, 051401 (2001).

[Van02] N. Vanhaecke, W. de Souza Melo, B. L. Tolra, D. Comparat, and P. Pillet, *Accumulation of Cold Cesium Molecules via Photoassociation in a Mixed Atomic and Molecular Trap*, Phys. Rev. Lett. **89**, 063001 (2002).

[Vol06] T. Volz, N. Syassen, D. M. Bauer, E. Hansis, S. Dürr, and G. Rempe, *Preparation of a quantum state with one molecule at each site of an optical lattice*, Nature Phys. **2**, 692 (2006).

[Vul99] V. Vuletić, A. J. Kerman, C. Chin, and S. Chu, *Observation of Low-Field Feshbach Resonances in Collisions of Cesium Atoms*, Phys. Rev. Lett. **82**, 1406 (1999).

[Web03a] T. Weber, *Bose-Einstein Condensation of Optically Trapped Cesium*, Ph.D. thesis, University of Innsbruck (2003).

[Web03b] T. Weber, J. Herbig, M. Mark, H.-C. Nägerl, and R. Grimm, *Bose-Einstein Condensation of Cesium*, Science **299**, 232 (2003).

[Web03c] T. Weber, J. Herbig, M. Mark, H.-C. Nägerl, and R. Grimm, *Three-body recombination at large scattering lengths in an ultracold atomic gas*, Phys. Rev. Lett. **91**, 123201 (2003).

[Wei85] H. Weichenmeier, U. Diemer, M. Wahl, M. Raab, W. Müller, and W. Demtröder, *Accurate ground state potential of Cs_2 up to the dissociation limit*, J. Chem. Phys. **82**, 5354 (1985).

[Wei98] J. D. Weinstein, R. Decarvalhor, T. Guillet, B. Friedrich, and J. M. Doyle, *Magnetic trapping of calcium monohydride molecules at millikelvin temperatures*, Nature **395**, 148 (1998).

[Wei99] J. Weiner, V. S. Bagnato, S. Zilio, and P. S. Julienne, *Experiments and theory in cold and ultracold collisions*, Rev. Mod. Phys. **71**, 1 (1999).

[Win06] K. Winkler, G. Thalhammer, F. Lang, R. Grimm, J. Hecker Denschlag, A. J. Daley, A. Kantian, H. P. Büchler, and P. Zoller, *Repulsively bound atom pairs in an optical lattice*, Nature **441**, 853 (2006).

[Win07] K. Winkler, F. Lang, G. Thalhammer, P. van der Straten, R. Grimm, and J. H. Denschlag, *Coherent Optical Transfer of Feshbach Molecules to a Lower Vibrational State*, Phys. Rev. Lett. **98**, 043201 (2007).

[Xu03] K. Xu, T. Mukaiyama, J. R. Abo-Shaeer, J. K. Chin, D. E. Miller, and W. Ketterle, *Formation of Quantum-Degenerate Sodium Molecules*, Phys. Rev. Lett. **91**, 210402 (2003).

[Yoa92] S. Yoakum, L. Sirko, and P. M. Koch, *Stueckelberg oscillations in the multiphoton excitation of helium Rydberg atoms: Observation with a pulse of coherent field and suppression by additive noise*, Phys. Rev. Lett. **69**, 1919 (1992).

[Zah06] N. Zahzam, T. Vogt, M. Mudrich, D. Comparat, and P. Pillet, *Atom-Molecule Collisions in an Optically Trapped Gas*, Phys. Rev. Lett. **96** (2006).

[Zen32] C. Zener, Proc. R. Soc. London, Ser. A **137**, 696 (1932).

[Zwi03] M. W. Zwierlein, C. A. Stan, C. H. Schunck, S. M. F. Raupach, S. Gupta, Z. Hadzibabic, and W. Ketterle, *Observation of Bose-Einstein Condensation of Molecules*, Phys. Rev. Lett. **91**, 250401 (2003).

[Zwi05] M. W. Zwierlein, C. A. Stan, C. H. Schunck, S. M. F. Raupach, S. Gupta, Z. Hadzibabic, and W. Ketterle, *Vortices and superfluidity in a strongly interacting Fermi gas*, Nature **435**, 1047 (2005).

Acknowledgement - Danksagung

Thanks

I have spent now some years in Rudi's group, dating back to my master thesis I did already at the Cs BEC experiment. I enjoyed my "growing up" within the group over these last few years and I have to say: I had a great time! Therefore, I would like to thank all the people who made my PhD a success and who accompanied me during this time.

I would like to thank my advisor Rudi Grimm for his encouraging and professional way of guiding the group, the experiment and myself. From him I did not only learn physics but also many other skills, which I appreciate maybe most. I would like to thank Hanns-Christoph Nägerl as he always had an ear for open questions and for his everlasting support for better lab equipment and new technologies. A big thanks belongs to Cheng Chin, for his great support and ideas and all our fruitful discussions. I would like to thank the post-docs Francesca Ferlaino and Steven Knoop for all their enthusiasm and great efforts they have shown in the 'final' phase of my PhD. I have enjoyed the time with them, both, inside and outside the lab.

Finally, I would like to thank all my current and former colleagues from the lab and the institute, the staff-members, my friends and family.

Danke schön oder einfach: Dånkschia

Tobias, der mit mir die meiste Zeit als Doktorand im Labor verbracht hat. Gemeinsam haben wir unzählige Messstunden erlebt und oft haarsträubende Probleme in den Griff bekommen. Trotzdem fanden wir immer wieder Zeit, gemeinsam klettern zu gehen oder Berge zu erklimmen.

Tino und Jens, die mich bereits als Diplomanden in die Tiefen des Experiments eingeweiht haben. Sie haben eine großartige Maschine aufgebaut.

"Meinen" ehemaligen Diplomanden Philipp, Hans und Harald, die mit Ihrer Arbeit nicht nur das Labor sondern auch das Arbeitsklima stets bereicherten.

Meinem Nachfolger Martin, der mit viel Wiener Charme und Humor voll motiviert nach

Innsbruck gekommen ist und den bisher gepflegten Labor-Mottos alle Ehre macht. In seinen Händen ist das Experiment bestens aufgehoben!

Der Werkstatt mit Toni und Helmut sowie ehemals Stefan und Josef. Ihr Know-How und Entgegenkommen bei vielen technischen und maschinellen Problemen schätze ich über alles.

Gleiches gilt auch für die Jungs vom Elektronik-Labor, Manuel und Arthur. Nicht nur zu 'Bürozeiten' waren sie mit Rat und Tat hilfreich - als kleine Entschädigung dafür gab's von mir vielleicht manchen Kletter- oder Ausrüstungstipp.

Ein herzliches Dankeschön gebührt den Sekretariaten im 4. Stock mit Christine, Patricia, Karin, Gabriel und Nicole. Für die großartige Unterstützung in vielen Bürokratieangelegenheiten aber auch für so manch reich gedecktes Buffet. Bei allem Einsatz blieb zwischendurch ein nettes Gespräch über Dies und Das und die schönen Berge nicht aus.

Außerdem möchte ich mich bei allen ehemaligen und aktiven Mitgliedern der Grimm-Gruppe bedanken. Für ihre großartige und freundliche Unterstützung bei technischen Schwierigkeiten, bei der Beantwortung vieler Fragen und nicht zuletzt für die stets angenehme und positive Gruppenatmosphäre.

Den Jungs vom Rb-Lab von Johannes sowie der Crew vom CsIII-Lab sei besonders gedankt. Laserlicht wird nicht 'einfach so' verteilt und wer koppelt schon gerne unzählige Male eine Faser ein? Danke!

Der gesamten FeLiKx-Gruppe unter Florian S. am IQOQI, für all Ihre Mühen und besonders für Ihre Unterstützung als "Laser-Reservoir". An dieser Stelle übrigens 'big thanks' an Devang für die Korrekturhilfe meiner Arbeit.

Bei Elmar und Stefan S. bedanke ich mich besonders für die nette Büroatmosphäre, die auch schon mit Markus B. gepflegt wurde. Sie alle hatten es vermutlich nicht immer leicht mit dem tiroler Oberländer und so gehörten sprachliche Verständigungsschwierigkeiten oder das Dulden lautstarker Telefonate zum Alltag... danke!

Schliesslich gilt ein besonderer Dank allen, die mich ausserhalb der Uni begleitet haben:

Klaus, für die coolen Zeiten auf unseren Konferenz-Wochen und als perfekter Arco-Guide.

Liesbeth, daß sie mich in Arzl immer so verwöhnt hat und für ihr großartiges Vertrauen.

Tommi, wilde Touren im steilen Gelände haben uns Beide mehr als ich je gedacht hätte zusammengeschweisst. Es war einfach immer eine Freude und Wohltat!

Chris, viele Kletterrouten und gute Gespräche gaben immer wieder Antrieb.

All meinen Freunden, die meine Höhen und Tiefen miterleben durften, mir zuhörten und die stets für mich da waren.

Meinen Geschwistern samt Anhang und Nachwuchs. Danke für all ihr Verständnis und ihre Nachsichtigkeit, daß sie so oft zu kurz gekommen sind und daß ich gewisse Dinge binnen kürzester Zeit auch einfach wieder vergessen habe.

Katrin, für die Süsse meines Lebens. Für ihr immerwährendes Verständnis bei meinem Tun und ihren Ansporn. Und nicht zuletzt für all die traumhafte Zeit, die wir auf unserer bergigen Spielwiese in den letzten Jahren gemeinsam erlebt haben.

Meinen Eltern Maria und Andreas, für all die Freiheiten und Möglichkeiten, die sie mir seit jeher geboten haben, um dieses Ziel zu erreichen.